FY22 Status Update: SNF Interim Storage Canister Corrosion and Surface Environment Investigations

Spent Fuel and Waste Disposition

Prepared for
US Department of Energy
Spent Fuel and Waste Science and Technology
Rebecca Schaller, Andrew Knight, Ryan Katona, Brendan Nation, Erin Karasz, and Charles Bryan
Sandia National Laboratories

September 28, 2022
M2SF-22SN010207056
SAND2022-xxxxx X

Sandia National Laboratories

Sandia National Laboratories is a multi-mission laboratory managed and operated by National Technology & Engineering Solutions of Sandia, LLC., a wholly owned subsidiary of Honeywell International, Inc., for the U.S. Department of Energy's National Nuclear Security Administration under contract DE-NA0003525.

APPENDIX E

NFCSC DOCUMENT COVER SHEET[1]

Name/Title of Deliverable/Milestone/Revision No. M2SF-22SN010207056: FY22 Status Update: SNF Interim Storage Canister Corrosion and Surface Environment Canisters

Work Package Title and Number SF-22SN01020705: SCC and Dry Storage Investigations – SNL

Work Package WBS Number 1.08.01.02.07

Responsible Work Package Manager Charles R. Bryan/ *Charles R. Bryan* 9.28.2022
(Name/Signature) Date Submitted

Quality Rigor Level for Deliverable/Milestone[2]	☐ QRL-1 ☐ Nuclear Data	☐ QRL-2	☒ QRL-3	☐ QRL-4 Lab QA Program[3]

This deliverable was prepared in accordance with QA program which meets the requirements of Sandia National Laboratories

☒ DOE Order 414.1 ☐ NQA-1 ☐ Other

This Deliverable was subjected to:

☒ Technical Review ☐ Peer Review

Technical Review (TR)
Review Documentation Provided

☐ Signed TR Report or,

☐ Signed TR Concurrence Sheet or,

or,

☒ Signature of TR Reviewer(s) below

below

Peer Review (PR)
Review Documentation Provided

☐ Signed PR Report or,

☐ Signed PR Concurrence Sheet

☐ Signature of PR Reviewer(s)

Name and Signature of Reviewers

Yifeng Wang 

NOTE 1: *Appendix E should be filled out and submitted with the deliverable. Or, if the PICS:NE system permits, completely enter all applicable information in the PICS:NE Deliverable Form. The requirement is to ensure that all applicable information is entered either in the PICS:NE system or by using the NFCSC Document Cover Sheet.*

- *In some cases there may be a milestone where an item is being fabricated, maintenance is being performed on a facility, or a document is being issued through a formal document control process where it specifically calls out a formal review of the document. In these cases, documentation (e.g., inspection report, maintenance request, work planning package documentation or the documented review of the issued document through the document control process) of the completion of the activity, along with the Document Cover Sheet, is sufficient to demonstrate achieving the milestone.*

NOTE 2: *If QRL 1, 2, or 3 is not assigned, then the QRL 4 box must be checked, and the work is understood to be performed using laboratory QA requirements. This includes any deliverable developed in conformance with the respective National Laboratory / Participant, DOE or NNSA-approved QA Program.*

NOTE 3: *If the lab has an NQA-1 program and the work to be conducted requires an NQA-1 program, then the QRL-1 box must be checked in the work Package and on the Appendix E cover sheet and the work must be performed in accordance with the Lab's NQA-1 program. The QRL-4 box should not be checked.*

This page is intentionally left blank

SUMMARY

High-level purpose of this work: This report summarizes work carried out by Sandia National Laboratories (SNL) in the fiscal year 2022 (FY22) to evaluate the potential occurrence of stress corrosion cracking (SCC) on spent nuclear fuel (SNF) dry storage canisters. The U.S. currently lacks a repository for permanent disposal of SNF; thus, dry storage systems will be in use for much longer time periods than originally intended. Gap analyses by the US Department of Energy (DOE), the Nuclear Regulatory Commission (NRC), the Nuclear Waste Technical Review Board (NWTRB), and the Electric Power Research Institute (EPRI) have all determined that an improved understanding of the occurrence and risk of canister SCC is critical to demonstrating the safety of long-term dry storage. Should canister penetration by SCC occur, the containment boundary represented by the canister would be breached. A loss of the inert environment (helium) within the canister could occur and intrusion of air and moisture could react with and damage the fuel within the canister. For this reason, the DOE is funding an effort to evaluate the potential occurrence and consequences of dry storage canister SCC and to develop prevention, mitigation, and repair technologies for this degradation mechanism.

The dry storage canister SCC program has three primary thrusts:

(1) Define the canister surface environment, as this affects corrosion initiation and growth.

(2) Evaluate corrosion as a function of material and environment: pitting, SCC initiation, and growth.

The context for these two thrusts is provided by a probabilistic model developed by SNL to estimate location and timing of canister SCC.

(3) Evaluate mitigation and repair technologies for SCC, should it occur on in-service canisters.

FY22 Accomplishments: The main accomplishments in FY22 include the following:

- **Updates to probabilistic SCC model:** Several parts of the probabilistic model were updated, are documented in a level 3 (L3) milestone in July 2022, and are mentioned briefly in this report.
- **Canister surface environment:**
  - Published manuscript (*Science of the Total Environment*) on the evolution of sea-salt deliquescent brines as a function of temperature (T) and relative humidity (RH) to determine the corrosive environment on canister surfaces.
  - Analyzed dusts collected from in-service dry storage canisters at two independent spent fuel storage installation sites (Section 2.1) to further define the range of probable environments.
  - Completion of a thermodynamic database for modeling $MgCl_2$ brine stability (Section 2.2) to enable the evaluation of Mg-brine stability critical to determining the potential for corrosion.
  - Support studies for the Canister Deposition Field Demonstration (CDFD) (Section 2.3) were documented in a L3 milestone submitted in April 2022; a summary and updates to this report are updated herein.
- **Corrosion testing:**
  - Pit morphology dependence correlated to brine composition (manuscript published in *CORROSION Journal*), material composition, and surface finish (Section 3.1.1).
  - Parameterization of the maximum pit size model to determine severity of a range of environmental conditions (Section 3.1.2).
  - Long-term atmospheric exposures of stainless-steel coupons to evaluate influence of three important environmental parameters on corrosion (Section 3.1.3):
    (1) Completion of diurnal cycle exposure to determine effects of changing T and RH.
    (2) Ongoing exposure of co-deposited dust and salt (potential brine spreading/crevicing).

(3) Ongoing immersion and atmospheric testing of brine chemistry (nitrate effects).

- Conducted a thorough review of the current literature on the pit to crack transition (submitted as an "invited critical review" to *CORROSION Journal*) to establish an informed matrix exploring environment and surface preparation effects on atmospheric U-bend exposures (Section 3.2).
- Developed a reactive transport finite element model (Section 3.3) to determine influence of environmental parameters on SCC (manuscript accepted 9/22 in *Corrosion Science*).
- Benchmarked direct current potential drop system (Section 4.0) for crack growth rate (CGR) measurements, correlated to fractography and crack morphologies to measure CGR under SNF canister-relevant conditions. Developed an in-situ crack tip chemistry measurement technique to correlate environmental influences and CGR; established influence of cathodic control on CGR.

- **Mitigation and Repair**
  - Evaluated the potential use of canister coatings for SCC mitigation and repair (Section 5.1) described in a L3 Milestone report submitted in August, 2022. Although a different work package, there is considerable technical overlap and is summarized here.
  - Continued to evaluate Cold Spray (CS) (summary Section 5.2) for mitigation and repair through accelerated testing to aid optimization and in relevant atmospheric exposures to understand aging and lifetime properties. Submitted a L3 Milestone in September 2022 and identified three areas of CS optimization for canister-relevant applications: 1) reduction of porosity, 2) proper selection of compatible materials, and 3) geometric optimization of the CS/base material edge interface.

Next stages for this work:

- **Canister surface environment**
  - Analysis of dust samples from in-service canisters at new Independent Spent Fuel Storage Installation (ISFSI) sites to further define canister surface environments (two sites in FY23).
  - Utilize the newly developed thermodynamic database to model $MgCl_2$ brine stabilities over a range of canister-relevant conditions to determine potential dry out (non-corrosive environment).
  - Use thermodynamic modeling and experimental studies to measure deliquescence RH values for complex brine mixtures (current databases offer conflicting predictions). These data are used to define the relevant T/RH ranges for corrosion testing.
  - CDFD: (1) Continue testing aerosol sampling equipment to verify proper operation and to train personnel. (2) Perform aerosol sampling at the proposed field site to determine site-specific sampling parameters. (3) Test laboratory-developed hand sampling protocols on a real canister.

- **Corrosion**
  - Continue environmental exposures to determine pertinent variables (diurnal cycling, inert dust, and nitrates) and post-test analysis to inform governing factors for corrosion.
  - Expand pit-to-crack transition work based upon knowledge gained from both large-scale corrosion exposures and initial U-bend matrices. Apply this to understand governing variables of pits that transition to a crack (critical pits) and conditions under which these occur.
  - Initiate exposures to evaluate the effects of iron contamination and rust on pitting and SCC.
  - Continue advancement of CGR studies to establish proper SCC testing protocol and collect valuable measurements under canister-relevant conditions, including atmospheric scenarios more representative of actual canister exposures.

- **Mitigation and Repair**
  - Begin Phase 2 of evaluating industry-provided corrosion-resistant coatings, with a focus on evaluating thermal/radiation degradation of those coatings that survived the initial screening tests.
  - Continue ongoing optimization evaluation and relevant ageing and lifetime exposures for CS samples with continued focus on the evaluation of edge effects.

ACKNOWLEDGEMENTS

This work was funded by the U.S. Department of Energy Office of Nuclear Energy Spent Fuel and Waste Deposition Research and Development Program. The authors would like to thank Ned Larson of the DOE:NE for program oversight. In addition, we would like to thank the following Sandians for their contributions: Jason Taylor, Carlos Jove-Colon, Luis Jaregui, Greg Koenig, Thad Vice, Sam Durbin, Makeila Maguire, Andres Sanchez, Laura Lemieux, Sarah Dickens, Jason Snow, Tim Ruggles, William Gilliland, Derek Wicchart, Mike Kracum, Nichole Garcia, and Sarah Goke. External contributors include Ken Ross of PNNL; Jay Srinivasan, Jenifer Locke, and Eric Schindelholz of the Ohio State University; Rob Kelly and Jimmy Burns of the University of Virginia; John Plumley of the University of New Mexico; Orano staff members Nate Williams, Jeffery Gagney, and Jason Billard; and Three Yankees staff members Neil Fales and Paul Plante.

This page is intentionally left blank.

CONTENTS

LIST OF FIGURES

LIST OF TABLES

ACRONYMS

ASME	American Society of Mechanical Engineers
ASTM	American Society of Testing and Materials
ASW	artificial seawater
BCC	body centered cubic
BSE	back-scattered electron
CASTNET	Clean Air Status and Trends Network
CDFD	Canister Deposition Field Demonstration
CGR	crack growth rate
CISCC	chloride-induced stress corrosion cracking
CPP	cyclic potentiodynamic polarization
CS	cold spray
CT	compact tension
DCPD	direct current potential drop
DI	deionized [water]
DIC	dissolved inorganic carbon
DOE	US Department of Energy
EAC	environmentally assisted cracking
EBSD	electron backscatter diffraction
EDS	energy-dispersive [X-ray] spectroscopy
EIS	electrochemical impedance spectroscopy
EPRI	Electric Power Research Institute
FC	Flora Coatings, Inc.
FEM	finite element modeling
FY	fiscal year
GIF	gamma irradiation facility
HEPA	high-efficiency particulate air
HER	hydrogen evolution reaction
HREBSD	high-resolution electron back-scattered diffraction
IC	ion chromatography
ISFSI	independent spent fuel storage installation
L3	level 3 [milestone]
LAP	laser aerosol particle [spectrometer]
LDRD	laboratory directed research & development

LSPS	least square plane level [method]
LUNA	LUNA Labs USA
MOU	memorandum of understanding
MS	mass spectrometer
NEUP	Nuclear Energy University Program
NRC	Nuclear Regulatory Commission
NWTRB	Nuclear Waste Technical Review Board
ORNL	Oak Ridge National Laboratory
OCP	open circuit potential
OPM	Oxford Performance Materials
ORR	oxygen reduction reaction
OSU	Ohio State University
PEKK	polyetherketoneketone
PNNL	Pacific Northwest National Laboratory
PP	potentiodynamic polarization
RH	relative humidity
RH_L	limiting relative humidity for corrosion to occur
RMS	root mean square
SCC	stress corrosion cracking
SE	secondary electron
SEM	scanning electron microscope
SFWST	Spent Fuel and Waste Science and Technology
SNF	spent nuclear fuel
SNL	Sandia National Laboratory
SRNL	Savannah River National Laboratory
SS	stainless steel
T	temperature
TC	thermocouple
TSP	total suspended particulate
UT	ultrasonic phase array
UVA	University of Virginia
WHRD	White Horse R&D
WL	water layer
XCT	X-ray computed tomography
XRD	X-ray diffraction

YS	yield strength

This page is intentionally left blank.

SPENT FUEL AND WASTE SCIENCE AND TECHNOLOGY

FY22 STATUS REPORT: SNF INTERIM STORAGE CANISTER CORROSION AND SURFACE ENVIRONMENT INVESTIGATIONS

1. INTRODUCTION

In the U.S., spent nuclear fuel (SNF) is stored for long-term interim storage in dry cask storage systems. Originally designed for a 20-year license period, the lack of a U.S. spent nuclear fuel repository for the permanent disposal of SNF means that the dry storage systems will be used for much longer time periods than originally intended. Understanding the safety of long-term interim storage is a priority for the Department of Energy (DOE), the Nuclear Regulatory Commission (NRC), and industry [1-5].

For interim storage, SNF is commonly stored in welded stainless steel (SS) canisters enclosed in passively ventilated overpacks. Over time, dust accumulates on the canister surfaces, and as the SNF cools, salts within that dust will deliquesce to form concentrated brines. If the salts contain aggressive species such as chloride, then the resulting brine can cause localized corrosion, and in weld regions with high residual stresses, stress corrosion cracking (SCC) can occur. Eventually, SCC cracks could penetrate the canister wall. The risk of corrosion and SCC is greatest in near-marine settings, where chloride-rich sea-salt aerosols are deposited on the canister surface. Developing an improved understanding of the occurrence and risk of SNF storage canister SCC is considered to be critical to demonstrating the safety of long-term dry storage of SNF [1-5]. For this reason, the Department of Energy (DOE) is funding a large effort to evaluate the occurrence and potential consequences of storage canister SCC as well as to develop prevention, mitigation, and repair technologies for this degradation mechanism, if it should occur. This effort includes work at several different national laboratories and a large DOE-funded effort at universities, as part of the Nuclear Energy University Program (NEUP) (Figure 1).

Sandia National Laboratory (SNL) plays a major role in this effort, leading work to develop a scientific basis for understanding canister corrosion and SCC initiation and growth, and to develop a probabilistic model for canister stress corrosion cracking. SNL is also evaluating the potential consequences of canister SCC. Pacific Northwest National Laboratories (PNNL) has a supporting role in many of these activities. Finally, SNL is evaluating potential coatings for prevention and mitigation of canister corrosion and SCC in collaboration with four industrial partners, and is performing corrosion experiments to support work to develop cold spray repair technologies at PNNL. It should be noted that the DOE has large NEUP efforts in both SCC mitigation and repair and corrosion coating development.

This report documents work done by SNL to develop a scientific basis for canister SCC—to define the canister surface environment and corrosion phenomena, including the occurrence and growth of canister pitting and SCC. Efforts by other national laboratories and collaborators, and by other parts of the SNL program are documented in other Spent Fuel and Waste Science and Technology (SFWST) reports.

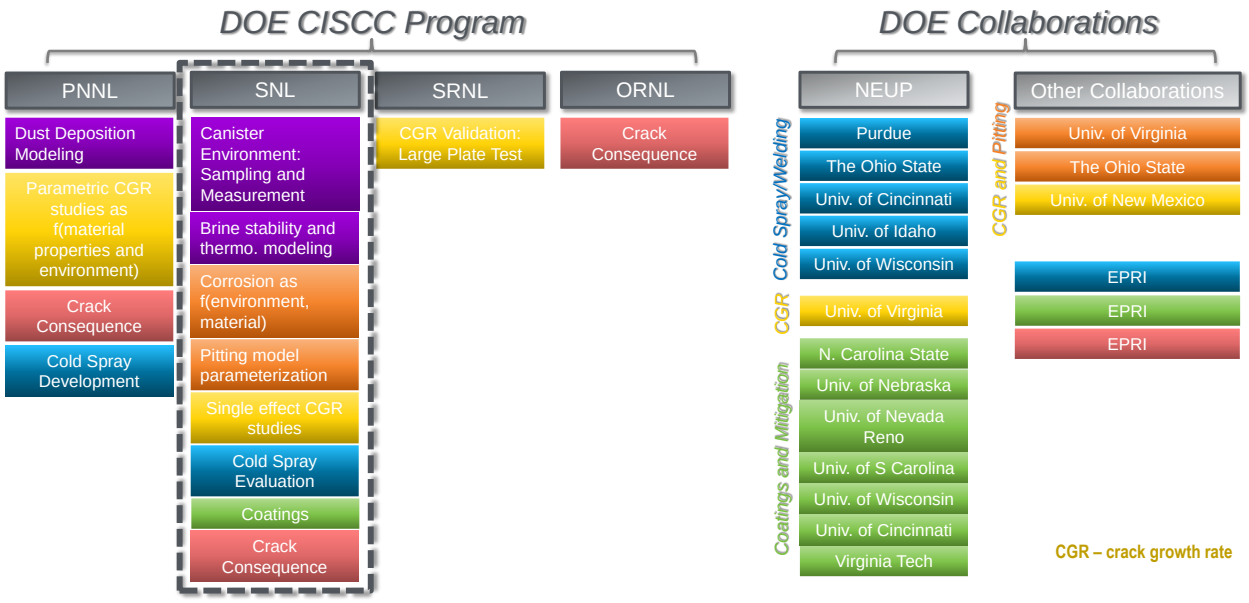

Figure 1. Experimental work on canister SCC currently being carried out by SNL, other national laboratories, and collaborators.

Over the past few years, SNL has worked to develop a probabilistic model for SCC which utilizes mechanistically-based sub-models to describe individual processes and events that occur during canister aging and that could eventually lead to canister SCC (Figure 2). The current model framework contains numerous assumptions and oversimplifications, many with insufficient scientific basis. Current SCC work at SNL focuses on acquiring data for improved sub-model development, concentrating mostly on determining the underlying mechanisms that govern (1) brine evolution, both before and after initiation of corrosion; (2) the corrosion processes of pitting, SCC crack initiation, and SCC crack growth. This includes developing high-quality data for salt compositions and deposition rates at Independent Spent Fuel Storage Installation (ISFSI) sites and for brine compositions in the evolving canister surface environment, and statistical pitting and SCC initiation and growth data for canister-relevant conditions. By improving sub-model parameterization and validation, this work will reduce the uncertainties in our estimates of the timing and occurrence of SCC.

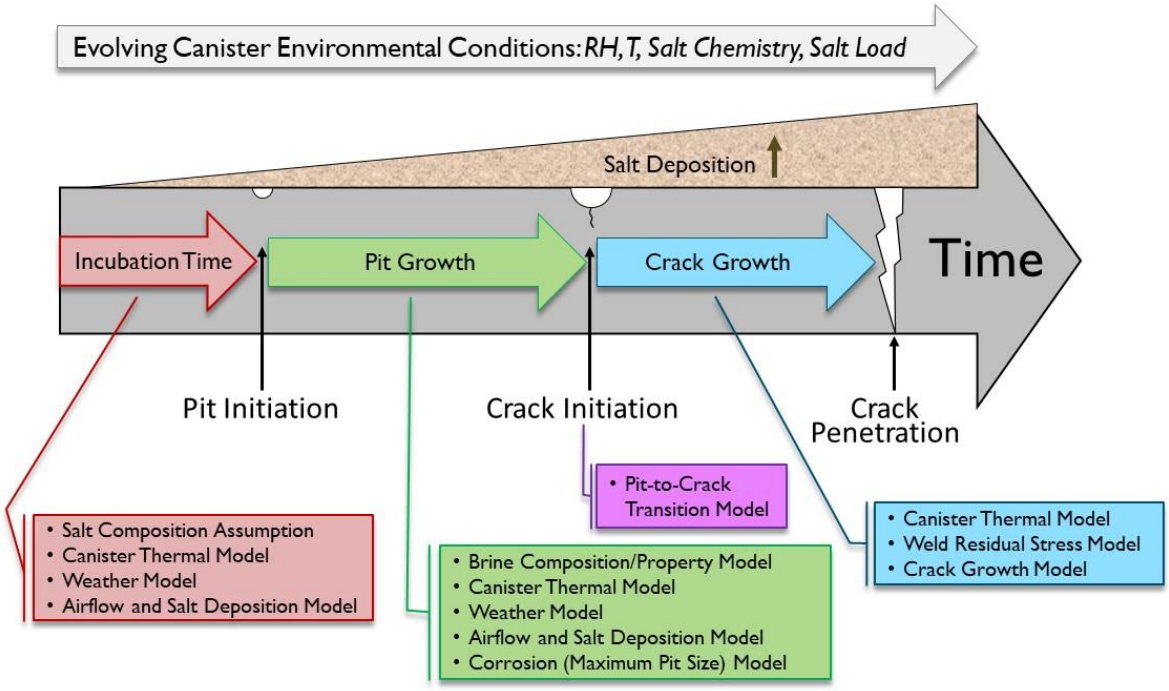

Figure 2. Probabilistic model for SNF dry storage canister SCC.

1.1 Background

A timeline for SCC of SNF dry storage canisters is shown in Figure 2. Several important events and processes occur during the development of through-wall SCC and understanding the timing of event initiation and the rates of these processes is critical to accurate prediction of possible SCC penetration times. These parameters are dependent upon the evolving physical and chemical environment on the canister surface and on the canister material properties, including composition, surface finish, and weld-related microstructure and residual stress levels. SNL and collaborators are working to understand these dependencies, and their effect on potential canister penetration rates by SCC.

Once a canister is placed in a ventilated overpack, dust and salt aerosols begin to deposit on the canister surface. Determining the composition of those salts is critical to understanding the risk of canister corrosion, and SNL participated in several campaigns to sample dust from in-service SNF storage canisters over the last several years. In FY21, canister dust and salt characterization was carried out for Sites A and B, two anonymous inland ISFSI sites; this was the first inland ISFSI data ever collected [6, 7]. In Section 2.1 of this report, results of the dust analysis for two additional sites are provided, an anonymous near-marine East Coast site referred to as "Site C", and the Yankee Rowe site. At Site C, surface deposits on a canister within a horizontal storage module were sampled during a canister inspection as part of the site aging management program. Dust characterization work for Site C was published in Bryan and Knight (2022) [8]; however, that report did not contain the scanning electron microscope energy dispersive X-ray spectroscopy (SEM/EDS) data that are presented here. Those analyses provide important insights into the form and origin of the salts deposited on the canisters at that site. At Yankee Rowe, surfaces within the outlet vents in a vertical canister system were sampled by hand during a storage system inspection. While not ideal, these samples do provide some information on the soluble salt compositions in atmospheric aerosols at the site.

Initially, canister surface temperatures may be too high to permit salt deliquescence or even development of adsorbed water layers on salts, and localized corrosion cannot occur. But as the canister cools, and

surface relative humidity (RH) values increase; eventually, salts will deliquesce and brines will form on the metal surface, permitting corrosion to occur. The period following emplacement and prior to corrosion is known as the incubation period and is a function of the physical environment—the temperature, RH, and salt load on the canister surface. As discussed in previous reports, that initial sea-salt deliquescence, forming $MgCl_2$-rich brines, may occur relatively soon after canister emplacement, but deliquescence of NaCl in the sea salts will not occur for hundreds of years. Thus, the only sea-salt deliquescent brines that will form of canister surfaces will be $MgCl_2$-rich brines for up to hundreds of years, and the long-term stability of $MgCl_2$-rich brines on the heated canister surface is of great interest. SNL has performed experimental and modeling studies of the stability and properties of $MgCl_2$-rich brines for several years, and an update on the current research into the brines is presented in Section 2.2. This update includes a full thermodynamic model for the magnesium chloride/hydroxychloride/water system, and the results of the latest $MgCl_2$ degassing experiment, run at 60ºC and 40% RH.

Once deliquescence occurs, if the deliquescent brine is chemically aggressive (e.g., chloride-rich), then pitting corrosion will initiate. One important factor controlling the timing and extent of corrosion, and possibly the initiation of SCC cracks, is the salt and dust load deposited on the canister surface. Salt and dust deposition rates on dry storage canisters are known only from surface sampling. However, only a small number of canisters at a few ISFSI sites have been sampled, and for any canister, only a few locations on the canister surface have been sampled; moreover, the range of canister heat loads examined has been relatively narrow. For this reason, the Canister Deposition Field Demonstration (CDFD) is being planned to evaluate salt and dust deposition on heated canister surfaces [9]. In this experiment, three canisters with different heat loads will be placed in overpacks at an ISFSI site, and deposited dusts and salts will be periodically sampled over several years. SNL will perform sampling and analysis of the dusts. In FY21, we began CDFD support studies [10], and those have continued into FY22, with an L3 milestone report published in April 2022 [11]. These include developing initial plans for CDFD canister and overpack surface sampling; developing methods for measurement of canister surface roughness, which may impact dust deposition or canister corrosion; and evaluating ways of attaching thermocouple wires and marking the canister surfaces to designate sampling sites. Only additional work since then is summarized here (Section 2.3).

SNL research into corrosion pitting and the phenomenon of pit to crack transition is discussed in Section 3. Pitting initiation, pit growth rates, pit morphology, and possible limitations on pit growth, are strongly controlled by environmental factors such as temperature, RH, brine composition, and salt load, but also by material properties, including metal composition, surface finish, microstructure, and stress level. SNL has several collaborations with university groups including work with Ohio State University (OSU) to evaluate environmental influence (brine chemistry) on pit damage morphology and extent (published manuscript in CORROSION Journal [12]). FY22 also saw further exercising and parameterization of the maximum pit size model as part of SNL's work on the overall probabilistic model for SCC prediction[13]. Through this work, a significant parameter space of environmental variables was evaluated and effects on maximum pit size established. SNL also has extensive experimental work evaluating influences of pertinent environmental (diurnal cycling, inert dust, and nitrates) and material (composition and surface finish) parameters on large scale/long term evaluations on both the subsequent corrosion damage and pit to crack transition. As these pits can act as stress/strain concentrators in the canister surface, it is important to understand their propensity towards transition to a crack. Significant efforts in FY22 were carried out to thoroughly evaluate the current literature and scientific understanding of the pit to crack transition, this was compiled and submitted as an "invited critical review" to CORROSION Journal [14]. Additionally, learnings from this review, and from the atmospheric exposures to evaluate pitting, provided the basis for a U-bend atmospheric exposure matrix to explore the environmental and material effects on the pit to crack transition. This matrix was completed in FY22 and full analysis of the samples will be carried out in FY23. Finally, in collaboration with the University of Virginia (UVA), SNL has developed a reactive transport finite element method model to further explore

the influences of the environment on the developed crack tip chemistry and how this in turn may govern SCC (manuscript accepted in Corrosion Science [15]).

Once an SCC crack initiates, the rate of crack growth will be controlled by the temperature and chemical environment, as well as, possibly, the salt surface load. The tensile stress profile through the metal is also important, as it is combined with the depth of the crack to determine the crack tip stress intensity factor [16, 17]. SNL is working with colleagues at PNNL and UVA to measure crack growth rates as a function of canister surface environment (brine composition and temperature) and material properties. In FY22, SNL validated their in-situ crack growth rate measurement capabilities (DCPD system) and carried out multiple investigations into the influence of brine chemistry on the crack growth rate and crack morphology. Additionally, in collaboration with a separately funded Laboratory-Directed Research and Development (LDRD) project, SNL developed methods for in-situ crack tip chemistry measurements to help further understand governing roles of the environment, sample geometry, and material properties on the crack growth rate. Sandia's crack growth rate measurement work is described in Section 4.

Finally, as industry begins to move towards strategies for mitigation and repair of SCC cracks, should they be observed on SNF dry storage canisters, SNL is supporting work to develop repair strategies. As a part of a complimentary work package, SNL is collaborating with four industrial partners on the development and testing of corrosion resistant coatings as potential mitigation and repair strategies. While this is outside the scope of this work package, since it compliments and supports some of the ongoing work within, the FY22 report [18] on these coatings is summarized in 5.1. Additionally, SNL has continued working with PNNL to evaluate cold spray repairs for material compatibility and corrosion resistance (Section 5.1). This work is presented in detail in a FY22 report [19] and is summarized in Section 5.2.

This page is intentionally left blank.

2. Canister Surface Environment

In FY22, several efforts focused on understanding the canister surface environment and how it evolves over time. First, SNL published a journal article on the evolution of sea-salt deliquescent brines as a function of T and RH (Appendix A; [20]). At near-marine sites, corrosive brines form by deliquescence of sea-salt aerosols on the canister surfaces. We have characterized those brine compositions and properties for a range of canister conditions and utilize this information for corrosion modeling and testing. Also, SNL analyzed dust samples collected from SNF dry storage canisters at two different ISFSI sites, an anonymous east coast estuarine site, and the Yankee Rowe site. These analyses are critical to understanding canister surface environments and defining the range of conditions necessary for geochemical modeling and corrosion testing. Experiments and calculations to evaluate $MgCl_2$ stability on heated surfaces were continued in FY22. Over the first few hundred years for canister storage, canister surface temperatures are sufficiently high that only $MgCl_2$-rich brines can form by sea-salt deliquescence, so these experiments are critical for determining the risk of canister SCC at near-marine sites. Finally, SNL performed several studies in support of the planned CDFD project. These include developing methods for measurement of canister surface roughness, which may impact dust deposition or canister corrosion; developing methods for quantitative collection of canister surface deposits; developing initial plans for CDFD canister and overpack surface marking and dust sampling; and developing equipment and testing procedures for monitoring of ambient weather and aerosol sampling at the test site. Each of these efforts is described in the following sections.

2.1 Analysis of Dust Samples from In-Service Canisters

In FY22, SNL received and analyzed dust samples from two different ISFSI sites, an anonymous east coast site on an estuary considered to be "near-marine" and referred to here as "Site C", and the inland Yankee Rowe site. Several east-coast ISFSI's are located on estuarian waterways, and the analyses from Site C helps define the characteristics of such locations, which are generally significantly more sheltered than shoreline sites. The Yankee Rowe site is only the third inland site yet to be sampled and provides additional information on the range of compositions of soluble salts at inland sites.

2.1.1 Site "C"

In June of 2022, dust samples were collected from the surface of an in-service horizontal SNF dry storage canister at a near-marine east coast ISFSI site, referred to here as "Site C". The samples were shipped to SNL for characterization, including leaching and analysis of soluble salts and scanning electron microscopy (SEM) to determine dust particle sizes, morphology, and mineralogy. This sampling operation offers the opportunity to characterize the chemistry and mineralogy of canister surface deposits at an additional ISFSI site, supporting the current understanding of site-to-site variability. These analyses also provide important information for evaluating the potential for storage canister stress corrosion cracking at the ISFSI site in question, and hence provide support for aging management plans at the site. The results of those analyses are presented in SAND report SAND2022-10884 *Analysis of Dust Samples Collected from a Near-Marine East Coast ISFSI Site ("Site C")* [8] and are briefly summarized here. At the time of the earlier report, SEM Energy Dispersive Spectroscopy (EDS) data were not available; those data are presented here and provide insights into the form and distribution of chlorides within the dust.

2.1.1.1 Sample Collection

In June of 2022, Orano, working with site operators, performed inspections on NUHOMS horizontal storage canisters at a near-marine, estuarine, east coast site. Such periodic inspections have been mandated by the Nuclear Regulatory Commission (NRC) at all ISFSI sites, in response to the concerns about canister SCC. A single canister was examined; because risk of canister SCC increases as the canister cools in storage, the chosen canister had been in service for a long period of time (since November of 1993) and had a low initial heat load of 5.19 kW. Surface temperature data were not collected.

One goal of the inspection was to collect dust samples to characterize the composition of the dust and the amount and composition of soluble salts on the canister surface. To achieve this goal, dust samples were collected from 6 locations on the canister surface—three circumferential locations, corresponding to clock positions of 2:00, 10:00, and 11:30 (observed from the overpack door), at two different longitudinal locations, 24 and 39 inches from the foot plate of the canister. The sampling was carried out by hand, using a probe on a long rod with a vacuum dust sampling tool on the end. The probe was moved a known distance over the surface of the canister, to sample a known surface area corresponding to 3 in^2. Each sample consisted of a glass fiber filter sandwiched between two Scotch-Brite™ abrasive pads; the 3-piece assembly was mounted inside a plastic sampling head.

After collection, the samples were shipped overnight to SNL for analysis. After a gamma counting to ensure that the samples were not radioactive, samples for SEM were collected from the sides of the sampling heads, to which had adhered excess dust not used for leaching analysis, using Biotape® adhesive films. Then, the heads were disassembled and the Scotch-Brite® pads and glass fiber filters that had trapped the dust were leached with deionized water, and the leachate was analyzed to determine the soluble salt compositions and concentrations.

2.1.1.2 Methods

The analytical methods used for chemical analysis and SEM analysis are detailed in [8]. The following analytical methods were used:

- Chemical analysis of soluble salts by ion chromatography (IC) and dissolved inorganic carbon (DIC) analysis. The soluble salts were leached from the samples with deionized water. Analysis of the leachate provided soluble salt compositions and concentrations in the samples. Measured anionic analytes include F^-, Cl^-, Br^-, NO_2^-, NO_3^-, SO_4^{-2}, PO_4^{-3} and HCO_3^- (by DIC); however, F^-, Br^-, and NO_2^- were not detected in any sample, and those species are not included here. Cationic analytes were Li^+, Na^+, NH_4^+, K^+, Mg^{+2}, and Ca^{+2}. Measured Li^+ concentrations were shown to be leachate from the Scotch-Brite™ pads, and were not considered further. The sample leachates were analyzed in duplicate, and stated standard deviations are based on the values obtained from the two IC analyses.
- SEM imaging. SEM analysis of the dry dust samples provided particle size and textural/morphological information on the dust and soluble salt species and allowed for visual identification of organic matter, including floral/faunal fragments.

2.1.1.3 Results and Discussion

Chemistry

The measured soluble salt compositions are shown graphically in Figure 3. Mass concentrations of soluble salt cations follow the trend: $Ca^{+2} > Na^+ \approx K^+ > Mg^{+2} > NH_4^+$. Mass concentrations of Ca^{+2} are about twice that of Na^+ and K^+, which in turn are much higher than concentrations of Mg^{+2}; only trace amounts of NH_4^+ were present.

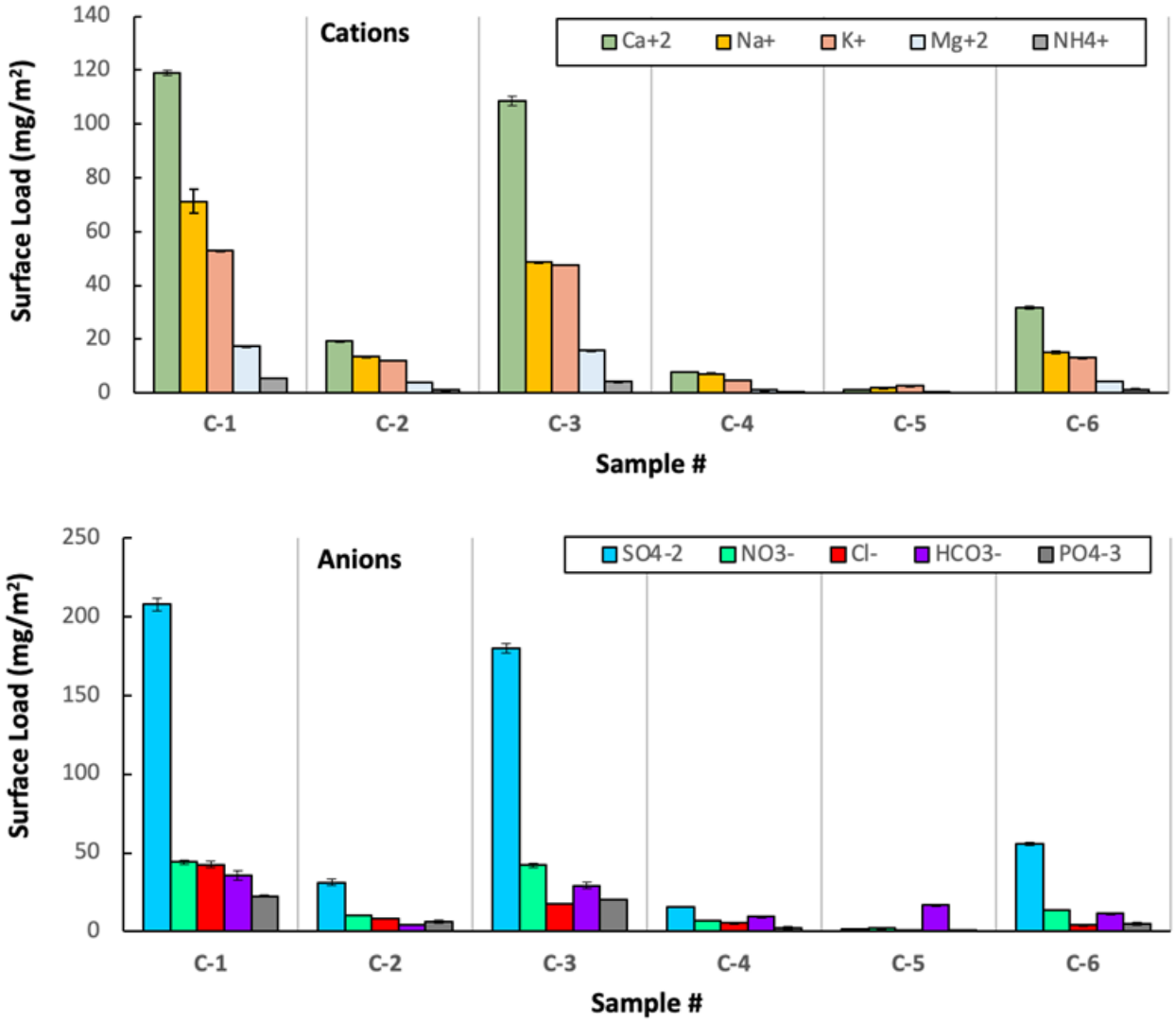

Figure 3. Compositions of the soluble salts leached from the Site C samples.

The anions follow the trend: SO_4^{-2} >> NO_3^- >> HCO_3^{-3} ≥ Cl^- > PO_4^{-3}. Sulfate greatly dominates the anions, with lesser subequal amounts of NO_3^- and total inorganic carbon reported as HCO_3^-. Cl^- is present in similar or slightly lower quantities than HCO_3^-. Phosphate is generally lower in concentration but is still measurable in all samples. This is unusual—in previous sampling campaigns, soluble phosphate has only been present in trace amounts. Note that fluoride, F^-, was not reported. There were several unidentified peaks, probably from organic anionic species, in the F^- region of the IC spectra, making discrimination of small fluoride peaks difficult. Overall, the charge balance errors demonstrated a deficiency in anions by ~25%. This was true for samples C-1, C-2, C-3, and C-6. Samples C-4 and C-5 had low solute concentrations and their charge balances were different than the rest. The charge balance for C-5 showed a deficiency in cations, but that was largely driven by a low total solute concentration and high analytical error.

The deficiency in the anions relative to cations can be largely attributed to the presence of organic acid species. Similar to the anion chromatograms at other sites[6, 7], there were several unidentified peaks of notable peak intensity. To identify the organic acid species that may be present in these samples, a qualitative survey using a mass spectrometer was performed. Preliminary characterization of samples

was performed using mass spectrometry (MS) with a Waters mass spectrometer using a direct infusion into an electrospray ionization source. MS/MS was performed on major ions observed in the mass spectrum to identify chemical species based upon their fragmentation. Due to the complexity of the samples, not all molecules present in the mass spectrum have been unambiguously identified. An example mass spectrum from C-3 is shown in Figure 4. Figure 4-a shows the entire mass over charge (m/z) range, and indicates that NO_3^- and HSO_4^- were the dominant ions observed in the mass spectrum for all samples. Figure 4-b shows the mass spectrum from 100 – 500 m/z for clarity of the organic peaks. No significant ion peaks were observed at m/z >500. Sites C-1 and C-3 had the highest abundance of organic species, as inferred by the maximum ion count in the mass spectrum (not including NO_3^- and HSO_4^-). This method cannot provide a quantitative determination of the concentrations of each of the organic acid complexes; however, it is clear they are present and plentiful in the leachates of the Site C samples. All samples contained a complex mix of organic species; however, only disaccharides ($C_{12}H_{22}O_{11} - H^-$), disaccharide adducts ($C_{12}H_{22}O_{11} - HSO_4^-$ or $C_{12}H_{22}O_{11} - Cl^-$), 2-hydroxyterpenylic acid, and a compound that resembles hydroxypivalic acid were specifically identified. The disaccharides originate from plant matter, and since pollen was abundant in these samples, this is expected. The exact identification of the disaccharide is not known. It is likely that other oxidation products of disaccharides are present due to thermal oxidation, radiolytic oxidation, and atmospheric oxidation; however, none were specifically identified in the mass spectrum. The 2-hydroxyterpenylic acid is an oxidized by-product of α-pinene, a volatile organic compound emitted from pine trees [21]. The hyroxypivalic acid-like compound would likely form from the oxidative degradation of isoprene. Isoprene is a 5-carbon compound that is commonly emitted by plants.

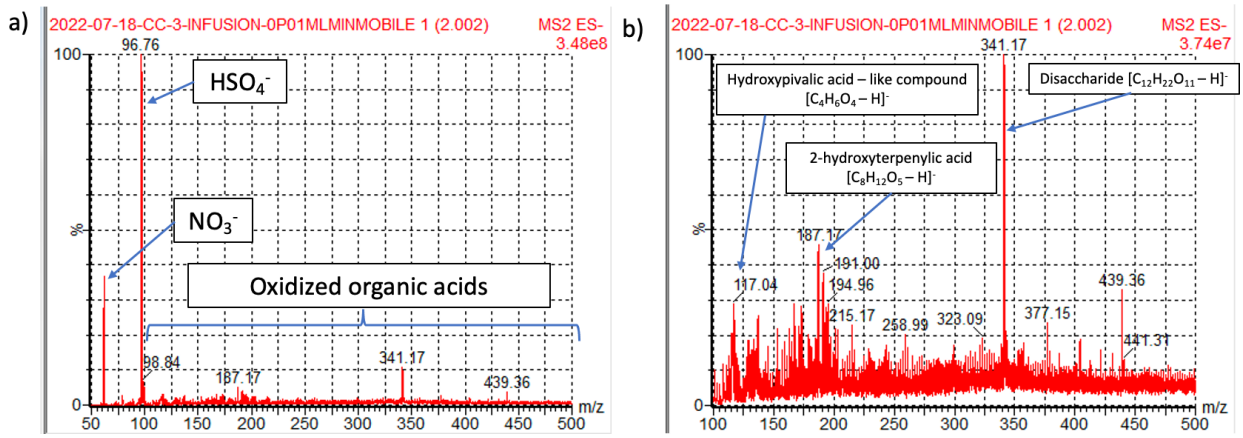

Figure 4. a) Mass spectrum obtained from the analysis of C-3 and b) mass spectrum zoomed into 100- 500 m/z showing the peaks associated with the organic acids from sample C-3.

The presence of organic species can influence the brine behavior by altering the deliquescence properties and/or by altering or buffering the solution pH. Both of these could affect the stability of a brine on the surface; however, it is very challenging to identify specific impacts as there are hundreds of possible compounds that exist and site-to-site variation would likely be significant. The presence of organic acids may explain why the charge balance errors generally are deficient in cations.

Total soluble salt loads are shown in Figure 5. Some strong trends are apparent. First, the salt loads were much higher along the 39-inch transect than along the 24-inch transect. The observed differences in salt loadings between the 39-inch transect and the 24-inch transect could be related to the airflow within the overpack; however, no design information for the overpack was provided to SNL, so this is speculative. Second, for both transects, the samples at 11:30 (near the top) contained less soluble salts than the samples collected at 2:00 and 10:00 o'clock. This result was unexpected; at other sites [6, 7], salt loads were highest at the 12:00 o'clock position. While these observations could represent the actual

distribution on the canister, it is also possible that they are artifacts, caused by variations in the sampling efficiency for different locations due to access limitations.

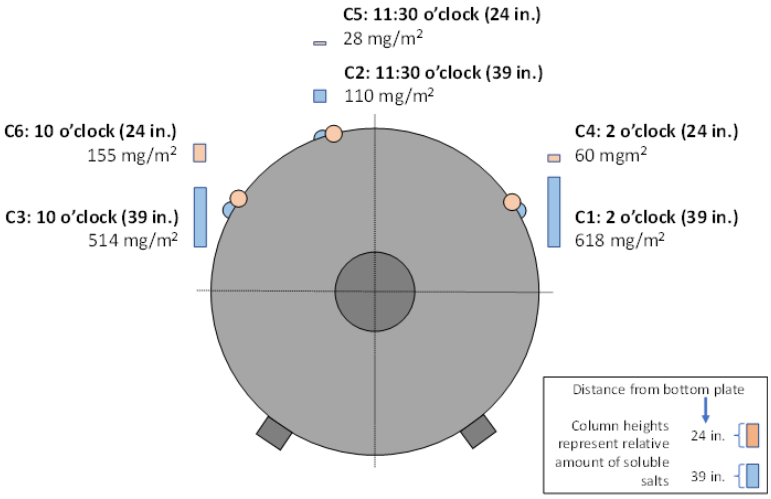

Figure 5. Total soluble salt loads (mg/m^2) at each sampled location.

Trends in Cl^- concentrations are similar to the total salt loading. In terms of chloride-induced SCC, the most important solute is Cl^-, and in the Site C samples, it is only present in small quantities. The maximum surface load of Cl^- present is 42.5 mg/m^2 in Sample C-1, collected at the 2:00 o'clock position on the 39-inches transect Figure 5. The total amount of soluble salts present in that sample is also the highest at that location, at 618 mg/m^2. Cl^- represents only ~7% of the total mass of the soluble ions at that location. However, in terms of *molar* concentrations, Cl^- is commonly the second most abundant anion behind SO_4^{-2} and is generally near-equal to NO_3^- in concentration. While the relationship between the Cl^-/NO_3^- ratio and atmospheric corrosion is not fully understood, higher amounts of NO_3^- have been shown increase passivity in full immersion conditions. However, while NO_3^- can potentially offer some corrosion protection, mixed Cl^- and NO_3^- salts generally have a lower deliquescence RH than just the Cl^- equivalents. Therefore, it is possible that a stable brine could form on the canister surface at higher temperatures than if NO_3^- was not present, potentially resulting in earlier canister corrosion, if corrosion is not suppressed by nitrate.

Scanning Electron Microscopy

SEM imaging was performed to determine particle morphology and size distributions, and to identify organic materials that might be in the dust. Two types of SEM images are shown here. The first are backscattered electron (BSE) images in which the brightness of the image is a reflection of the average atomic number (Z) of the backscattered particles; the higher the Z, the brighter the particles. Mineral grains, which are largely silicates, appear brighter than organic materials in BSE images. The second type of images are secondary electron (SE) images. SE images are better at discriminating texture and topology, but do not discriminate between materials with a higher or lower Z.

SEM imaging of the Site C dust samples showed that there are three main components in the dust.

- Mineral grains (Figure 6-a). Mineral grains occur as angular particles that are brighter than organic materials in BSE images.
- Pollen grains (Figure 6-b). Pollen grains occur as spongy, globular, prolate (football-shaped) or lobed grains (several sizes and morphologies are present), darker than the mineral grains in

backscattered electron images. Pollen grains may have significantly degraded over time and be present as wrinkled or torn sponge-like particles.

- Stellate trichomes (Figure 6-c). Trichomes are hairlike filaments with various functions that form on the surface of many plants. Some common plants, such as oak trees, have trichomes with a stellate morphology that form on the lower surfaces of their leaves. Stellate trichomes are abundant in the Site C dusts.

These three components are present in all of the Site C samples, in roughly the same proportions. Several examples are given in Figure 6. Pollen is quite abundant in the dusts, comprising as much as half of the larger particles. Stellate trichomes are less abundant than pollen, but are still common in the dust, and represent the largest particles in the dust. Mineral fragments are commonly finer than the organic materials, although a few larger grains are present. This is consistent with the relative aerodynamic properties of the grains; the organic materials have a much lower density than the mineral grains, and hence, larger organic particles will have the same equivalent aerodynamic diameter as much smaller mineral grains and would be transported and potentially deposited in the same location as the smaller mineral grains. It is important to note, however, that there may be a sampling bias—the Biotape® samples used for the SEM imaging were collected from the smooth sides of the sampling heads, and larger mineral grains may have simply not adhered to the head. The abundance of organic particulates such as pollen and stellate trichomes supports the hypothesis that soluble organic species may be abundant in the leachates analyzed by the IC.

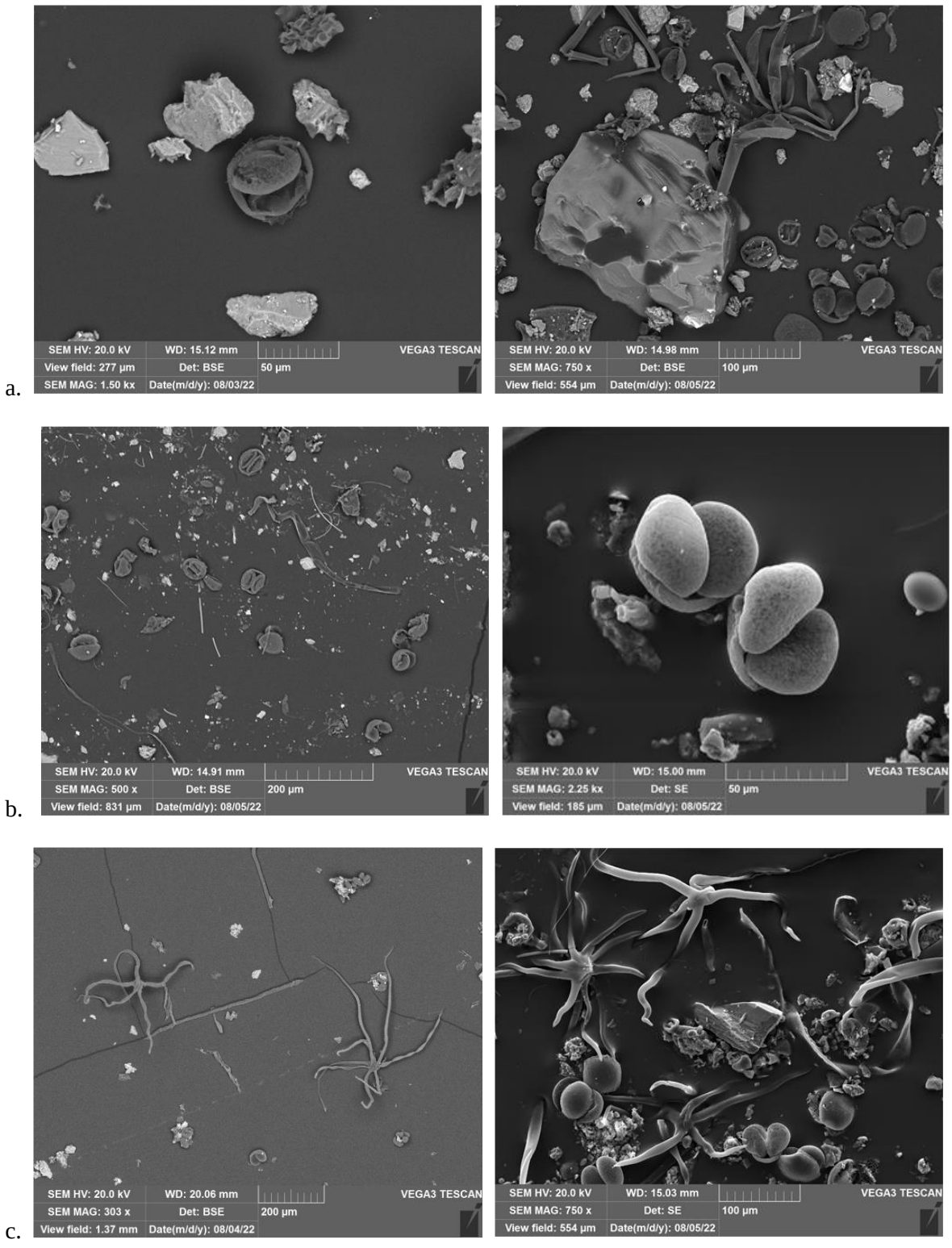

Figure 6. a) BSE images of mineral grains (brighter) with organic material (darker), consisting of pollen grains and stellate trichomes. b) BSE (left) and SE (right) images of globular and lobed pollen grains with mineral detritus. c) BSE (left) and SE (right) images of stellate trichomes with angular mineral grains and pollen.

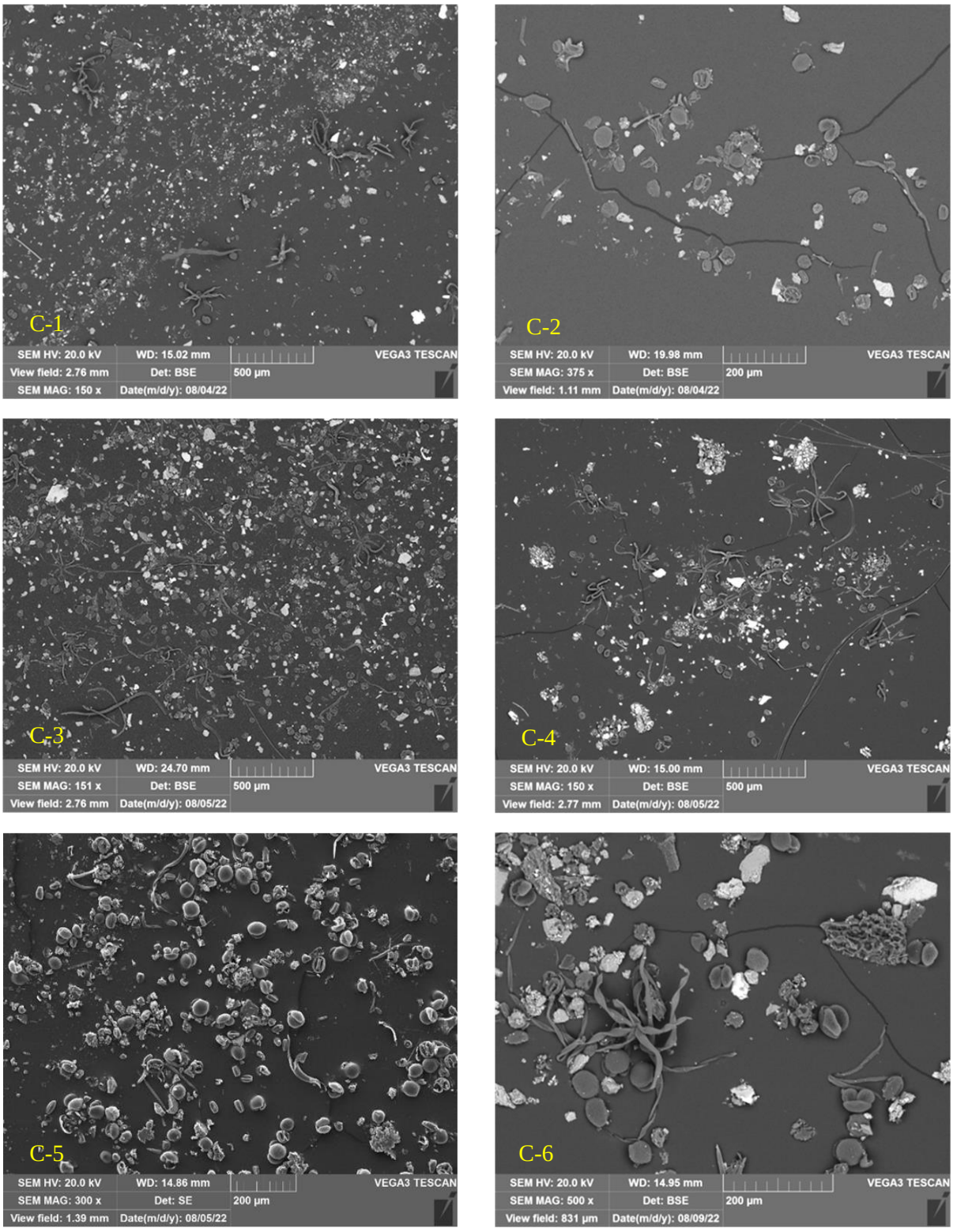

Figure 7. Low magnification SEM images from samples C-1 to C-6, illustrating the relative abundance of organic grains (pollen and stellate trichomes) and mineral grains. All images are BSE images, except for C-5, which is an SE image.

EDS elemental mapping of the Biotape™ samples was not available when the report *Analysis of Dust Samples Collected from a Near-Marine East Coast ISFSI Site ("Site C")* [8] was issued, but has since been carried out. The EDS mapping was used to determine the mineralogy of the inert dust particles present, and the location and morphology of the salt minerals. Relatively low magnification imaging and mapping was used to survey the compositions of the mineral grains present; single point EDS analysis was used to confirm compositions. An example is given in Figure 8. Detrital mineral grains consisted largely of quartz, indicated by concentrations of Si and O on the EDS element maps, and aluminosilicate minerals, including biotite (Fe-Mg-K-Si-Al-O), potassium feldspar (K-Al Si-O) and sodium/calcium feldspar (Na-Ca-Al-Si-O). Although carbon is not distinguishable on the plastic Biotape™ adhesive strips, irregular minerals enriched in Ca-O, and Ca-Mg-O are interpreted to be carbonate phases, detrital calcite ($CaCO_3$), and dolomite $CaMg(CO)_3)_2$.

Soluble salt phases were not uncommon. Chloride was strongly associated with sodium as NaCl, which occurred as relatively large (>10 micron) individual grains, sometimes euhedral (Figure 9-a), and sometimes highly corroded (Figure 9-b). An additional occurrence of NaCl is associated with pollen or plant fibers (Figure 9-c). This is interpreted to indicate that the plant matter contacted a deliquesced droplet of salt in the atmosphere, prior to deposition onto the canister. NaCl also occurs in clusters with Mg-SO_4 (Figure 10); this association is clearly indicative of sea-salt aerosols [22], as the dominant ions in seawater are Na^+, Cl^-, Mg^{+2}, and SO_4^{-2}. Moreover, some grains exhibited the characteristic spherical morphology (Figure 10-b) seen in sea-salt aggregates from canisters at Diablo Canyon. Sulfate occurred primarily as calcium sulfate in coarse, several micron-sized, grains, or as finely disseminated grains on pollen; in a few cases, sulfate appeared to be associated with potassium. Nitrogen was not clearly present as any mineral phase but did appear to be associated with pollen and plant fibers, as it is a significant component of plant matter. The identification of nitrogen in the dust was complicated by the fact that nitrogen is in the Biotape™ substrate.

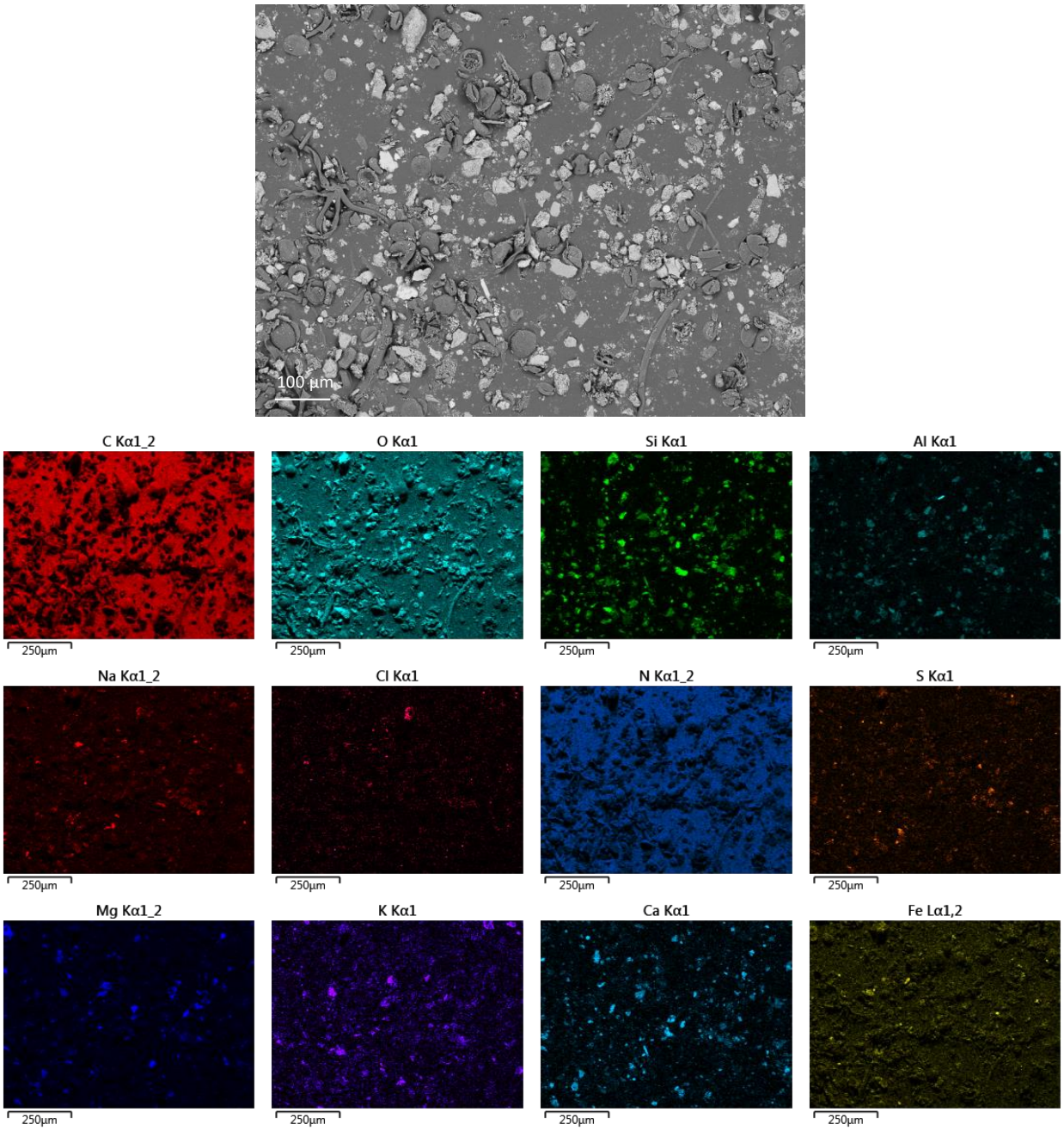

Figure 8. SEM BSE image and EDS element maps for a region on the sample C-3 Biotape™. Image shows mineral grains and organic particles and fibers. Chloride-rich grains were then evaluated at higher magnification to determine morphology and mineralogy.

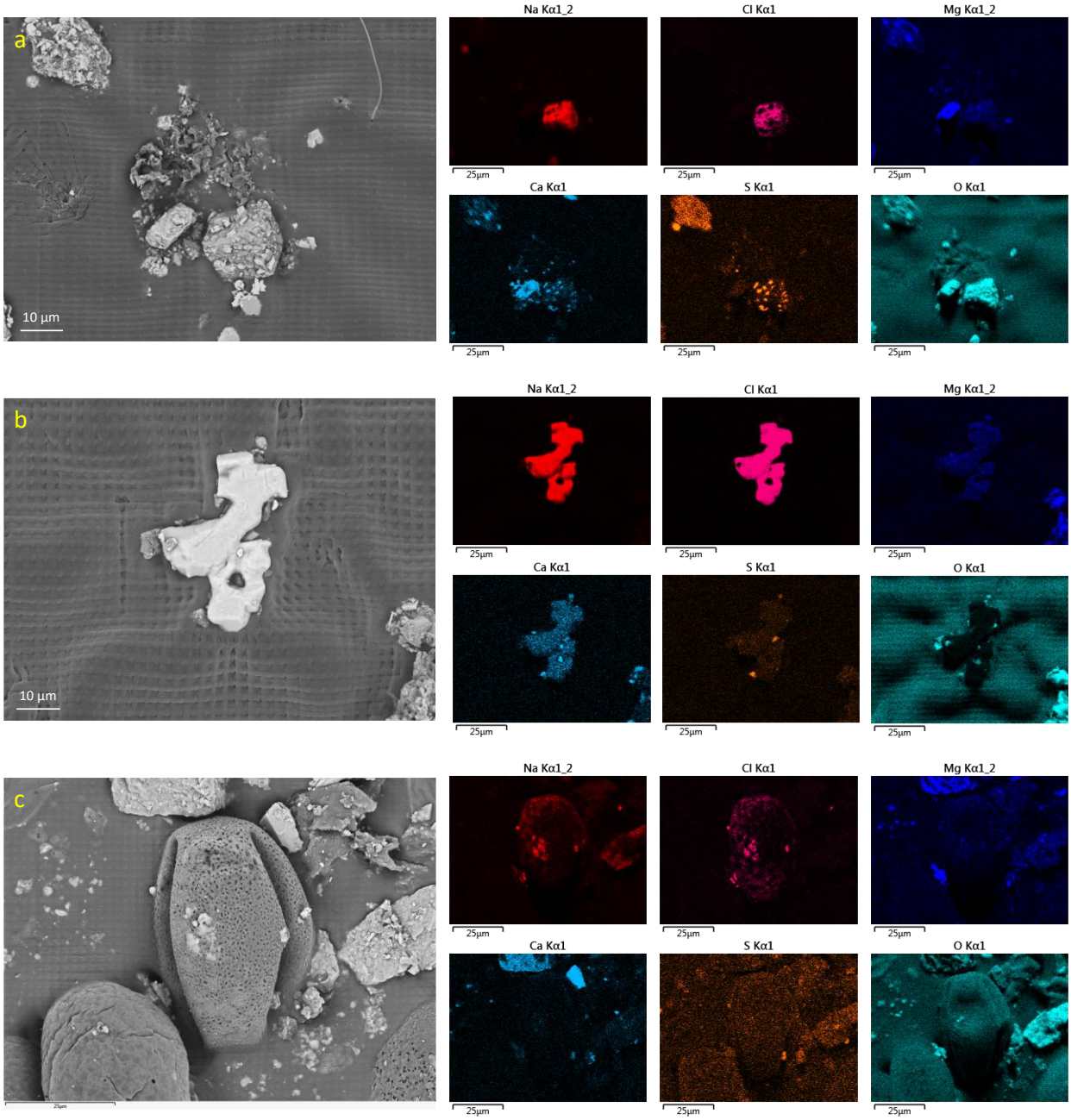

Figure 9. SEM BSE images and EDS element maps of sea-salt aggregates. a) Sample C-1. Euhedral halite cube decorated with small calcium sulfate crystals. Adjacent grain is detrital dolomite, $CaMg(CO_3)_2$. b) Sample C-3. Large, heavily corroded halite grain with a few small grains of calcium sulfate. c) Sample C-3. Halite plating out on a pollen grain. Note that other sea-salt components do not appear to be present.

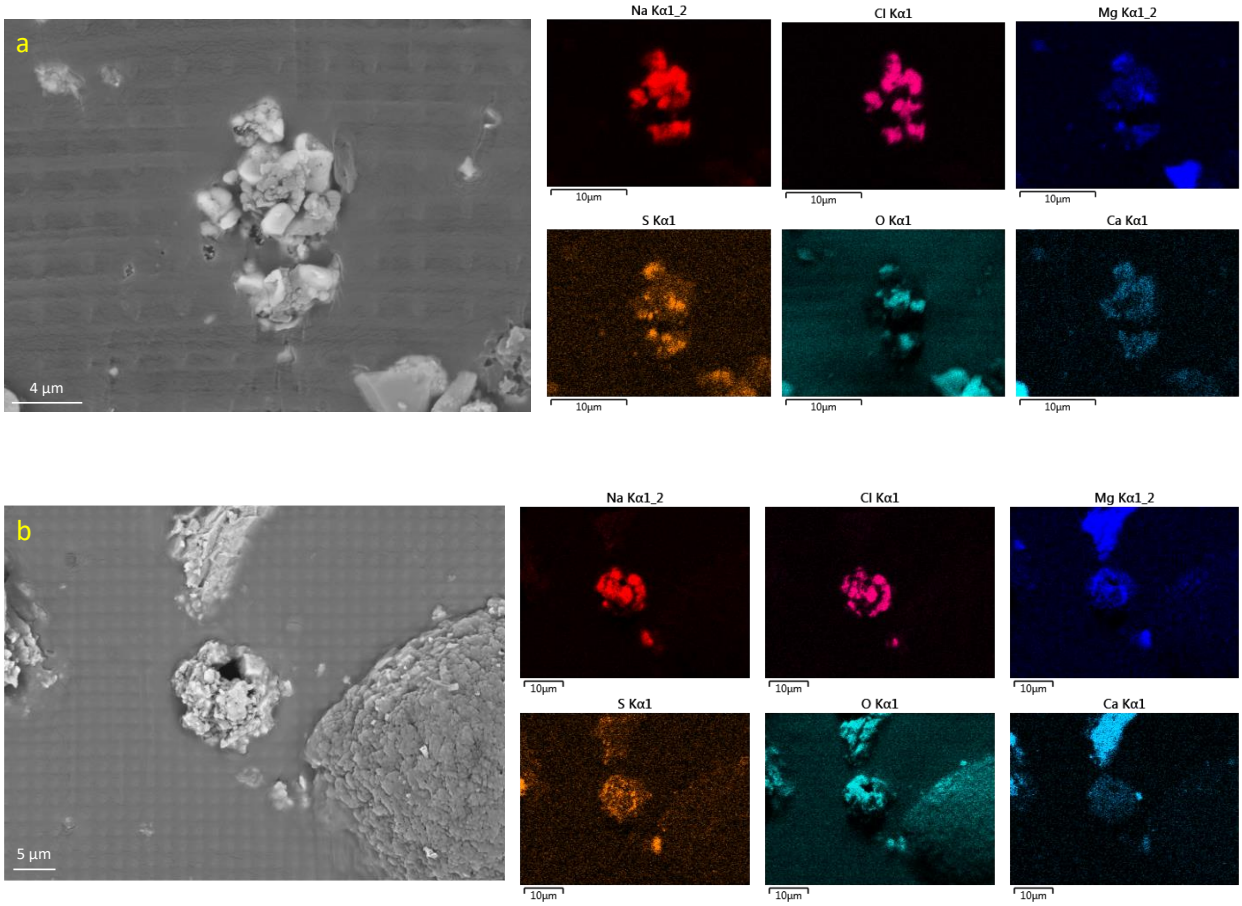

Figure 10. SEM BSE images and EDS element maps of sea-salt aggregates, consisting of NaCl and Mg-SO4. a) Sample # C-1. Note that the grain was crushed when the Biotape™ was applied. b) Sample #C-3. Sea-salt aggregate showing typical spherical morphology.

2.1.1.4 Summary of Site C Results

These analyses provide important information for evaluating the potential for storage canister SCC at the ISFSI site in question, and hence provide support for aging management plans at the site. SEM analysis of the Site C dust samples showed that the dusts are dominantly detrital mineral grains and organic matter in subequal amounts. The organic particles are mostly comprised of pollen grains of different morphologies and sizes, and of large stellate trichomes. Chemical analysis of the dust leachates show that soluble salts are present in the dust recovered from the canister surface. The SEM and EDS data for the Site C samples show clearly that sea-salt aerosols do get deposited on the canisters at this estuarine site. However, most of the soluble salts at Site C are not chloride-rich aerosols. Calcium, potassium, and sulfate salts are present in far larger amounts relative to chloride than they are in seawater, and sea-salts do not contain nitrate or ammonium. The salt compositions from the sampled locations suggest that the soluble salts are a combination of both sea-salts (rich in Na, Cl, and Mg), and salts derived from continental sources, rich in NH_4^+, K^+, Ca^{+2}, NO_3^-, and SO_4^{-2} [23]. It is reasonable to assume that most of the Cl^- was deposited as sea-salts because chloride is only a trace component in continental aerosols. However, in seawater (and in initially-formed sea-salt aerosols), the molar ratio of Cl^- to Na^+ is equal to 1.16. In these samples, Cl/Na ratios range from 0.17 to 0.40. If all of the Na+ were deposited as sea-salts, then the salt particles must have partially undergone particle-gas conversion reactions prior to or

after deposition. Such reactions convert chloride-rich sea-salts to nitrate and sulfate minerals. By reducing the chloride load on the canister surface, these reactions reduce the risk of canister SCC.

Assuming that the surface sampling was 100% efficient and the area sampled is accurately known, then the measured salt concentrations represent total soluble salt and chloride surface loads. Dust was sampled at the 2:00, 10:00, and 11:30 o'clock positions at two different axial locations, 24 and 39 inches from the bottom cover plate. Surprisingly, dust and salt loads were lower at the 11:30 positions and higher further down the flanks of the canister. This differs from observations of dust on canisters at other sites, where the top of the canister (near 12:00 positions) had the highest salt loads. Also, salt loads were much higher on the 39-inch transect than on the 24-inch transect; the 39-inch transect had soluble salt loads of 618 and 514 mg/m^2, at the 2:00 and 10:00 o'clock positions, respectively. Chloride distributions were consistent with the overall dust distributions, with the maximum chloride surface load of 42.5 mg/m^2, also at the 2:00 o'clock position on the 39-inch transect. Many studies have shown that the extent of corrosion and the risk of chloride-induced stress corrosion cracking is a function of chloride salt load. If the deposited dusts on this low heat load, long storage time "lead" canister are typical of canisters at Site C, then the low chloride load, combined with relatively high concentrations of nitrate, suggests that risk of canister chloride-induced stress corrosion cracking may be low at this site.

2.1.2 Yankee Rowe

In July, 2022, the site operator at the Yankee Rowe performed an aging management inspection of a SNF dry storage system at the Yankee Rowe ISFSI. As part of this, the site operator offered to collect dust samples for SNL to analyze. Original plans called for sampling dust on the canister surface, using sponges for wet sampling of the surface to determine soluble salt loads per unit area, and cellulose filters (Whatman #41) for dry sampling of the dust for SEM analysis. These materials were used in a previous sampling campaign [24], and it was known that the sponges contributed little to the soluble salts collected, and the Whatman #41 filters contributed nothing. However, the decision was made not to sample dusts from the canister surface during the inspection. Instead, the site operators (the Yankee Companies), volunteered to perform hand sampling of dusts in the outlet vents of the vertical storage system. The hand sampling was done using the dry filters to collect swipes of the dust just inside the vents; wet samples were not collected, and no effort was made to estimate the area sampled. The samples collected are listed in Table 1.

Table 1. List of Yankee Rowe dust samples and sample locations.

Sample #	Location Sampled
YR-1	North outlet vent
YR-2	South outlet vent
YR-3	East outlet vent
YR-4	West outlet vent

2.1.2.1 Sample Collection

The swipe samples were collected on 11 cm diameter filters, which were then folded and placed in sealable plastic baggies, and then sealed within a plastic Tupperware® style container containing desiccant cartridges to eliminate moisture. The samples were shipped overnight to SNL, where they were counted using gamma spectroscopy to ensure that they were not radioactive. Then, the samples were removed from the baggies, unfolded, and photographed. Sample photos are shown in Figure 11. Each pad was significantly abraded from being rubbed across the metal surface of the outlet vents and was discolored; one pad, YR-3, had pale rust-like stains. A whitish residue was observed on all samples.

Samples of the deposited material on the filters were taken with Biotape® adhesive strips for SEM analysis. However, the samples appeared to consist mostly of filter fibers. For sample YR-4, a small piece of the filter and deposited dust was cut off for examination by SEM to determine particle

mineralogies and morphologies. The remaining filter material was leached and the leachate analyzed to determine soluble salts. It should be noted that although the dust loads on the filters appeared light, the leachate was milky after leaching the samples, and thermodynamic modeling suggests that the leachate may have been saturated with respect to Ca-carbonate and/or Ca-sulfate; hence, the number provided here may be underestimating the amount of those soluble species present in the dust. In addition to the Yankee Rowe samples, two samples of the Whatman #41 filters from the lot sent to Yankee Rowe were analyzed as blanks.

2.1.2.2 Methods

The analytical methods used are the same as those used previously for other sites (Section 2.1.1.2). Measured anionic analytes include F^-, Cl^-, Br^-, NO_2^-, NO_3^-, SO_4^{-2}, PO_4^{-3} and HCO_3^- (by DIC); however, F^-, Br^-, and NO_2^- were not detected in any sample, and those species are not included here. Cationic analytes were Li^+, Na^+, NH_4^+, K^+, Mg^{+2}, and Ca^{+2}. Measured Li^+ concentrations were well below the limit of quantitation defined by lowest standard and can only be described as trace. The sample leachates were analyzed in duplicate, and stated standard deviations are based on the values obtained from the two IC analyses.

Sample YR-1

Sample YR-2

Sample YR-3

Sample YR-4

Figure 11. Photographs of the filters after collection of the canister dust at Yankee Rowe.

2.1.2.3 Results and Discussion

Chemical Analysis of soluble salts

All data are shown in the tables on the following pages (Table 2 to Table 5). Concentrations in micrograms per sample are shown for cations in Table 2 and for anions in Table 3; filter blank values are included. Sample values after subtracting the contribution from the filter blanks are shown in Table 4 and Table 5. Overall, the dust and soluble salt loadings on these samples were well above the detection limits and were sufficient to obtain quality data. In the tables, gray numbers indicate that there was a distinct peak in the IC spectra, but that the amount present was below the lowest standard, and hence, was not quantifiable. The analyte concentrations were generally consistent between the replicates, the measured uncertainties were consistently less than 1% for most samples. However, for sample YR-1, ion concentrations were very low and uncertainties for analytes were several % to 20%.

Note that the filter blank values in Table 2 and Table 3 are high for some analytes. The Whatman #41 filters used previously did not leach any salts [24], and it was not anticipated that these would. Unfortunately, the filters did leach significant amounts of some critical analytes. In particular, the amounts of Cl^- and Na^+ that leach from the filters are significant relative to the total amount measured in the samples; nearly all of the Cl^- and ½ to ¼ of the total Na^+ comes from the filters. The blank values for Cl^- are quite consistent, and if representative of the filters in general, then only a small amount of chloride, if any, is present in the dust. It was hoped that the SEM/EDS data would clarify whether chloride species were present in the dust, but as discussed later in this chapter, the dust was so fine grained that chemical discrimination of individual grains was impossible.

The blank-subtracted measured soluble salt compositions are shown graphically in Figure 12 for the cations, and Figure 13 for the anions. The cations are strongly dominated by Ca^{+2}, with much lower amounts of K^+ and Na^+ and trace Mg^{+2} and NH_4^+. Anions are dominated by HCO_3^- in the two most concentrated samples, YR-2 and YR-3 from the south and east outlet vents, respectively. In samples YR-1 and YR-4, from the north and west outlet vents, concentrations are much lower, and the anions are dominated by NO_3^- and SO_4^{-2}, with lesser amounts of HCO_3^-. For all four samples, the measured chloride concentrations are only slightly higher than the blank concentrations. No fluoride was detected; however, there were several unidentified peaks in the anion spectra, probably from organic anionic species, making discrimination of small fluoride peaks difficult. A single large peak at long elution times also probably represented an organic species.

The strong differences in composition and concentration with outlet vent sampled may be related to the dominant wind direction at the site. However, it should be noted that the sampling was done via hand swipes and no information is available on the size of the area sampled, or how consistent that was. While the measured compositions may be accurate, it is not clear that the measured concentrations are representative of what is present in each outlet vent.

Table 2. Cation concentrations in Yankee Rowe Dusts, µg/sample.

Sample #	Li^+	Na^+	NH_4^+	K^+	Mg^{+2}	Ca^{+2}
YR-1	*0.05* ± 0.001	13.0 ± 0.01	5.16 ± 0.02	3.4 ± 0.8	3.97 ± 0.03	38.4 ± 0.8
YR-2	*0.07* ± 0.002	27.0 ± 0.03	6.63 ± 0.02	42.1 ± 0.5	9.21 ± 0.08	206.3 ± 0.5
YR-3	*0.07* ± 0.001	19.2 ± 0.01	3.44 ± 0.03	27.0 ± 0.8	6.99 ± 0.01	232.1 ± 0.8
YR-4	*0.05* ± 0.001	37.9 ± 0.22	5.82 ± 0.06	26.5 ± 0.7	7.85 ± 0.02	124.0 ± 0.7
Filter blank-1	*0.03* ± 0.001	8.10 ± 0.07	2.26 ± 0.02	*0.54* ± 0.12	1.90 ± 0.01	5.56 ± 0.1
Filter blank-2	*0.04* ± 0.000	8.25 ± 0.02	2.33 ± 0.00	*0.66* ± 0.01	1.86 ± 0.00	5.44 ± 0.04

Table 3. Anion concentrations in Yankee Rowe Dusts, µg/sample.

Sample #	Cl^-	NO_3^-	PO_4^{-3}	SO_4^{-2}	HCO_3^-
YR-1	45.4 ± 1.1	10.7 ± 0.2	n.d. —	5.0 ± 0.2	7.8 ± 0.6
YR-2	54.4 ± 0.5	44.5 ± 0.3	*1.16* ± 0.5	102.5 ± 0.2	266.4 ± 0.9
YR-3	51.7 ± 0.5	20.5 ± 0.1	2.80 ± 0.5	21.7 ± 0.4	435.6 ± 0.4
YR-4	46.1 ± 0.1	61.3 ± 0.4	*0.74* —	154.2 ± 0.4	24.7 ± 0.8
Filter blank-1	41.26 ± 0.2	*0.77* ± 0.1	n.d. —	*0.71* ± 0.2	5.55 ± 0.3
Filter blank-2	41.74 ± 0.0	*0.88* ± 0.4	n.d. —	*0.68* ± 0.1	5.80 ± 0.1

Table 4. Blank-subtracted cation concentrations in Yankee Rowe Dusts, µg/sample.

Sample #	Li^+	Na^+		NH_4^+		K^+		Mg^{+2}		Ca^{+2}	
YR-1	*Trace*	4.8	± 0.01	2.87	± 0.02	2.8	± 0.8	2.09	± 0.03	32.9	± 0.8
YR-2	*Trace*	18.8	± 0.03	4.34	± 0.02	41.5	± 0.5	7.34	± 0.08	200.8	± 0.5
YR-3	*Trace*	11.0	± 0.01	1.15	± 0.03	26.4	± 0.8	5.11	± 0.01	226.6	± 0.8
YR-4	*Trace*	29.7	± 0.22	3.53	± 0.06	25.9	± 0.7	5.97	± 0.02	118.5	± 0.7

Table 5. Blank-subtracted anion concentrations in Yankee Rowe Dusts, µg/sample.

Sample #	Cl^-		NO_3^-		PO_4^{-3}	SO_4^{-2}		HCO_3^-	
YR-1	3.9	± 1.1	9.8	± 0.2	n.d. —	4.3	± 0.2	2.2	± 0.6
YR-2	12.9	± 0.5	43.7	± 0.3	*1.16* ± 0.5	101.8	± 0.2	260.8	± 0.9
YR-3	10.2	± 0.5	19.7	± 0.1	2.80 ± 0.5	21.1	± 0.4	430.0	± 0.4
YR-4	4.6	± 0.1	60.5	± 0.4	*0.74* —	153.5	± 0.4	19.0	± 0.8

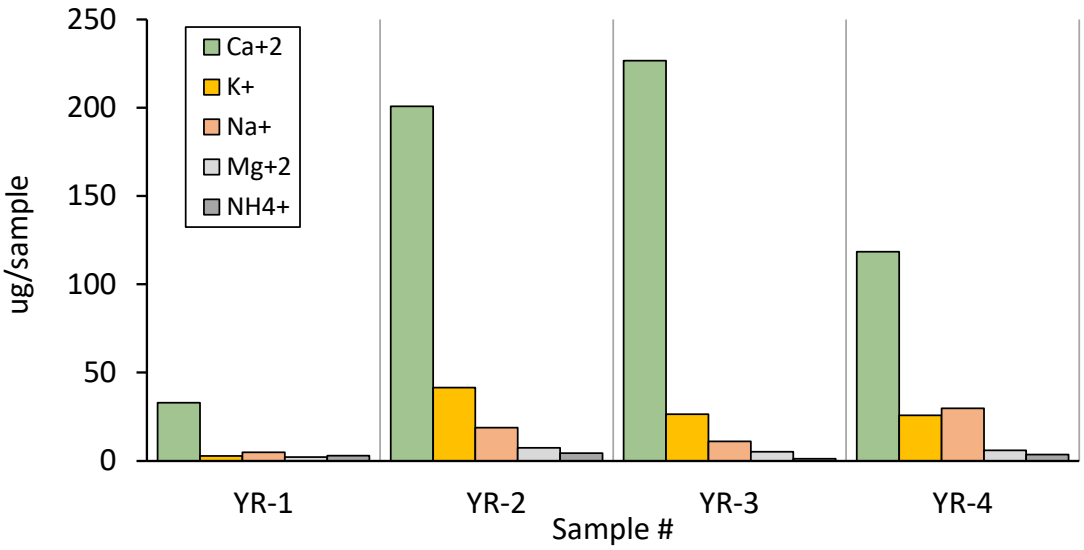

Figure 12. Background subtracted cation abundances in Yankee Rowe ISFSI samples.

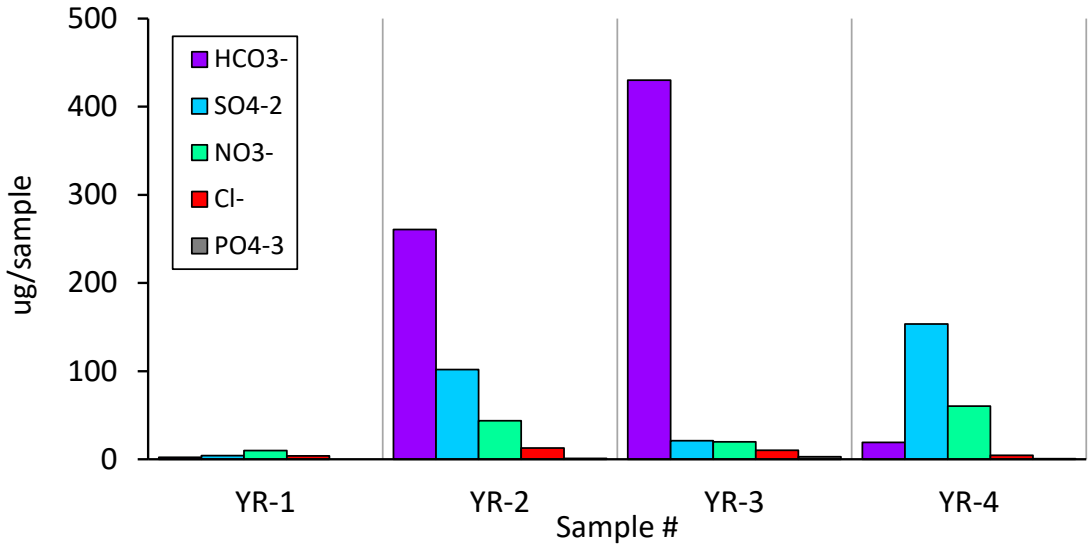

Figure 13. Background subtracted anion abundances in Yankee Rowe ISFSI samples.

Charge balances

Charge balances for the Yankee Rowe salts are shown in Table 6. The charge balance is very poor for YR-1, probably because the solute concentrations were very low and the analytical uncertainties high. For the other three samples, the charge balance errors were 20-30%. The charge balance errors indicate that anionic species are not being measured, and the presence of relatively large unidentified peaks in the anion spectrum shows that this is correct. The missing anionic species are almost certainly organic species. Significant charge balance errors and peaks for organic anionic species in IC spectra have been frequently observed in canister dusts [6-8].

Table 6. Charge balance errors for Yankee Rowe salts.

Sample #	Charge balance, %
YR-1	70.2
YR-2	25.9
YR-3	22.6
YR-4	29.7

$$Charge\ balance\ error, \% = \frac{(\sum eq_{cations} - \sum eq_{anions})}{(\sum eq_{cations} + \sum eq_{anions})} \times 100$$

SEM analysis of dust on Yankee Rowe filters

During leaching of the Yankee Rowe filters, a small segment of one filter, YR-4, was collected and retained for SEM analysis. After coating with Au/Pd to minimize charging, the sample was imaged using BSE imaging. Typical images of the dust are shown in Figure 14. Although a few large detrital mineral grains are present, the dust consists almost entirely of submicron-sized grains adhering to the filter fibers. Based on the chemistry, they are mostly calcium sulfate and calcium carbonate. One possible source for these particles is concrete efflorescence, which was observed deeper into the vents; however, when observed previously, efflorescence is coarsely crystalline as opposed to being very fine particles. The size and morphology of the particles on the Yankee Rowe filters suggests that they are atmospheric aerosols. The particles were too fine to analyze by EDS (the electron beam interaction volume is several

microns in size), so it was not possible to determine if any chloride phases were present in the dust. Given the high chloride concentrations in the filter blanks, it cannot be determined if the dust collected from the in-service canister at Yankee Rowe contains chloride.

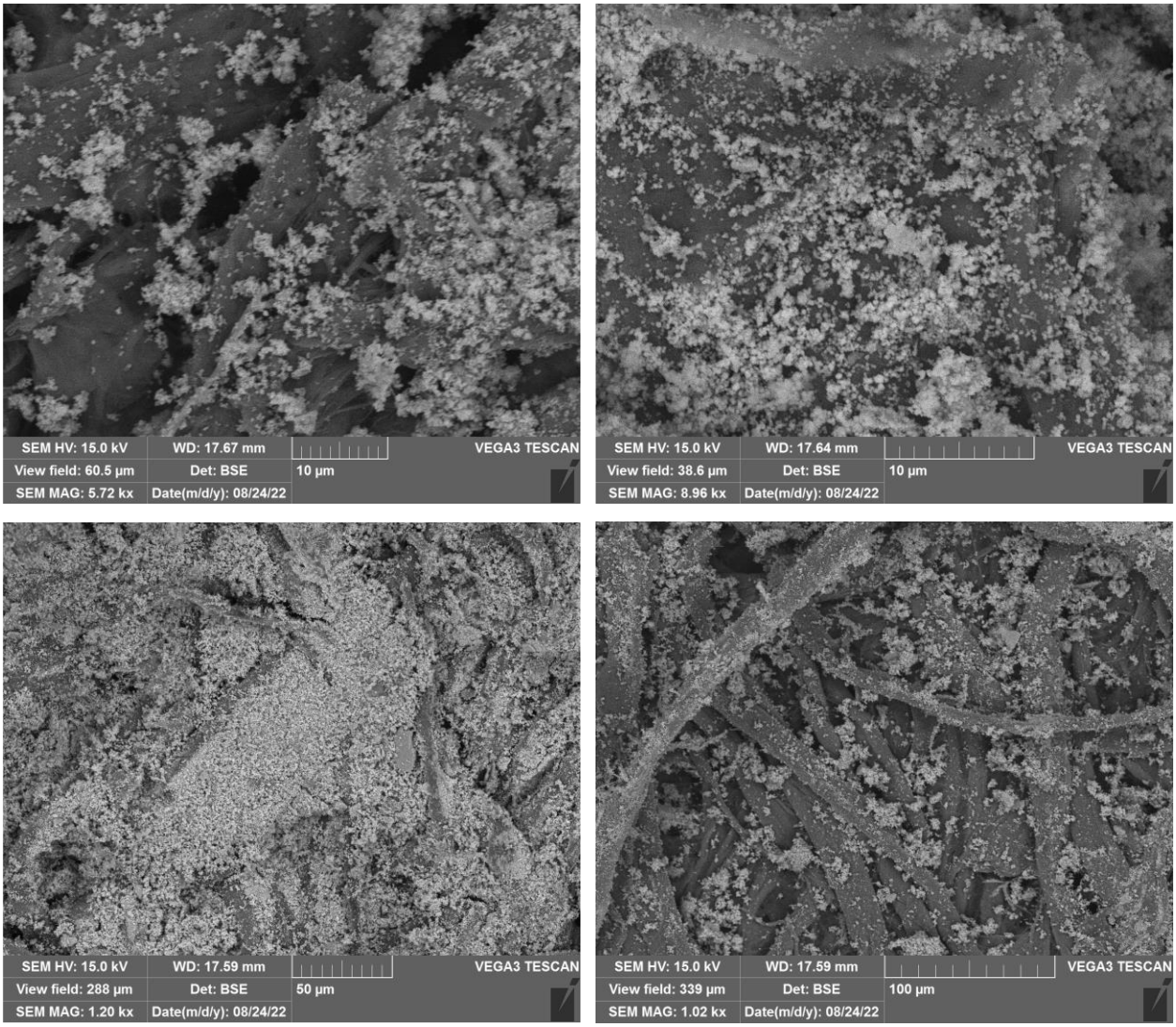

Figure 14. SEM BSE images of dust particles adhering to the Whatman #41 filter paper used to sample at Yankee Rowe.

Summary

To summarize, the dust collected from the outlet vents of the SNF dry storage system at Yankee Rowe was extremely fine, almost entirely <1 µm in size, and consisted largely of calcium sulfate and/or calcium carbonate. Lesser amounts of Na^+, K^+, and NO_3^- were also present, and possibly trace amounts of Cl^- however, high Cl^- from filter blanks made chloride quantification difficult. The dust is interpreted to be atmospheric aerosols. Only a few large detrital mineral grains were present. For any given ISFSI site, soluble salt compositions are commonly very consistent, and it is unusual at Yankee Rowe that the different inlet vents have different soluble salt compositions, with YR-2 and YR-3 being rich in carbonate, and YR-4 being rich in sulfate. No observational data were provided but it is speculated that rainwater intrusion may have occurred into some of the vents, and, may have reacted with the dust and

modified the salt compositions. Sulfate-rich acid rain is a problem in the northeastern U.S., and if blown into some of the vents, it may have converted calcium carbonate particles into calcium sulfates. Because the dust from the vents may have been modified by efflorescence or by interactions with rainwater, it is difficult to make any inferences about the chemistry on the canister surfaces, based on these samples.

2.2 Magnesium Chloride Brine Stability

The sustained presence and the stability of $MgCl_2$ brines impact the risk of SCC susceptibility of SNF dry storage canisters [25-28]. This is because $MgCl_2$-rich brines are the first to form by deliquescence of sea-salts on the surface of SNF dry storage canisters as the temperature decreases and the RH increases. Also, $MgCl_2$ brines lead to the formation of irregularly-shaped pits on SS, which may promote pit to crack transition by affecting stress distributions around the pit [29]. However, once formed, a $MgCl_2$ brine may not stably persist on the metal surface because of corrosion and degassing reactions that can raise the brine pH, resulting in precipitation of hydroxides, hydroxychlorides, or carbonate species. Eventually, these reactions can lead to brine dry-out. Understanding the stability of $MgCl_2$ brines is also important because pH changes in cathodic regions supporting pit growth may result in precipitation of Mg-hydroxide/hydroxychlorides. These precipitates suppress the oxygen reduction reaction (ORR) by forming a surface film that blocks oxygen diffusion to the surface [30, 31]. As a result, the dominant cathodic reaction becomes the hydrogen evolution reaction (HER), which may promote hydrogen embrittlement (HE) and stress corrosion cracking of the near-surface SS. Therefore, understanding the stability of $MgCl_2$ brine is critical for evaluating the risk of SCC.

$MgCl_2$ brines have been shown to be unstable at elevated temperatures, readily degassing $HCl_{(g)}$ to convert to Mg-carbonate or Mg-hydroxychloride phases [25, 26, 28]. If Mg-carbonate/hydroxychloride phases do form, brine dry-out may occur because the deliquescence RH values of these phases are higher than that of bischofite ($MgCl_2{:}6H_2O$). As a result, corrosion may halt until the temperature drops and RH rises sufficiently for other phases in the deposited salts (e.g., NaCl) to deliquesce, thus potentially delaying SCC for decades or even hundreds of years. Previous experiments by SNL have demonstrated brine dry-out from conversion of $MgCl_2$ brines to less deliquescent Mg phases [25, 28]. For example, a SS plate from the SNL canister mockup, was coated with $MgCl_2$ and exposed to a static deliquescent condition for several months, the brine completely dried out when the 2-1-4 Mg-hydroxychloride phase precipitated in the high pH cathodic regions around the corroding areas [25]. In a separate experiment, when $MgCl_2$ brine droplets were deposited on an inert substrate and heated to 80 ºC at 35% RH [25, 26], acid degassing resulted in conversion to the 2-1-4 Mg-hydroxychloride phase. These experiments illustrate two different phenomena resulting in conversion of $MgCl_2$ brines to precipitated Mg-carbonate, Mg-hydroxide, or hydroxychlorides: 1) temperature-driven degassing of $HCl_{(g)}$ to raise the pH or 2) an increase in pH in the cathodic region of a corrosion cell, due to hydroxide production [31]. Understanding the stability of $MgCl_2$ brines as a function of T, RH, and ambient acid gas concentrations (e.g. $HCl_{(g)}$) allows prediction of when a corrosive brine can persist on the canister surface, and when initiation and growth of pitting and stress corrosion cracking can occur.

In FY22, SNL continued experimental and geochemical modeling efforts to evaluate $MgCl_2$ brine stability as a function of temperature and environment. SNL has completed development of a consistent thermodynamic Pitzer database for modeling the $Mg(OH)_2 – MgCl_2 – H_2O$ ternary system as a function of temperature, which includes formation of the Mg-hydroxychloride phases from 25 °C to 120 °C (See Section 2.2.1). SNL has continued experimental work evaluating the stability of $MgCl_2$ droplets deposited onto an inert substrate and aged in an environmental chamber with continuous airflow. These studies evaluate the conversion of $MgCl_2$ to Mg-hydroxychloride and Mg-carbonate phases. In FY22, SNL completed two additional experiments. The first was initiated in FY21, where $MgCl_2$ droplets were deposited using a nebulizer system to generate smaller droplets than possible with the ink jet printer, to achieve higher surface areas to increase the reaction rate. These samples were exposed at 48 ºC at 40% RH for 16 weeks. The second experiment deposited $MgCl_2$ with the nebulizer but exposed the brine to

higher T, 60 ºC at 40% RH, to fill out the dataset with respect to T. Sampling has been completed on these experiments and the results are shown in Section 2.2.2.

2.2.1 Thermodynamic Modeling

In FY22, SNL completed efforts to create an internally consistent Pitzer thermodynamic database, built off the Yucca Mountain Project Database *data0.ypf.R2* [32]. to include a suite of Mg-hydroxychloride phases. The results are summarized in a current manuscript draft entitled *Development of a Consistent Geochemical Model of the $Mg(OH)_2$–$MgCl_2$–H_2O system from 25 ºC to 120ºC*, which is in the final stages of preparation. The details of this study have been summarized in previous reports [25-28]. Presented here is the final updated thermodynamic database, which incorporates (1) updates made to the Mg^{++} basis species, consistent with Mg^{2+} reported in CODATA (referred to here as Mg^{2+}_CODATA) and other recent publications; (2) updates to brucite ($Mg(OH)_2$), bischofite ($MgCl_2$:$6H_2O$), $MgCl_2$:$4H_2O_{(s)}$, 3-1-8 ($Mg_2(OH)_3Cl$:$4H_2O$), and $MgOH^+_{(aq)}$ to match available solubility data and to be consistent with Mg^{2+}_CODATA; and (3) incorporation of additional Mg-hydroxychloride phases, including the 2-1-4 ($Mg_3(OH)_4Cl_2$:$4H_2O$), 2-1-2 ($Mg_3(OH)_4Cl_2$:$2H_2O$), and 9-1-4 ($Mg_{10}(OH)_{18}Cl$:$4H_2O$) phases, into the database. These were accomplished by derivation of new thermodynamic data (ΔGf^o, ΔHf^o, S^o, and C_p) for the phases and adjustment the $\beta^{(0)}$ and $\beta^{(1)}$ Pitzer interaction parameters, and their temperature dependent coefficients (c_1-c_5), for the ion pair [$MgOH^+$ — Cl^-]. The new values were developed by fitting available experimental solubility data to calculate LogK values as a function of temperature. The resulting ΔGf^o, ΔHf^o, and S^o values calculated in this study are shown in Table 7. The heat capacities and heat capacity coefficients are shown in Table 8. The LogK values for the dissociation reactions of each of the Mg-containing phases evaluated in this study are presented in Table 9. Lastly, the final $\beta^{(0)}$ and $\beta^{(1)}$ Pitzer interaction parameters for the ion pair [MgOH+ — Cl^-], and their temperature dependence coefficients (c_1-c_5), are presented in Table 10.

Table 7. Thermodynamic values calculated from this study for several magnesium minerals and $MgOH^+_{(aq)}$.

Phase	Short Name	ΔG_f^o (kJ mol^{-1})	ΔH_f^o (kJ mol^{-1})	S^o (J mol^{-1}K^{-1})
$Mg(OH)_{2(s)}$	Brucite	-831.798	-922.826	63.199
$MgCl_2$:$6H_2O_{(s)}$	Bischofite	-2115.074	-2499.458	366.083
$MgOH^+_{(aq)}$	-	-626.503	-706.391	-67.36
$MgCl_2$:$4H_2O_{(s)}$	-	-1624.923	-1900.649	263.982
$Mg_2(OH)_3Cl$:$4H_2O_{(s)}$	3-1-8 Phase	-2554.73	-2942.309	313.700
$2Mg(OH)_2$-$MgCl_2$:$2H_2O_{(s)}$	2-1-2 Phase	-2815.800	-3158.670	309.170
$2Mg(OH)_2$-$MgCl_2$:$4H_2O_{(s)}$	2-1-4 Phase	-3306.055	-3762.785	393.890
$9Mg(OH)_2$-$MgCl_2$:$4H_2O_{(s)}$	9-1-4 Phase	-9136.206	-9602.377	842.430

Table 8. Heat capacity and coefficients calculated from this study for several magnesium minerals and $MgOH^{+}_{(aq)}$.

Phase	C_P (J $g^{-1}mol^{-1}$ $K)^{-1}$	*a* (J $g^{1}mol^{-1}$ K^{-1})	b (J mol^{-1} K^{2})	c (J K mol^{-1})	d (J K^{-2} mol^{-1})	e (J K^{-2} mol^{-1})
$Mg(OH)_{2(s)}$	74.99	80.764	$1.57x10^{-3}$	$-5.50x10^{5}$	-	$-5.77x10^{-7}$
$MgCl_2{:}6H_2O_{(s)}$	389.74	300	$3.87x10^{-1}$	$-5.05x10^{5}$	-	$-2.24x10^{-4}$
$MgOH^{+}_{(aq)}$	129.1	131.969	$1.36x10^{-3}$	-	-	$-3.33x10^{-5}$
$MgCl_2{:}4H_2O_{(s)}$	255.44	255.44	-	-	-	$-1.04x10^{-10}$
$Mg_2(OH)_3Cl{:}4H_2O_{(s)}$	286.07	204.93	$2.86x10^{-1}$	$-2.72x10^{5}$	-	$-1.22x10^{-5}$
$2Mg(OH)_2$-$MgCl_2{:}2H_2O_{(s)}$	293.73	243.72	$2.75x10^{-1}$	$-2.30x10^{6}$	-	$-6.85x10^{-5}$
$2Mg(OH)_2$-$MgCl_2{:}4H_2O_{(s)}$	362.08	336.37	$2.62x10^{-8}$	-	-	$-6.76x10^{-5}$
$9Mg(OH)_2$-$MgCl_2{:}4H_2O_{(s)}$	885.06	766.40	$8.34x10^{-1}$	$-1.07x10^{7}$	-	$-1.08x10^{-4}$

Table 9. Derived LogK grid [0-25-60-100-150-200] for the dissociation reactions of the Mg-bearing mineral phases.

Reaction	LogK					
	0 ºC	25 ºC	60 ºC	100 ºC	150 ºC	200 ºC
$Mg(OH)_{2\,(s)} + 2H^{+}_{(aq)} \leftrightarrow Mg^{++}_{(aq)} + 2\,H_2O$	19.02	17.16	15.04	13.15	11.32	9.89
$MgCl_2{:}6H_2O_{(s)} \leftrightarrow Mg^{++}_{(aq)} + 2Cl^{-}_{(aq)} + 6\,H_2O$	4.76	4.55	4.17	3.69	3.03	2.26
$MgOH^{+}_{(aq)} + H^{+}_{(aq)} \leftrightarrow Mg^{++}_{(aq)} + H_2O$	12.81	11.68	10.33	9.22	8.06	7.14
$Mg_2(OH)_3Cl{:}4H_2O_{(s)} + 3\,H^{+}_{(aq)} \leftrightarrow 2\,Mg^{++}_{(aq)} + Cl^{-}_{(aq)} + 7\,H_2O$	28.42	25.86	22.94	20.34	17.83	15.81
$Mg_3(OH)_4Cl_2{:}2H_2O_{(s)} + 4\,H^{+}_{(aq)} \leftrightarrow 3\,Mg^{++}_{(aq)} + 2\,Cl^{-}_{(aq)} + 6\,H_2O$	45.97	41.35	35.92	30.88	25.75	21.46
$Mg_3(OH)_4Cl_2{:}4H_2O_{(s)} + 4\,H^{+}_{(aq)} \leftrightarrow 3\,Mg^{++}_{(aq)} + 2\,Cl^{-}_{(aq)} + 8\,H_2O$	42.70	38.56	33.78	29.41	25.07	21.51
$Mg_{10}(OH)18Cl_2{:}4H_2O_{(s)} + 18\,H^{+}_{(aq)} \leftrightarrow 10\,Mg^{++}_{(aq)} + 2\,Cl^{-}_{(aq)} + 22\,H_2O$	174.39	157.35	137.79	120.08	102.70	88.78

Table 10. Pitzer interaction parameters for the [$MgOH^+$--Cl^-] interaction, including $\beta^{(0)}$, $\beta^{(1)}$, $\beta^{(2)}$, c^{φ}, $\alpha^{(1)}$, and $\alpha^{(2)}$ along with temperature dependent values, c_1- c_5.

Pitzer Interaction Parameter			c_1	c_2	c_3	c_4	c_5
$MgOH^+$ -- Cl^-	$\beta^{(0)}$	-0.0125	1.64389×10^{-6}	22.1680	3.4418×10^{-9}	0	0.1343
	$\beta^{(1)}$	-0.3	8.13389×10^{-5}	2783.7256	1.7249×10^{-7}	0	16.8295
	$\beta^{(2)}$	0	0	0	0	0	0
	c^{φ}	0	0	0	0	0	0
	$\alpha^{(1)}$	2	0	0	0	0	0
	$\alpha^{(2)}$	12	0	0	0	0	0

Using the values in Table 7 - Table 10, phase solubilities for the $Mg(OH)_2$ – $MgCl_2$ – H_2O ternary system at 25, 40, 60, 80, 100, and 120 °C were calculated, and are compared to available experimental data in Figure 15. This work was made possible due to the recent availability of experimental data [33-35] and modeling efforts [36-38] to aid in developing a consistent understanding of this system. The internally consistent changes made to the initial thermodynamic database (*data0.ymp.R2*) allow for the generation of phase diagrams for the $Mg(OH)_2$–$MgCl_2$–-H_2O system that accurately reflect experimental data as a function of temperature.

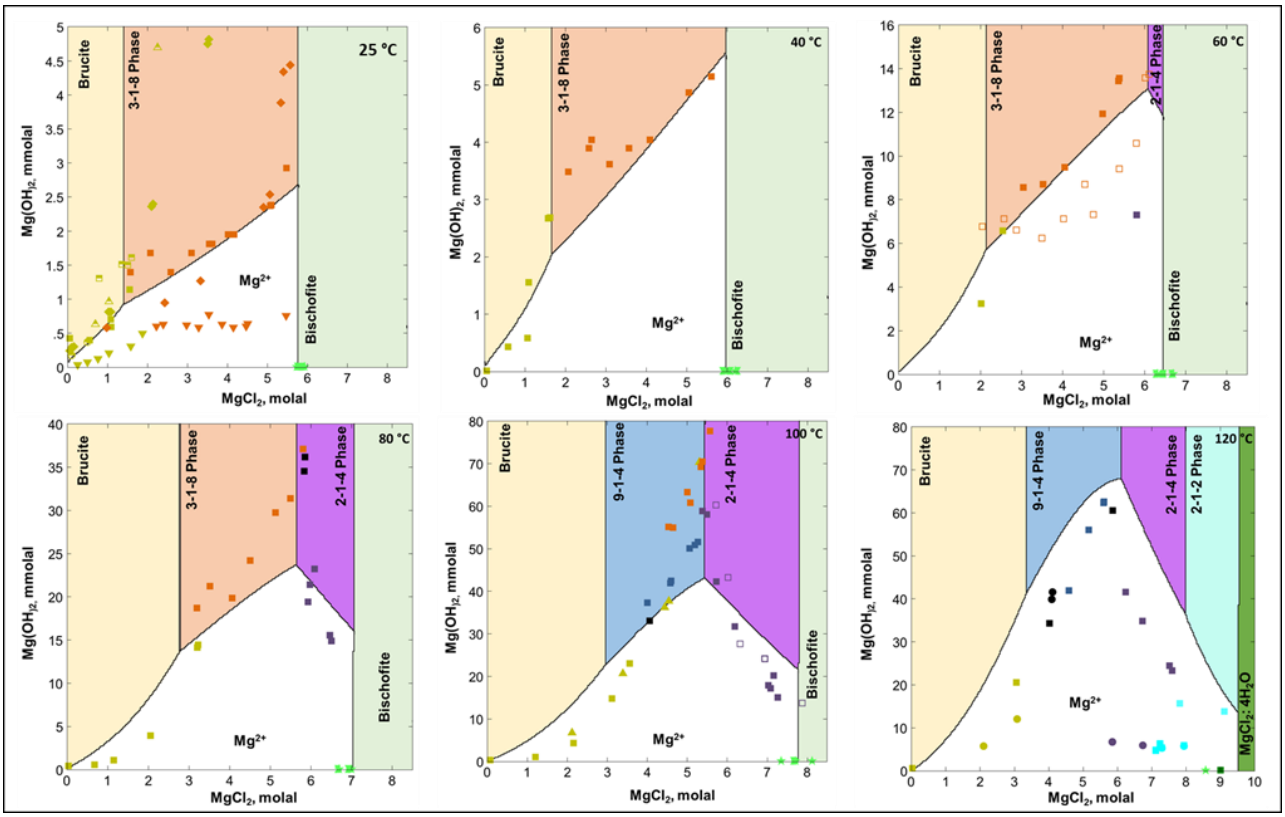

Figure 15. Calculated solubility diagrams of the $Mg(OH)_2$ – $MgCl_2$ – H_2O ternary system at 25°C, 40 °C, 60°C, 80 °C, 100 °C, and 120 °C shown with available experimental data.

2.2.2 $MgCl_2$ degassing experiments

Experimental efforts at SNL to further evaluate the stability of $MgCl_2$ brines, adding to previous experiments performed in FY17 – FY20 [25-28], involved completing an experiment that began in FY21, carrying out a second experiment, and performing initial analyses of the samples. As mentioned previously, understanding the stability of $MgCl_2$ brines is important due to their impact on canister corrosion and potential CISCC. A stable $MgCl_2$ brine will not only cause irregular pitting, which may be more susceptible to pit to crack transition, but also results in brine formation earlier and at a higher temperature because bischofite ($MgCl_2 \bullet 6H_2O$) is the first sea-salt to deliquesce on the canister surface as the temperature decreases, and the RH increases. Thermal modeling has demonstrated that a $MgCl_2$-rich brine could potentially exist on the canister surface, depending on the initial heat load and local weather data, as soon as 20-30 years after the fuel is loaded [25-27]. However, as discussed previously, $MgCl_2$ brines may react with the atmosphere and degas Cl^- and/or absorb CO_2. During this process, $MgCl_2$ brines may form less deliquescent phases, such as Mg-hydroxychlorides (Section 2.2.1), Mg-hydroxide, or Mg-carbonate phases, leading to brine dry-out.

Two experiments were completed in FY22 to investigate the ageing of a $MgCl_2$ brine at elevated temperatures on an inert substrate. The experimental procedure was similar to previous experiments; $MgCl_2$ was deposited onto an inert substrate (25 mm diameter silicon wafers), and placed in an environmentally controlled chamber (T and RH; Figure 22) with continuous airflow, generated with a Zero Air Generating system that removes all contaminants (acid gases, organics) from the air stream (importantly CO_2 is not removed by the Zero Air Generating system). Samples were periodically extracted for analysis (sampled at 4, 8, and 16 weeks). The first experiment was initiated in FY21, and the exposure conditions for this experiment were 48 °C, 40 % RH, with an air flow rate of 9 L/min. These conditions were the same as in an earlier experiment; however, the deposited $MgCl_2$ droplets were smaller. This modification was made by depositing the droplets using a nebulizer in an aerosol chamber, rather than with the inkjet printer as had been done previously [39], and was made for both practical and scientific reasons. First, highly concentrated $MgCl_2$ brines are viscous and can clog the inkjet printer. Second, the smaller nebulizer droplets have a higher surface area-to-volume ratio, and hence were expected to react more quickly, degassing HCl and absorbing CO_2 at a higher rate than the coarser inkjet printer droplets. Previous work using inkjet-deposited drops under these conditions resulted in minimal conversion over the experimental duration, where the calculated Cl^- loss was <10% in 16 weeks and the carbonate gain was ~0.1 µmol/µmol of Mg [27]. SEM/EDS analyses suggested the formation of Mg-CO_3 and Mg-hydroxychloride species was preferential to smaller droplets (where the surface area-to-volume ratio is largest). This was the motivation to perform the experiment with smaller $MgCl_2$ droplets in FY21.

In the second experiment, the Si-wafers coated with $MgCl_2$ were aged in the environmental chamber at 60 ºC, 40 % RH, with an airflow of 2 L/min. This condition represents an intermediate temperature to compare with the 40 and 80 ºC experiments run previously. The previous study at 80 °C and 35 % RH, which represent accelerated conditions, saw a significant amount Cl^- degassing [26]. In these studies, nearly 20% of the Cl^- was lost within 4 weeks and upwards of 40% was lost over 8 weeks. X-ray diffraction (XRD) analysis demonstrated the formation of a high temperature Mg-hydroxychloride phase (2-1-4 phase), agreeing with the phase predicted by geochemical modeling (Section 2.2.1) and with other studies where 2-1-4 phase was observed under similar conditions [25, 26]. For tests performed at 60 ºC, more degassing would be expected as compared to the 48 ºC experiments, but significantly less than the 80 ºC tests. Also, at 60 ºC it is anticipated that the 3-1-8 phase would be the dominant Mg-hydroxychloride phase, similar to the expected phase at 48 ºC, in contrast to the 2-1-4 phase that occurred at 80 ºC. It is also expected that the brine absorbs CO_2 from the atmosphere; however, the exact Mg-carbonate phase to form is not known – though its formation would lead to a less soluble salt assemblage. [25, 26]. For tests performed at 60 ºC, more degassing would be expected as compared to the 48 ºC experiments, but significantly less than the 80 ºC tests.

Figure 16. Photos of the modified environmental chamber in order to increase the airflow rate to 9 L/min [40].

Three experiments have been performed at 48 ºC and 40 % RH. These experiments differed in order to evaluate different experimental parameters. In the first (FY19;[26]), the airflow was 2 L/min with ~100 μg/cm^3 $MgCl_2$, in the second (FY20; [27]) the airflow was 9 L/min and the salt loading was ~300 μg/cm^3; and in the third (begun in FY21 and completed in FY22), the airflow was 9 L/min and the salt loading was ~75 μg/cm^3. The changes in the airflow were anticipated to affect the degassing rate by enhancing atmospheric gas exchange. The lighter surface loads corresponded to smaller brine droplets with a greater surface area, and again were anticipated to result in more rapid degassing. The bulk composition of the FY21 experiment is shown in Figure 17-a. Overall, the deposition of Mg was relatively consistent, and it appears as though Cl^- decreases and CO_2 increases over exposure time. In contrast, for the FY22 experiment at 60 ºC, 40% RH, the amount of Mg appears to decrease with exposure time. This is likely due to deposition differences between samples, possibly as a function of location in the nebulizer chamber. An alternative explanation is that, as the $MgCl_2$ converts to a crystalline phase, it is forming a flaky, nonadherent phase and falling or being blown off the wafer. One wafer from each exposure time has been set aside for additional analysis, including XRD, SEM, and spectroscopy to determine compositional changes to the Mg assemblages.

The amount of Cl^- also seems to decrease with time while the amount of CO_2 appears to increase — however, given the observed variations in Mg, absolute concentrations may be deceptive; ion ratios and charge balances are a better metrics to determine how the brine composition changes over time.

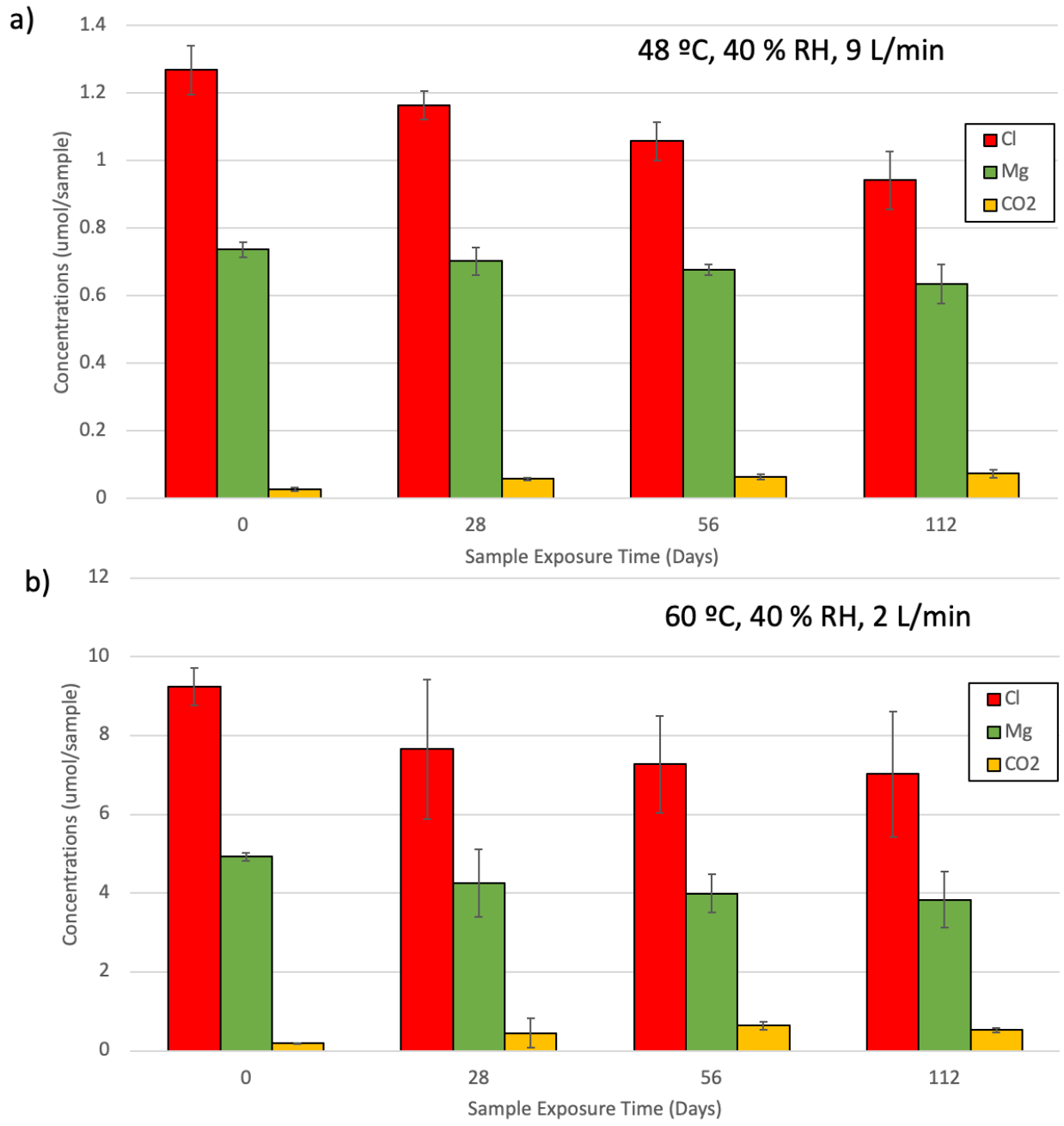

Figure 17. Average composition of the salt after environmental exposure for a) FY21 study at 48 ºC, 40% RH and 9 L/min airflow, and b) FY22 study at 60 ºCº, 40% RH, and 2 L/min airflow.

Specifically, the ratio of the Cl:Mg and CO_2:Mg will elucidate how the phase composition may be shifting as a function of the exposure time. Figure 18 shows the ratio of Cl:Mg as a function of exposure time for all of the experiments performed, where the most recent experiments are shown in orange (FY21) and red (FY22). Also shown are Cl:Mg ratios for possible Mg-bearing mineral phases that might form due to degassing. Figure 19 shows the %Cl loss, normalized to the amount of Mg present, for each sample as function of exposure time. Unexposed samples are expected to have a Cl:Mg ratio = 2 and the %Cl loss = 0. Over time, as Cl^- degasses, the Cl:Mg ratio and % Cl lost will decrease until a precipitate begins to form. For the 80 ºC sample, the Cl:Mg ratio rapidly decreases and is below 0.5 at ~60 days.

XRD results from that experiment showed that the 2-1-4 phase was present on the wafer, which has a Cl:Mg ratio of 0.66. Adsorption of carbonate could lead to a decrease in the Cl:Mg ratio beyond the expected ratio of the 2-1-4 phase, however SNL did not have the capability to quantify carbonate when this experiment was run. Over the 60 days, nearly 80% of the Cl^- was lost due to degassing. At 60 ºC, there was significantly less change in the Cl:Mg ratio; the results more closely resemble the trends seen for the 48 ºC experiments. After 16 weeks, the Cl:Mg ratio was ~1.7. Under these conditions, it would be expected that Cl^- could degas until the 3-1-8 phase forms (Cl:Mg = 0.5), however after 16 weeks the measured ratio was still well above that value. The three 48 ºC datasets differed in airflow and in salt loading, but it is not clear if either of those variables significantly impacted the resulting degassing rates and Cl:Mg ratio. The FY21 dataset (orange) showed the most Cl^- loss, with a Cl:Mg ratio of ~1.5 after 16 weeks; however, control samples (0 weeks) had a Cl:Mg ratio of ~1.8. The control samples for several of the data sets were significantly below the expected Cl/Mg ratio of 2.0; potential causes for this are currently being explored. Similar observations can be seen in Figure 19, where the % Cl loss for the 60 ºC dataset is of a similar magnitude as the 48 ºC data and the FY21 (orange) dataset is systemically higher than all the other datasets; again, for several experiments, the controls (0 days) show significant chloride loss.

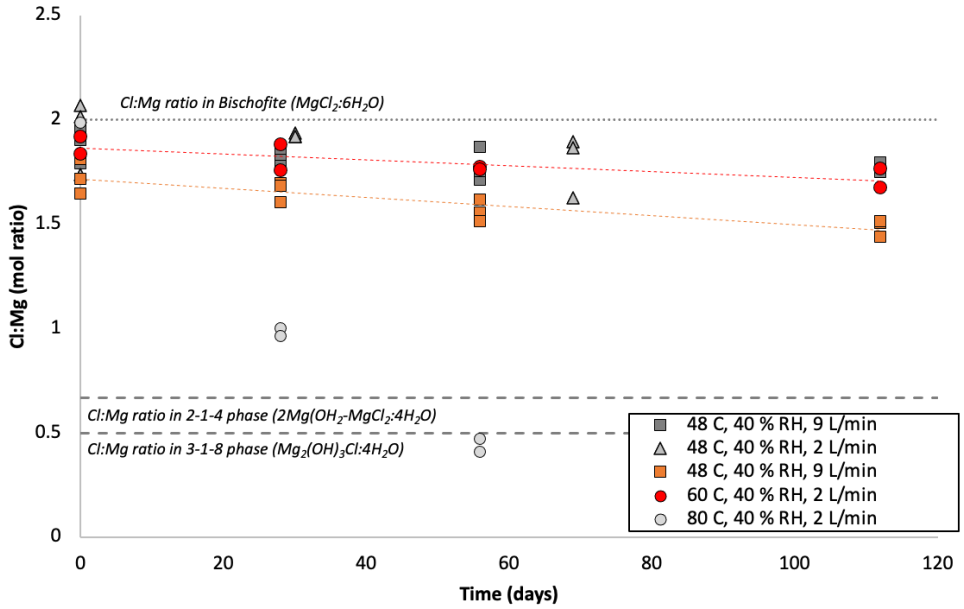

Figure 18. Cl:Mg ratio as a function of exposure time of all $MgCl_2$ degas experiments performed to date shown with Cl:Mg ratio of possible Mg-bearing mineral phases.

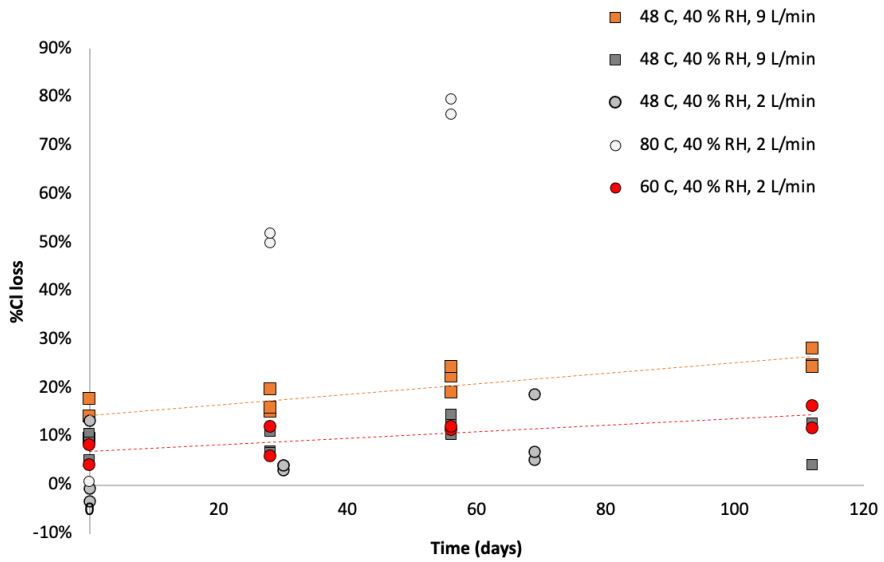

Figure 19. The %Cl loss as a function of exposure time for each of the $MgCl_2$ degas experiments.

In FY20, SNL acquired a dissolved inorganic carbon analyzer (DIC), and subsequent experiments have quantified carbonate (reported as CO_2) in the exposed samples. Figure 20 shows the CO_2:Mg ratio as a function of exposure time. Overall, CO_2 is absorbed by the system and the CO_2:Mg ratio increases with time. The 60 ºC dataset absorbed the most CO_2 even though the flow rate was 2 L/min as compared with 9 L/min for the two previous experiments, and achieved a CO_2:Mg ratio ~ 0.2 after 16 weeks. This is expected as the partial pressure of HCl(g) generated by the brine is higher at higher T, supporting more rapid degassing. The other two data sets at 48 ºC differed in salt loading, but generally agree well with respect to the CO_2:Mg ratio as a function of exposure time. The conversion of $MgCl_2$ to Mg-carbonate phases would likely lead to brine dry-out as the Mg-carbonate phases are much less soluble and deliquescent than the $MgCl_2$ phases. No carbonate phases were identified in the XRD and very little carbon was identified by SEM/EDS for the 48 ºC experiments. For the 60 ºC experiment, a sample corresponding to each exposure period (0, 4, 8, and 16 weeks) has been reserved for XRD and SEM analysis, though this has not yet been completed.

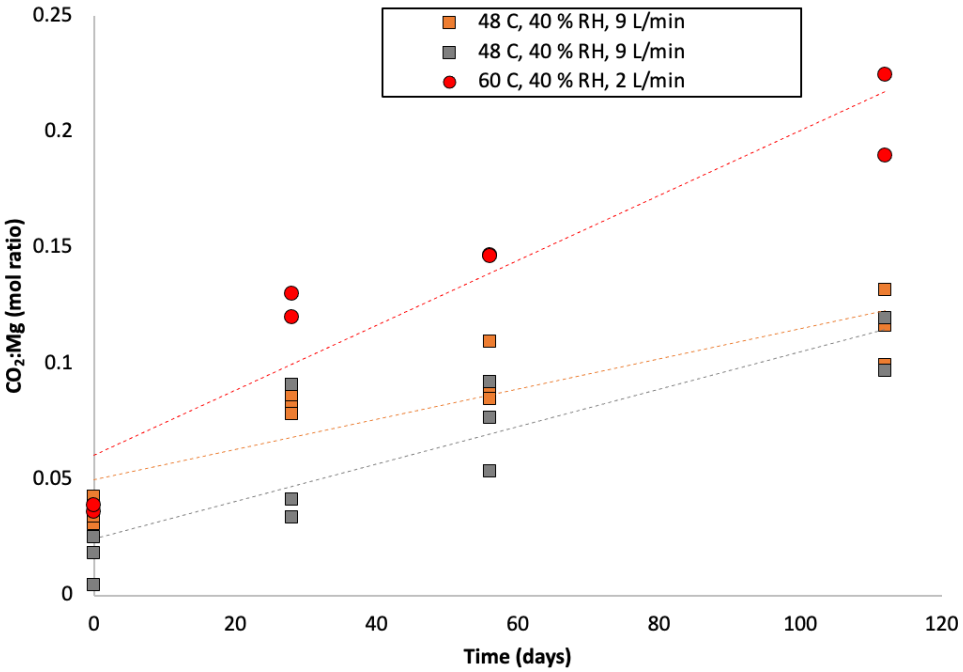

Figure 20. CO_2:Mg ratio as a function of exposure time of all $MgCl_2$ degas experiments performed since SNL obtained the dissolved organic carbon analyzer.

Another possible assessment of the degree of $MgCl_2$ conversion is through the charge balances. The IC measures Mg^{2+} and Cl^-, and the DIC measures carbonate as CO_2, but the contribution of hydroxide is not accounted for. If Mg-hydroxychlorides or hydroxycarbonates form, an anion deficiency is expected in the charge balance. Figure 21 shows the charge balances as a function of time for all three of the experiments performed at 48 ºC and the experiment at 60 ºC. The anion deficiency increases as a function of exposure time, suggesting increased conversion to hydroxide-bearing mineral phases; however, there is significant scatter. The anion deficiency for the 60 ºC experiment was generally lower than the 48 ºC experiments, and generally was < 4%. This suggests that degassing at 60 ºC was dominantly balanced by carbonate adsorption and precipitation, rather than hydroxy-chloride precipitation (Figure 20), where more of the anions are accounted for by the measurement techniques. The experiments at 48 ºC generally had charge balances of < 12%, but in some cases the charge balances were very high even with no exposure time. Specifically, for the FY21 data (red points in Figure 21), the anion deficiency increases throughout the experiment, but is high throughout the entirety of the experiment; the cause for this is unknown at this time, but it may be due to degassing during salt deposition.

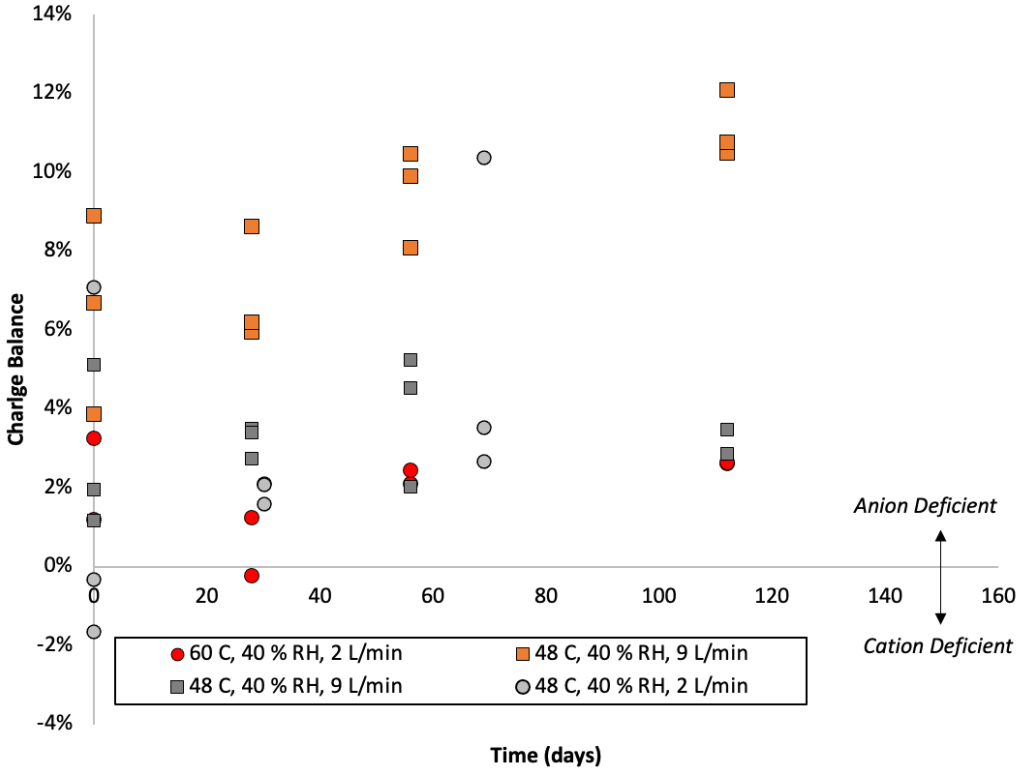

Figure 21. Charge balances for the $MgCl_2$ degas experiments (excluding the experiment at 80ºC) demonstrating how the anionic deficiency changes with exposure time.

In FY23, SNL will complete the analyses of the 60 ºC dataset, including SEM, XRD, and spectroscopy as needed to identify the specific phases that exist. These studies, in conjunction with the thermodynamic modeling, help improve our understanding of the stability of Mg-rich brines as a function of temperature and increase our ability to predict deliquescence behavior. Following these experiments with clean air, SNL will perform experiments with known amounts of common atmospheric acid gases. Evidence of acid gas reactions with the salts present on the canisters has been observed in SEM images of samples collected from canisters at ISFSI sites [41, 42]. However, the implications of these reactions on canister corrosion and the potential for CISCC are not fully understood. Experimental analysis of the stability of $MgCl_2$ brines under atmospheric conditions with environmental levels of $HCl_{(g)}$, $SO_{2(g)}$, and/or $NO_{x(g)}$ will be performed, and the results will be compared with the thermodynamic modeling to better understand the impact of these reactions.

2.3 Canister Deposition Field Demonstration Studies

The SCC group has performed several studies in support of the CDFD project. For the CDFD project, dusts and salts will be collected from the surfaces of three commercial 32PTH2 NUHOMS welded stainless steel storage canisters in Advanced Horizontal Storage Modules, with planned exposure testing for up to 10 years at an operating ISFSI site. One of the canisters will be left in an ambient condition, unheated, while the other two will have heaters to achieve canister surface temperatures that match, to the degree possible, SNF loaded canisters with heat loads of 10 and 40 kW. The overall goal of the project is to measure the dust deposited onto the canister surfaces to gain an understanding of dust deposition rates over time, and also to monitor potential changes in the dust/salt compositions in response to the elevated

temperatures on the heated canister surface. Additional required information to fully understand dust deposition model is ambient aerosol characteristics (particle size distributions, compositions, and abundances) and site-specific weather data. The information obtained from the CDFD will be critical for ongoing efforts by Pacific Northwest National Laboratories to develop and validate a dust deposition model, and in a larger sense, to develop an improved understanding of the potential for SCC of SNF dry storage canisters.

To prepare for the CDFD, SNL is evaluating methods of canister dust sampling and aerosol sampling. These activities include characterization of the canister surface roughness, development of techniques for marking the sampling locations on the canisters and for quantitatively sampling the dust on the canister surface, and training with the aerosol sampling equipment.

2.3.1 Canister Sampling

In FY21, SNL completed a preliminary plan for sampling surface dust from the CDFD dry storage canisters. It was published as a Level 4 Milestone, *Surface Sampling Techniques for the Canister Deposition Field Demonstration* [10]. The report described possible sampling locations on the canister surfaces, sampling intervals, and possible sampling techniques. Surface sampling campaigns for dust collection are planned to occur yearly or bi-yearly, with a goal to evaluate important environmental parameters that might impact the potential occurrence of SCC. Specifically, measured dust deposition rates and deposited particle sizes will improve parameterization of salt/dust deposition models; salt load is an important risk factor for canister SCC. The size, morphology, and composition of the deposited dust and salt particles will be quantified, as well as the soluble salt load per unit area and the rate of deposition, as a function of canister surface temperature, location, time, and surface orientation. In FY22, SNL began testing the surface sampling techniques. The results of these activities were described in detail in a Level 3 Milestone, *FY22 Update: Development of Surface Sampling Techniques for the Canister Deposition Field Demonstration*, which was completed in April 2022 [11]. Specifically, this report focused on three different tasks; (i) canister surface roughness measurements were made via surface-replicating molds at several locations on one of the test canisters (surface roughness is a potentially important parameter for air flow and dust deposition); (ii) corrosion testing of thermocouple wires, spot welds, and attachments was carried out to evaluate the potential aging and lifetimes, and possible use of these for indexing sample locations; (iii) hand sampling protocols were developed for sampling the dust on the canisters, and initial testing was carried out to validate the sampling method.

Canister surface roughness measurements were collected from 17 locations on a single canister (32PTH2-S023-C-H-001) used for the CDFD project. For each roughness measurement a negative replica of the surface was prepared by adhering a 3D printed sample cell to the location of interest and injecting PlatSil73-25, which formed a mold of the metal surface. Once cured, the molds were removed from the canister and analyzed by laser profilometry. The line scans were averaged to determine the R_a and R_z for each sample representing specific canister locations and features. R_a represents the arithmetic mean of the absolute surface roughness [43-45], calculated by:

$$R_a = \frac{1}{l}\int_0^l |z(x)|dx \qquad eq\ (1)$$

Where l is the length of the line scan, and |z(x)| is the absolute value of the surface topography as a function of position in the x direction. R_z is the deviation between the highest peaks to the lowest valley on the surface [43, 45]. This is calculated by:

$$R_z = R_P + R_V \qquad eq\ (2)$$

Where R_P is the height of the peak and R_v is the depth of the valley. Long range waviness was removed using an automatic tilt correction value of Λ_c = 0.025 mm and was applied to all samples. The approach was validated using surface roughness standards covering 4 different roughnesses from 0.1 μm < R_a < 3.2

μm and 0.90 μm < R_z < 18.5 μm). Figure 22 shows examples of the canister locations and features measured using the surface-replicating molds. It also shows examples of the resulting mold surfaces linked with the photometric map [46] and the 3D topographic map as measured by the laser profilometry to determine the surface roughness. The results for each location are shown in Table 11.

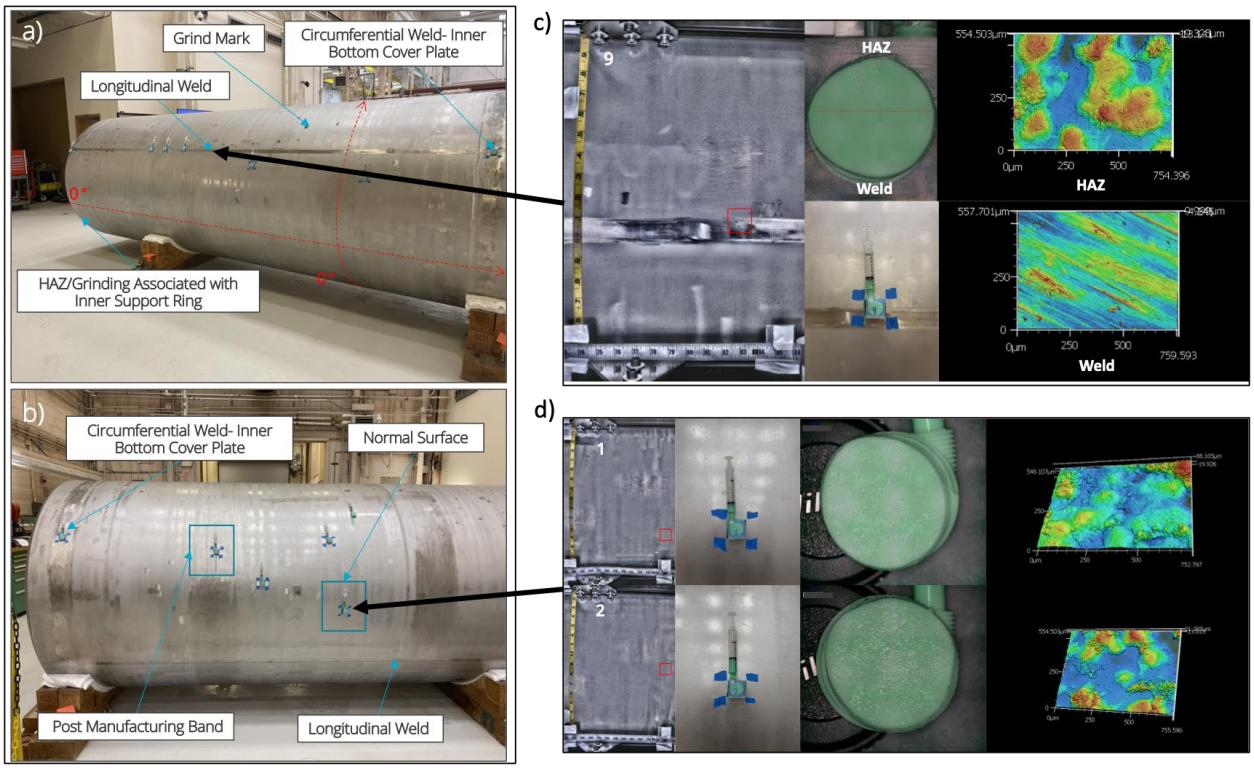

Figure 22. a) and b) are photos of the canister with the surface roughness molds attached highlighting various canister location and features. c) shows a sample collected from within and adjacent to the longitudinal weld and d) shows two examples of the mill finish, or "normal surface" roughness. Both c) and d) show the mapped location on the photometric map (red square), photographs of the mold location, optical images of the mold surface, and a 3D topographic map of the surface obtained by laser profilometry [11].

Table 11. Sample number, canister feature, approximate canister location, measured surface roughness (R_a and R_z), and scan direction for each surface mold collected from the canister from Knight et al. 2022 [11].

Sample #	Canister Feature	Approx. Coordinates[1] (inches)	R_a (μm)	R_z (μm)	Scan Direction
1	Normal Surface	(130.875, 154.875)	0.78	4.27	Vertical
2	Normal Surface	(59.625, 146.500)	0.78	4.33	Vertical
3	Normal Surface	(20.250, 146.250)	0.84	4.40	Vertical
4	Normal Surface	(115.250, 166.000)	0.84	4.51	Horizontal
5	Normal Surface	(118.375, 67.500)	0.76	3.88	Horizontal
6	Normal Surface	(158.875, 64.875)	0.75	3.75	Vertical
7	Circumferential Weld (Inner Bottom Cover Plate)	(190.250, 146.250)	0.52	2.65	Vertical
8	Circumferential Weld (Inner Bottom Cover Plate)	(190.125, 73.125)	0.53	3.00	Vertical
9-Weld	Longitudinal Weld	(82.625, 73.750)	1.41	1.86	Vertical
9-HAZ	HAZ	(82.625, 73.750)	3.19	3.33	Vertical
10-Weld	Longitudinal Weld	(71.375, 73.500)	1.05	1.54	Vertical
10-HAZ	HAZ	(71.375, 73.500)	3.02	3.15	Vertical
11	Longitudinal Weld	(73.250, 73.250)	0.81	1.58	Vertical
12	Post Manufacturing Band	(111.000, 138.750)	0.53	2.54	Vertical
13	HAZ/Grinding Associated with Support Ring Inner Circumferential Weld	(1.500, 72.250)	1.30	2.34	Vertical
14	Grind Mark	(149.750, 150.250)	0.80	2.36	Vertical
15	Grind Mark	(137.375, 158.750)	1.08	3.43	Vertical
16	Canister bottom – Grind Mark[2]	(240.625, 48.50)	0.61	3.14	Horizontal
17	Canister bottom[2,3]	(180.750, -156.625)	2.66	11.34	Horizontal

[1]The coordinates are reported (longitudinal, axial) in inches, where the open end of the canister represents 0 inches longitudinally and increase toward the bottom of the canister. To determine the axial position, the center of the canister underside represents 0 inches radially and increases counterclockwise. The locations were determined by approximating the midpoint of the sample cell on the canister.
[2] The axial position on the canister bottom is split down the middle where the underside 0 point to the top counterclockwise are positive values, and underside 0 point to the top clockwise are negative values.
[3] Λ_c filter was not applied

Updated corrosion testing of the thermocouple wires, spot welds and attachments as well as hand sampling tests have continued since publication of this report. No additional surface roughness measurements have been made.

2.3.1.1 Updates -Design and Setup of Mockup Plate for Corrosion Testing

As described previously [11], the three canisters for the CDFD will be exposed at three different heat loads and it will be desirable to monitor the canister surface temperatures. To do so, thermocouples (TC) will be attached at specific locations on the canister, with TC wires running around the circumference of the canisters. It is necessary to determine whether the wires and attachment techniques may influence or exacerbate canister surface corrosion, thus potentially disrupting dust deposition testing and/or leading to failure of the TCs. Additionally, these wires and attachments may serve a dual purpose as markings for orientation on the canister surface for dust sampling. In order to examine the TC wires and attachments aging and lifetime potential, a mock-up plate was designed and exposed under accelerated canister relevant conditions.

The sample plate was designed as shown in the mock-up plate schematic and image in Figure 23. An SS 316L (SS316L) sheet was procured, cut into two sheets (~ 6 x 12”), and welded. The plate was prepared as previously described in [11]. In Figure 23, the upper portion was ground to a 50-grit SiC paper while the lower portion was finished with a mill finish to mimic various regions across the canister surface. A single V-groove butt weld was used to join the two pieces, which were fused together with 316L filler metal. While this is not the exact welding procedure applied to the SNF canisters (due to scale and availability of tooling), it was used to represent a canister weld region on the surface. A matrix of materials, wires, and cutting techniques were examined to determine the best (least detrimental) selection for aging and lifetime over the CDFD exposure period, following the pattern laid out in Figure 23-a.

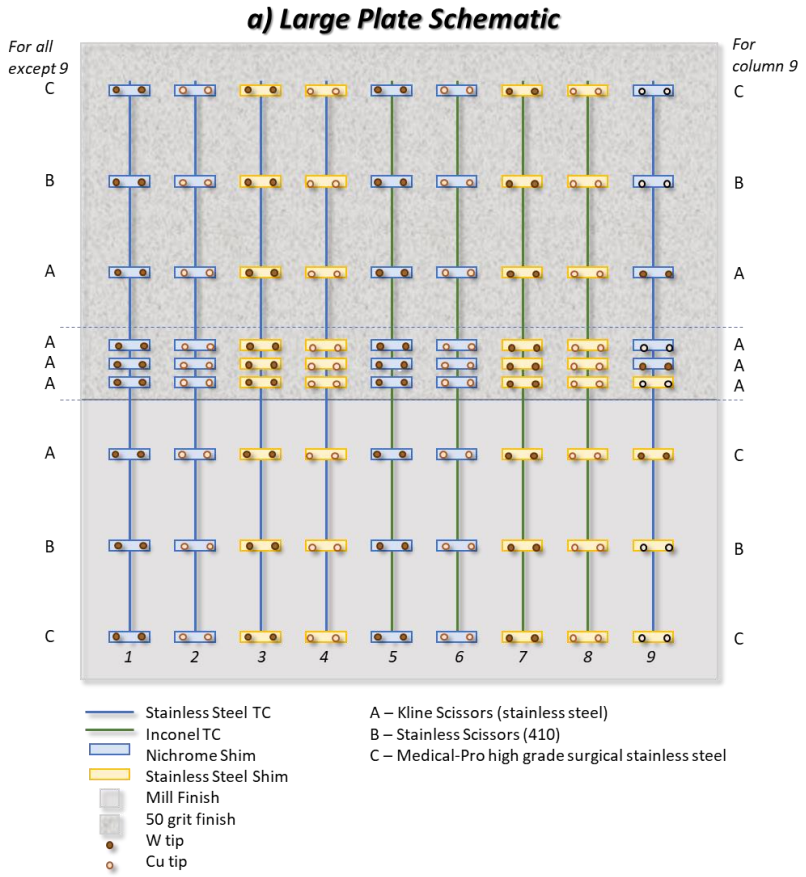

Figure 23. a) Schematic of plate mockup for spot weld, attachment shim, and thermocouple testing, and b) image of actual plate (red boxes highlight shims shown in Figure 25).

Atmospheric testing of mockup plate

Atmospheric testing of the mockup plate was carried out in accelerated canister relevant exposure conditions. Prior to exposure, the plate was coated with 300 µg/cm^2 chloride as American Society of Testing and Materials (ASTM) sea water solution using an SNL built nebulizer system. An example of the salt deposition process is shown for the plate in Figure 24-a with representative salt deposition (shown on a sapphire surface) in Figure 24-b. Salt particles are distributed uniformly and evenly across the surface.

a) b)

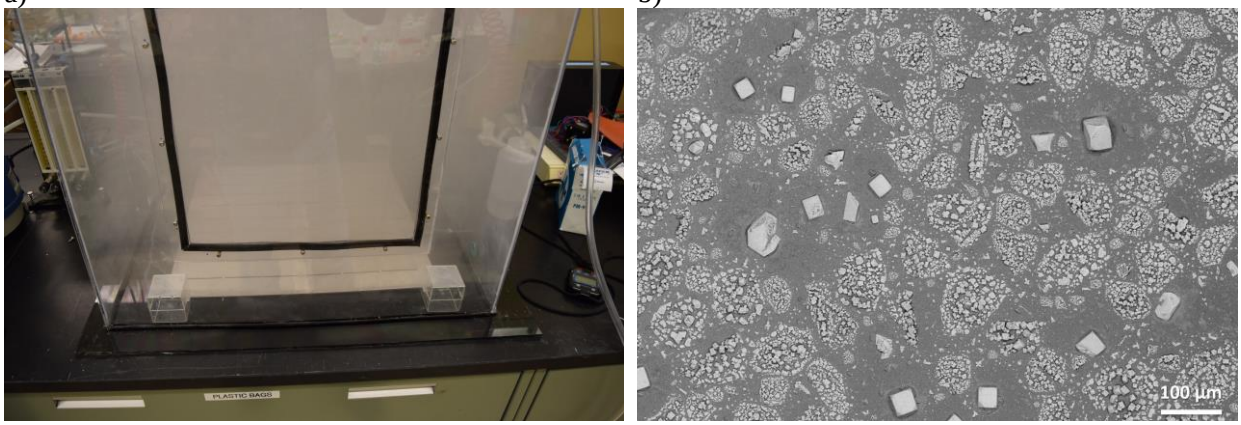

Figure 24. Salt deposition a) image of SS316L mockup plate in nebulizer chamber with salt fog and b) example SEM image of nebulized sea salt deposition.

After deposition of salt on the surface, the mock-up plate was then loaded into a temperature- and humidity-controlled chamber and exposed for 3 months under diurnal cyclic conditions (cycle presented in 3.1.3.1 and [47]). Under these conditions, the $MgCl_2$ component of the deposited salts will periodically deliquesce. The plate was intermittently removed (24 h, 72 h, 7 days, 14, days, 1 month, and 3 months) to assess the potential for ongoing corrosion damage. After three months, the plate was re-deposited with 300 µg/cm^2 of ASTM sea water with the nebulizer and exposed for an additional two weeks under static 75 % RH and 50 ºC. These higher RH conditions produce a higher brine volume on the plate surface, as the NaCl present in the deposited salts will also deliquesce. Post-exposure imaging was again carried out and will be presented below.

Updates to atmospheric exposure results

Example sample images for pre-exposure and post-initial atmospheric exposure are shown in Figure 26. No optically observable corrosion occurred on or near the shims, spot welds, or TC wires. No changes were observed to these materials over time. However, corrosion was observed on the 50 grit ground side of the SS316L plate. This can be further observed in Figure 26, where a) shows the mill finish surface, with obvious salt, but no corrosion, b) the weld region with salt, and only corrosion on the ground surface, and c) the ground surface and inset close-up of the shim. Additionally, it can be seen that while salt is present on the shim and wire, no enhanced corrosion was observed optically on either, and was only present on the ground plate surface.

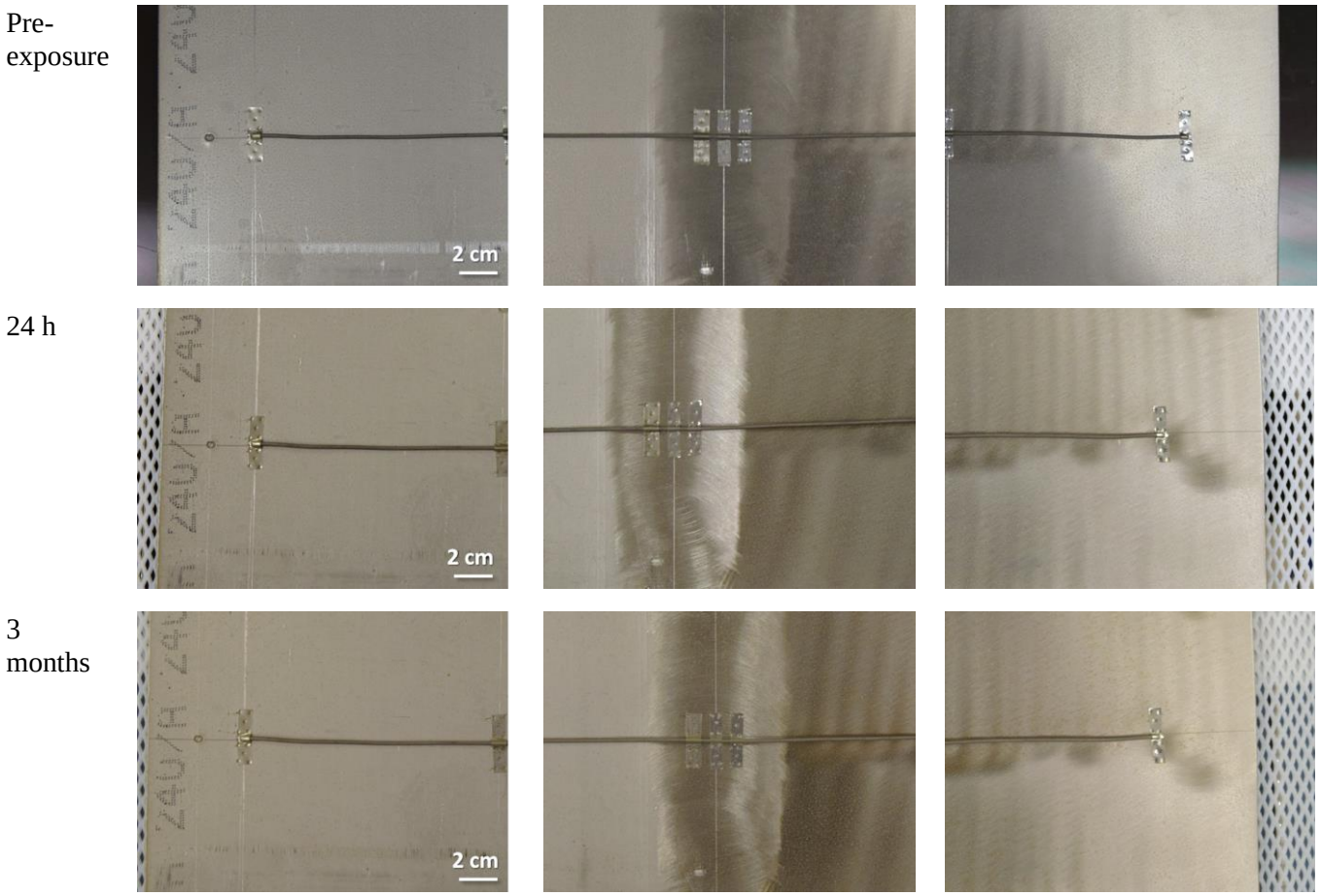

Figure 25. Select shim locations versus exposure time (left on mill scale, center in the weld, and right on ground surface).

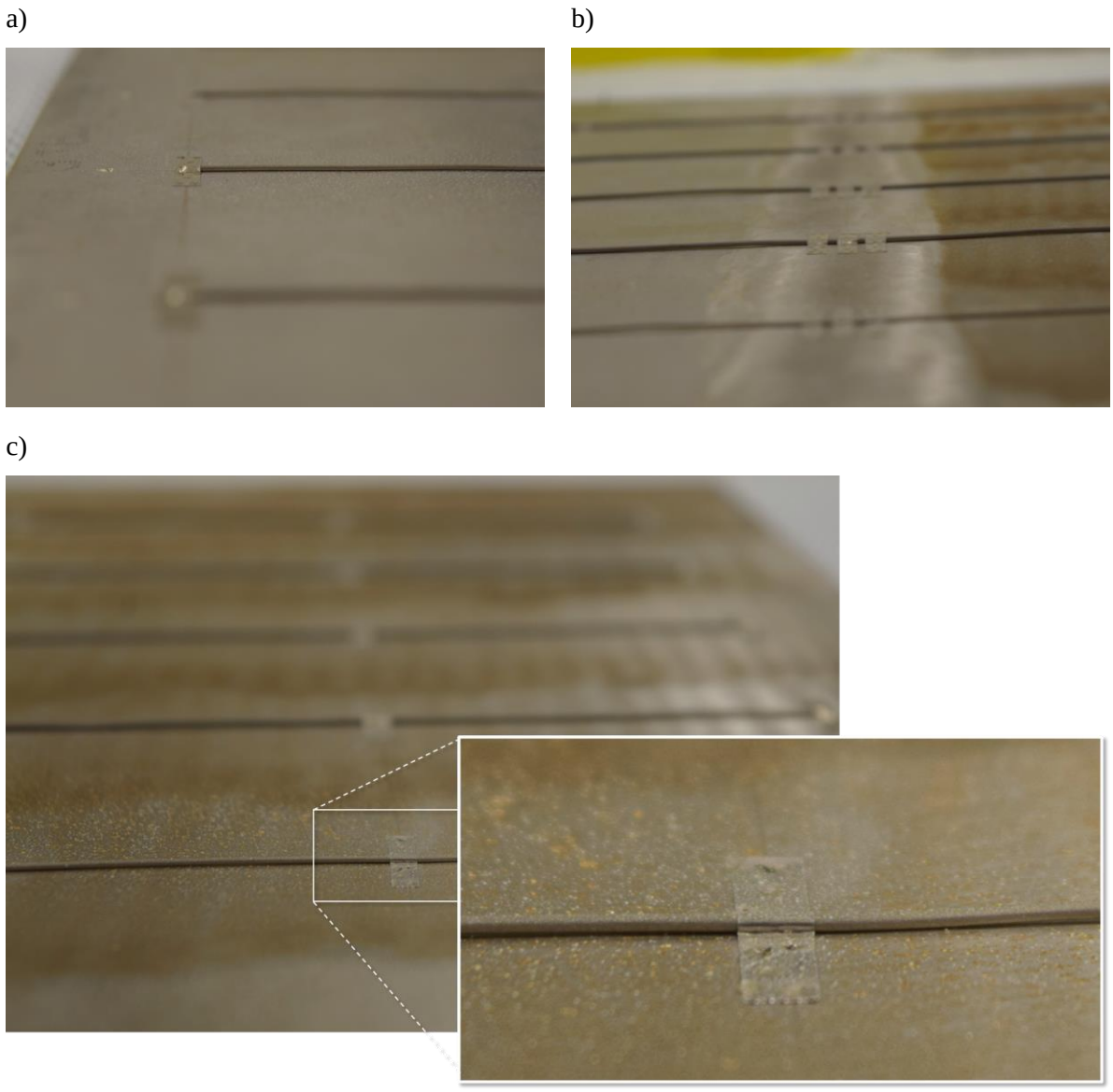

Figure 26. Representative shim locations after 3 months exposure for a) mill scale, b) within the weld, and c) rough grind. Images are angled to better view salt and potential corrosion product.

As no corrosion was observed optically over the course of the 3-month cyclic accelerated exposure on the TC wires, shims, or spot welds, additional atmospheric tests were developed. To further determine the accelerated aging and potential effects of the shim and TC materials, an exposure with increased salt deposition was carried out. The initial salt load was doubled by adding an additional 300 µg/cm^2 ASTM sea water with the nebulizer, to create a total coating of 600 µg/cm^2 and the plate was exposed further for two-weeks at static 75 % RH and 50 ^{o}C. Initial plans were to expose the plate for an additional month, however, after 2 weeks of additional static exposure the test was terminated as significant corrosion had occurred. The plate was removed and imaged to observe corrosion damage; results are presented below. Figure 27 displays optical images of the entire plate post atmospheric exposure in the cyclic conditions for 3 months (a) and with the additional 2 weeks of exposure in the static, high RH conditions (b). As can be seen, the higher RH conditions greatly accelerated the corrosion response across the surface. When compared to the plate schematic (Figure 23-a), it can be observed that the Nichrome shims in general

displayed enhanced corrosion. This can be seen detailed in Figure 27, this particular TC wire transitions from Nichrome shims on the rough ground surface to stainless steel shims on the mill finish surface, which may be driving the enhanced corrosion observed as some galvanic effects could be influencing the response. Additionally, the corrosion observed on the rough ground side appears to be increased. In many cases, the shims act as crevice formers with enhanced corrosion occurring not on the shim itself, but at the edge where it is in contact with the base plate material. However, there are clear choices of materials that appeared to have a less severe response to the static high RH exposure.

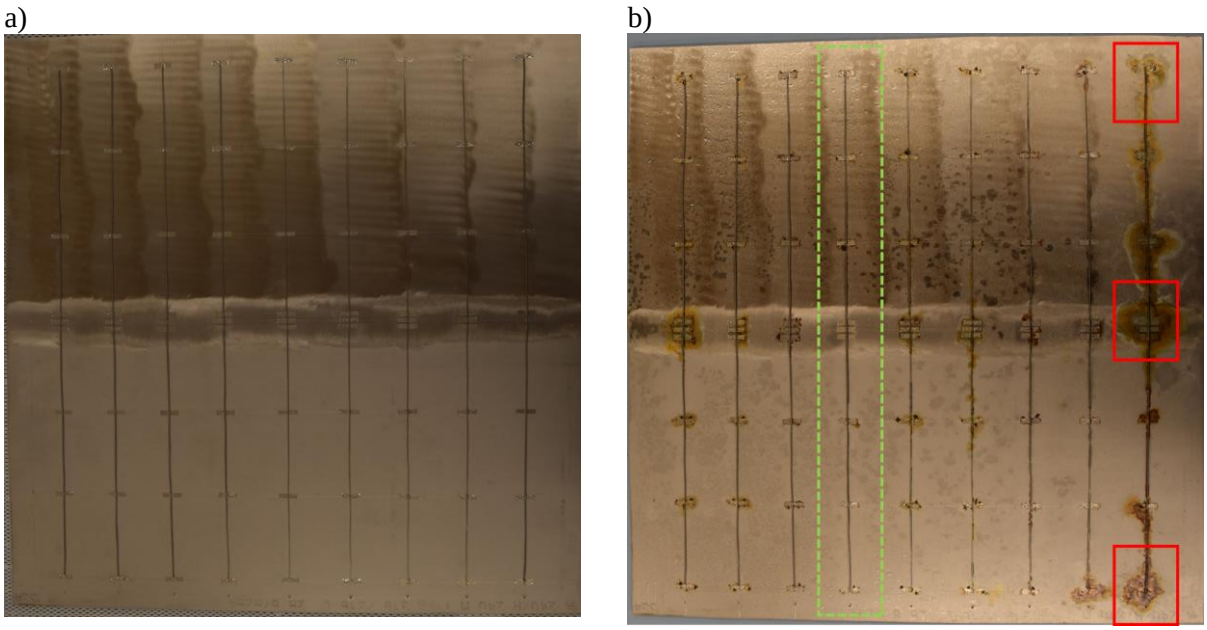

Figure 27. Overall plate images post atmospheric exposure a) 3-month in cyclic conditions and b) with additional salt deposition and 2 weeks in static 75 %RH and 25 ºC. Red boxes highlight shims shown in Figure 25 and Figure 28. Green dotted box highlights shims displayed in

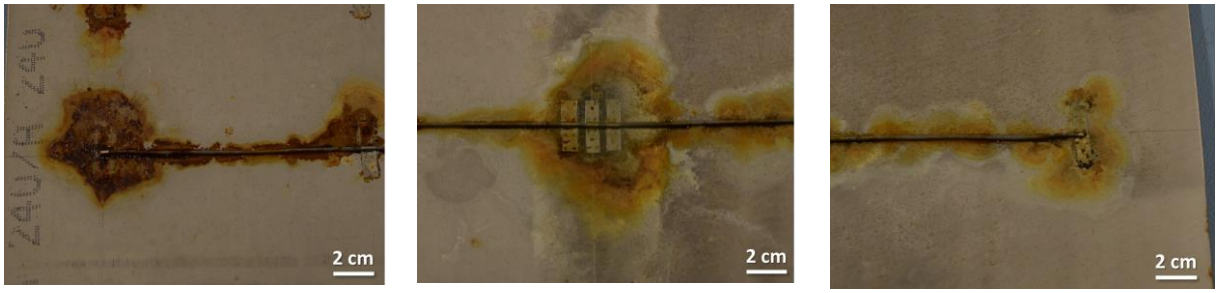

Figure 28. Select shim locations (same as Figure 25) versus exposure time after redeposition of sea salt and second exposure (left on mill scale, center in the weld, and right on ground surface).

Figure 29 displays materials and shims that had the least severe corrosion response under the accelerated atmospheric conditions. The stainless-steel TC wire with stainless steel shims and Cu tip spot welds resulted in the least severe corrosion response under the conditions examined (Figure 29). This appears to be independent of the material of the scissors used to prepare the shims. However, these shims still continued to display crevice corrosion at the edges during the two-week exposure (Figure 29-d-f).

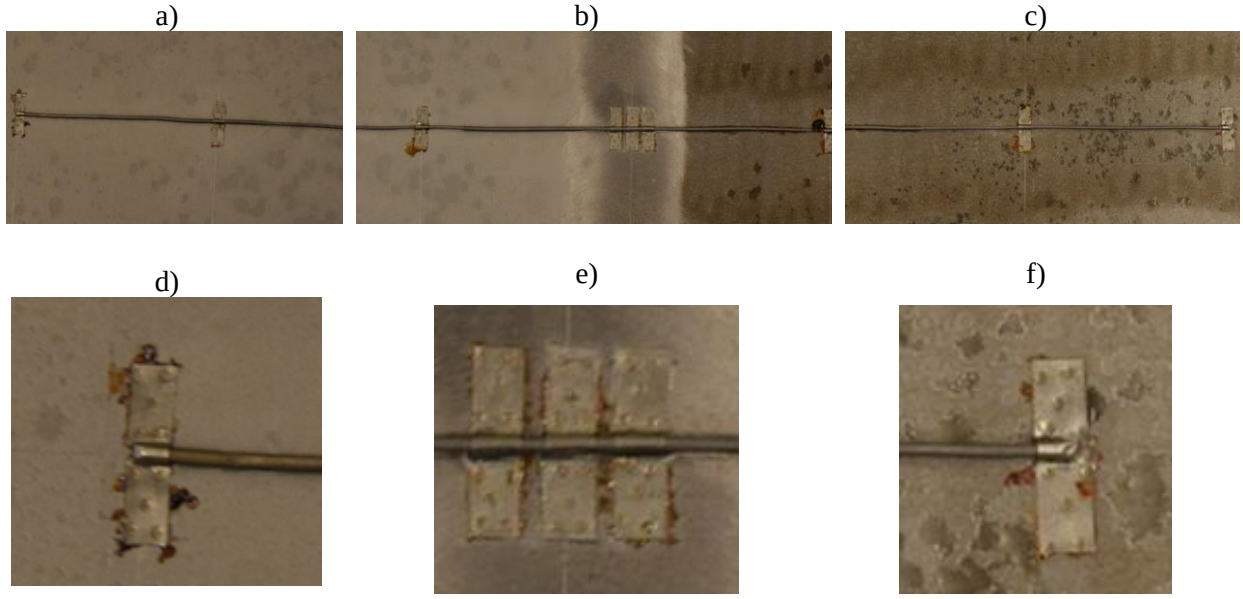

Figure 29. Images of stainless shims with Stainless TC along entire TC line (a, b, and c) and select shims d) shim at edge on mill scale side of plate, e) shims on weld, and f) shim at edge on ground side of plate.

Overall, initial cyclic diurnal cycles did not display a large corrosion response across the plate due to the attached TC wires and shims. Only surface roughness across the plate appeared to impact the corrosion response. When redeposited with salt and exposed at higher RH conditions, all TC wires and shims exhibited a corrosion response, which was material dependent. The stainless-steel shims combined with the stainless-steel wire and Cu tip displayed the least severe response, yet still had evidence of crevice corrosion. This may have implications for the low heat load (unheated) canister as the larger brine volumes associated with higher RH conditions and cooler surfaces may form on the canister surfaces; however, it is unknown if the high salt load (comparable to those examined in these exposures) will be present. In FY23, further detailed post-mortem analysis of the plate will be carried out to determine the viability of the use of any of these techniques for canister marking and TC attachment.

2.3.1.2 Updates to Hand-Sampling Techniques

Beyond the tests performed for the previous report, two additional hand sampling tests were performed to continue to validate the technique. These tests were done in the same way as described previously [48]. Briefly, a 20″ x 14″ plate of the Sandia mockup canister, which has approximately the same curvature as a typical SNF canister and has a mill finish, was used for the tests [49]. The plate was thoroughly cleaned and a sampling grid with 3″ × 3″ squares was applied using an engine enamel (the engine enamel will not be used for marking the actual heated CDFD canisters as it does not withstand elevated temperatures). Then, several 1″ × 2″ SS witness coupons were attached to the surface, using conductive carbon tape to minimize static issues. The SS plate was coated with approximately 200-300 µg/cm^2 ASTM sea-salts. Following salt deposition, the witness coupons were removed from the plate surface, transferred to sample vials, and leached with 20 mL of deionized water (DI) to extract the salts. As it was expected that salt surface load would vary with location on the plate, measuring the salt on the witness coupons, which surrounded the sampling grids, allowed for more accurate estimation of the salt load within the sampling grid. After removing the witness coupons, a dust sampling mask was pressed against the surface and each 3″ x 3″ region within the sampling grid was hand-sampled using two moist 1″ cubes of blue Tru-CLEAN polyethylene sponge. For sampling, the sponges were wetted with DI water and then gently squeezed to eject most of the water, leaving the sponge damp. The first sponge was used to wipe the surface within

the sampling mask, and then transferred to a 50 mL sample vial. Then, the second moist sponge was used to collect any remaining salts. After addition of 40 mL DI water and agitation to extract the salts, the conductivity of the leachate from each of the witness coupons and grid samples was measured using a Jenway 4510 conductivity meter and a Jenway conductivity probe. Measured conductivities were normalized by the sampled area (2 in^2 for the witness coupons, and 9 in^2 for the grid cells) for comparison, yielding units of $\mu S/cm^2$. To accurately estimate the salt loads in the grid cells, the data for the witness coupons were fitted with a surface, and the deposited salt at the center of each grid cell was calculated by cubic interpolation. Sampling efficiencies were calculated by comparing the measured salt loads for each grid square to those predicted by the surface fit to the witness coupon data. The estimated sampling error in Tests #1-#4 for the grid cells varied from -3.7 to -24.8 %, but most were in the range of -10 to -15 %, corresponding to sampling efficiencies of 85 - 90 %. The low sampling values indicated incomplete recovery of the salts from the surface. This may have been due to the surface roughness of the mill finish, or possibly due to missing the edge and corner regions of the grid squares.

In previous tests, the witness coupons in the middle of the sampling grid had given erroneous results (specifically shown to Test #4 [48]), which complicated calculating the expected value for each sampling grid. This was suspected to be due to static because the two grid-center witness coupons were not affixed directly to the SS surface, but rather to the engine enamel grid lines. To mitigate this, for Test #5 and Test #6, additional carbon tape was used to ensure sufficient contact with the SS surface to alleviate static issues.

The results from Test #5 are shown in Figure 30. Both of the grid-center witness coupons are consistent with nearby coupon values. In this case, the coupons were apparently well-grounded and both values were acceptable to include in the fitting. In Test #5, the sampling errors varied from -6.0 to -21.8%, which was on average, a higher degree of under-sampling than was observed in Tests #3 and #4, where results were consistently ~ -10 %. As discussed later, one possible explanation for this is variations in sponge wetness; with drier sponges being less efficient at collecting the salt.

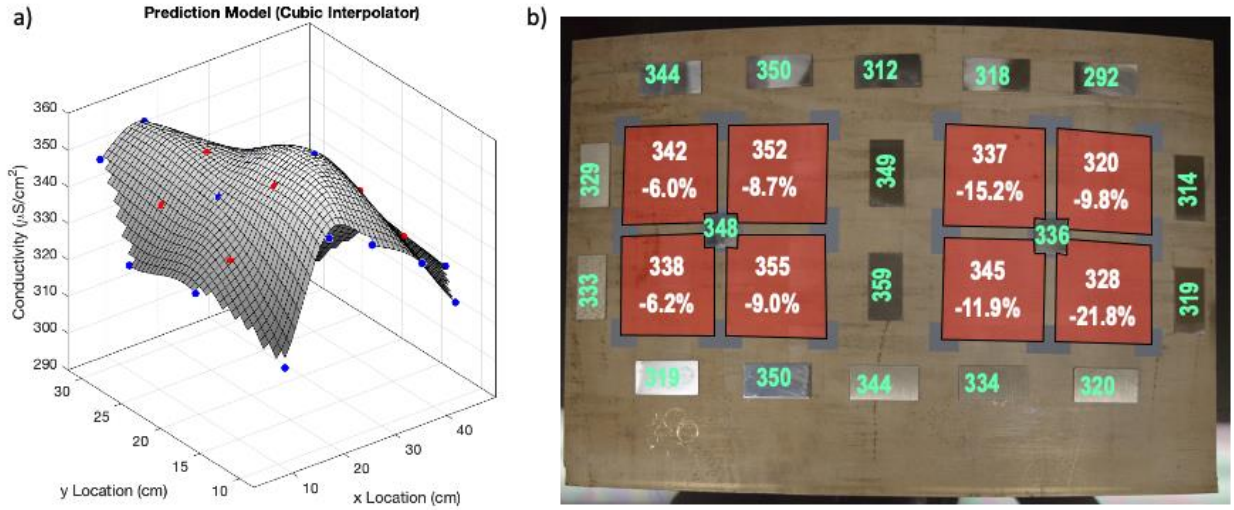

Figure 30. Test #5. a) Surface fitted to the measured conductivities for the witness coupons (blue points) and used estimate the expected conductivity of the grid cells (red points). b) Measured conductivities for the witness coupons and the calculated conductivities for the sampling areas, shown with the % of under-sampling.

The results from Test #6 are shown in Figure 31. In Test #6, efforts were made ensure the sponges were sufficiently wet and to effectively ground the grid-center witness coupons to alleviate static. In this case,

the left grid-center witness coupon provided a reasonable value, but the right grid-center coupon was very high, relative to all the surrounding coupons; for this reason, it was omitted from the surface fit, and from the prediction calculation. Additionally in Test #6, effort was made to wet the sponges slightly more than the previous tests. This was done because there appears to be a strong relationship between the sponge wetness and the sampling efficiency (Figure 32); when the sponge was wetter, the % under-sampling was consistently lower. Overall, in Test #6, the results were relatively consistent, where the left side averaged -9.35 ± 1.7 %, and the right side averaged -3.15 ± 0.8 %. The right side was the best recovery and most consistent of all the tests to date with an overall recovery of 96.85 %. The left side was consistent and resulted in a recovery > 90 %, which was consistent with many of the previous tests.

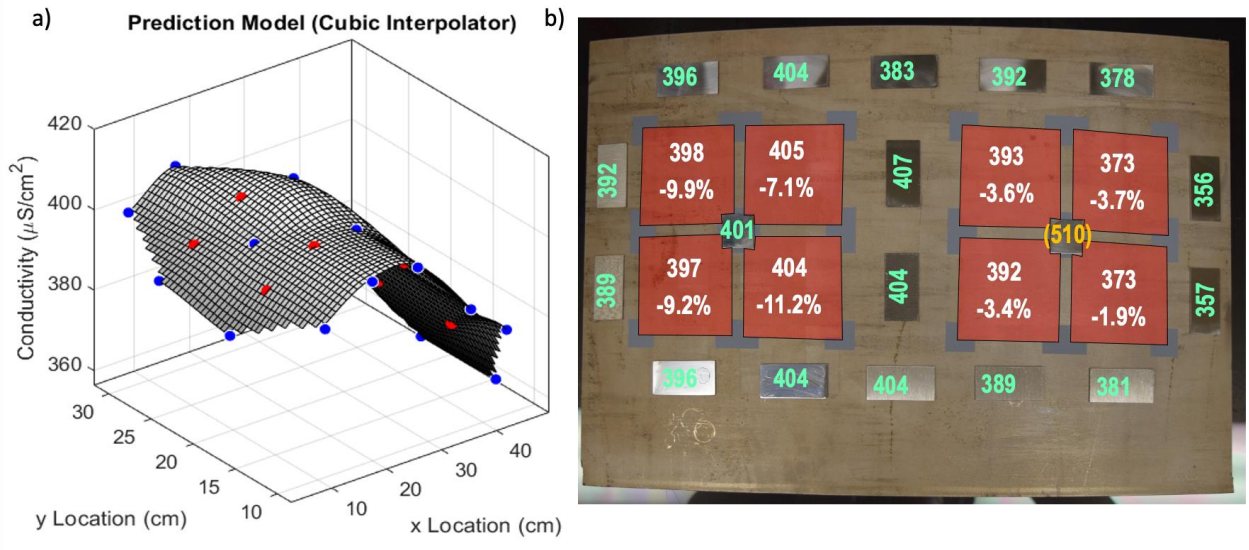

Figure 31. Test #6. a) Surface fitted to the measured conductivities for the witness coupons (blue points) and used estimate the expected conductivity of the grid cells (red points). b) Measured conductivities for the witness coupons and the calculated conductivities for the sampling areas, shown with the % of under-sampling. Note that the right grid-center coupon (shown in yellow) was not used to fit the plane due to being unrealistically high.

As mentioned previously, the wetness of the sponge appears to significantly affect the recovery of the salts form the surface (Figure 32), with wetter sponges improving recovery. This may indicate that the sponge needs to be sufficiently wet for the water to infiltrate the irregularities on the metal surface. Throughout the experiments, the sponge wetness varied from ~1 to 10 g of entrained water. In general, sponges with less water resulted in less recovery of the salts and recovery increased, with sponge wetness to asymptotically approach total recovery. The data were fit to the following equation:

$$\%undersampling = -100 * \left(1 - e^{(-k * sponge\ mass^{n})}\right) \qquad eq\ (3)$$

where the -100 represents the lower bound, of no recovery, and the equation approaches an asymptote of 0%, or 100% recovery. There were two clear outliers from Test #2, these were determined to be too low due to insufficient leaching of the salts from the sponge and have been omitted from the fitting. The coefficients *k* and *n* were calculated using the MatLab curve fitting module and were -0.3636 and -1.296, respectively. Overall, the equation fits reasonably well, with an $R^2 = 0.62$. This relationship could potentially be used to improve the recovery when testing on the actual CDFD canisters and to approximate the expected recovery based upon the sponge wetness.

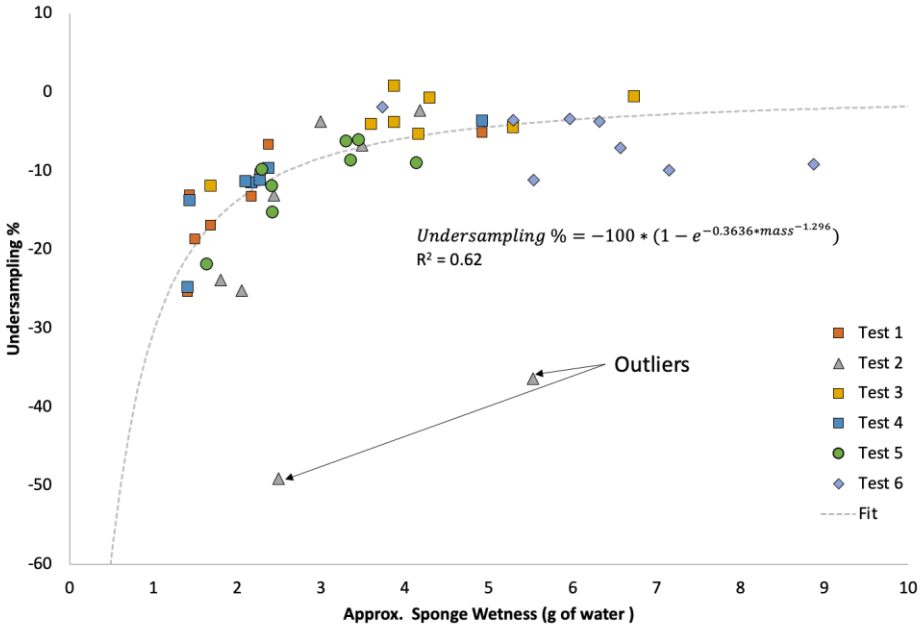

Figure 32. Plot of the % of under-sampling versus the approximate sponge wetness fit with an exponential equation (omitting the two outliers).

In FY23, additional tests will be carried out to continue to improve the sampling methodology. In addition, SNL plans to test this method on oriented metal surfaces that mimic what is expected for the CDFD sampling campaign. A field test on a real canister or a larger-scale mockup will also be carried out to evaluate the feasibility of the applying the hand-sampling procedure to vertical and overhanging canister surfaces while on a lift, as will be carried out at the CDFD field site.

2.3.2 Environmental Monitoring and Aerosol Sampling

In addition to sampling the CDFD canister surface to quantify the salt loading and to identify the mineralogy/morphology of dust and debris deposited on the canister as a function of canister heat load and surface location, it is necessary to monitor ambient conditions, including aerosol particle size distributions and compositions. Ambient weather conditions, including the ambient aerosol source term, are required to parameterize the PNNL dust deposition model. This knowledge is required to define the boundary conditions at the overpack inlet and outlet vents as well as at the overpack walls. Weather data will be collected continuously using a weather station, aerosol particle size distributions and compositions will be continuously monitored; and atmospheric acid gas concentrations will be measured. SNL has previously summarized the specific goals for each of these tasks [40]. Specifically, SNL provided background information regarding the expected aerosol particle size ranges at the potential CDFD site. Because the CDFD site is a coastal site, it is expected that large, deliquesced sea-salt aerosols will be common, which upon drying out will have significantly smaller diameters. Based upon this site-specific knowledge, it was determined that a Dekati ELPI+ Cascade Impactor and a Topas Laser Particle Sizer (LAP323) equipped with driers would be effective at collecting and monitoring the aerosol data to characterize this site. In addition, a filter pack system supported by the Clean Air Status and Trends Network (CASTNET) will also be used to determine the composition of particles and concentrations of acid gas species.

In FY22, the ELPI+ cascade impactor and the LAP 323 laser particle sizer were acquired (Figure 33), and initial testing has begun. Also, contracts are in development regarding collection and maintenance protocols for integrated use between SNL, the CDFD site, and the environmental analysis lab that will characterize the collected materials. In FY22 an application scientist who supports the cascade impactor

and laser particle sizer came out to SNL for a 2 day on site training. Both the cascade impactor and laser particle sizer are instruments that will be employed to monitor and collect ambient aerosol particle size information. The CASTNET system will be acquired once the site is confirmed, and the supporting tower will be erected on site. Each of the three aerosol-collection/monitoring systems will provide specific, unique, and complimentary pieces of information that can be used collectively to develop an in-depth understanding of the ambient aerosol particle sizes and compositions.

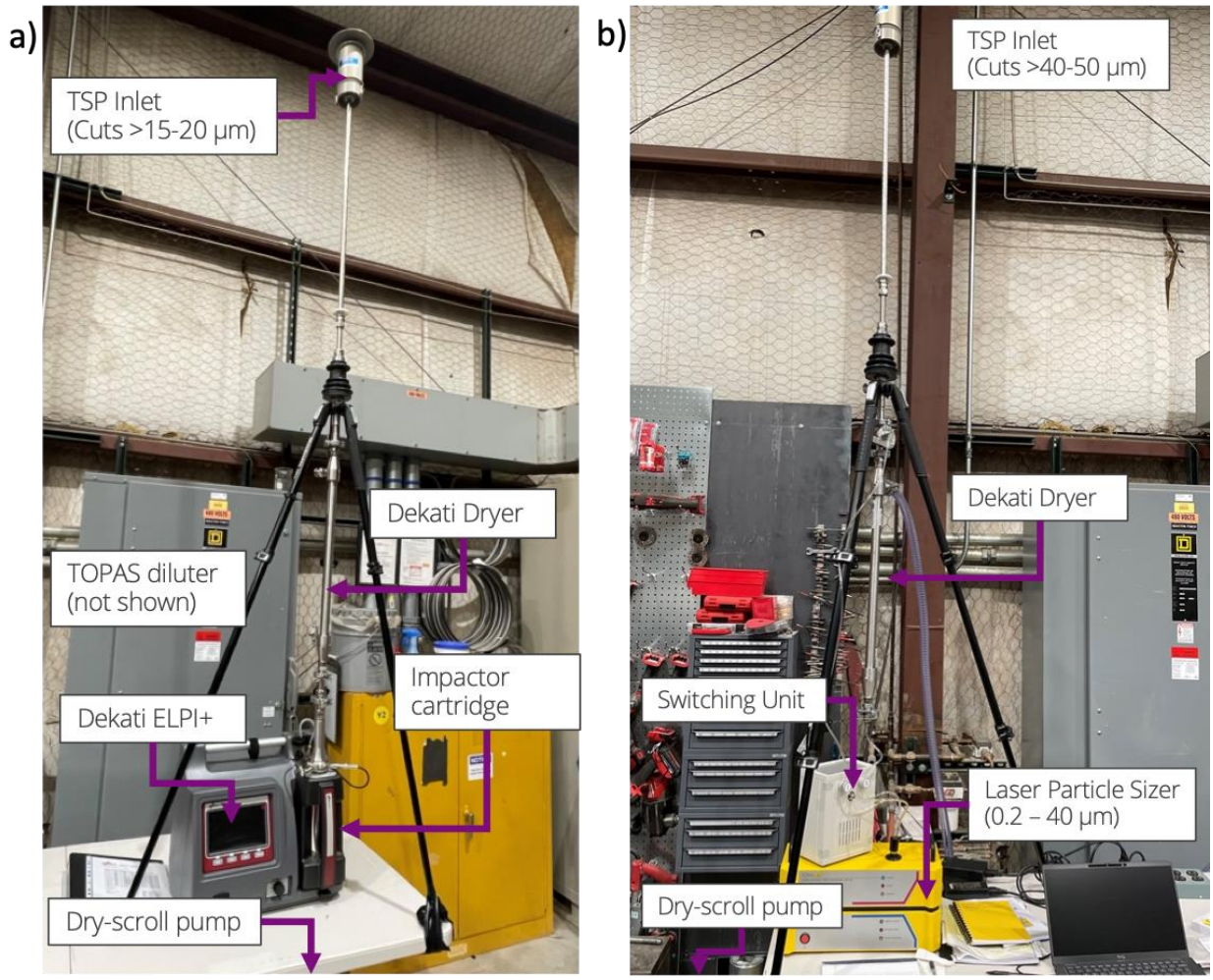

Figure 33. Pictures of the assembled aerosol equipment at SNL showing a) the Dekati ELPI+ cascade impactor and b) the TOPAS LAP323.

2.3.2.1 CASTNET and Weather Station

The details for the CASTNET system and plans for the weather station are summarized in the FY21 report [40]. For the CASTNET tower, the contracted purchase order is being written and will be placed once the site has been finalized. This will allow for SNL to purchase the CASTNET tower and erect it onsite.

2.3.2.2 Cascade Impactor

The Dekati ELPI+ cascade impactor will provide particle size distributions for particles in the size range of 0.016 to 10 µm in several stages, and the stage targets can be analyzed to determine the composition as

a function of particle size. The instrument is described in detail (including all the components and accessories) in the FY21 report [40]. Briefly, the ELPI+ is a 14-stage impactor covering a size range from 0.016 μ to 10 μm, operating with a flow rate of 10 L/min. At this flow rate, the total suspended particulate (TSP) inlet excludes particle >20 μm. The top 10 μm stage is collected, but not monitored electronically, therefore the weight of the 10 μm cut must be determined by the weight difference between the clean target and the target after use, at a known RH. Particles too small to be captured by the final target (<0.016 μm) are collected by a high-efficiency particulate air (HEPA) filter after the final target. This filter is fixed—it cannot be removed for sample retrieval and therefore no chemical analysis can be provided for these particles. The collection plates in each stage accept 25 mm polycarbonate collection targets which must be greased prior to loading on the compactor tower. These targets can be extracted for post-measurement chemical analysis to determine aerosol compositions. In this system, aerosol particles pass through a unipolar corona charger where a known positive charge is applied. In the impactor, the particles are size classified into 14 size classes onto the impactor plates. The charge deposited in each stage is measured, allowing real-time measurement of the particle number size distribution and concentrations. To convert to a mass distribution, a density must be assumed for the particles. Alternatively, the targets can be weighed at a known RH before and after use, as with a standard cascade impactor. The high-resolution collection mode of the instrument offers 100 particle size channels instead of 14 channels; the extra cuts are achieved through software and can be performed after the data is collected.

Initial tests have been performed at SNL to determine what the collection parameters may be at the CDFD site and how to process the data output. One important parameter that still must be determined is how to set the diluter on the cascade impactor to achieve a reasonable sampling frequency (1-4 weeks). This can only be determined by analysis of aerosols at the actual test site. However, these initial tests provide useful information to gain familiarity with the equipment, data collection procedures, maintenance, and calibration. As much of this work will be performed by contractors at the CDFD site or at the analytical laboratory supplying sample analysis support, SNL is developing standard operating procedures for equipment use and sample handling.

Prior to measurement, the cascade impactor tower must be cleaned, the targets greased, and the tower reassembled with the targets. This task will be performed at the laboratory that will perform the chemical analysis of the targets. In FY23, SNL will write a detailed procedure for this task and visit the analysis lab to demonstrate the procedure. A few steps are shown in Figure 34. The tower must be removed from the cartridge (a) and the impactor stages removed (b) and fully disassembled (c). Then all parts must be washed in DI water with sonication (d) and set out to fully dry (e). The maroon O-rings will need to be greased on occasion to ensure a proper seal. The polycarbonate targets must be greased with Apiezon™ vacuum grease using the template provided by Dekati (f, g). Once greased, the polycarbonate targets must be carefully mounted on the target stages using the metal O-rings. Then, the cascade impactor must be reassembled. Each unique piece is numbered, and the assembly must follow the correct number order. Each impactor stage consists of several pieces (Figure 35) and must be assembled in the correct order. Once the tower is fully re-constructed, it can be remounted in the cartridge and placed into the ELPI+.

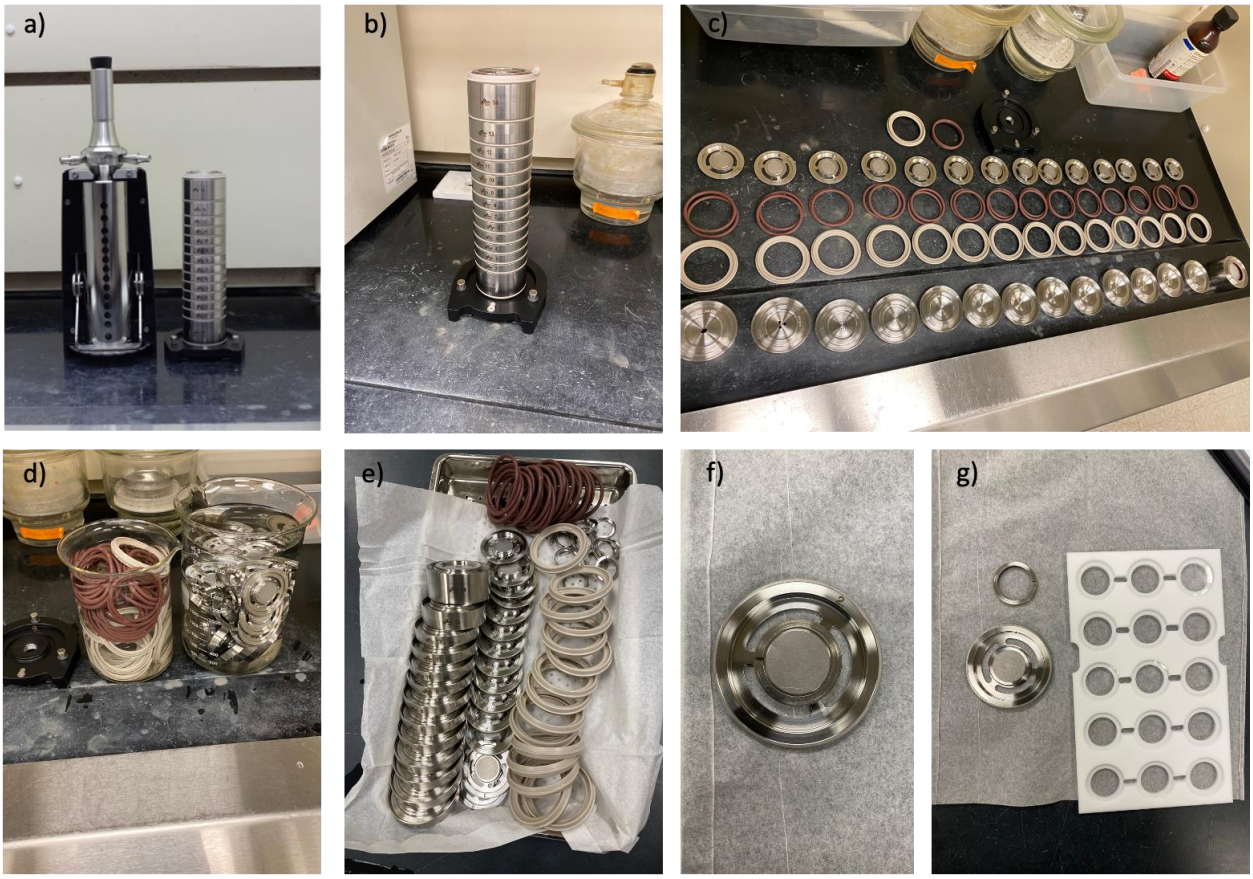

Figure 34. Photos demonstrating the disassembly of the cascade impactor column (a-c), cleaning of each component (d-e), and mounting the greased polycarbonate targets on a impactor stage (f-g).

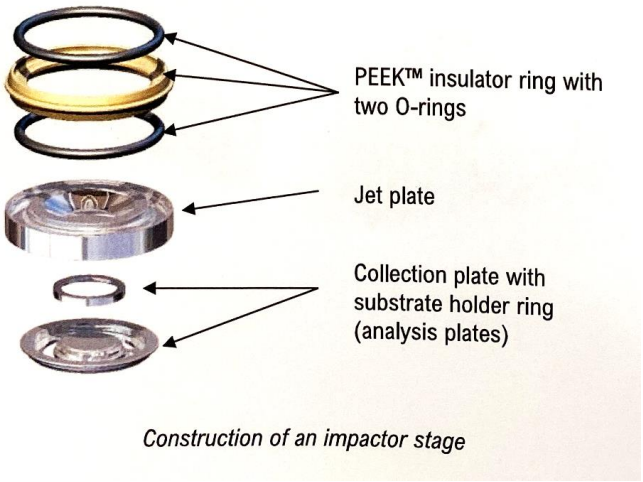

Figure 35. Examples provided in the Dekati ELPI+ manual of the pieces associated with each impactor stage.

Once fully assembled, the ELPI+ is ready for measurement. At SNL, several measurements were made with a 1 Hz collection time and saving an average every 60 seconds. The instrument was run for several days (8/18/2022 – 8/18/2022). Figure 36 is an example output of the raw data, showing the total current

(sum of the current at each stage) as a function of the total collection time (top) and the raw current of each individual stage for a 20-hour period (8/19/2022 12:00:00 – 08/20/2022 8:00:00) using the Dekati ELPI+ Data Analysis Tool (beta mode).

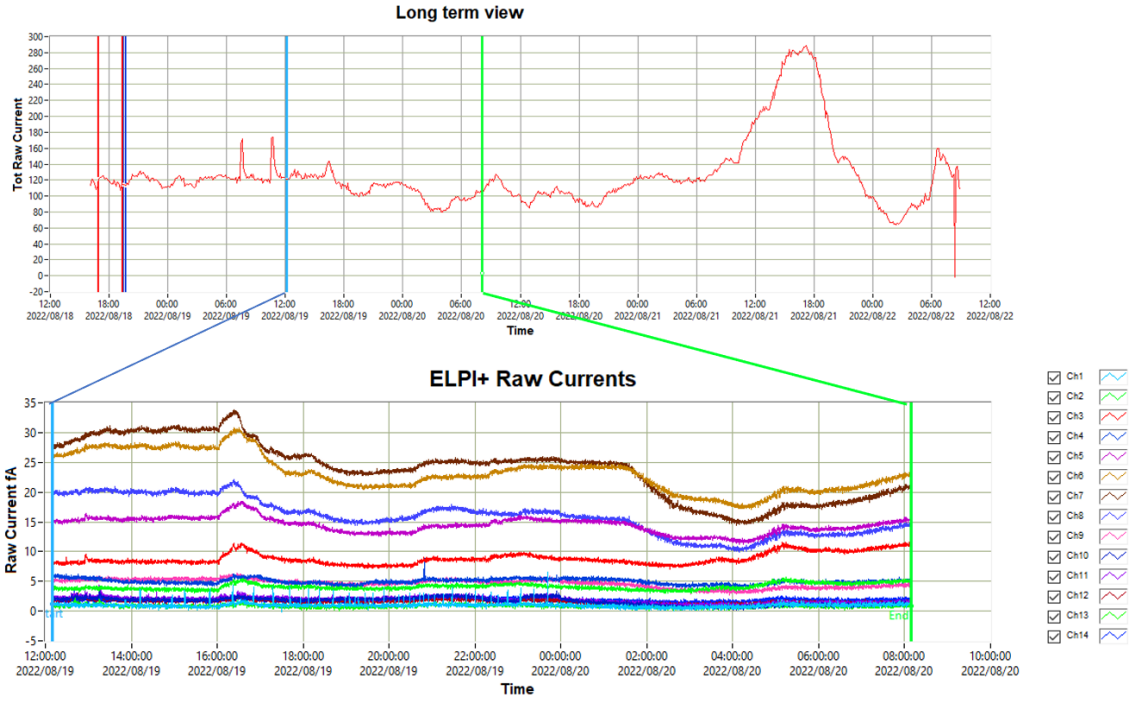

Figure 36. Long term view showing the total raw current, of all stages, collected from 8/19/2022 12:00:00 – 08/20/2022 8:00:00 (top), and raw current of each individual stage for a 20-hour period (8/19/2022 12:00:00 – 08/20/2022 8:00:00) (bottom) using the Dekati ELPI+ Data Analysis Tool (beta mode)

In the time period from 8/19/2022 12:00:00 – 08/20/2022 8:00:00, the particle number and mass concentration and distributions can be determined from the raw current (mass is determined here using a density = 1). The top figures in Figure 37 show the total particle number (a) and mass (b) for each time step over the selected time-period. Some events (e.g. the spike at ~16:30:00 on 08/19/2022) can be seen in both the number count and the mass, however other events, such as the periodic spikes in the number count, are not observed in the mass plot. These spikes are likely caused by a large number of small particles, that have almost no impact on the total mass. The middle plots show the concentration density in particle number (c) and particle mass (d). It is clear from these plots that the largest concentration of particles exists on the smallest impact stages, but the majority of the mass is associated with the largest particles collected on the upper impactor stages. Lastly, the bottom plots show the particle size distributions in terms of number (e) and mass (f). Similar to the concentration plots, the distributions show that the greatest number of particles are < 0.1 μm, but the majority of the mass is associated with particles > 5 μm. The total accumulated mass on each stage can be determined by integrating the mass accumulation over the collection time. For these studies the impactor measurements have been stopped and restarted several times, and therefore the actual mass accumulated is not known. In addition, the polycarbonate targets have not yet been extracted and analyzed, so no chemical data are available.

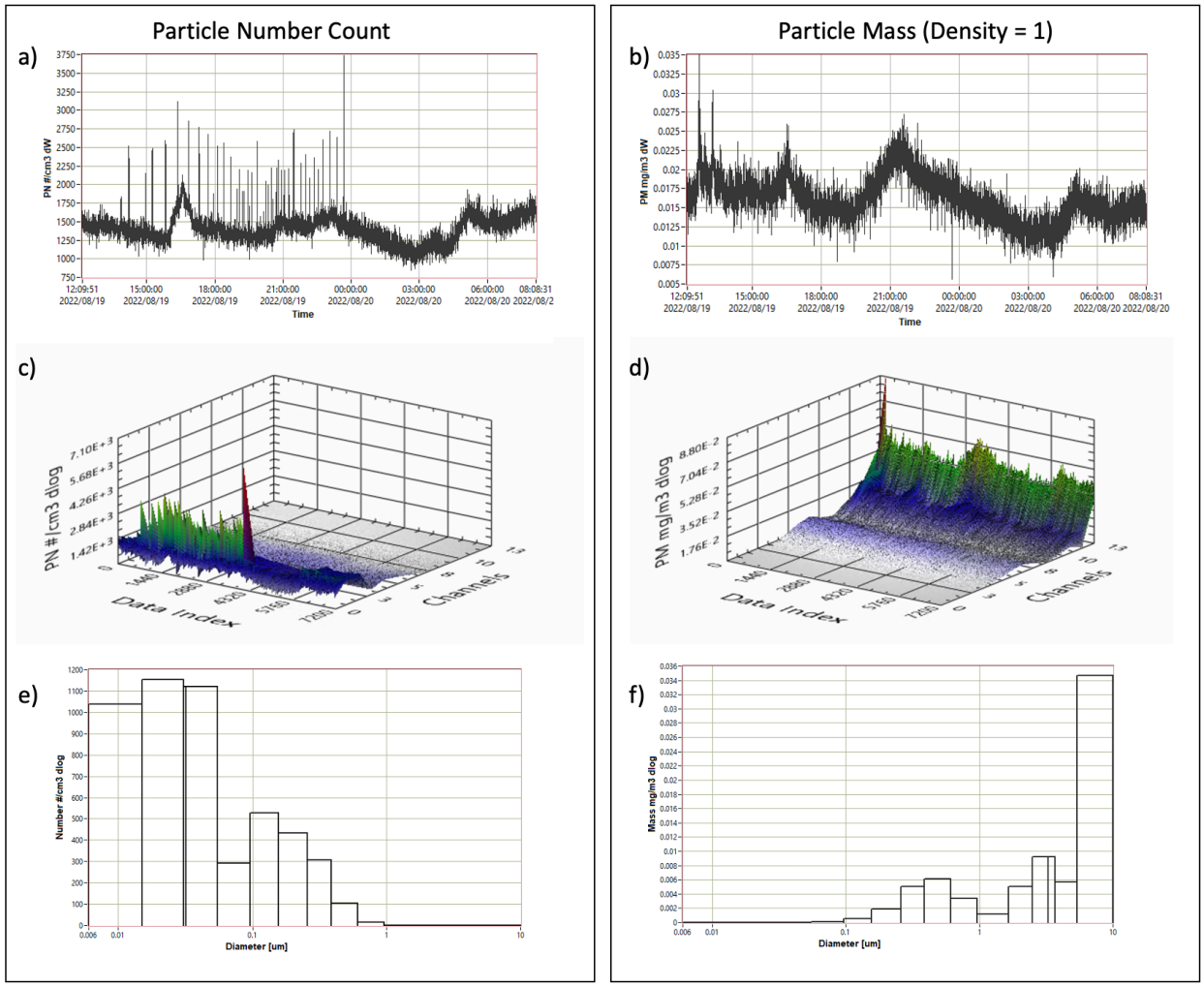

Figure 37. From the raw currents collected during the 20-hour period (8/19/2022 12:00:00 – 08/20/2022 8:00:00) the total particle number count (a) and mass assuming a density of 1 (b), the particle number concentrations (c) and mass concentrations (d), the particle number distribution (e), and mass distribution (f).

In FY23, SNL will perform a full collection cycle for the cascade impactor, including new greased targets on a clean impactor tower, a continuous run for 1-2 weeks, extraction of the targets, and subsequent chemical analysis. This collection will be performed outside in an effort to collect a wider range of particulates and experience greater environmental variation due to wind and other factors. Also, in FY23, there are plans to bring the aerosol sampling equipment out to the CDFD site and collect a limited dataset to develop an understanding of the aerosol concentrations at the stie. These measurements are critical for determining effective use of the diluter and developing a sampling frequency schedule.

2.3.2.3 Laser Particle Sizer

The TOPAS Laser Particle Sizer (LAP323) is complementary to the cascade impactor, capable of measuring a much larger particle size range. Specific details regarding the LAP323 and its accessories are provided in the FY21 report [40]. Briefly, the LAP323 is a ruggedized unit designed for environment monitoring and can size particles from 0.2 µ to 40 µm (0.2 to 5 µm or 0.7 to 40 µm) in 64-128 channels. The LAP323 is equipped with the Dekati® TSP inlet to cut very large particles. The LAP323 is operated at ~ 3 L/min, and therefore it is estimated by Dekati that the inlet will reject particles > 40-50 um – which

is sufficient to allow passage of all anticipated sea-salt aerosols. The TOPAS LAP has its own internal pump, and so does not need a separate pump (however, the LAP323 inlet line has a Dekati inline dryer, that will use the same vacuum pump as the EPLI+). The LAP323 is equipped with an automated switching valve that allows for sampling of two different air streams. This will be used to sample the air stream both above and below the dryer. The dryer is capable of drying out brine particles potentially as large as 40-50 μm at the relatively low flow rate (and hence, long residence time in the dryer) associated with the LAP323. Using the switching unit in this way will provide a complete particle size distribution for both the ambient air and for the dried particles to estimate the shift in particle size distribution as deliquesced particles dry out. A humidity sensor will be installed at the TSP inlet and at the outlet of the dryer to monitor the dryer performance. It should be noted that laser scattering spectrometers measure a "scattered light equivalent diameter", which is the diameter of a spherical particle with the same light scattering characteristics as the actual aerosol particles. This parameter is strongly affected by particle shape. Because of this, correlating the particle size distribution collected by the LAP323 and the ELPI+ may not be a direct comparison.

Tests have been initiated to develop operating procedures and an understanding of the system (e.g. the efficiency of the dryer for different particle sizes). Unlike the ELPI+, there is no preparation work prior to data collection. There is also no sample retained for analysis; the LAP323 simply provides real time monitoring of particle numbers and size distributions. Two goals of the testing at SNL are to determine the sampling rate and understand the efficiency of the dryer. The sampling rate is the total amount of time the instrument collects and counts particles and is a selectable parameter. Collecting for longer periods of time provides a greater particle count, but at the expense of time resolution. For example, a 5 min acquisition time will collect for 5 min and report the total counts of particles during those 5 min. In contrast, if the acquisition is one hour, the instrument will continuously count particles for 1 hour and report the distribution and total particles collected over the entire hour as one data set. If a weather event (e.g. wind gust) is brief, aerosol changes during that event may not be captured if the collection time is too long. However, if the collection time is too short, the counting statistics may not be sufficient to draw conclusions. An additional handicap with short sampling times is that they produce larger data sets, potentially straining Sandia's data transfer capabilities from the CDFD site.

Another reason for these tests is to understand the sampling efficiencies as a function of flow path around or through the dryer. The upstream sample (Port 1) is collected upstream of the dryer and in the current configuration, draws an air sample through a right-angle Tee connected to the inlet column. This sharp corner in the flow path could lead to particle losses. The dryer itself has a known efficiency which varies with particle size; it has been measured by Dekati (Figure 38) up to ~5 μm. It is clear that for particles over 1 μm, as the particle size increases, the losses increase substantially. It is expected that larger particulates may have even more losses; however, it is not clear how to extrapolate this relationship given the data available. Regardless, it is clear that testing is required to determine the effects of sampling upstream and downstream of the dryer.

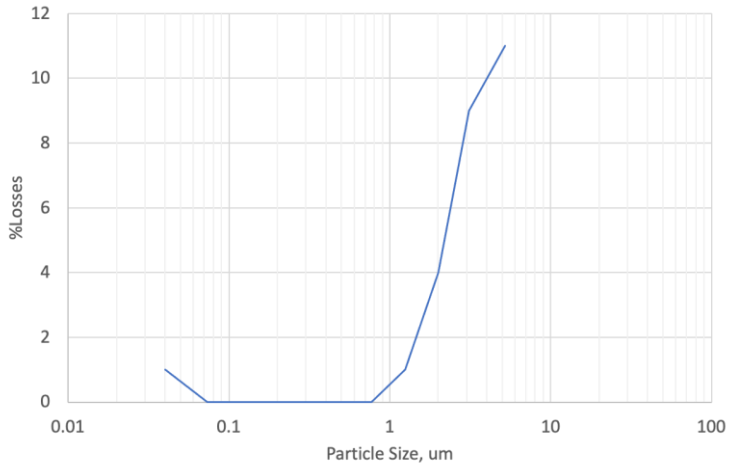

Figure 38. Measured particle losses in the DD-600 dryer as reported by Dekati [50].

At SNL, which has an arid climate, very few, if any, aerosol particles will be deliquesced. Therefore, tests at SNL can provide a good environment to determine sampling times and understand the flow path efficiencies. Using the Fractional Efficiency Module in the PASWIN software, SNL performed a series of tests to determine the differences between the upstream and downstream measurements with different measurement times. For all measurements, the sequence went as follows; 10 measurements for each upstream and downstream sampling port, with a 60 second purge followed by a 30 second stabilization period prior to each measurement (Figure 39). The only parameter changed in these measurements was the measurement time, which ranged from 30 to 3600 seconds. The upstream and downstream times were always kept equal.

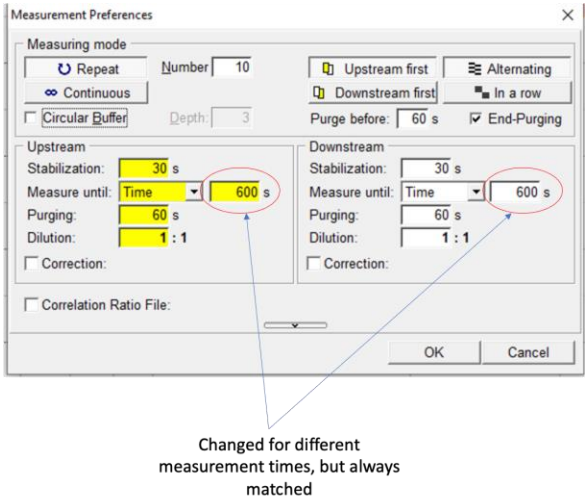

Figure 39. Measurement parameters for the fractional efficiency tests performed a SNL to understand the losses in the flow path and collection times.

An example measurement with an acquisition time of 60 seconds is shown in Figure 40. Each individual measurement has a corresponding particle size distribution that is time stamped at the end of the 60 second acquisition period; upstream and downstream measurements alternate. In this case, 10 measurements were made and the results of those can be seen on the right side of the figure. Overall, it is clear there is some variability in the particle count and distribution with each acquisition time though it is relatively consistent.

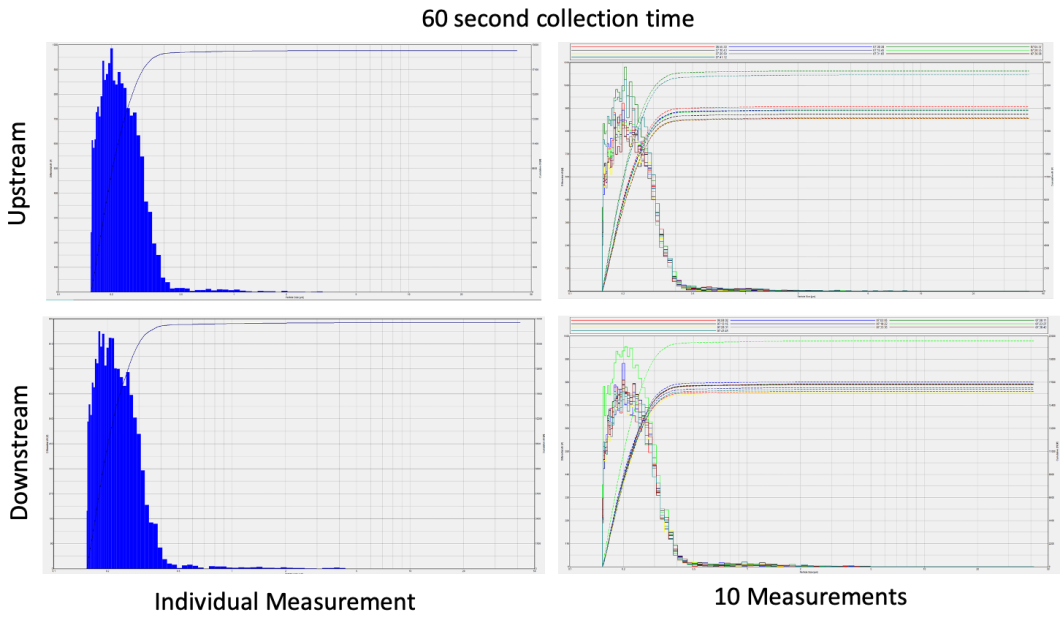

Figure 40. Example data showing a individual measurement resulting from a 60 second acquisition time and all 10 measurements for upstream and downstream of the dryer which were collecting alternating between up and downstream measurements.

Figure 41-a shows the sum of all upstream and downstream collection and compares the particle size distribution and total cumulative particle count. The red line is upstream, and the blue line is downstream. From this plot it is clear that more total particles were counted upstream, and the count of small particles is higher. The number of particles measured upstream versus downstream can be determined for each binned particle size, where the % Particles through the dryer for a particular particle size can be calculated by:

$$\%Particles\ through\ the\ dryer = 100 * \frac{n_{upstream} - n_{downstream}}{n_{upstream}} \qquad eq\ (4)$$

Where n is the number of particles counted in a specific particle size channel. This comparison can allow for an understanding of differences in the flow path for particles of a specific size. Since we do not expect hygroscopic particles to be present, any differences between upstream and downstream counts can be due to losses in the flow path. Figure 41-b shows a plot of the % particles that were counted through the dryer as a function of particle size. With a 60 second acquisition time, the count for small particles (up to about 1 μm) is relatively consistent between upstream and downstream and is slightly below 100%. As particle sizes increase, the %particles through the dryer starts to deviate significantly from 100% and generally trends >100%. One reason for this deviation is that larger particles may not be able to make the bend in the 90-degree angle for collection upstream of the dryer, however there is large uncertainty in this conclusion, because only a very small number of larger particles were sampled. For example, in the sum of 10 measurements, the channel associated with 0.154 μm particles counted 3040 particles upstream and 2656 downstream, whereas the 4.806 μm channel had 2 counts upstream and 4 downstream. With such poor counting statistics for particles > 1 μm, very little information about the flow path can be determined for larger particles.

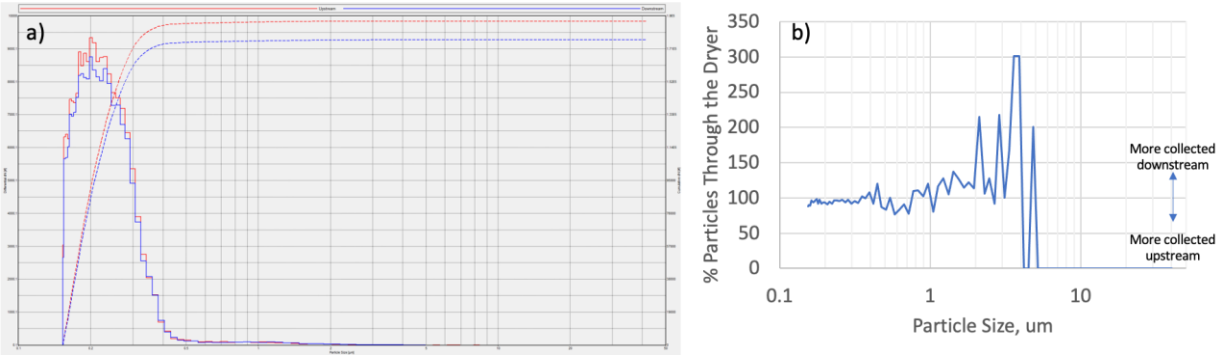

Figure 41. (a) Upstream and downstream comparison of the sum of all 10 measurements with 60 second acquisition time, and (b) the % of particles that passed through the dryer as a function of particle size from the sum of all 10 measurements.

In order to improve the statistics for larger particles, the same measurements were repeated with increasing acquisition times from 60 to 3600 seconds. Figure 42 shows the particle size distributions collected from the sum of 10 measurements for each acquisition time and Figure 43 shows the % of particles through the dryer. It is clear that with increased acquisition time, more particles are counted. This is especially obvious for particles < 0.5 μm in size; moreover, the % of particles passing through the dryer is close to 100% for all the experiments. However, even with long acquisition times, the total count for large particles is relatively small. For example, the sum of 10 measurements with a 3600 second acquisition time only resulted in 32 counts upstream and 70 counts downstream for the 4.8 μm particle bin. While the acquisition time increased 60x, the upstream counts only increased 8x and the downstream counts 17.5x. The % particles through the dryer is consistently ~100% for particles up to 1 μm in size, but larger particles still show a similar noisy trend as was seen in the shorter acquisition times. Therefore, increasing the acquisition time (at least to times measured) has displayed diminishing returns when it comes to particle counts. Additionally, with long acquisition times, the upstream and downstream measurements may not be measuring the same weather phenomena, as short-term events have a significant impact on ambient particle size distributions.

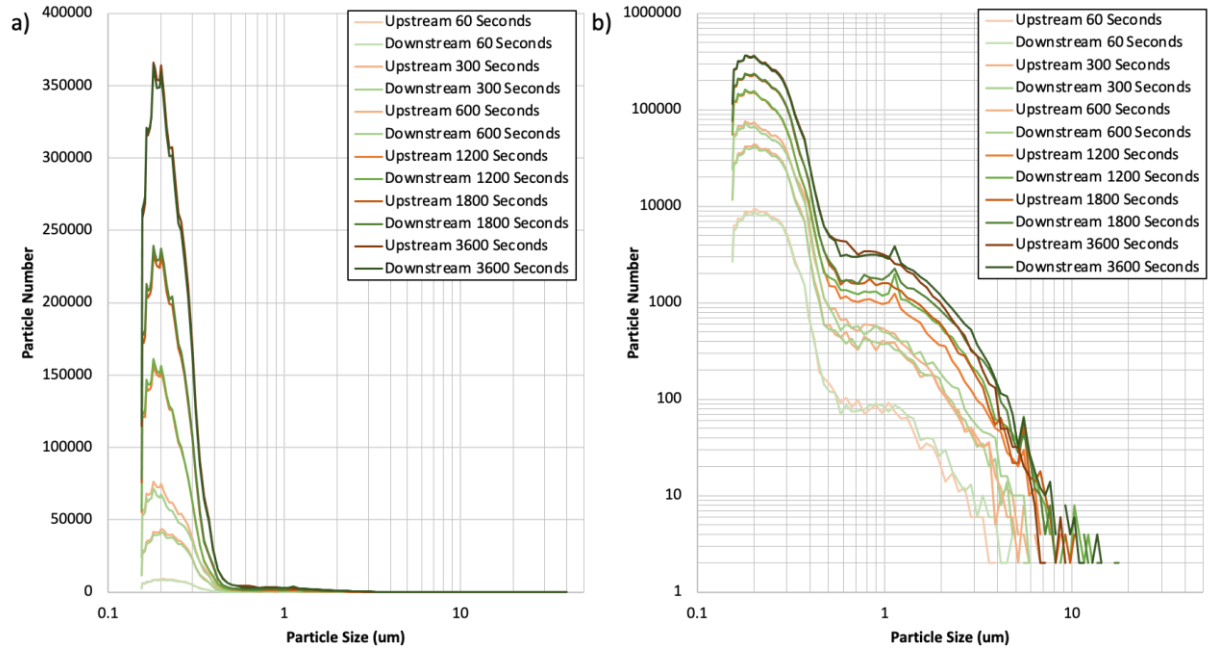

Figure 42. The Particle size distribution measurements for upstream and downstream sampling with acquisition times ranging from 60 second to 3600 seconds in where the particle count is in (a) normal scale and (b) logarithmic scale.

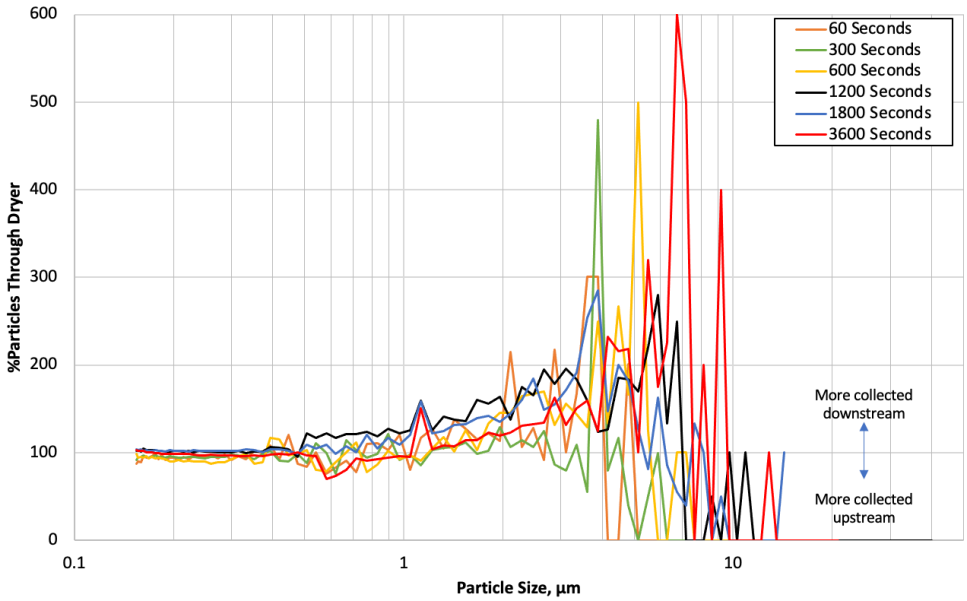

Figure 43. The %particles collected downstream relative to upstream as a function of particle size with acquisition times ranging from 60 second to 3600 seconds.

In order to get a wider distribution of particles to estimate the flow path efficiency, in FY23 the TOPAS LAP323 will be moved outside for the subsequent acquisition runs. Informed by these previous experiments, SNL will use an acquisition time of 600-900 seconds to achieve high particle counts, while retaining some sensitivity to changes in weather. In addition, the TOPAS LAP323 will be transported out to the CDFD site for site-specific testing.

3. Canister Corrosion: Pitting and Pit to Crack Transition

As discussed in the following sections, much of the corrosion efforts in FY22 have continued to refine our understanding of environmental factors controlling pitting. Determination of correlations between pit morphology and specific environmental stimuli, brine compositions, and material properties will be detailed within. Continued parameterization and exercising of the maximum pit size model was carried out and submitted as part of the SCC modeling L3 [51] and summarized below. Additionally, efforts in FY22 regarding the pit to a stress corrosion crack transition have focused on two main areas: 1) summarizing the current understanding of the pit to crack transition within the scientific community (through a comprehensive invited critical review manuscript submitted in August 2022 [14]) and 2) applying this understanding to the development of a U-bend exposure set that explores significant material and environmental influences on the pit to crack transition. Finally, crack tip modeling, applying a reactive transport finite element method, was further explored to understand influencing factors of the corrosive environment that forms locally at a crack tip, and how, this in turn, effects SCC and crack growth [15]. Overall, in FY22, the corrosion work has advanced the understanding of significant variables influencing corrosion damage morphology and extent, specifically delving further into the roles of environment (brine composition), material composition, and surface finish, and how their influence on damage extent and morphology plays into the subsequent pit to crack transition and implications for crack growth.

3.1 Environmental Effects on Pitting

Research in FY22 has continued to push our understanding of the effect of environmental variables on corrosion damage, specifically, pitting and the pit to crack transition. In collaboration with the Ohio State University, a manuscript was published in Corrosion Journal revealing the novel findings of the influence of carbonate containing brines (typical of seawater) on pit morphology and the implications for SCC [12]. Environmental variables were further explored through exercising the maximum pit size model as detailed in the FY22 L3 [13]. Finally, SNL continued the large-scale, long-term exposure testing under canister relevant environments, including exploration of specific environmental variables; diurnal cycling, inert dust, and nitrates, that may play large roles in resultant corrosion damage. Developing a deeper understanding of the environmental and material influences that govern corrosion damage, and how this in turn will influence the pit to crack transition and SCC, will enable better overall lifetime predictions for aging canisters.

3.1.1 Effects of Brine Composition on Pit Morphology

From work carried out since FY19, it has become apparent that SS304 specimens exposed to seawater brines at a lower relative humidity (below the deliquescence of NaCl) exhibit more irregular corrosion damage morphologies. These pit morphologies were hypothesized to form due to the presence of high concentrations of Mg^{2+} ions in the brine. In FY20, full immersion experiments on SS304 coupons were explored to isolate the effects of brine composition, by essentially removing the cathodic limitations observed in atmospheric exposures [27]. This work provided the basis for a manuscript published in CORROSION Journal in 2022 (Appendix B).[12] It was observed that surface micro-cracking was associated only with cross-hatched pits formed in brines equivalent to sea-sea salts at low RH exposures, and appeared to correlate with a high concentration of dissolved carbonate species, as shown in Figure 44 [12]. However, micro-cracking was not observed in the high-RH equivalent sea-salt brines (Figure 44-b & d). The correlation of morphology to the brine composition implied that the concentrations of $MgCl_2$ and dissolved carbonate species in the brines could, in the presence of machining-induced surface microstructure and residual stress, determine pit morphology in marine atmospheres, which may potentially impact SCC and lifetime prediction.

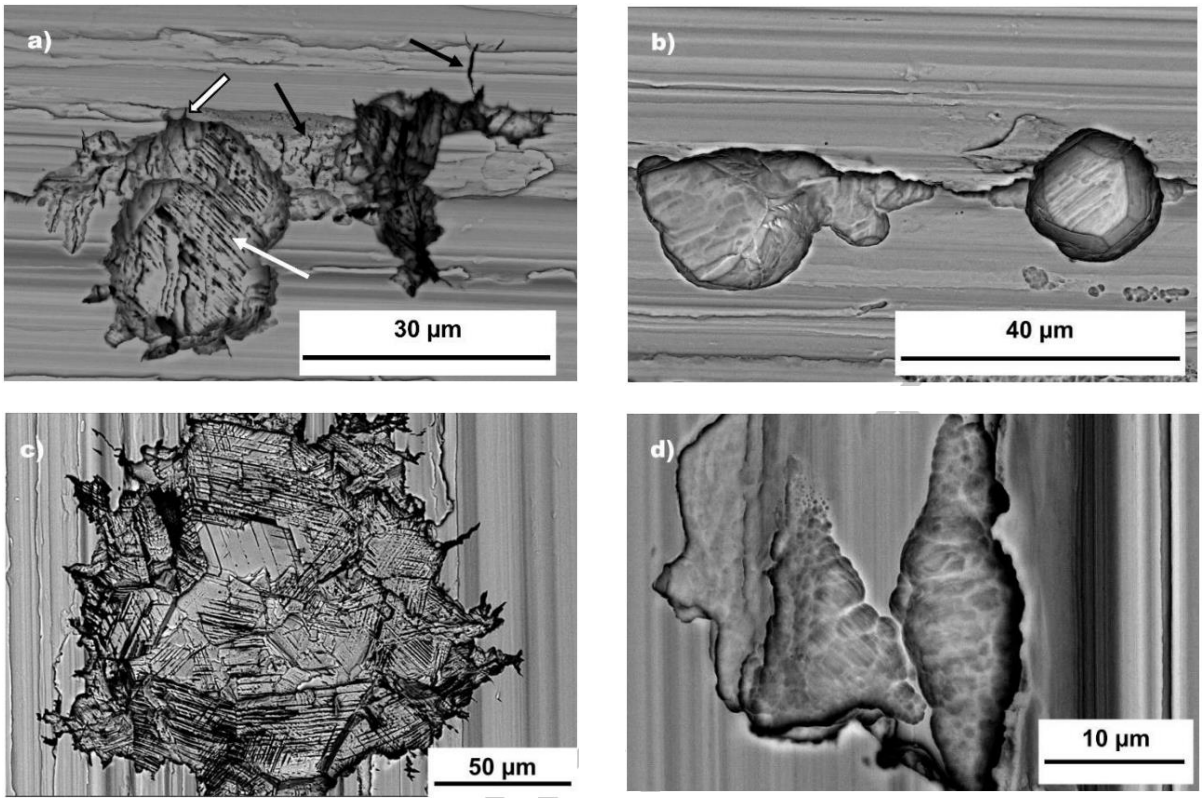

Figure 44. Example SEM comparison of pit morphology observed on stainless steel exposed under atmospheric and fully immersed conditions. Atmospheric exposures for 4 weeks at 35 °C with sea salt brines equilibrated to a) 40% RH and b) 76% RH, and full immersion exposures for 47 days in bulk solutions of equivalent compositions for c) 40% RH and d) 76% RH. In a), white arrows indicate cross-hatching, black arrows indicate micro-cracks, and white arrows with a black border indicate smaller fissures.[12]

The observation that these varied morphologies are dependent on exposure environment (and material surface finish) has multiple implications for the lifetime and SCC predictions developed for SNF canisters. First, these exposures continue to support the findings that ellipsoidal shaped pits may likely not dominate the corrosion attack possible under canister relevant environments. This further impacts the estimated lifetime predictions developed for maximum pit depths, which assume hemispherical geometries. In addition to the potential inaccuracies or assumptions made in the corrosion maximum defect models, these irregular shaped pits may also influence potential pit to crack transitions. Initial studies throughout literature have displayed effects of geometry on the pit to crack transition, indicating that the stress/strain concentration may be dependent not only on the maximum depth, but also the localized geometry.[14] Thus, developing a better understanding of the dependence of corrosion damage morphology on the exposure environment, and the key influencing parameters, will enable enhanced understanding of assumptions made in overall lifetime SCC predictions and enhance future model/prediction capabilities.

3.1.2 Environmental Influences: Parameterizing Maximum Pit Size Predictions in Marine Environments

As has been shown through the corrosion work carried out in FY21 and FY22, brine composition, brine evolution during corrosion, and material influences can significantly affect the corrosion damage across austenitic SS under canister relevant conditions. Accounting for these real-world effects in modeling can

greatly enhance predictions for maximum pit sizes which, in-turn, will result in better overall SCC predictions.

Earlier this year, SNL produced an SFWST report, "FY22 Status Report: A Probabilistic Model for Stress Corrosion Cracking of SNF Dry Storage Canisters" [13]. In this report the maximum pit size model was exercised, and the model results were discussed. Parameters governing pit evolution on the canister surface were identified. Future updates to account for brine composition/evolution and mineral precipitation have been identified.

As has been described previously, when the SNF canisters cool with time, the canister surface RH can increase to greater than the RH_L (the deliquescence RH), deposited salts on the surface can deliquesce, and corrosion (pitting) can occur. The pits, which act as stress/strain concentrators, may grow large enough to serve as nucleation sites for SCC. Therefore, estimation of the maximum pit that can form in a given environment is an important step in the probabilistic modeling of SCC. The growth of pits is modeled using the formulism of Chen and Kelly [52] and has been detailed in previous reports ([40, 51]). Briefly, the maximum pit size model relies on the fact that under freely corroding conditions, pitting can be considered a galvanic couple with the pit being the anode and the surrounding area, the cathode. The pit can only grow as long as the anodic current required to maintain the critical solution chemistry is predominantly supported by current from the surrounding material (the cathode). For atmospheric exposure conditions, significant ohmic drop in thin electrolyte layers over short distances limits the size of the surrounding cathode area and thus the cathodic current available to support anodic dissolution. The maximum pit model considers the contributions and coupling of (1) anode pit kinetics (I_a), (2) cathode kinetics, and (3) ohmic drop. In the current application of the model, once pits form, they are assumed to be hemispherical, and electrochemical kinetics are used to calculate the radius.

In FY21, efforts focused on an experimentally-informed maximum pit size model. The integral effects that changes in the i_{eq} (the equivalent anode current), ΔE_{max} (the potential drop), and I_{pit}/r_{pit} (the pit stability criterion) will have on the maximum pit size were documented. The results for each of these parameters and the overall effects on pit size were reported in [51]. In FY22, this model was expanded to parameterize maximum pit size predictions across relevant environments[13], a summary of which is presented below.

First, a review of the inputs for the maximum pit size model (both solution parameters and alloy parameters) is provided. Predicted conductivity (κ) values for representative sea-salt brines as a function of RH and temperature are shown in Figure 45-a. As can be seen, increasing RH results in an increase in κ, measured as the solution composition changes from Mg-rich to Na-rich. Further increasing RH from 75 to 98%, results in a decrease in κ, as the solution becomes increasingly dilute. This pattern holds true for all temperatures. A linear increase in κ was measured with an increase in temperature at all RHs. Figure 45-b displays a decrease in the calculated water layer (WL) thickness with a decrease in RH. Inflections in each curve represent RH conditions at which a salt mineral precipitates. Temperature has a relatively minor effect on the predicted WL, for NaCl it would increase proportionally to solubility, but the effect is negligible. The critical pit stability (I_{pit}/r_{pit}) is shown to increase with an increase in RH and temperature (Figure 45-c). As such, at the same pit depth, more current is needed to support anodic dissolution with an increase in RH and an increase in temperature. Additionally, the i_{eq} also increases with both temperature and RH (Figure 45-d).

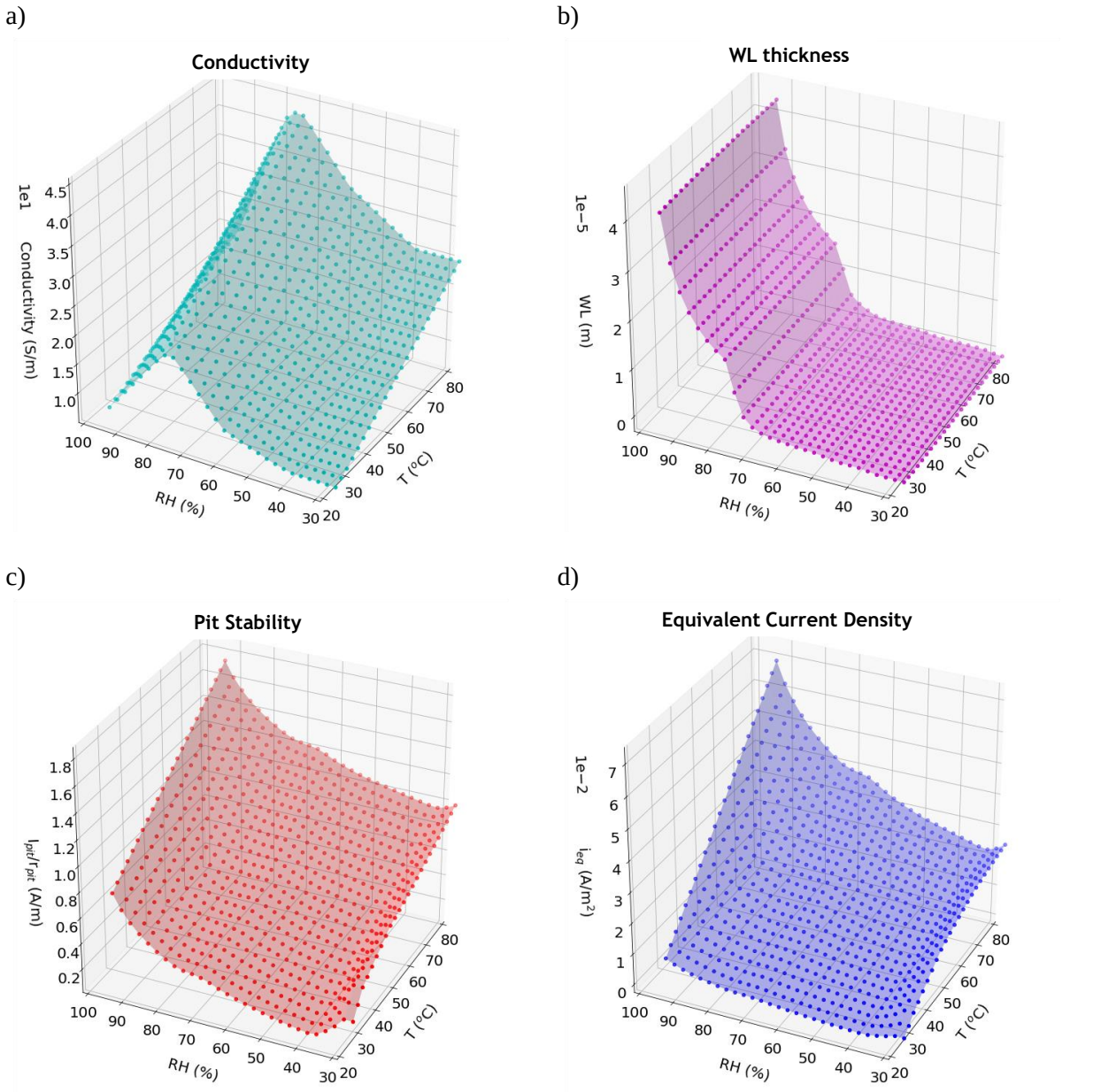

Figure 45. Significant parameters to the maximum pit size model as function of RH and temperature: a) Brine conductivity (Siemens/meter), b) calculated brine thickness for a chloride loading density of 1 g/m^2, c) critical pit stability product (assumed to be 50 % of saturation) for a hemisphere pit, and d) equivalent current density.

The experimentally determined parameters from Figure 45 were utilized to predict maximum pit sizes under loading densities of 0.1, 3, and 10 g/m^2 chloride in Figure 46. With an increase in RH, an increase in predicted maximum pit size is modeled up to about 75% RH. Further increasing RH greater than 75% yields a predicted decrease in the maximum pit size. With increasing temperature, a slight decrease in the maximum pit size is predicted. The cause for the maximum pit size at 75% RH is a combination of the influences of the increase in the solution conductivity and the pit stability at this point. These trends hold true across all loading densities examined, however it is also noted that maximum pit size increases with an increase in the loading density, from a to c in Figure 46.

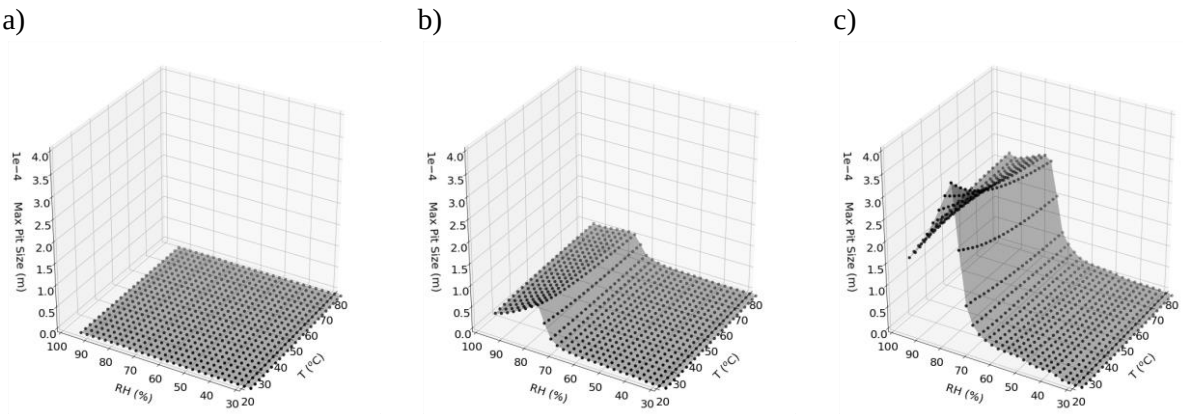

Figure 46. Maximum pit size versus RH and temperature for salt loading densities of a) 0.1, b) 3, and c) 10 g/m^2 of chloride.

Developing and parameterizing the maximum pit size predictions over such a large variable space has enabled a better understanding of the key influencing variables and prediction of environments and conditions that will likely lead to higher corrosion susceptibility, and thus SCC susceptibility. Results of the FY22 modeling report [13] will be further explored and expanded in FY23. Future work will look to incorporate the influence of non-static environments, including, but not limited to updates to the maximum pit size model to capture the additional effects of mineral precipitation and the presence of inert dust.

3.1.3 Atmospheric Environmental Exposures

In the FY20 status report [27] three modified environments were developed and discussed for corrosion testing, and experimental explorations for each were initiated in FY21[40]. The intent of these environmental examinations was to identify key parameters to more realistically capture aspects of the natural environment that may have significant effects on corrosion damage and subsequent SCC on canister surfaces. The first of these environments implements a diurnal cycle—a 24-hour cycle in temperature and RH—that was chosen to be representative of conditions that would eventually occur on a canister surface as the canister cooled. The second addresses the potential effects of inert mineral grains on the metal surface. The third environment of interest explores other potential chemical influences in the brine, specifically the influence of nitrates. The environments were previously described in both [27, 40] but the status of the exposures and resultant corrosion studies will be detailed below. The primary goal of these exposures overall is to develop a better understanding of the controlling factors for corrosion specific to SNF canister relevant environments and how these will influence subsequent pit to crack transitions and SCC.

3.1.3.1 Cyclic Diurnal Influences on Corrosion

The goal of the cyclic diurnal exposures is to investigate the influence of the diurnal T and RH fluctuations on the resultant corrosion behavior of austenitic stainless steels. Additionally, as samples of SS304, SS304H, and SS316L were exposed with three varied surface finishes for each material, influences of material composition and surface state will be explored. Stainless steel coupons are currently under exposure in a diurnal atmospheric chamber, with tests completed up to 1 year of exposure and ongoing tests planned for 2 years. The subsequent corrosion damage was evaluated using optical and electron microscopy, profilometry, and compared to full immersion electrochemistry. A summary of the initial results will be presented.

Experimental Setup and Cyclic Exposure

The alloy compositions for the three austenitic stainless steels examined are provided in Table 12. Each coupon was prepared at three different surface finishes: (i) a rough mechanical grind (#4 finish), (ii) a 600-grit surface finish by hand polishing, and (iii) a #8 mirror finish (mirror finish). The #4 finish and #8 mirror finish were prepared by Polished Metals Ltd, Incorporated (Hillside, New Jersey). The #4 finish consisted of a 180-grit mechanical grind with abrasive belts and has an average surface roughness (R_A) value of 30 μm. The 600-grit finish was achieved by hand polishing on a Pace Technologies Nano 2000 polisher with 600-grit silicon carbide grinding pads and a deionized (DI) water rinse. Following grinding, all samples at a 600-grit finish were rinsed with DI water and dried with nitrogen gas. The #8 mirror finish was achieved mechanically through a series of abrasive belts up to 1200 grit followed by abrasive compound and buffing wheels and has an average R_A value of 4-8 µm. All coupons were cleaned again prior to salt deposition and exposure using a previously developed procedure consisting of ultrasonication in acetone (3 min), ethanol rinse, ultrasonication in Liquinox ® detergent (3 min), ultrasonication in deionized water (3 min), ethanol rinse, and finally drying with compressed nitrogen [29]

Table 12. Composition of 304H, 304, and 316L SS used in this study (weight %). Nominal composition is reported as received from NSL Analytical.

Alloy	C	Cr	Cu	Mn	Fe	Mo	N	Ni	P	S	Si
304H	0.057	18.13	0.24	0.87	69.16	0.2	0.048	8.23	0.028	0.004	0.37
304	0.045	18.48	<0.1	0.83	71.96	0.018	0.055	8.18	0.027	0.002	0.4
316L	0.03	16.77	0.45	1.15	71.82	2.04	0.04	9.98	0.022	<0.001	<0.02

A LogoJet Pro H4-2400 industrial inkjet printer was used to deposit ASTM seawater onto the coupons with a salt loading density of 300 µg/cm^2 (3 g/m^2) at a RH of 80% and temperature of 21 ºC. After deposition, all salt-printed coupons were placed in RH chambers and set to a developed 24-hour diurnal atmospheric cycle shown in Table 13. This cycle was previously developed based on the Arkansas Nuclear 1 weather data and is fully described in [27, 40].

Table 13. Cyclic atmospheric parameters modeled after Arkansas nuclear 1 weather data.

Hour	Temperature, ºC	RH, %
2	41.68	30.33
4	36.45	41.68
6	35.27	43.92
8	34.35	46.69
10	33.69	48.68
12	32.74	49.54
14	33.44	49.57
16	38.24	40.98
18	40.55	34.62
20	42.69	30.62
22	43.51	27.82
24	42.97	29.15

All samples were imaged pre- and post-exposure to determine both the salt distribution and corrosion damage morphology. Optical microscopy was carried out on a Keyence VHX-5000 Digital Microscope. Additional images were taken using scanning electron microscopy both pre- and post-corrosion product removal. Corrosion product removal was performed following the ASTM G-1; coupons were brushed with a Nylon bristle brush in DI water and then sonicated in 10 vol. % HNO_3 for 60 minutes at room temperature, followed by another rinse with DI water. Samples were then imaged using a Zeiss Gemini 500 Field Emission SEM at 20 kV accelerating voltage with secondary and backscatter detection modes.

Additionally, in FY22, a system of qualitative analysis measurements of pit morphology was developed to determine potential environmental and material factors that influence corrosion damage. Observed pit damage morphologies could be categorized into eight main groups with the following morphologies: (i) hemispherical, (ii) crystallographic attack, (iii) crevicing, (iv) cross hatching, (v) undercutting, (vi) spongey, (vii) microcracking, (viii) and fissures. Example images of each morphology are provided in Figure 47. For pit morphology characterization a minimum of 8 images were analyzed manually per sample. For each image, the presence or absence of each morphology was recorded as a 1 or 0. The values were summed and averaged over the set of images for each sample and each characteristic morphology. It should be noted that this process is somewhat subjective.

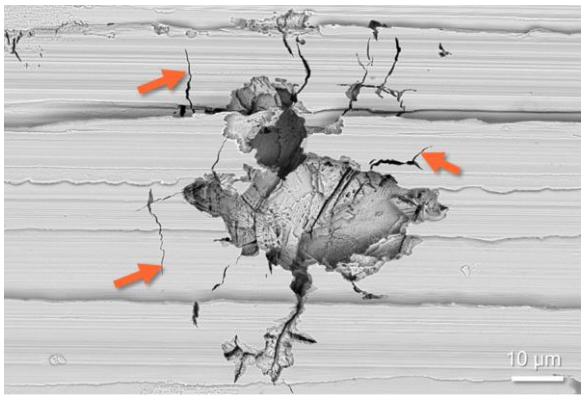

a) Microcracking

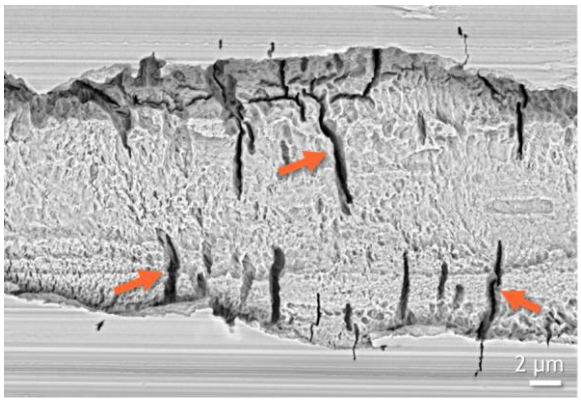

b) Fissures

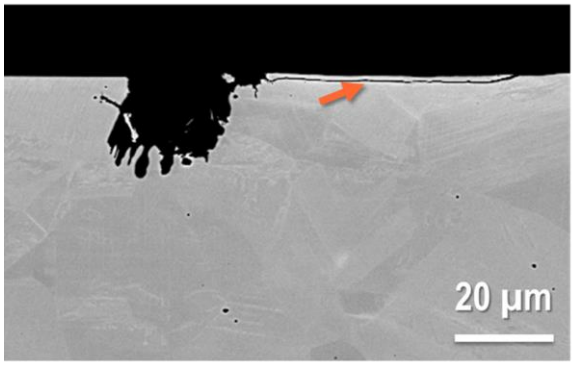

c) Undercutting

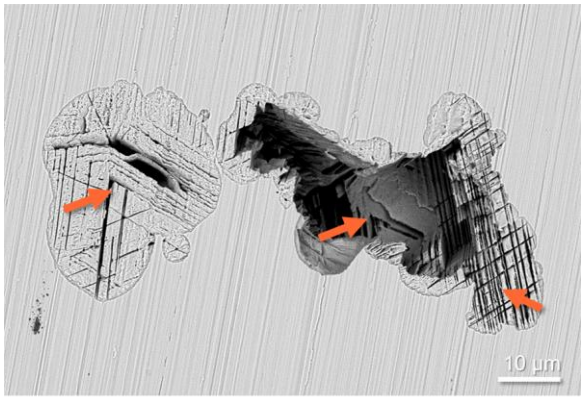

d) Cross-hatching

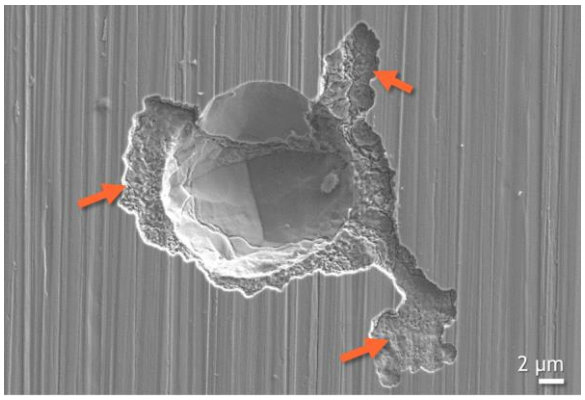

e) Crevicing

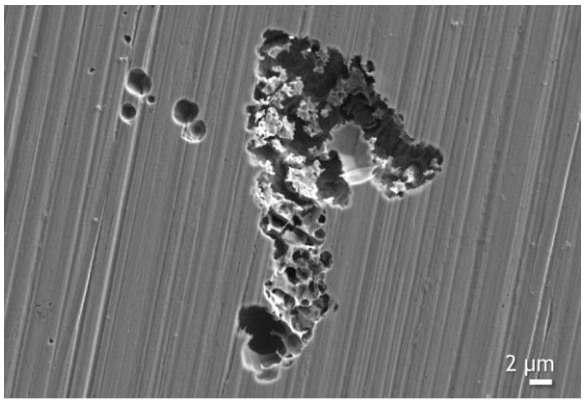

f) Spongy

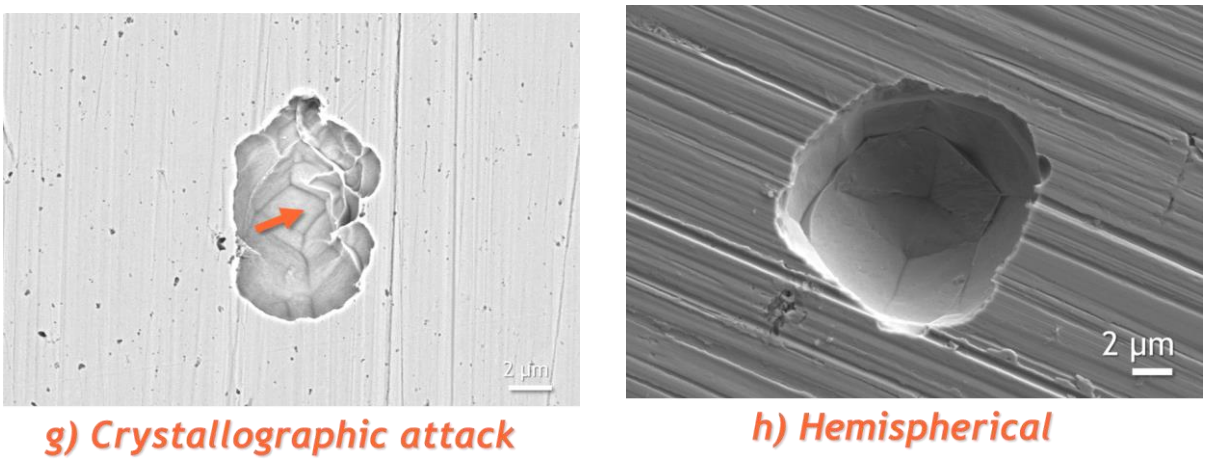

Figure 47. Representative pit morphologies post-exposure in diurnal cyclic conditions, the eight morphology groups fall under a) microcracking, b) fissures, c) under-cutting, d) cross-hatching, e) crevicing, f) spongy, g) crystallographic attack, and h) hemispherical.

In addition to top-down SEM, images were acquired on a few select cross-sections of post-exposure samples. Selected pits were sectioned and polished to mirror polish finishes to obtain both SEM images as well as electron back-scattered detection (EBSD) and high-resolution EBSD (HREBSD) for future strain distribution calculations to explore the potential influences of surface finish. Initial results will be presented herein,

In addition to the qualitative assessment of pit morphology through SEM, profilometry was applied to provide a semi-quantitative measurement for pit growth. A Zygo Nexview 3D optical profilometer was used to measure corrosion damage. The profilometer used green light and a 5x objective resulting in a quoted lateral resolution of 1.63 µm, and a quoted vertical resolution of <1 nm. Three 12 x 12 mm areas were measured on each coupon with each measurement taken at least 5 mm away from the edge of the sample similar to previous work [29]. Corrosion damage was quantified by maximum pit depth from the three 12 x 12 mm areas on each sample. All pitting data were analyzed using the particle analysis feature within Digital Surf MountainMaps® 8 profilometer software. For analysis, each measurement was leveled using a least square plane level method (LSPL), and the z-axis was mirrored to flip the corrosion damage above the mean plane on the z-axis. Once the z-axis was mirrored, a threshold procedure was applied in reference to the 10.4 µm above (average scratch depth) the mean. All non-measured points were filled through nearest neighbor interpolation. In some cases, automatic quantification of pit depth was convoluted with surface roughness and will be further discussed within this paper. In order to identify pits, thresholds for the projected area (10^{-5} μm^2) volume (56 μm^3), and roundness (0.2; the minimum ratio for the surface area of an object to the area of the circle whose diameter is equal to the maximum diameter of the object) were utilized to filter automatically identified features within Mountains Maps. Features shallower than these values could not be differentiated from surface features that were not associated with corrosion.

To establish a better understanding of corrosion kinetics on the coupon finishes exposed under diurnal cycling, electrochemical tests were performed for comparison. Open circuit potential (OCP) and cyclic potentiodynamic polarization (CPP) scans were carried out using a Biologic Potentiostat (SP-200). All electrochemical tests were conducted in 0.6 M NaCl solution at room temperature (~22 ℃) where the solution was placed in a three-electrode cell configuration consisting of the sample as the working electrode, platinum mesh as the counter electrode, and an Ag/AgCl reference electrode. OCP was equilibrated for one hour followed by a CPP scan with a scan rate of 0.167 mV/s, a voltage range of -0.2 V_{OCP} to 1.2 $V_{Ag/AgCl}$, and a cutoff current at 1 mA. A total of three curves were obtained for each surface finish condition on each stainless steel.

Cyclic Exposure Analysis

In FY21, sample exposures were initiated for cyclic conditions and were continued throughout FY22 for exposures up to 56 weeks. These tests are still ongoing with the final exposure duration up to two years to be completed in early FY23. The results of the continued discussion with updated analysis from FY21 will be presented here and discussed in the following pages.

Optical images continue to show significant amounts of surface rust and corrosion products on the rough ground (#4) samples, which is visible across all materials and times of exposure in Figure 48. Rust, or corrosion damage, somewhat visibly increases with time of exposure and is dependent on alloy type, with SS316L exhibiting lower corrosion damage. The corrosion damage also appears to align with the grind lines from surface finishing for the #4 surface finish, but does not for the 600 grit or mirror polish, as apparent in Figure 49.

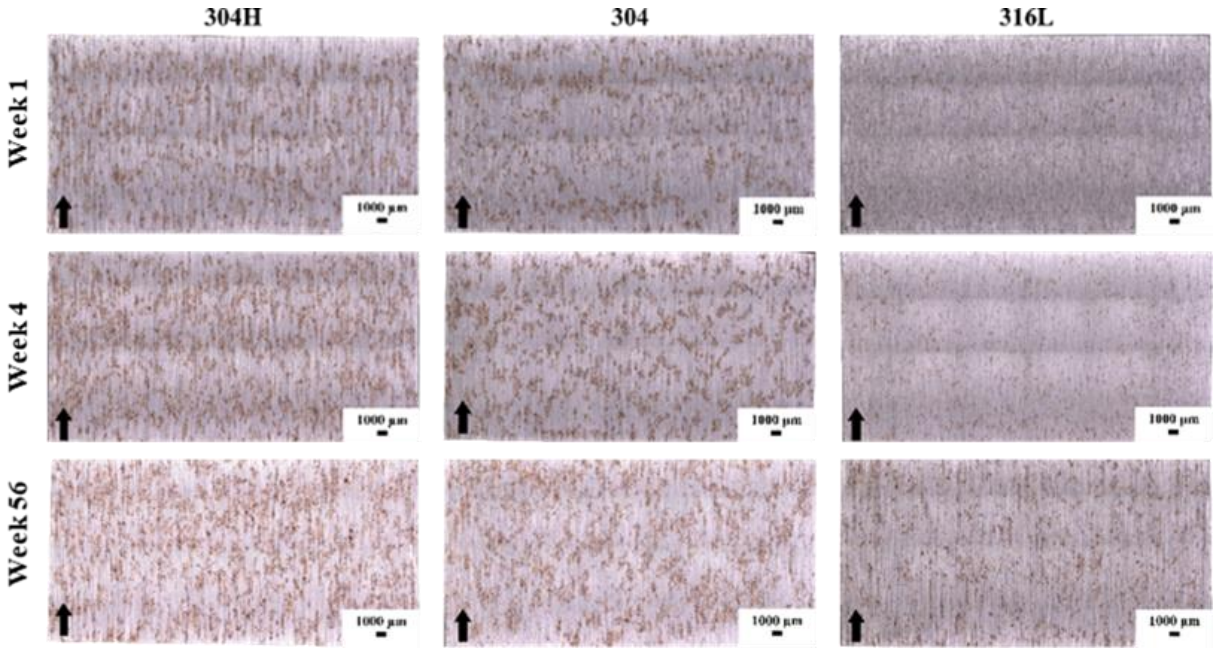

Figure 48. Example optical imaging of post-exposure rough ground (#4 finish) 304H, 304, and 316L coupons versus exposure time in weeks. Black arrows indicate grind direction.

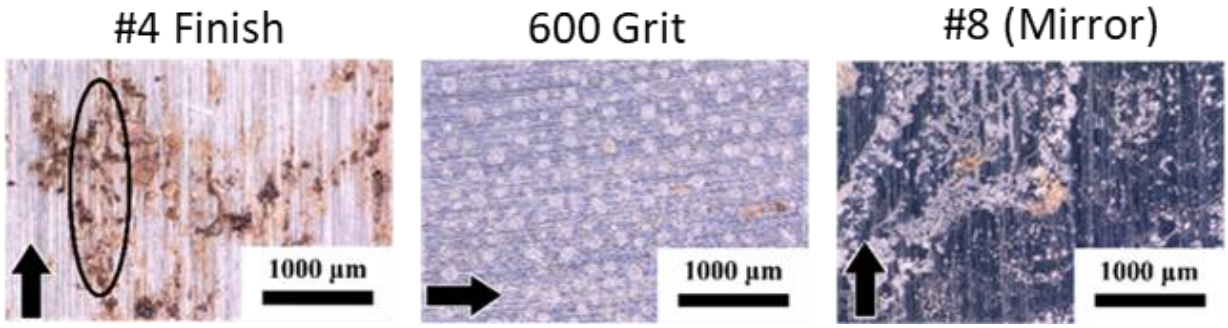

Figure 49. Higher magnification example optical images of post-exposure coupons versus surface finish after 26 weeks exposure. Ovals indicate corrosion product grind lines for #4 finish and black arrows indicate grind direction.

Observed pit morphologies continue to follow similar trends as those established in initial results in FY21 [40]. Pit morphology appears to continue to correlate with both surface finish and material composition. As can be seen in Figure 50, all materials exposed with a #4 surface finish exhibited irregular shaped pits, with microcracking or fissures extending from the pits. However, coupons exposed with a 600 grit surface finish (finer surface finish) exhibited more hemispherical like pits with no apparent microcracking. The morphology of the pit surface for the 600 grit coupons also depended on material type, with SS304H displaying cross-hatching, and SS304 and SS316L displaying crystallographically - etched pits.

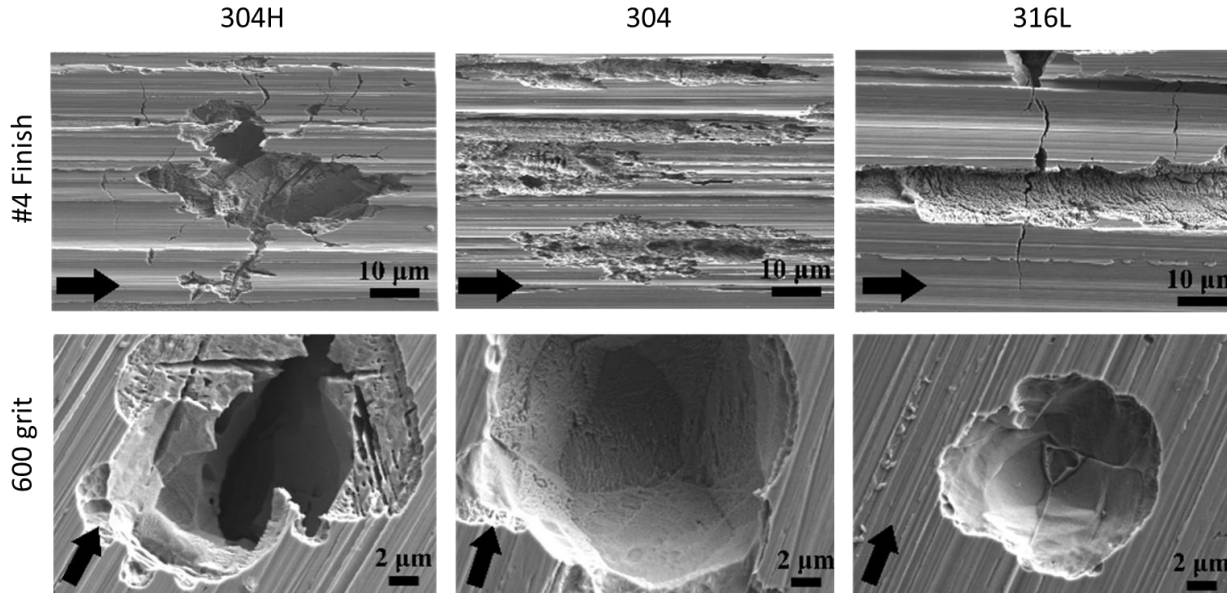

Figure 50. Example post exposure corrosion analysis of pits after 52 weeks exposure in cyclic conditions. Pits continue to exhibit similar morphologies as observed in FY21, with morphology dependent on both surface roughness and alloy.

Post-exposure and post-corrosion product removal, initial profilometry measurements were collected for all samples. For all cases, the ten deepest pits appear to increase in depth over time, and in some cases may plateau at longer times as observed previously with static exposures (Figure 51)[53]. However, longer time step exposures (up to two years) need to be analyzed to confirm these trends. From the initial comparison of profilometry results, there appears to be an influence of surface finish, in that deeper pits

were observed in general across all materials for the #4 surface finish. Potential trends in the 600 grit and #8 mirror finish are less clear. Additionally, some of these measurements may be influenced by thresholding inconsistencies due to surface roughness.

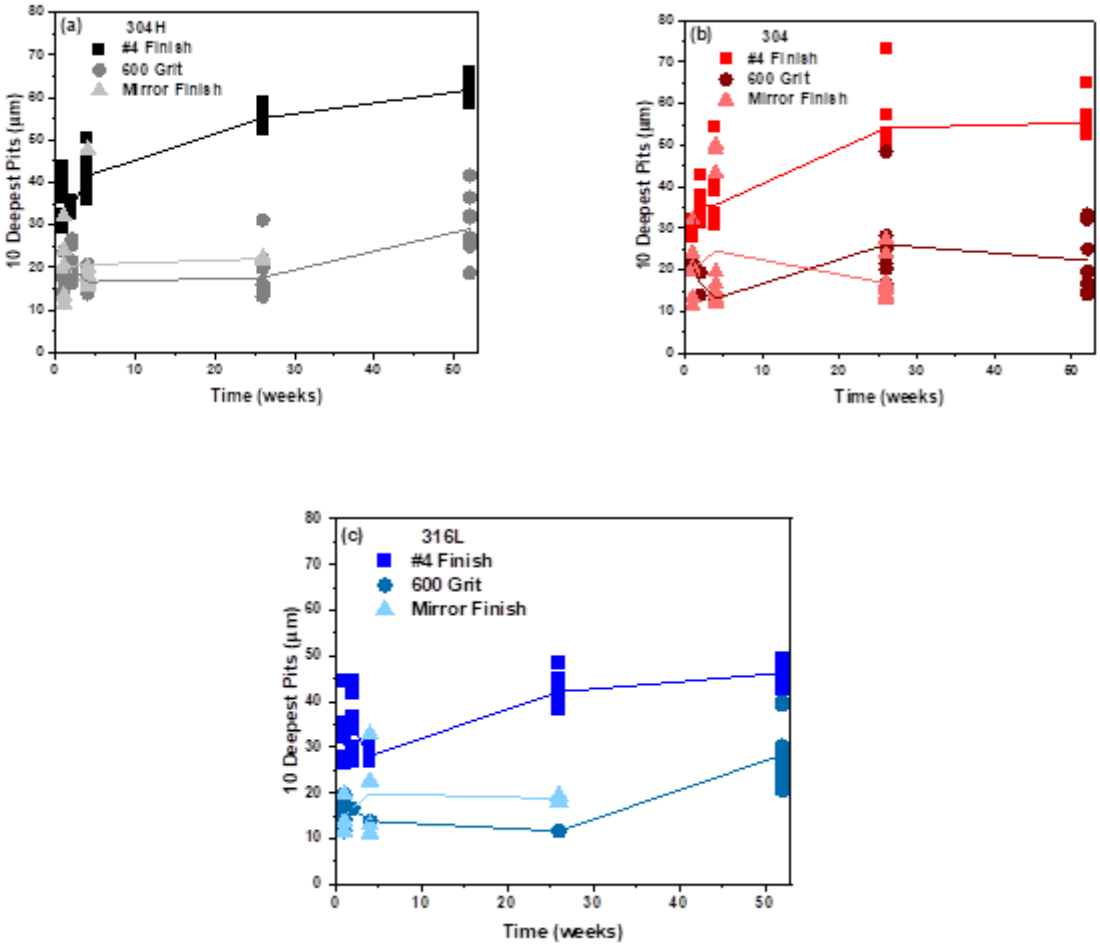

Figure 51. Ten deepest pits measured by profilometry across all surface finishes for a) SS304H, b) SS304, and c) SS316L.

Profilometry measurements can only observe line of site corrosion damage. Measurements such as 10 deepest pits, density, or volume loss inherently make some assumptions about the pit morphologies. While these may be useful to enable collection of data to validate maximum pit size predictions, it has been shown that pits that form on austenitic stainless steels under SNF relevant environments often exhibit more complex morphologies than the assumed hemispherical pit geometry [29]. Developing a more holistic understanding of the pit morphology produced may have larger implications for pit to crack transition and the potential for SCC under a given environment. As pits can act as stress/strain concentrators, which may be dependent not just on the maximum depth, but on the pit morphology, understanding how the environment and material govern pit shape is significant to the pit to crack transition. To gain a more semi-quantitative measurement of the pit morphology developed under cyclic atmospheric conditions versus material and surface finish, as discussed previously, analysis of multiple SEM images was carried out across all exposure times to date (up to 1 year exposure). Pit morphologies

observed in SEM images were qualitatively categorized according to the eight morphologies presented in Figure 47. Summaries for each surface finish are shown in Figure 52. As can be seen, there is a strong correlation between pit morphology and surface finish. Microcracks, fissures, and undercutting were very prevalent for the #4 surface finish (Figure 52-a), but were rarely observed on the 600 grit or mirror finish coupon exposures (Figure 52-b&c). Cross-hatching, which was prevalent for all materials on the #4 surface finish coupons, became material dependent as the surface finish became finer. Cross-hatching was only observed on the SS304H coupons with a 600 or #8 mirror polish finish (Figure 52-b&c). Spongy attack was observed across all samples and surface finishes, however, was more prevalent for the rough grind samples. Crystallographic attack and hemispherical morphologies were more prevalent for the 600 grit and mirror polish finish and, also displayed a material dependence. At 600 grit, some crystallographic attack was observed on SS304H samples, however, for the mirror surface finish, no crystallographic attack was observed on SS304H, only on SS304 and SS316L. Overall, in general, more irregular shaped pits with sharp features (cracks, fissures, undercutting) occurred on rougher surfaces with less corrosion resistant material, SS304H, whereas the more smooth, hemispherical geometries were prevalent on the finer finishes with more corrosion resistant materials (SS304 and SS316L).

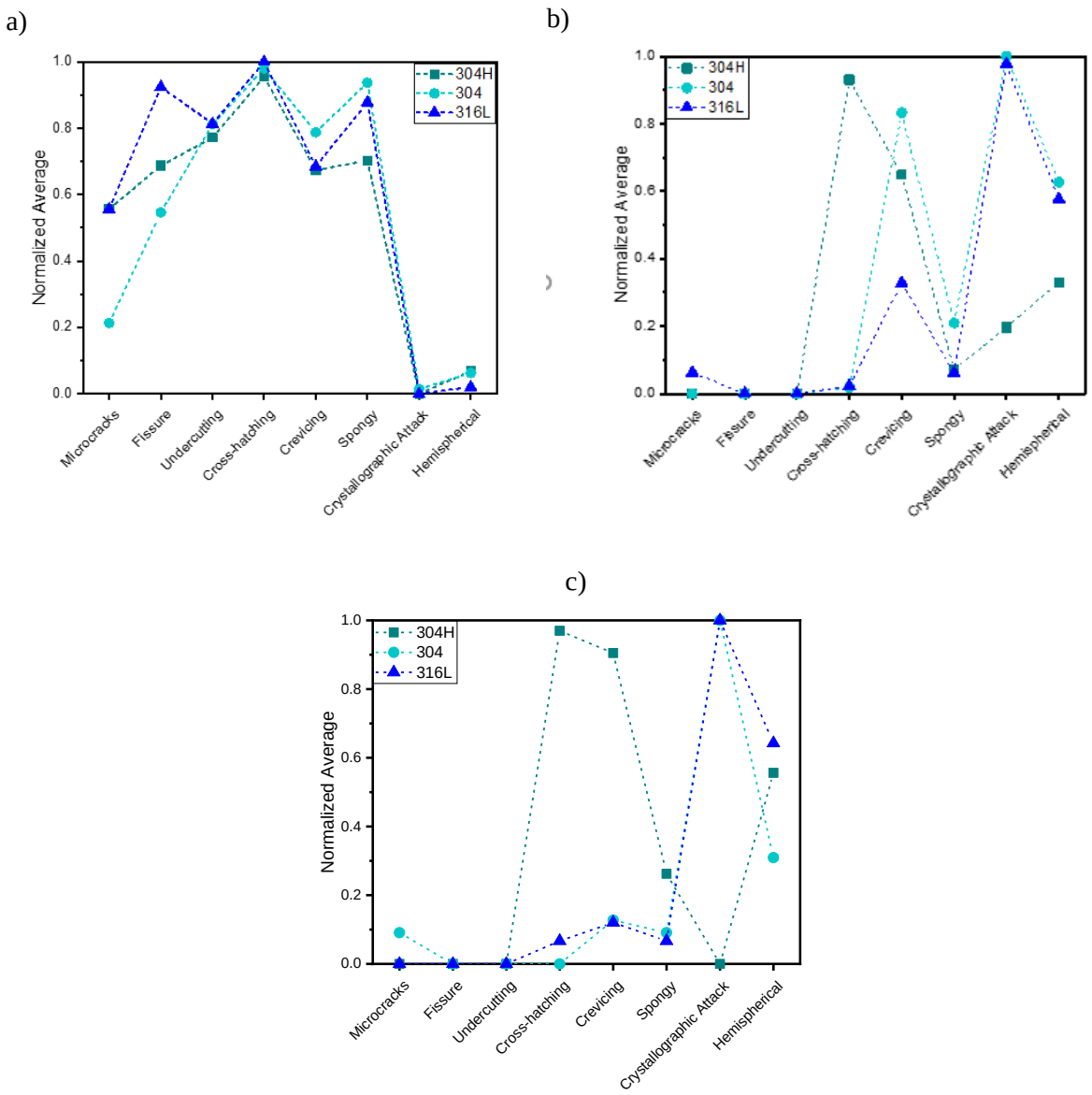

Figure 52. Qualitative assessment of pit morphology for SS304H, SS304, and SS316L for a) #4 finish, b) 600 grit, and c) #8 (mirror) finish.

These observations of pit morphology dependence on surface roughness and material composition do not contradict those of previous years' findings of brine composition influences[27, 29]. These pits were all observed from corrosion occurring in lower RH brines (the diurnal cycles did not exceed 50% RH), thus continue to support the findings that the lower RH, or $MgCl_2$ dominant brines are necessary to produce the more irregular morphologies. However, these studies do highlight that there are multiple influences on the resultant pit morphology in a given environment, and that surface finish and alloy composition combined with the environment of exposure govern the resultant geometry. To obtain the irregular pit morphologies, specifically the microcracking observed, it is not only necessary to have the lower RH ($MgCl_2$ dominant brines), but near surface residual stresses are necessary, as present in these coupons due to the rough grind surface finishing. Developing this enhanced understanding of the influence of material composition and surface finish on subsequent corrosion damage will aid in an enhanced ability to assess a canisters' susceptibility to corrosion and potential SCC. To further study the influences of material

composition and surface finish, potentiodynamic polarizations were carried out to determine electrochemical kinetics, Figure 53.

a) b)

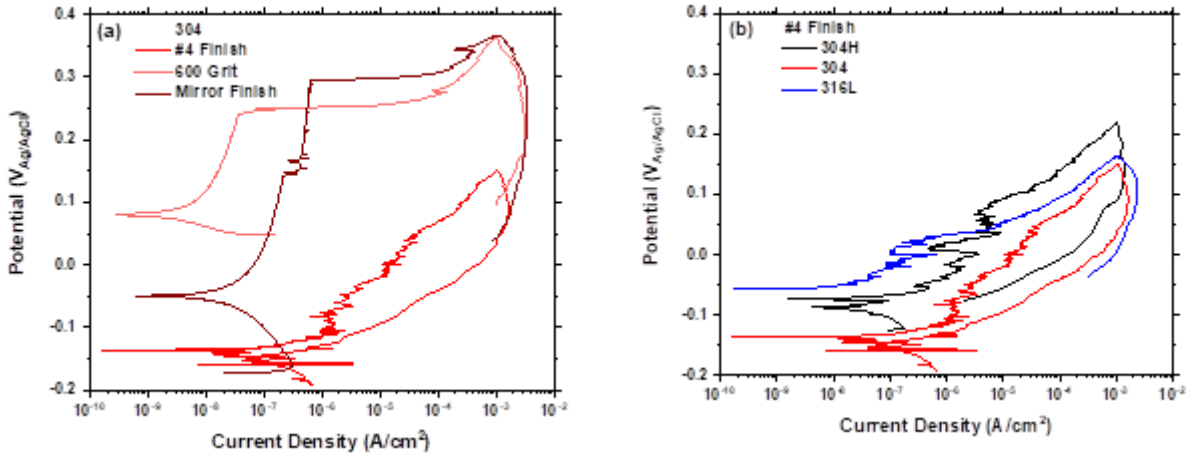

Figure 53. CPP scan comparison for SS304 at a) different surface finishes and (b) CPP for all SS compositions with #4 finish.

As can be seen in the example polarization scans for SS304 in Figure 53-a, the corrosion response of the material is highly dependent on the surface finish. For a rough ground surface, the SS304H displays active behavior, however, when finished to 600 grit, displays a passive behavior. The passive region is even further increased when the sample surface is finished to a mirror polish. Additionally, while austenitic stainless steels are considered passive alloys, all three materials display active behavior in the rough ground condition, as shown in Figure 53-b. The changes in corrosion kinetics based on surface roughness for these austenitic stainless steels provides some insight into the morphology and depth of attack observed in the atmospheric exposures. The reduced corrosion resistance observed with the rough surface finish in the polarization scans correlates with the deeper pits and irregular morphologies observed in the atmospheric exposures. While the profilometry combined with the SEM analysis and polarization scans begins to help piece together a better understanding of the corrosion susceptibility of these materials, the underlying pit morphology and extent of attack is still not fully captured in any of these previously described analyses. Therefore, in FY22, SEM images of the cross-sections of the corrosion damage were acquired along with HREBSD. From the HREBSD data collected, dislocation densities and localized strain maps will be developed in in FY23. These will help to inform the extent and potential influence of the surface finish on the resultant pit geometry. Initial examples of cross-sectional images with corresponding dislocation density maps are presented in Figure 54 and Figure 55.

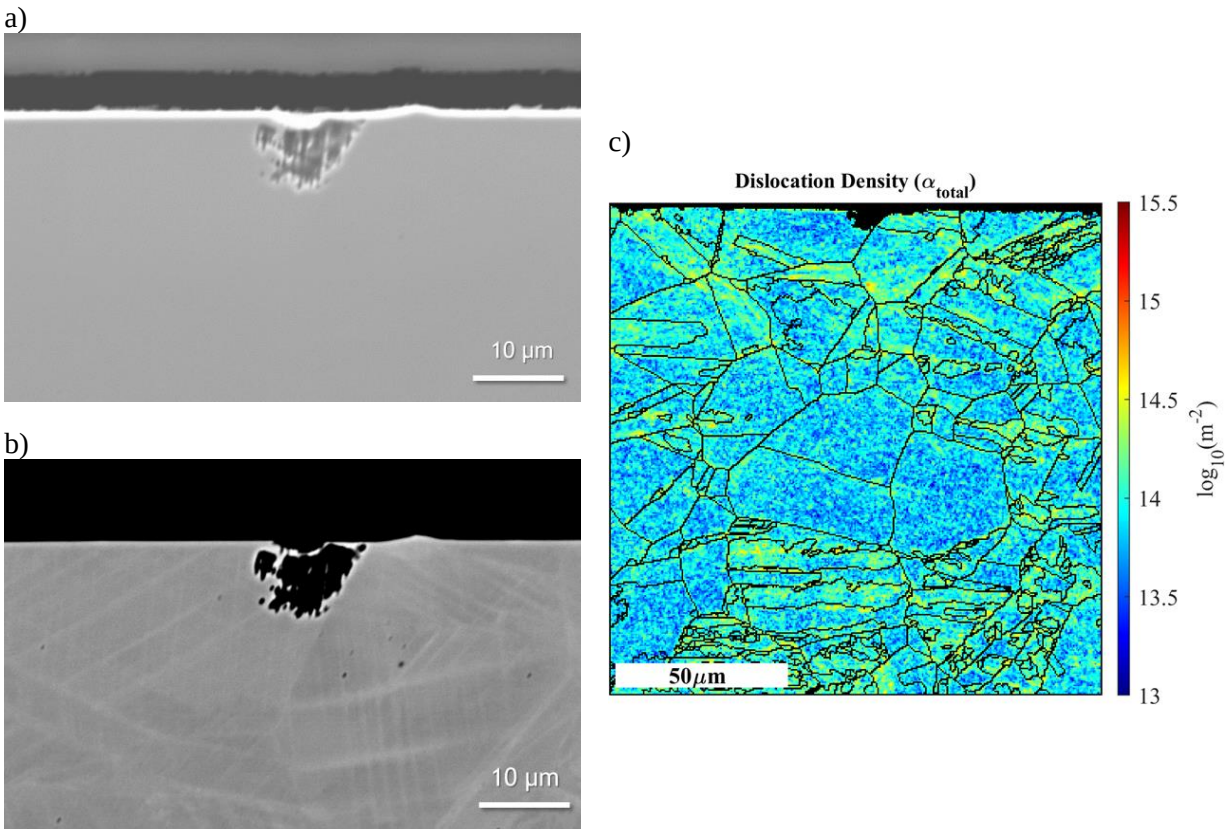

Figure 54. Example cross-sectional images of SS304H #8 mirror finish exposed for 1 month under diurnal cyclic conditions; a) SEM SE image, b) SEM BSE image, and c) corresponding dislocation density developed from HREBSD mapping.

Figure 54 displays both SE and BSE SEM images of a cross-sectioned pit in SS304H polished to a #8 mirror surface finish formed after one month of exposure in cyclic diurnal conditions. In the SE image, some cross-hatching can be observed in the pit itself, with the BSE image indicating the presence of some undercutting. The cross-hatching also appears to align with potential deformation twins formed in the material. Additionally, a dislocation density map was developed from HREBSD data collected at the same locations. While there are grains and grain boundaries that appear to exhibit slightly increased dislocation densities, there appears to be no influence of the surface finishing or materials processing on the distribution of dislocations present, rather there is a random distribution. Additionally, there does not appear to be a correlation between the pit formed and the dislocation density. However, it is important to note that this is one singular cross-section example for one corrosion defect.

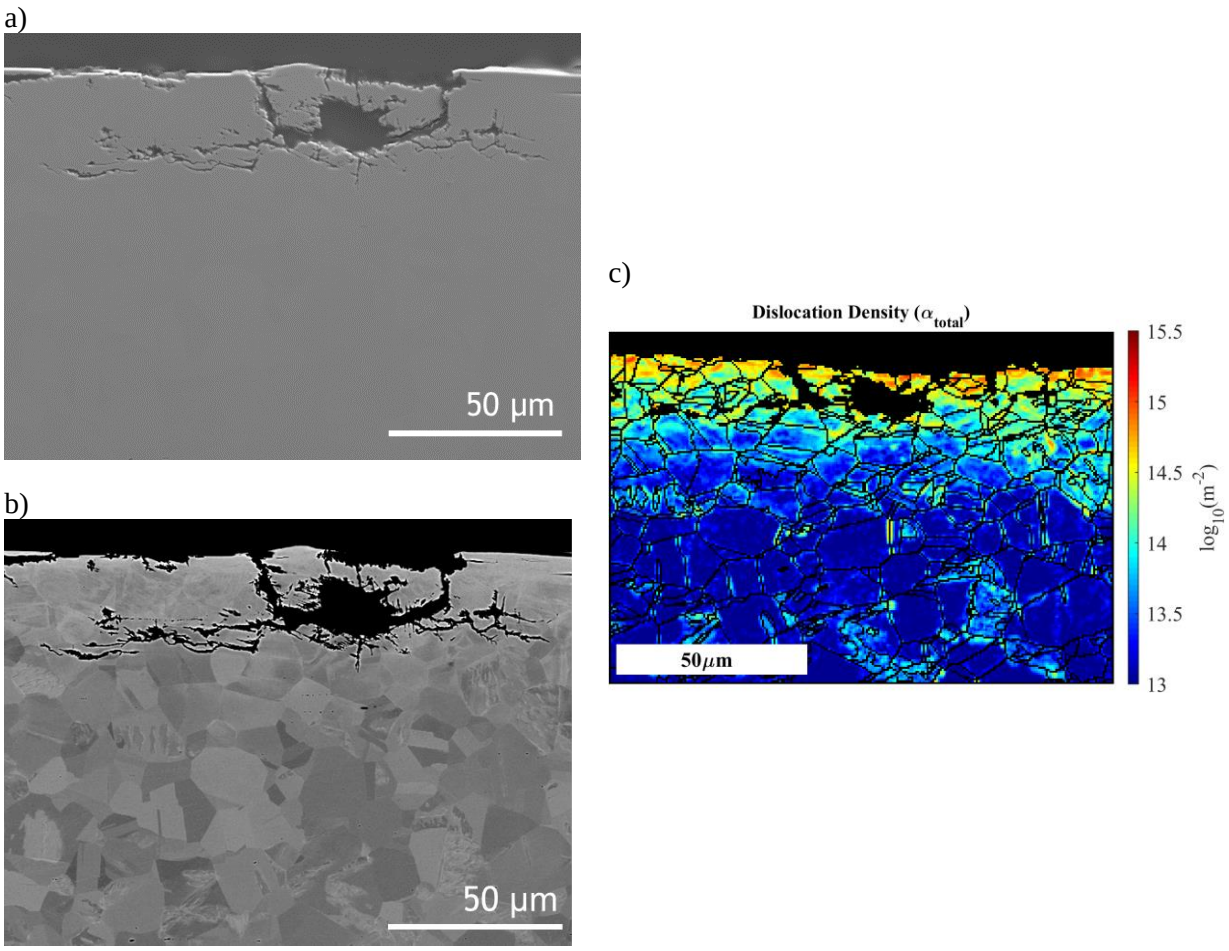

Figure 55. Example cross-sectional images of SS304 #4 rough finish exposed for 1 month under diurnal cyclic conditions; a) SEM SE image, b) SEM BSE image, and c) corresponding dislocation density developed from HREBSD mapping.

Figure 55 presents similar SEM SE and BSE images for a corrosion pit formed in SS304 after one month of diurnal cyclic atmospheric exposure. In this case, the morphology of the pit walls in the SE image is not perceptible, likely indicating that the pit diameter (or depth into the plane of the image) is fairly large, at least comparable to the radius observed in cross-section. The pit is very irregular in morphology with extensive undercutting and many fissure/microcrack like formations. However, the pit does appear to stall, or end, at about a depth of 20-25 µm. When these images are compared to the dislocation density map corresponding to this region in Figure 55-c, the pit growth, or maximum depth, appears to correlate with the region of highest dislocation density. Unlike the map measured for the mirror surface finish, for the rough surface finish, there exists a strong correlation of dislocation density with the near surface region, likely due to the high residual stress and strain formed during mechanical polishing. Additionally, this cross-section may be an indication that dislocation density plays a governing role in pit formation and depth of corrosion attack. Further studies will need to be carried out as this again, only represents one singular cross-section through one corrosion pit, and may not fully characterize the general influences on the corrosion attack observed across these surfaces.

In general, with respect to the influence of cyclic diurnal conditions as compared to static atmospheric exposure conditions, some observations can be made, however, definitive comparisons are difficult as profilometry applied to analyze each exposure was performed on different instruments. In comparison to

previous datasets, it appears that the cyclic conditions resulted in slightly deeper corrosion pits for the SS304H coupons as compared to static exposures at 40% RH and 35 ºC as reported in the FY21 report [47]. However, as the damage depths were only on the order of a 5-10 µm increase in depth, this needs further analysis to determine if it is due to the environmental exposure or difference in profilometer. In FY23, with the complete dataset out to 2 years of exposure, this will be explored further.

In FY22, the development of qualitative SEM analysis combined with electrochemistry and cross-sectional images with HREBSD for dislocation density maps, has helped to elucidate additional influential variables for corrosion damage and morphology. Initial observations have shown that a combined influence of brine composition, material surface finish, and material composition govern the pit morphology, with rougher surface, $MgCl_2$ dominated brines, and less corrosion resistant SS resulting in more irregular shaped pits with microcracking. In environments with brines that are dominated by NaCl, reduced surface roughness (and residual stresses), and more passive SS, the pit morphologies become more hemispherical with crystallographic attack. As the cyclic exposure coupon matrix is completed and removed from the exposure chambers (early FY23), increased datasets will be collected out to two years of exposure. Coupons will be examined across all material types and surface roughness and general trends from profilometry will continue to be compared to the qualitative SEM analysis and electrochemical data. FY23 will continue the development of these improved analytical techniques to enhance the understanding of the quantitative measurements of pitting statistics across these exposure samples as well as identify key influential variables. The cross-sectional SEM and HREBSD will be further explored to develop localized strain maps. These strain maps, combined with the information gained from dislocation density mapping, will help determine governing factors for pit morphology and potential roles they might play in exacerbating or controlling corrosion damage.

3.1.3.2 Impact of Inert Dust on Corrosion

As discussed in FY20 and 21, inert dust present on the SNF canisters may impact how the brine interacts with the canister surface as well as the form and severity of subsequent corrosion damage. In FY21, tests were initiated co-depositing quartz dust with artificial seawater (ASW) on SS304 coupons and in FY22 atmospheric corrosion tests were carried out. Two size ranges, a 74 and 5 µm dust, were co-deposited with salt and put in three different atmospheric exposures. The effects on corrosion of each size fraction will be evaluated individually, which will be used to examine coupled effects representing a wide distribution of dust present on the canister surface. Thus far, exposures for 1 and 6 months for SS304 coupons with 74 µm dust and ASW co-deposited have been completed. Longer time frame exposures are underway as well as exposures with ASW and 5 µm dust co-deposited. Initial analyses of resultant corrosion damage will be presented herein.

Experimental Setup and Dust Evaluation

In FY22, SNL continued to develop the test capabilities to deposit dust and ASW on SS coupons and completed coating coupons for corrosion exposure testing as described previously in [40]. The finalized matrix for exposures is detailed in Table 14. Exposures include two static atmospheric environments, comparable to those from previous corrosion tests [27], except at an elevated temperature (50 ºC), and the diurnal cyclic condition as described in the previous section. While all exposures were initiated in FY22, to date, only samples for the 1 and 6-month exposures of 75 µm dust co-deposited with ASW have been completed. Initial analysis of samples is underway and is presented below.

Table 14. Exposure matrix for samples being analyzed for the impact of the presence of dust under static exposure conditions.

304 Coupon Size, in.	Condition	Dust Deposited (300 µg/cm² ASW)	Total Sample Count	1 m	6 m	12 m	24 m
8x8	75% RH 50°C	SIL-CO-SIL® 75	2	1	0	1	0
		MIN-U-SIL® 5	2	1	0	1	0
		No Dust	1	0	0	1	0
	40% RH 50°C	SIL-CO-SIL® 75	0	0	0	0	0
		MIN-U-SIL® 5	2	1	0	1	0
		No Dust	1	0	0	1	0
4x4	75% RH 50°C	SIL-CO-SIL® 75	5	1	1	1	2
		MIN-U-SIL® 5	7	2	2	2	1
		No Dust	2	1	0	1	0
	40% RH 50°C	SIL-CO-SIL® 75	0	0	0	0	0
		MIN-U-SIL® 5	7	2	2	2	1
		No Dust	2	1	0	1	0
	Cyclic	SIL-CO-SIL® 75	0	0	0	0	0
		MIN-U-SIL® 5	4	1	1	1	1
		No Dust	1	0	0	1	0
2x2	75% RH 50°C	SIL-CO-SIL® 75	5	1	1	2	1
		MIN-U-SIL® 5	8	2	2	2	2
		No Dust	4	1	1	1	1
	40% RH 50°C	SIL-CO-SIL® 75	8	2	2	2	2
		MIN-U-SIL® 5	8	2	2	2	2
		No Dust	4	1	1	1	1
	Cyclic	SIL-CO-SIL® 75	5	1	1	2	1
		MIN-U-SIL® 5	8	2	2	2	2
		No Dust	4	1	1	1	1
2x1	75% RH 50°C	SIL-CO-SIL® 75	6	1	2	2	1
		MIN-U-SIL® 5	8	2	2	2	2
		No Dust	4	1	1	1	1
	40% RH 50°C	SIL-CO-SIL® 75	11	2	3	3	3
		MIN-U-SIL® 5	11	2	3	3	3
		No Dust	4	1	1	1	1
	Cyclic	SIL-CO-SIL® 75	5	1	2	2	1
		MIN-U-SIL® 5	8	2	2	2	2
		No Dust	4	1	1	1	1

Dust Exposure Analysis

To date in FY22, samples exposed with ASW co-deposited with 75 µm dust have been completed for the 1 and 6-month static and cyclic exposures. An example comparison of the resultant corrosion product morphology with the dust and ASW present on the SS304 coupon surface is shown in Figure 56. It was hypothesized that the dust particles may lead to spreading of the brine due to capillary action. In the SEM images, brine spreading, or droplet formation extending beyond the salt particles, is only apparent for the 75% RH exposure condition, under which higher volumes of brine will deliquesce. This is even more evident when viewed at higher magnification, as seen in Figure 57. Residual salts and corrosion product appear to form rings around larger particles, indicating the presence of larger volume salt droplets on the surfaces. Again, this only occurs at the 75% RH exposure condition and is not visible at the lower RH.

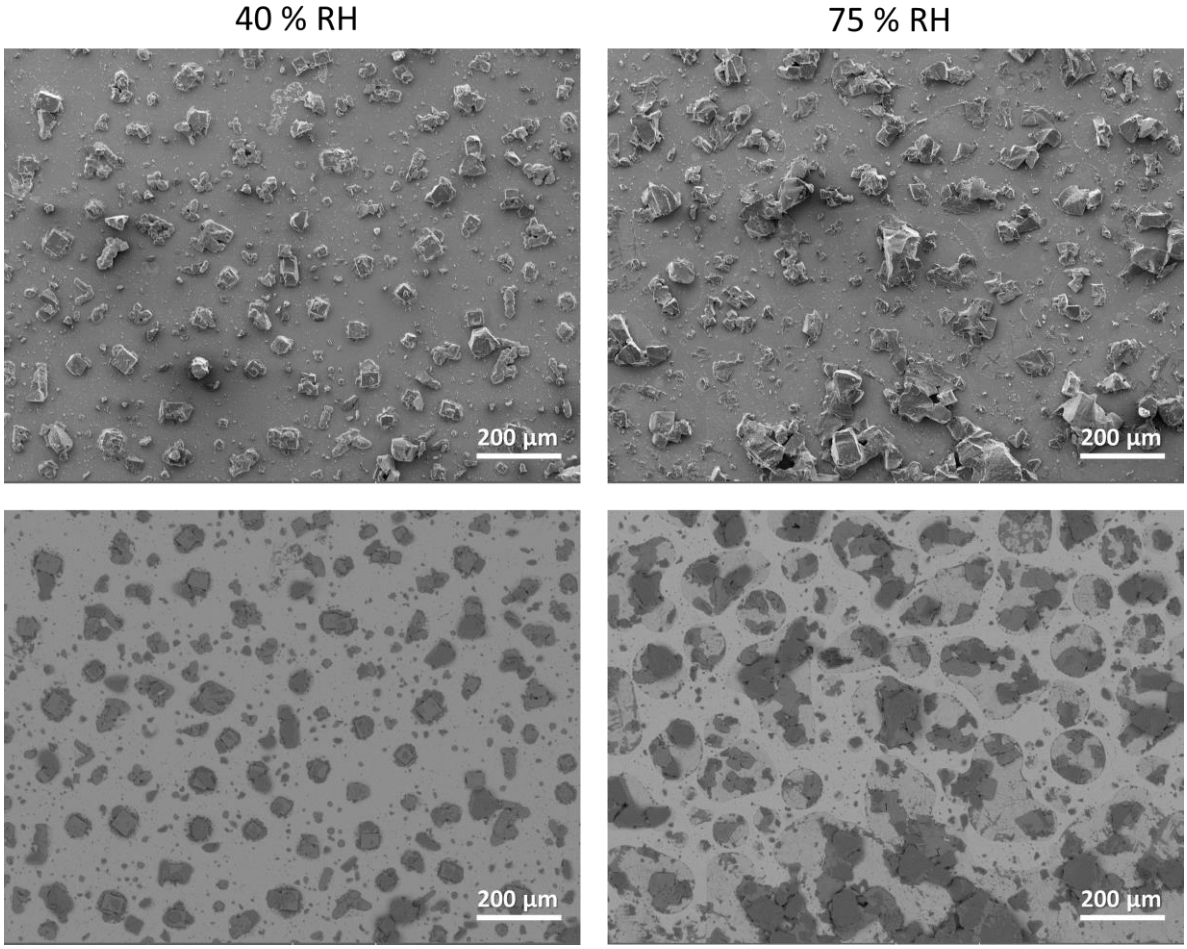

Figure 56. Example images of SS304 coupons post 1-month atmospheric exposure with 300 µg/cm^2 deposited 74 µm dust and ASW at static 40% or 75% RH and 50 ºC. SE SEM in top row with corresponding BSE SEM below. All images taken prior to corrosion product removal.

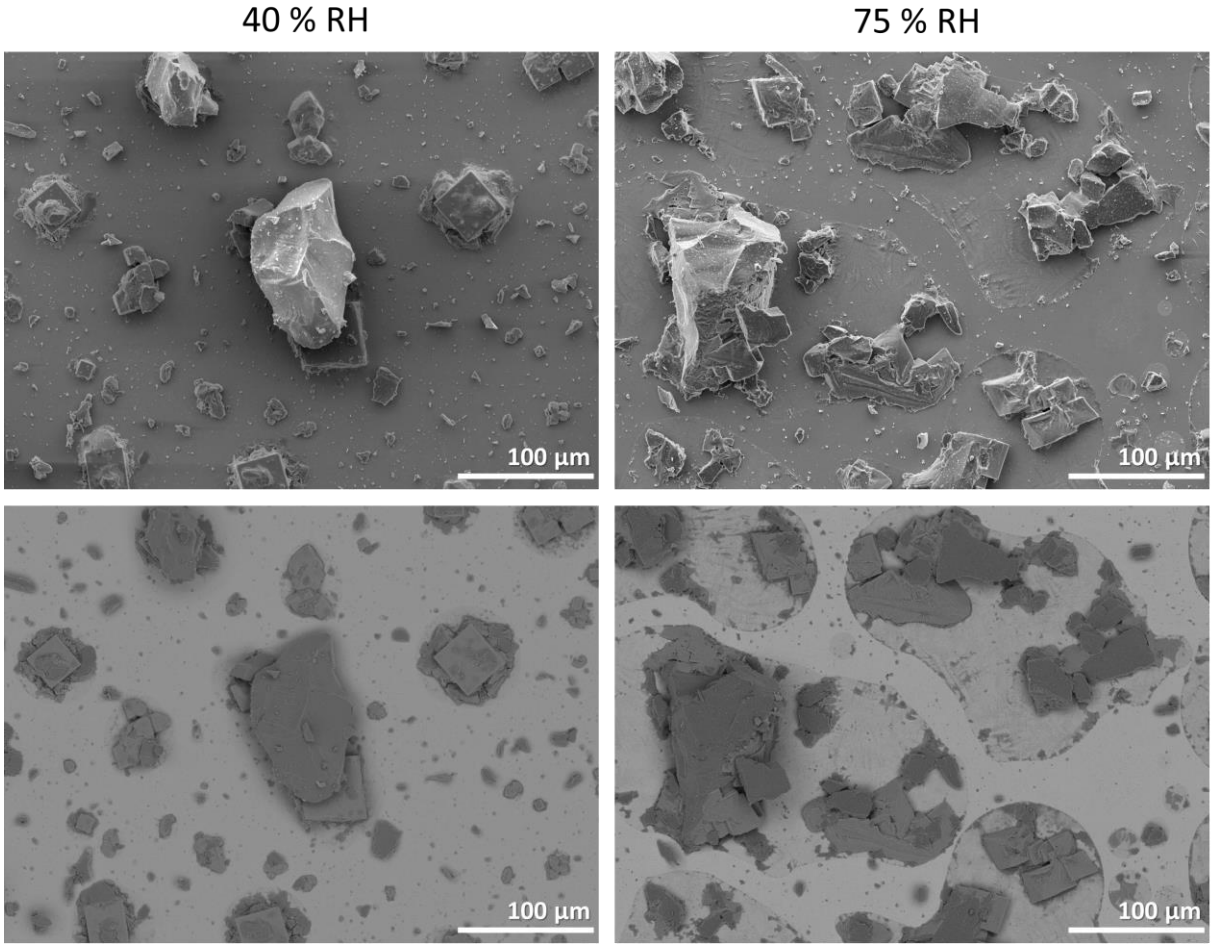

Figure 57. Higher resolution example images of SS304 coupons post 1-month atmospheric exposure with 300 µg/cm^2 deposited 74 µm dust and ASW at static 40% or 75% RH and 50 ºC. SE SEM in top row with corresponding BSE SEM below. All images taken prior to corrosion product removal.

Figure 58 displays SEM images of residual salts and corrosion product on the surface of SS304 coupons exposed for 1 and 6 months under diurnal cyclic conditions with 74 µm dust and ASW. Similar to the static low RH exposures, these coupons do not display droplet rings or droplet spreading around the particles or salt on the surfaces even throughout the extended 6-month time period of exposure. As this diurnal cycle does not exceed 50% RH, the NaCl present would not be expected to fully deliquesce during exposure, thus brine volumes would remain low, and spreading or formation of larger droplets is not fully expected. Additionally, large differences in the salt distribution or corrosion product development do not appear to occur, at least at the observed resolution, between the 1- and 6-month exposure.

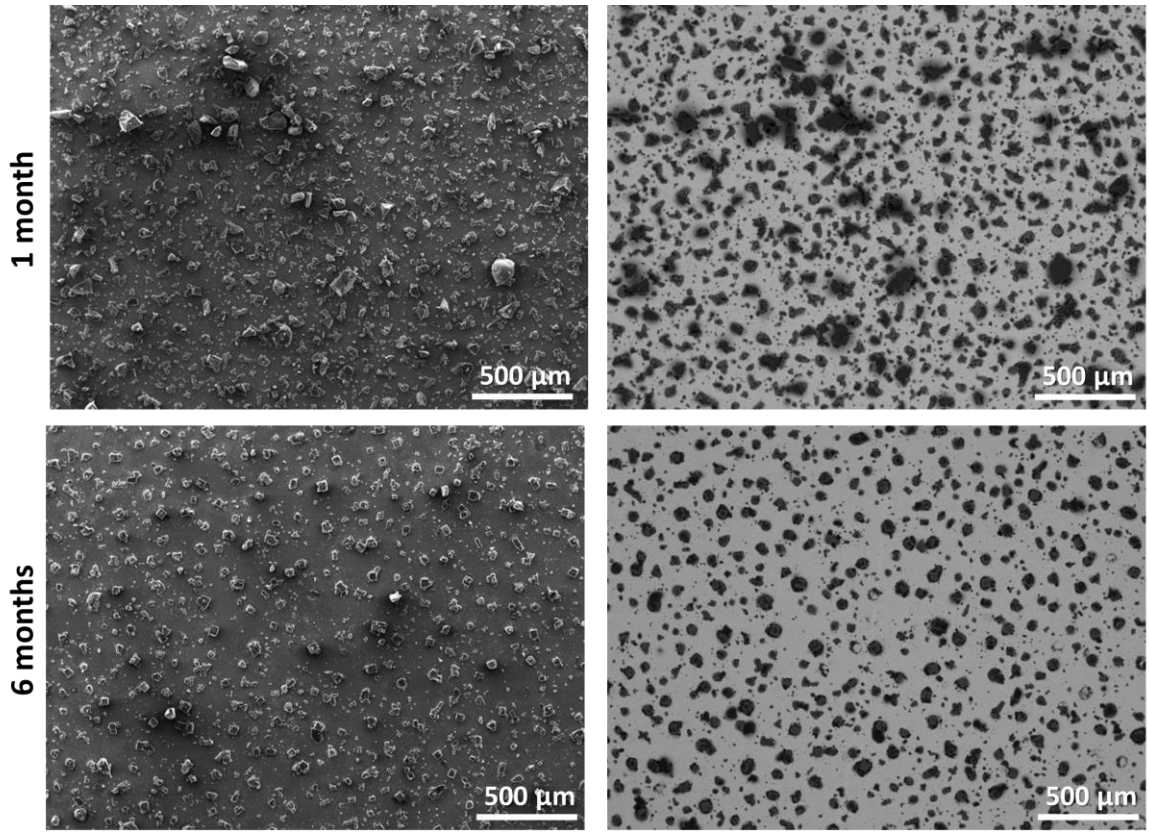

Figure 58. Example images of SS304 coupons post 1 and 6-month atmospheric exposure with 300 µg/cm^2 deposited 74 µm dust and ASW under cyclic conditions. SE SEM in left column with corresponding BSE SEM to the right. All images taken prior to corrosion product removal.

Further examination of these coupons will be carried out in FY23 to better understand the relationship between the combined dust and ASW deposition on the electrolyte brine morphology and spreading across the surface. Coupons with 5 µm dust and ASW will be examined, which may influence spreading or capillary action differently than these larger sized particles. Finally, correlation of the corrosion product, salt, and electrolyte morphology on the surfaces of these coupons post exposure to the resultant corrosion damage will be analyzed. Initial images of some notable corrosion features are presented below.

Samples exposed for one month in the static 75% RH and 50 ^{o}C conditions with 74 µm dust and ASW are presented in Figure 59. Example corrosion features are identified and displayed both with the corrosion product and post-corrosion product removal to show the underlying damage. While the features are much larger than those observed in general for previous static exposures [29, 53], they continue to exhibit a similar pit morphology as those formed at high RH brines. The pits are more hemispherical in nature with faceted crystallographic attack, characteristic of pits previously observed in NaCl dominant brines.

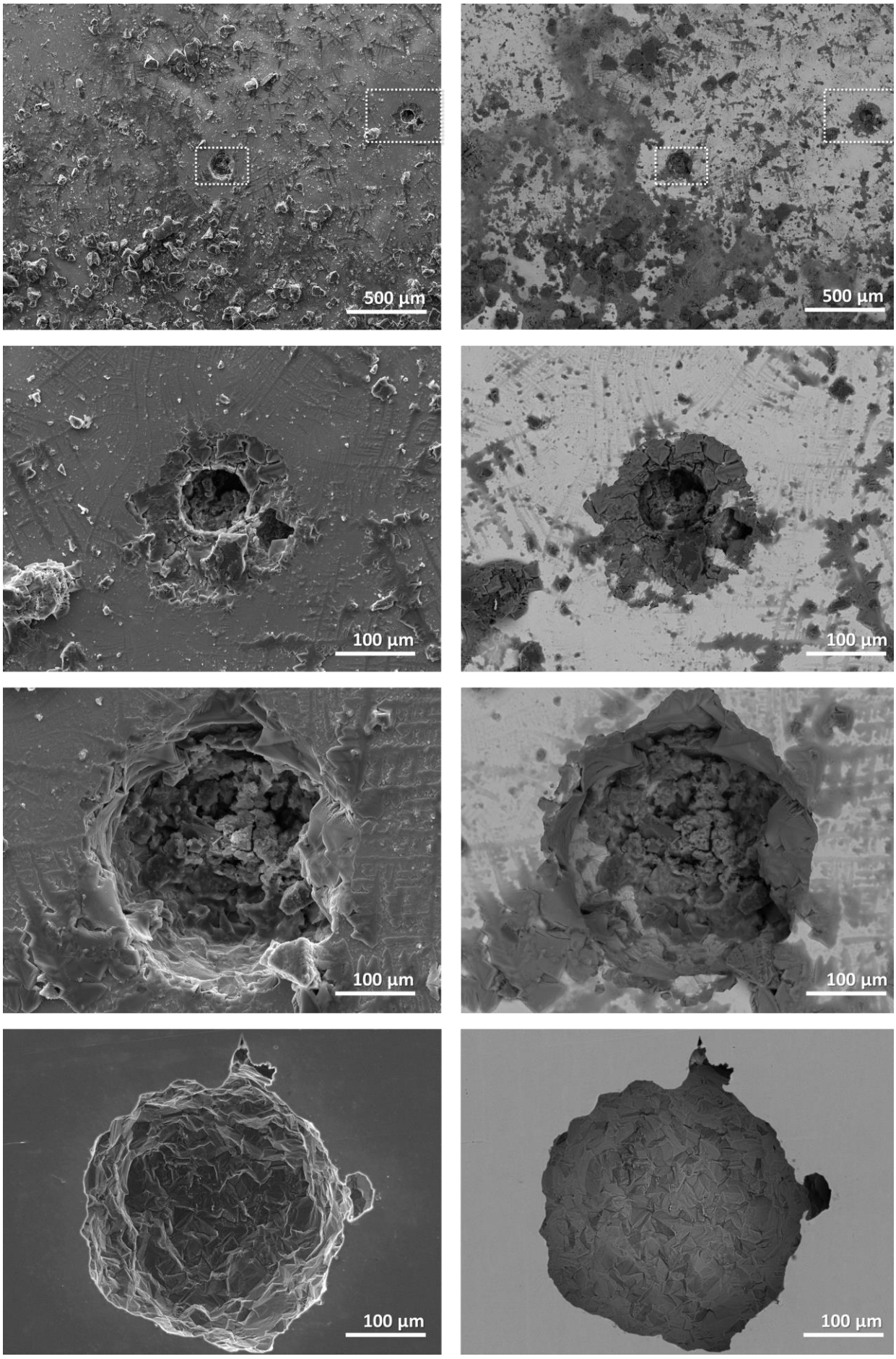
500 µm
500 µm
100 µm
100 µm
100 µm
100 µm
100 µm
100 µm

Figure 59. Example pits observed on the SS304 coupons post 1-month atmospheric exposure with 300 µg/cm^2 deposited 74 µm dust and ASW at static 75% RH and 50 ºC. SE SEM images to the left with corresponding BSE SEM to the right. All images taken prior to corrosion product removal except the last row.

While further and continued analysis needs to be carried out on the inert dust and ASW coupon exposures, some initial inferences can be made from the results thus far. It appears that at least for the 1- and 6-month exposures, the larger dust particles (75 µm) do not play a role in spreading electrolyte on the surface for the lower RH or cyclic exposures. For coupons exposed at higher RH, larger droplet or electrolyte spreading can be observed, however this needs further comparison against the coupons exposed without dust to fully understand the role of the 75 µm particles in potentially affecting electrolyte distribution. Additionally, very preliminary corrosion observations have maintained that characteristic pit morphologies form under the higher RH exposures, even in the presence of dust. However, these pits appear to be much larger in size than those previously observed. Further analysis with increased quantitative pitting statistics is necessary (to be carried out in FY23) to better understand the relationship between pit size, morphology, and the various exposure environments.

3.1.3.3 Effect of Nitrate and Other Anionic Components

Realistic near-marine brine chemistries are not solely sea-salts brine. As reported previously, significant amounts of nitrate and sulfate are present, both from particle/gas conversion reactions with atmospheric gases, and because of the presence of a significant component of continental salts, which are enriched in these species [27]. The actual brines that will be present on the canister surfaces will vary with the exposure RH, thus nitrate to chloride ratios within a brine will vary. Work in FY22 sought to further examine the influence of the NaCl/$NaNO_3$ ratio on the corrosion response of SS304 through both electrochemical testing and atmospheric exposures.

Initial Nitrate Exposure Analysis

Polarization scans of SS304 (same material as previously examined in the above sections with the 600 grit hand ground surface) were carried out in various chloride containing solutions to understand the potential for nitrates to inhibit pitting initiation. Samples were allowed to equilibrate in a 3-electrode cell for a 24-hour open circuit potential (OCP), followed by linear sweep voltammetry from -0.2 V vs. OCP, to roughly 1.2 $V_{Ag/AgCl}$, at a scan rate of 0.167 mV/s unless otherwise specified. The effect of varying nitrate:chloride ratios is presented in Figure 60 at 40 ˚C. It is noted that the chloride concentration is constant at 4.3 m NaCl. A breakdown potential of 0.2 $V_{Ag/AgCl}$ is measured for nitrate:chloride ratios of 1:9 and lower. A ratio of 1:4 and higher exhibited passive behavior until roughly 1 $V_{Ag/AgCl}$.

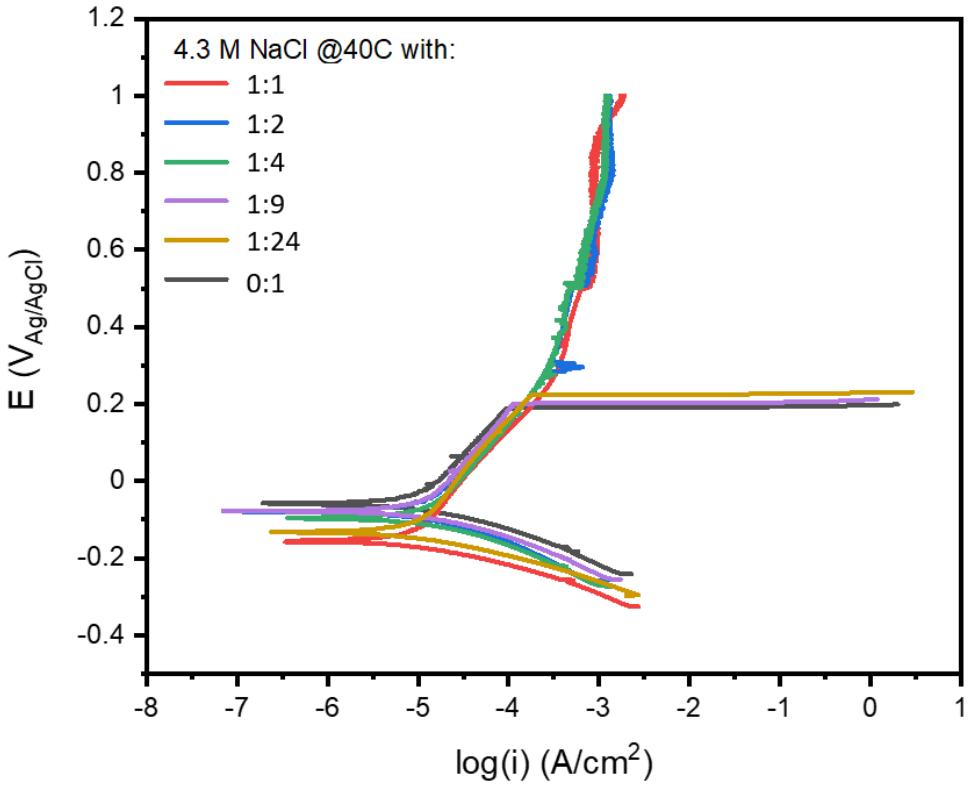

Figure 60: Polarization scans exploring the influence of varying nitrate:chloride ratios at 40 ˚C in 4.3 m NaCl.

As shown Figure 60-a, an SS304 alloy exhibits passive behavior in 4.3 m NaCl with a 1:4 ratio of $NaNO_3$ at 60 ˚C until transpassive dissolution is reached at roughly 1 $V_{Ag/AgCl}$ for a scan rate of 0.1667 mV/s. However, once this scan rate is slowed, to either 0.084 or 0.042 mV/s, this behavior becomes stochastic, and breakdown can occur at a lower potential (roughly 0.1 to 0.4 $V_{Ag/AgCl}$). This is in contrast to the 1:1 ratio of $NaNO_3$ shown in Figure 61-b, which does not display any breakdown behavior. This was shown for two different scan rates (0.167 and 0.042 mV/s) indicating a strong effect of $NaNO_3$ inhibiting potential for corrosion initiation under these higher concentration conditions. The influence of temperature on the inhibiting nature of nitrates was also examined in Figure 61-b & d. For both 4.3 m NaCl with a 1:4 or 1:1 ratio of $NaNO_3$ at 40 ˚C, inhibiting behavior was observed. However, when the temperature was increased by just 10 degrees to 50 ºC for the 1:4 ratio, the behavior again became stochastic and breakdown occurred. For the 1:1 ratio, even at 60 ºC, the nitrates continued to display inhibiting behavior.

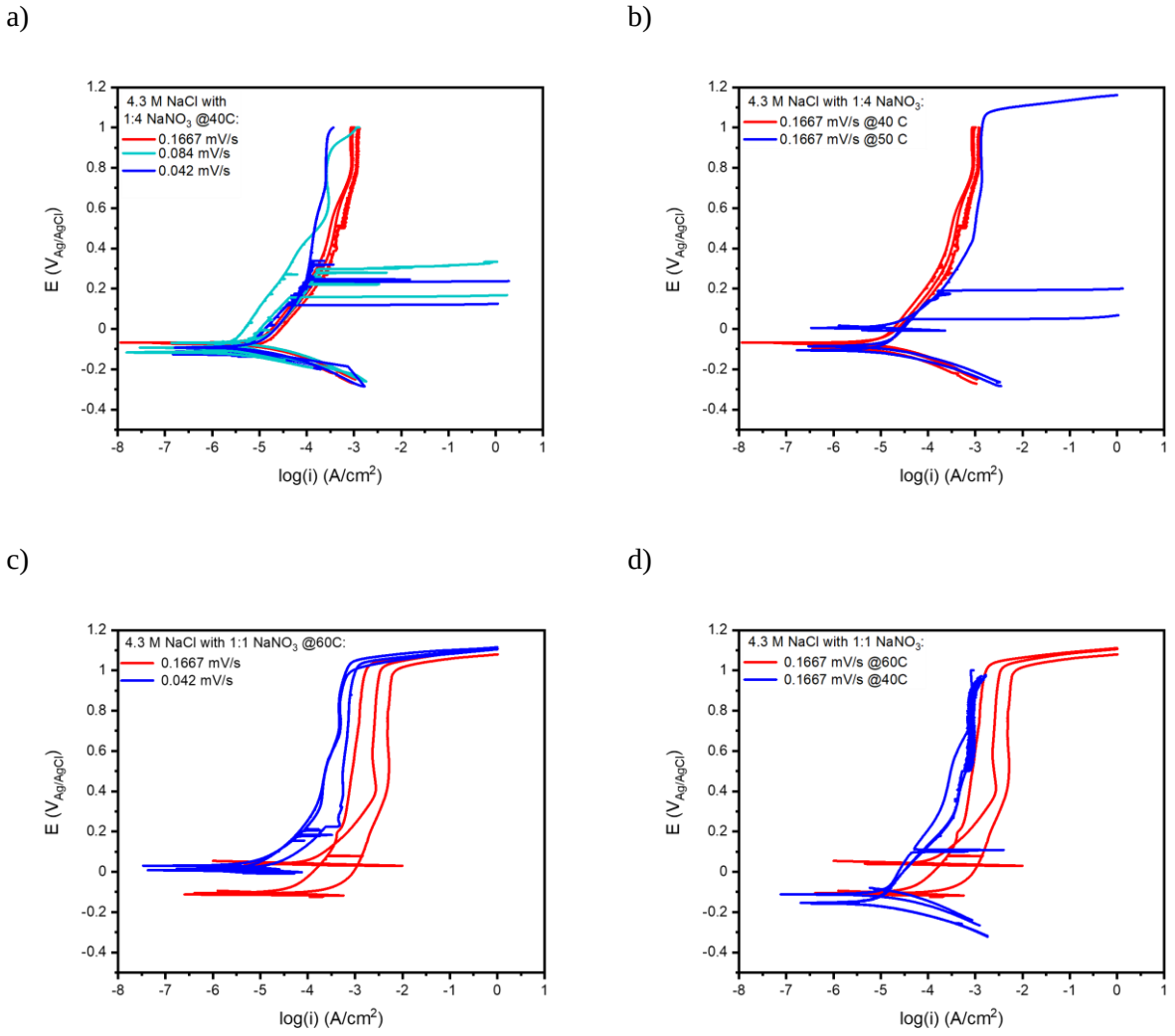

Figure 61: Polarization scans of SS304 in 4.3 m NaCl with 1:4 nitrate:chloride ratio at (a) 60 ˚C at three different scan rates and (b) comparison of 40 and 50 ˚C, and 1:1 nitrate:chloride ratio at (a) 60 ˚C at two different scan rates and (b) comparison of 40 and 60 ˚C.

Polarization scans were presented in Figure 60 and Figure 61 for SS304 in various nitrate:chloride ratios and indicate a dependence of the inhibiting behavior on the nitrate ratio, scan rate, and temperature. However, the inhibition of corrosion was found for 1:1 nitrate:chloride brines up to 60 ˚C at a scan rate of 0.1667 mV/s. That is, under the static bulk solution compositions explored in the polarization scans, it would be suggested that nitrates have a significant influence on the initiation of corrosion.

To further explore the influence of nitrates under more relevant SNF conditions, atmospheric exposures were developed. The efficacy of nitrates on the corrosion behavior of SS304 (composition presented in Table 12) under droplets with cycling RH conditions and constant temperature (35 ˚C) was evaluated. The RH profile for the exposure (Figure 62) consisted of a starting RH of 20 %, increasing to 80 % over 6 hours, holding for 6 hours, decreasing from 80 to 20 % RH over 6 hours and then a hold at 20 % RH for 6 hours. Thus, the total cycle time for the droplet testing was 24 hours. This cycle was repeated 7 times and, therefore, exposures were carried out for a week. While this does not fully represent a diurnal cycle observed at a real world SNF ISFSI, it helps to elucidate influences of significant environmental variables present under these conditions. Both the composition of the droplet (chloride concentration and

nitrate:chloride ratio) and droplet size were varied and are presented in Table 15. No more than six droplets were placed on a coupon and were arranged as shown in Figure 63-a. After testing, samples were immediately placed into a desiccator. Samples were then optically imaged with salt on the surface as presented in Figure 63-a. Optical imaging helps obtain information regarding salt spreading present during the cyclic RH profile. Samples were cleaned by sonicating in water and methanol for 15 min. each. After cleaning, samples were optically imaged again (Figure 63-b). It is evident that corrosion occurred under some of the droplets due to the presence of rust on the surface of the alloy, as highlighted in Figure 63-c and d. After optical imaging, samples were imaged in the SEM for the identification of corrosion features. In FY23, this work will be extended to look at the size of the corrosion damage through profilometry measurements.

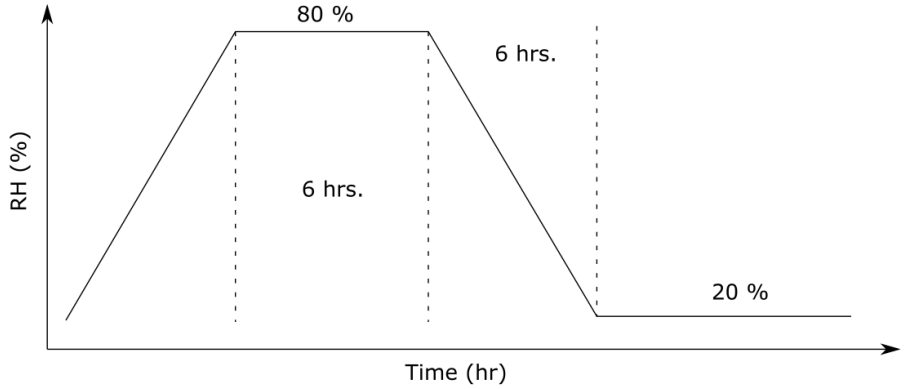

Figure 62: RH profile utilized for nitrate testing of SS304 nitrate droplets.

Table 15: Exposure matrix for testing the efficacy of nitrates as corrosion inhibitors.

Droplet composition	Nitrate : Chloride	Droplet Sizes (µL)
4.3 m NaCl	2:1, 1:1, 1:2, 1:4, 1:9, 0:1	4
4.3 m NaCl	1:1	1, 2, 3, 4
2.15 m NaCl	2:1, 1:1, 0:1	1, 2, 3, 4
1.075 m NaCl	4:1, 1:1, 1:2, 1:4, 1:9	4
1.075 m NaCl	1:1	1, 2, 3, 4
2.15 m $MgCl_2$	0:1	4

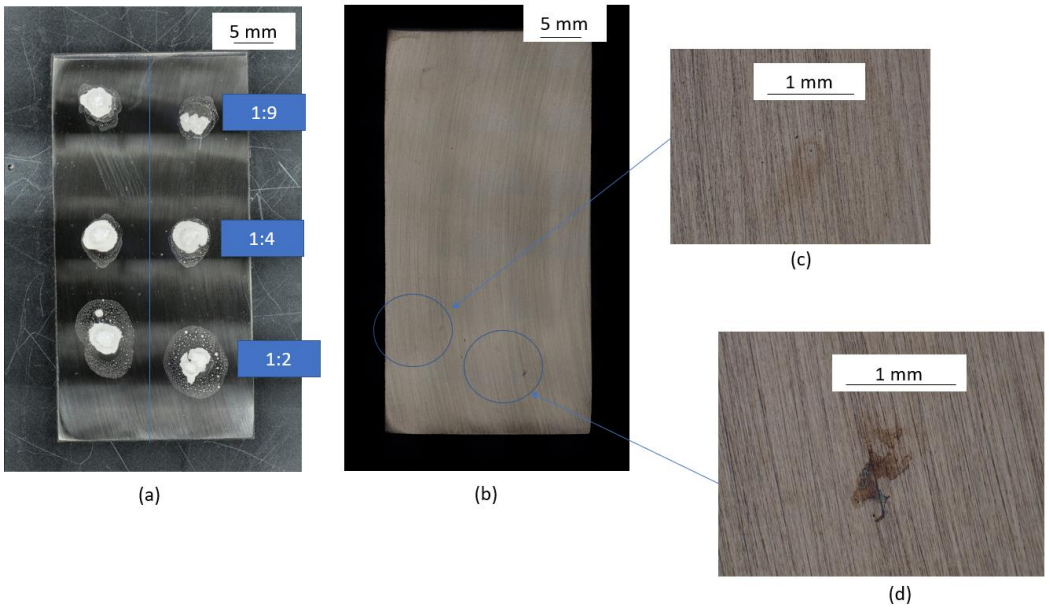

Figure 63: Exposure of SS304 under droplets to 4.3 m NaCl with varying droplet compositions of Nitrate:Chloride ratios (NO_3:Cl). (a) Salt distributions after exposure to the RH cycle in Figure 62. (b) Optical imaging after salt cleaning. (c) and (d) represent optical images of rust spots observed in (b).

The influence of droplet size was investigated for 4.3 m NaCl with a ratio of 1:1 nitrate:chloride and SEM images of localized corrosion are presented in Figure 64. A 3 µL droplet is shown in Figure 64-a displaying three pits present on the surface and Figure 64-b shows a detailed view of the two pits denoted in (a). The top pit appears to be roughly hemispherical while the bottom pit appears to be elongated in nature and roughly 10 µm in length. It is unknown at this time if there is significant undercutting in the pit and whether these two pits are connected under the surface. In Figure 64-c, the droplet size was reduced to 2 µL and contained fewer pits on the surface as well as generally smaller corrosion features. Although not shown here, pits were also observed under a 1 µL droplet. Therefore, for the 4.3 m NaCl droplets, pits were observed in all droplet sizes examined for the ratio of 1:1 (nitrate:chloride). This corrosion formation is not evident from the static polarization scan measurements in Figure 61 as both 40 and 60 ˚C scans indicated passive behavior. Thus, under the cyclic RH conditions (Figure 62), the passivating nature of nitrate is reduced. However, as this cycle alters both the brine volume and brine composition as the RH changes, and additionally, as precipitates may form, this does not necessarily contradict the full immersion experiments, but highlights the need to better understand the dynamic nature of the electrolyte and the resultant corrosion response under atmospheric conditions.

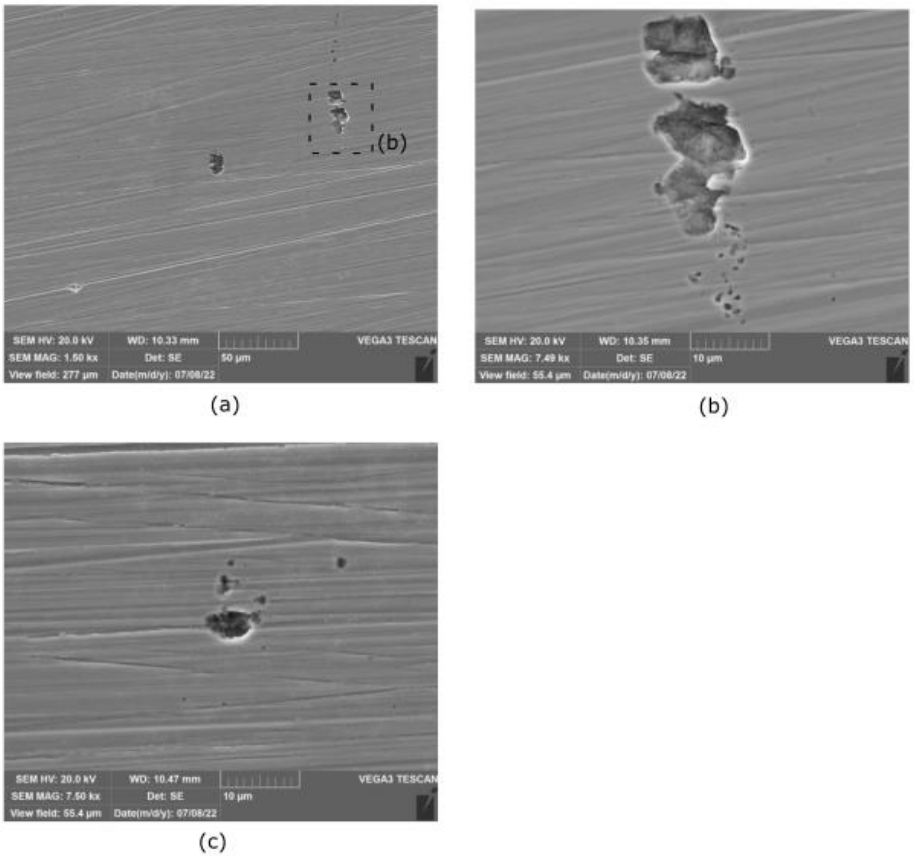

Figure 64: SS304 coupon exposed to (a) 4.3 m NaCl (1:1 NO_3:Cl; 3 µL) under the relative humidity cycle presented in Figure 62. (b) Detailed view of pits noted in (a). (c) Pit observed after exposure to 4.3 m NaCl (1:1 NO_3:Cl; 2 µL).

As presented in Figure 65, a fairly large pit was observed after SS304L was exposed to a 4 µL droplet of 2.15 m NaCl droplet with a ratio of 1:1 nitrate:chloride. The pit is roughly 30 µm in length and appears to have crystallographic attack at the base of the pit. Comparing the pits observed in Figure 64 and Figure 65, it is possible that the pits in Figure 64 still contain corrosion product and were not sufficiently cleaned. As such, a limited amount of the test matrix (Table 15) will be presented due to further cleaning being carried out on the coupons.

Finally, SS304 was exposed to 1.075 m NaCl under various nitrate:chloride ratios (Figure 66) and various droplet sizes under a 1:1 nitrate:chloride ratio (Figure 67) and, under all explored conditions, pitting was observed on the surface. It is worth noting that even under a nitrate:chloride ratio of 4:1 (i.e., 4x more nitrate than chloride) that pitting was observed (Figure 66(d)).

Across the atmospheric exposures, the starting ratio of nitrate:chloride was varied along with droplet sizes. The deliquescence RH values for a mixed salt of nitrate and chloride have been previously explored and it is likely that the RH cycle ran caused for wetting and drying of the droplets over the 24-hour period. Localized corrosion was observed in all coupons presented. It is interesting to note that even at a ratio of 4:1 nitrate:chloride in 1.075 m NaCl, pitting was observed (Figure 66-d). This indicates that the passivating effects of nitrate as shown in the polarization scans (Figure 60 and Figure 61) are not representative of the RH cycling to which the coupons were exposed. As previously stated, it is likely that the salt solutions underwent cycles of wetting and drying. As this cycle is carried out, solution

composition (and thus nitrate:chloride) can vary. It is also possible, that similar to seawater solutions [53, 54], NaCl salt crystals precipitated on the alloy surface creating potential crevice formers. These crevices may lead to micro-environments on the surface of the alloy. The composition of the solution underneath the precipitated salt crystal could vary in terms of the concentration and composition from bulk solution composition. If more aggressive conditions were present underneath the precipitated crystal, than it is possible that initiation could occur and pits could subsequently propagate. Therefore, while polarization scans give a good measure of initiation in static, near constant brine compositions, they are not necessarily representative of pitting under cyclic RH conditions. Further, while significant concentrations of nitrate (i.e., high nitrate:chloride ratios) have been observed on canister surfaces in field studies (Section 2.1), the passivating nature of the nitrates may not be as significant as previously thought, especially under cyclic RH conditions.

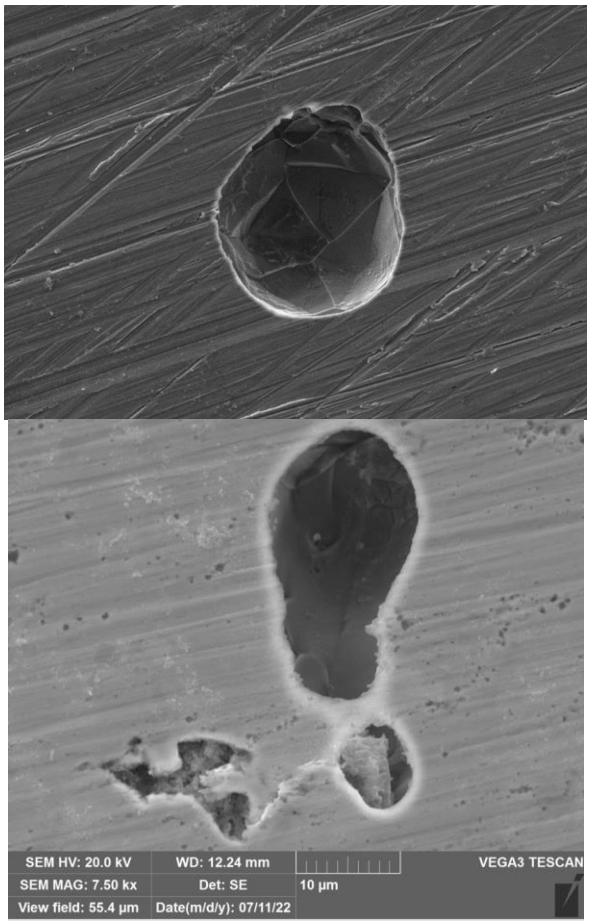

Figure 65: SS304 exposed to a 4 µL droplet of 2.15 m NaCl (upper)) and to 2.15 m NaCl: 2.15 m NaNO3 (lower) at the RH cycle presented in Figure 62. Note that images are at the same scale.

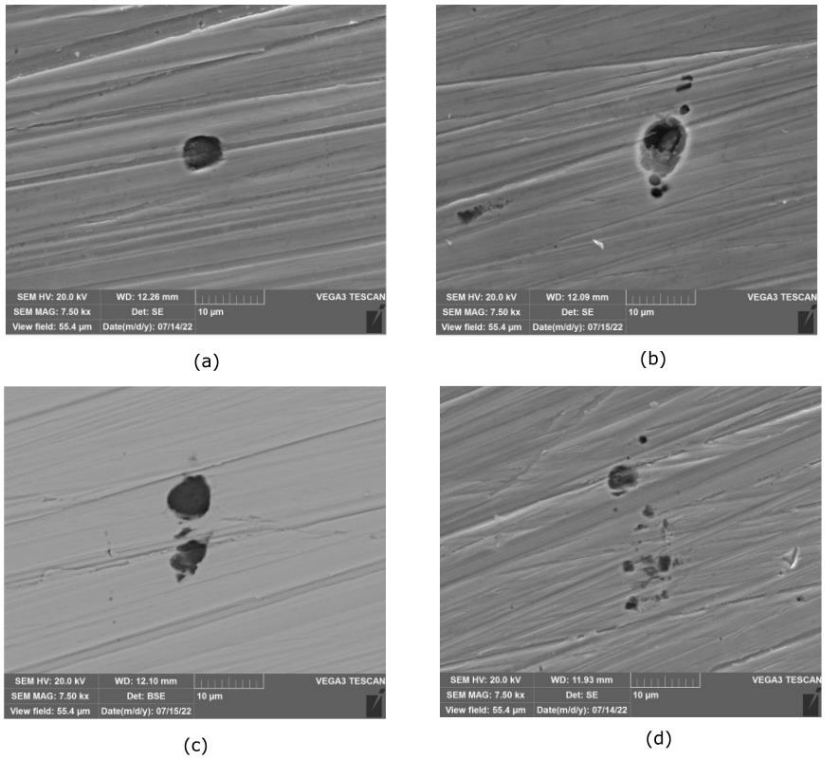

Figure 66: SS304 exposed to the RH cycle in Figure 62 with (a) 1.075 m NaCl (1:2 NO_3:Cl), (b) 1.075 m NaCl (1:1 NO_3:Cl), (c) 1.075 m NaCl (1:1 NO_3:Cl), and (d) 1.075 m NaCl (4:1 NO_3:Cl). All droplets were 4 µL.

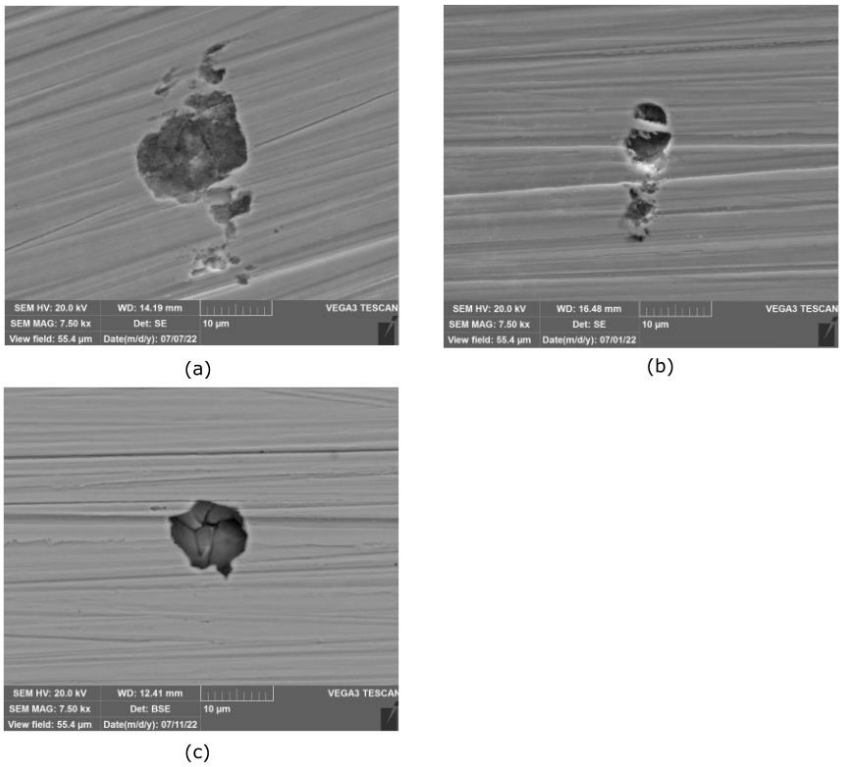

Figure 67: SS304 exposed to the RH cycle in Figure 62 with (a) 1.075 m NaCl (1:1 NO_3:Cl; 4 µL), (b) 1.075 m NaCl (1:1 NO_3:Cl; 3 µL), and (c) 1.075 m NaCl (1:1 NO_3:Cl; 1 µL)

3.2 Pit to Crack Transition

As was discussed in the previous sections, environmental effects, including brine composition, and materials properties, significantly influence the resultant corrosion damage morphology, which may play a role in governing crack initiation. Through an exhaustive study of the literature over the past FY, a review of the current understanding of the pit to crack transition was developed (Appendix C, [14]). This supported similar conclusions to SNL's work, in that a better understanding of environmental and material properties and the specific roles they play in the pit to crack transition needs to be developed. A matrix was made for U-bend testing of these influences on the pit to crack transition and initiated in FY21. The initial studies sought to address hierarchal identification of features controlling pit to crack transitions (environment, material, pit morphology, etc.). It is significant to not only understand canister-relevant material and environmental influences on crack growth rates (which are being heavily studied both by PNNL and SNL), but also on the potential for cracks to initiate. This was established through work started in FY21 and ongoing through FY22 at SNL and initial progress is detailed in the following sections.

3.2.1 Understanding the Influence of Pit Morphology on Crack Initiation

In FY22, an extensive review of the current literature on the pit to crack transition was carried out and developed into a manuscript which is currently under review as an invited critical review in CORROSION Journal (Appendix C, [14]). Key areas were identified as topics where further research is needed to understand the pit to crack transition, including the influence of the exposure environment, specifically in marine conditions. There exists a current lack in understanding of the role of the environment on the pit formation (morphology and size) and how this governs the pit to crack transition.

As it has been shown that the canister surface environment, both from the perspective of the exposure environment as well as the surface properties of the material (roughness, residual stress, etc.), can influence the pitting morphology, a matrix was developed to explore how these properties may also influence the pit to crack transition.

U-bend SS304L samples were exposed and compared to test coupons of the same materials and similar surface finishes under accelerated atmospheric exposure environments relevant to canister conditions. The details of this planned matrix were described in [47], samples were prepared and exposures initiated in FY22. The exposure matrix is presented in Table 16; coupons were exposed under three conditions, diurnal cyclic conditions (as described previously in 3.1.3.1) and two static conditions relevant for SNF ISFSI locations. Samples were exposed for two different time periods at three different surface finishes.

Table 16. U-bend exposure matrix with comparative witness coupons.

Sample	Cyclic		40% RH 35 °C		75% RH 35 °C	
	3 Day	4 week	3 Day	4 week	3 Day	4 week
U bend Machine #4	#4-03	#4-06	#4-01	#4-04	#4-02	#4-05
U-bend Machine #6	#6-03	#6-06	#6-01	#6-04	#6-02	#6-05
U-bend Machine #8	#8-03	#8-06	#8-01	#8-04	#8-02	#8-05
witness #4	x	#4-03	x	#4-01	x	#4-02
witness #6	x	#6-03	x	#6-01	x	#6-02
witness #8	x	#8-03	x	#8-01	x	#8-02

Prior to exposure, U-bend samples were bent according to the ASTM-G30. The maximum principal stress was calculated through finite element method (FEM) modeling for the sample bending procedure and is presented in Figure 68-a. After bending, and prior to atmospheric exposure, samples were deposited with 300 μg/cm^2 of ASW using the SNL nebulizer system depicted in Figure 68-b.

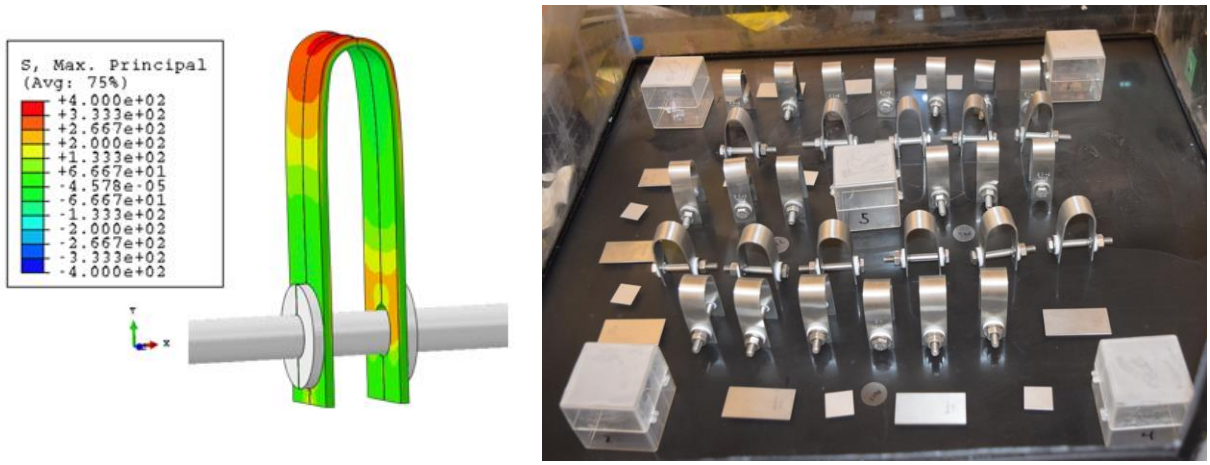

Figure 68. a) Schematic of maximum principle stress in the U-bends as calculated through FEM modeling (sample was assumed to be bent through horizontal displacement as described in the ASTM G30. b) Example of ASW deposition using the SNL nebulizer system.

Post exposure, U-bend samples were characterized first through optical imaging. Samples were imaged in the un-cleaned condition, meaning that any residual salts and corrosion product would still be present on the surface. Overview images are presented in Figure 69 for the three-day exposures. At the scale shown, no significant corrosion damage is observable.

Figure 69. Optical images post 3-day atmospheric exposure of the U-bend samples finished to three different surface finishes.

Example higher resolution images are also shown for the three-day exposures in Figure 70. At higher resolution, localized corrosion was observed across all surface finishes and exposures optically. Samples were cleaned and further imaged through SEM to gain an understanding of the corrosion attack and potential SCC.

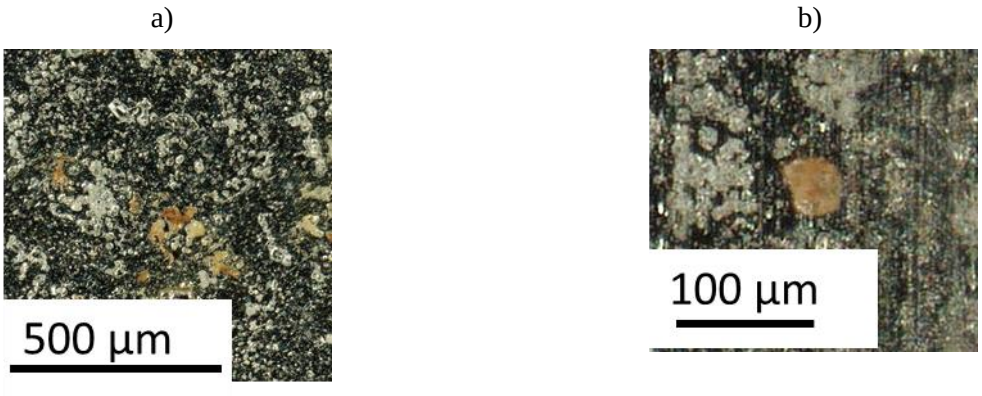

Figure 70. Example higher resolution optical images of post-exposure corrosion damage on a) the #8 surface finish diurnal cyclic exposure and b) the #4 surface finish 75 %RH static exposure.

After optical imaging characterization, samples were cleaned according to the ASTM-G1 procedure. They were sonicated in a 10% by volume nitric acid solution for 30 min, rinsed with DI, and dried with air. Once the corrosion product was removed, corrosion attack morphologies (pits) and potential cracking could be analyzed through SEM. This characterization was initiated in FY22 and is currently underway for all exposed samples, including the witness coupons.

An initial summary of the one-month exposures at 75 %RH static conditions is presented in Figure 71. The top row of this figure represents characteristic corrosion damage observed across the U-bend samples, while the bottom presents crack or crack like features observed through SEM. Pits observed in all samples at this higher RH (NaCl dominated brine) exposure displayed crystallographically-etched surfaces, consistent with previous coupon exposures. In all cases, under these high RH conditions, no cracking or microcracking was observed to originate from or near the pits. However, micro-cracks or crack-like indications were observed across all samples. The morphology and extent of these cracks does appear to correlate with the surface finish, in that those that form on the rougher surfaces appear to have deeper, sharper attack (Figure 71, #4 and #6), whereas the crack like features on the mirror surface (#8) are broader and appear more shallow.

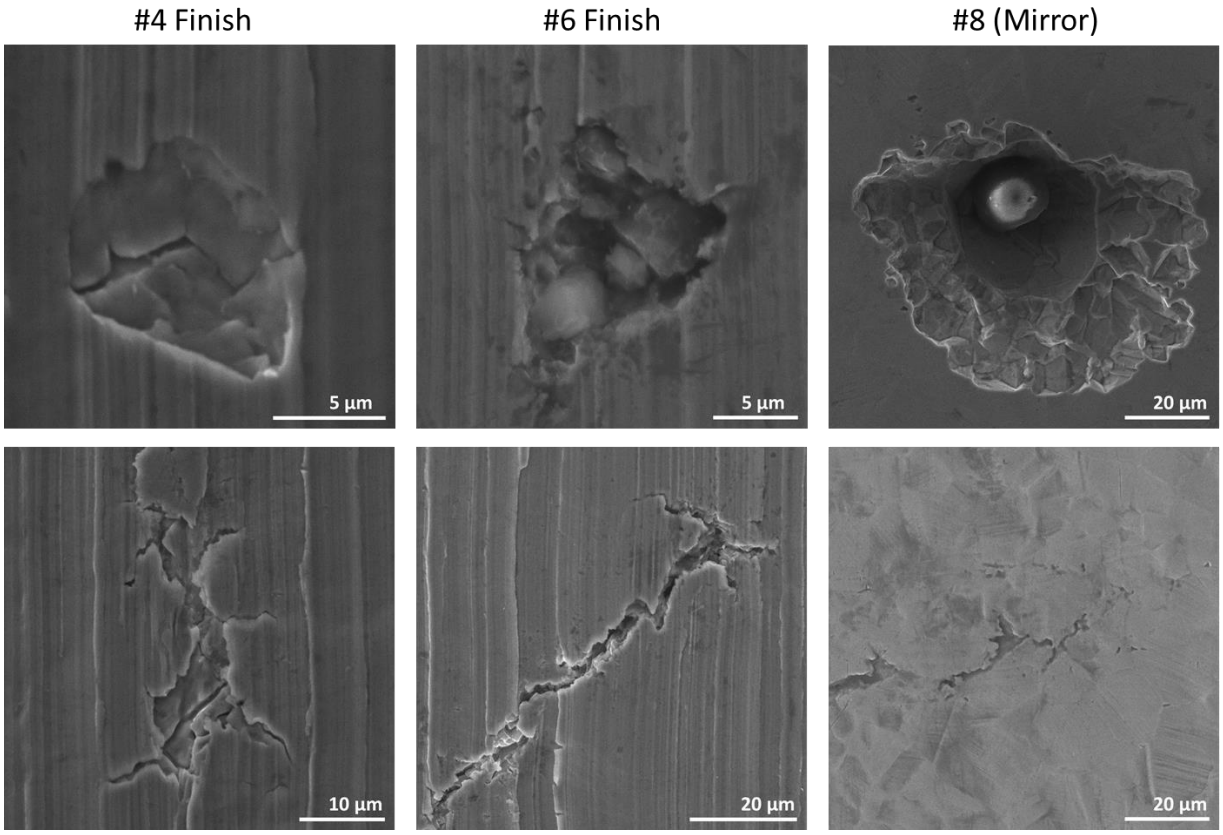

Figure 71. Exemplar pit and surface crack morphologies on SS340 U-bend samples exposed for 1 month at 75% RH, 35 ºC with 300 µg/cm^2 ASW printed on the surface for #4, 6, and 8 surface finishes.

Initial observations of morphology and attack across the U-bend samples are qualitative but provide some insight into the influence or role of surface finish. FY23 will focus to expand this analysis across the whole exposed matrix to gain both a more statistical analysis of the resultant behavior as well as a comparison of the behavior in the various exposure environments. Further investigation may include cross-sectional imaging to gain a better idea of the extent or depth of potential cracking attack beneath the material surface.

3.3 Crack Tip Modeling

In FY21, a crack tip model to determine pertinent electrochemical parameters was developed. In FY22, the model was further enhanced and exercised to aid in determination of similitude between laboratory accelerated testing and real-world cracks to enhance overall CISCC prediction. Crack tip electrochemical conditions were explored utilizing a reactive transport FEM (as detailed in [40]). In FY22, with additional support from a late start Laboratory Directed Research and Development project (with Ryan Katona as PI), the FEM was compared to in-situ crack tip measurements. This model formed the basis of a submitted manuscript presented in Appendix D[15]. A short summary of significant findings from both the FEM model and validating experiments will be detailed below.

Crack tip electrochemical conditions were explored utilizing the reactive transport FEM model. Electrochemical boundary conditions were determined through polarizations in simulated crack tip environments. Diffusivities and conductivities were determined in OLI Studio while equilibrium reaction

values were determined from literature. Changes in external polarization, external cathode size (i.e., sample size), water layer thickness, and decreasing crack sizes were compared (Appendix D). It was determined that an increase in the applied external potential increased metal chloride concentrations, decreased pH, and decreased the fraction of local cathodic current. This was confirmed through SCC testing with in-situ measurement as shown in Figure 72-a & b. Fixing the external potential in models or experiments severely impacts crack tip conditions, leading to a decrease in pH, confirmed through both modeling and experimental analysis (Figure 72-c & d). This decreased pH is just one indication that the electrochemical severity of the crack tip is influenced by external polarization. These modeling and measurement efforts indicate that care must be taken in implementation of polarization of samples during SCC measurement as this may not always be relevant to the environment of interest.

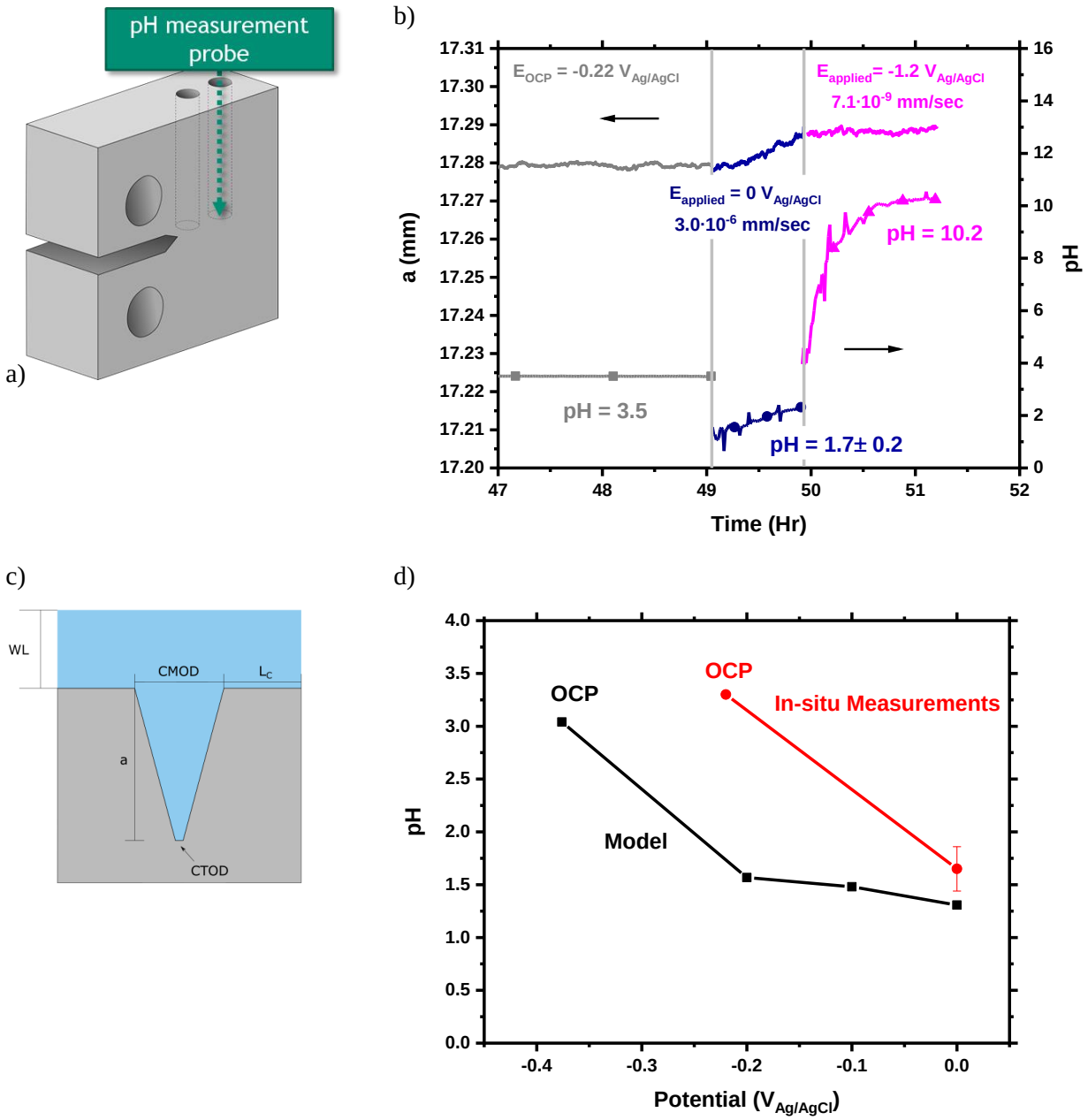

Figure 72. a) Schematic of a compact tension specimen altered for in-situ pH probe measurement, b) crack length vs. time for 304L exposed to room temperature 3 M NaCl and 20 MPa(m)$^{1/2}$ at various external polarizations (none, anodic, and cathodic) compared to in-situ pH measurement, c) schematic of FEM crack tip, and d) modeled vs measured pH as a function of applied potential.

Overall, this modeling effort combined with in-situ measurement enables SNL to better understand and establish effective crack growth rate testing protocol for SNF canister relevant conditions. Determining the controlling influences of the corrosive environment combined with the in-situ cracking kinetics will better establish fracture mechanics similitude for SCC in these aggressive chloride environments.

This page is intentionally left blank.

4. Crack Growth Rate

To better understand predictions for SNF canister lifetimes and develop potential mitigation and repair strategies, determining not only the propensity of a corrosion defect to transition to a crack, but how quickly an SCC crack might grow is a significant priority of the SNL program. Specifically, developing how SCC susceptibility is affected by the atmospheric exposure environment and material condition is a goal of this work. As there currently exists very limited data in the literature on crack growth rates (CGR) for SS304L, let alone atmospheric cracking data pertinent to ISFSI sites, there remains a large amount of work to pursue in this area. One of the main goals of the Sandia-led effort in FY 22 is to determine the relationship between the environmental conditions, the cathodic kinetics, and the subsequent control of the crack initiation and crack growth. Knowledge of this will enable better prediction of the occurrence and rate of SCC cracking and identification of deleterious factors, potentially leading to new mitigation strategies.

In FY20 and 21 the set-up and reduction of noise on four servomechanical load frames was carried out. Three frames were oriented vertically to enable the use of full-immersion exposure cells and one was oriented horizontally to enable the development and study of atmospheric exposure methods. The Direct Current Potential Drop (DCPD) system features a precision power supply, a nanovoltmeter, a solid-state relay and a computer-controlled multi-channel relay card which are together used to measure the change in crack length in a test specimen. The precision power supply is used to source a constant current flow through the test specimen. The nanovolt meter is used to measure the voltage drop across the mouth of crack tip and from a reference attached on the rear surface of the specimen. The computer-controlled relay card switches between signals measured by the nanovoltmeter, which can only make measurements on one channel at a time. The open-circuit potential, temperature, reference voltage, and DCPD voltage are the four signals which are switched between with the multichannel relay and measured with the nanovoltmeter. Further details on the function, layout, and accuracy/precision of this equipment can be found in the FY20 final report [27]. The results presented within from FY23 contain a summary of frame calibration, crack growth rates, and fracture morphologies in $MgCl_2$ and NaCl environments, as well as a summary of testing to date. The strong influence of solution chemistry, loading protocol, and polarization levels are highlighted through this work. These tests provide the foundation for both enhancing SCC CGR measurements under SNF relevant environments and the basis for building an overall understanding of both environment and material influences on resultant CGR under these conditions.

4.1 Testing Methodologies and Materials

Similar methods to determining crack growth rates (CGRs) were implemented in FY22 as were presented in FY21. Briefly, *in-situ* CGR was determined by the direct current potential drop method (DCPD) utilizing Johnsons Equation according to ASTM E1457 [55]. Compact tension (CT) specimens were utilized according to ASTM E1681-03 [56] and ASTM E647 [57]. Diagrams of these specimens were presented in the FY21 report [47]. Both ¾ CT and ½ CT specimens were examined (example schematic in Figure 73-a). CGR tests were performed under constant stress intensity conditions (K) determined by ASTM E1457 [55]. DCPD measurements were performed using Ni wires of 1 mm for the current and potential drop measurements (Figure 73-b). The wires were heat shrunk in Teflon and spot welded to the sample. The spot weld location between the sample and the wires were epoxy coated to prevent galvanic coupling between the Ni wires and the sample. A current of 2 A was applied to the sample and was reversed every 1 s to minimize thermoelectric effects. The absolute values of the measured potentials associated with the reversing current were averaged to obtain a single data point. The measured crack length was used to estimate the load required to maintain the desired K level. Load adjustments were made when the K deviated from the target value by more than 0.1%.

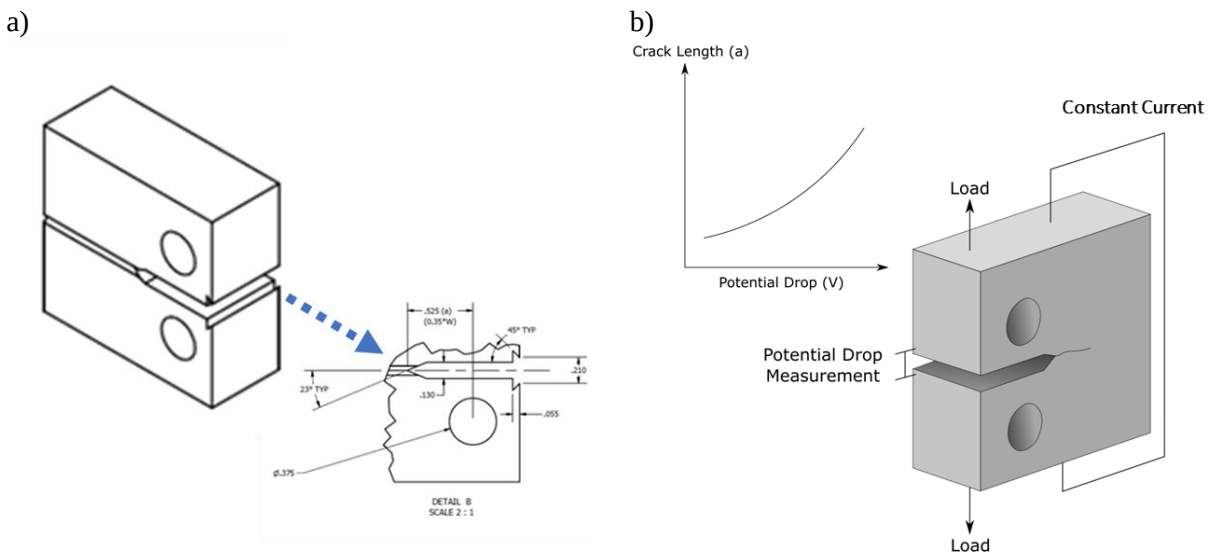

Figure 73. Schematic of a) CT specimen with notch dimensions and b) DCPD measurement setup and "example" measurement output.

Each specimen was fatigue pre-cracked in laboratory air prior to environmentally-assisted cracking (EAC) testing using a frequency of 1 Hz, $K_{max} = 15\ MPa\sqrt{m}$, and R-ratio of 0.1. CT specimens were tested under full immersion conditions. All tests were performed in a circular cell made of acrylic mounted in a load frame. The volume of the cell was roughly 3 L. The solution in the test cell was recirculated (225 mL/min) from an external reservoir containing another roughly 3 L of solution. In all tests, a silver-silver chloride (Ag/AgCl) electrode was used as a reference electrode and a platinized niobium mesh was used as a counter electrode. The samples were loaded in the load train via clevises (C-276) and electrically isolated using ceramic coated pins to prevent galvanic coupling between the sample and the load train. After being placed in the mechanical load frame, specimens were aligned with the clevises to allow for free rotation, in compliance with the K solution boundary conditions [55]. Schematics and pictures of the set-up were presented in the FY21 report [47].

Under full immersion conditions, two test methodologies were utilized: (i) decreasing frequency to constant *K* and (ii) monotonically increasing stress intensity. First, decreasing frequency tests start out at a relatively high frequency (~ 0.1 Hz) and subsequently decrease the frequency until constant *K* is reached. Initially, a saw tooth wave form is utilized, transitioning to a trapezoidal wave form, and eventually to constant *K* condition as displayed in Figure 74-a. For rising K tests, a defined loading rate (dK/dt) was specified until the K_{max} of interest was reached and the crack extension was monitored. This is shown schematically in Figure 74-b. Following test completion, samples were typically heat tinted at a temperature 450 ^{o}C for 1 hour and allowed to air cool. After heat tinting, the samples were reloaded into the frame in air and fatigued at an R-ratio (K_{min}/K_{max}) = 0.1, frequency of 1 Hz for roughly 10 mm of crack extension. After the fatigue cycle, samples were subjected to ductile failure and torn apart for fractography analysis. In some cases, samples were sliced at 1/3 thickness (prior to fatigue and final failure) for crack tip analysis as depicted in Figure 75. Material lots used herein with descriptions, mechanical properties, and material compositions are presented in Table 17, Table 18, and Table 19 respectively.

Finally, tests were also performed under potentiostatic polarization. In these experiments, a 3-electrode cell was utilized with the CT sample as the working electrode, platinized niobium as the counter electrode, and a Ag/AgCl reference electrode. Upon transition to constant K utilized the decreasing

frequency method, anodic polarizations were applied to the sample. That is, electrochemical polarization levels above the open circuit potential were applied to the sample. Crack growth was observed for over 72 hours to ensure stable crack growth.

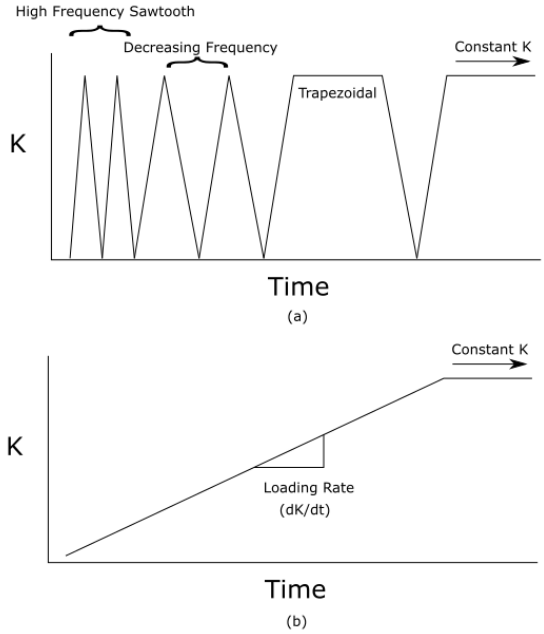

Figure 74: Loading protocol for (a) decreasing frequency tests and (b) rising *K* tests.

Table 17. Basic lot identification information.

Lot ID	Plate #	Heat #	PNNL Reference #	Form	Nominal Alloy
1	206972	SD23822	n/a	Plate, 12" x 12" x 1"	SS304
2	208866	863831	n/a	Plate, 12" x 12" x 1"	SS304- EZ
3	213104	04E28VAA	P304L1	Plate, 12" x 12" x 1.5"	SS304L
4	213156	SD41059	P304L2	Plate, 12" x 12" x 1.5"	SS304L
5	212828	02D84WAB	P316L1	Plate, 12" x 12" x 1.5"	SS316L

Table 18. Lot mechanical properties from manufacturer certificates (UTS – ultimate tensile strength, YS – yield strength, Elongation - % strain at failure, HRB – Rockwell Hardness B).

Lot ID	UTS (MPa)	YS 0.2% (MPa)	Elongation(%)	HRB
1	647	267	57.6	82.2
2	562	251	51.7	75
3	623	292	62.9	81
4	593	242	61.3	78
5		270		81

Table 19. Nominal lot composition from manufacturer certification.

Lot ID	C	Co	Cr	Cu	Mn	Mo	N	Nb	Ni	P	S	Si	Ti
1	0.02	0.2	18.14	0.25	1.7	0.08	0.07	-	8.04	0.031	0.004	0.4	0.001
2	0.01	0.14	18.28	0.34	1.4	0.27	0.07	-	8.16	0.025	0.023	0.4	0.003
3	0.017	0.234	18.1	0.412	1.782	0.414	0.08	0.014	8.03	0.037	0.001	0.236	0.002
4	0.019	0.21	18.2	0.335	1.63	0.1	0.073	0.01	8.155	0.028	0.008	0.385	0.003
5	0.017	0.36	16.7	0.477	1.178	2.002	0.062	0.023	10.085	0.037	0.001	0.282	0.004

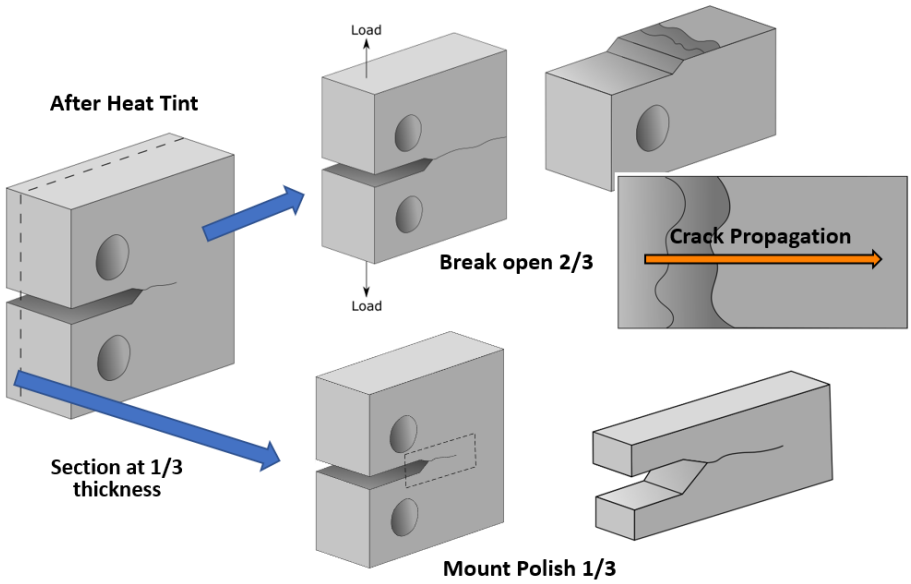

Figure 75: Techniques for sample analysis.

4.2 Benchmarking DCPD and Fractography Analysis

In FY21, various measures were taken to improve the noise levels on the SNL systems. In order to benchmark systems in FY22 and ensure that the DCPD equipment correctly functioned at the desired resolution, air fatigue analysis (similar to a pre-crack) was performed on a ¾ CT (L-T) from Lot 1 and DCPD indicated crack extension was compared with post-mortem fractography analysis. The test was performed with a saw tooth waveform (Figure 74-a) with $K_{max} = 20MPa\sqrt{m}$. The R-ratio ($R = K_{min}/K_{max}$) was varied in order to ensure delineations between the various regions of fatigue (denoted in Figure 76-b). The test protocol consisted of a region of fatigue with R = 0.1, heat tint, R = 0.1, 0.7, 0.5, and 0.1. The crack length vs. time for the air fatigue test is presented in Figure 76-a with optical fractography presented in Figure 76-b and c. Overall, great agreement (< 2 % error) was observed between the DCPD indicated crack growth and the measured crack extension through fractography for the first four fatigue cycles as presented by the lines and symbols respectively in Figure 76-a. A greater error was observed between the DCPD and measured crack length for the final fatigue at R = 0.1, however this was likely due to a non-linear reference signal during this portion. In most tests going forward, a reference is not used due to the non-linear behavior observed. This same procedure was repeated on two frames and good agreement was observed on those frames as well. Therefore, confidence in the SNL DCPD systems was established prior moving forward with full immersion testing.

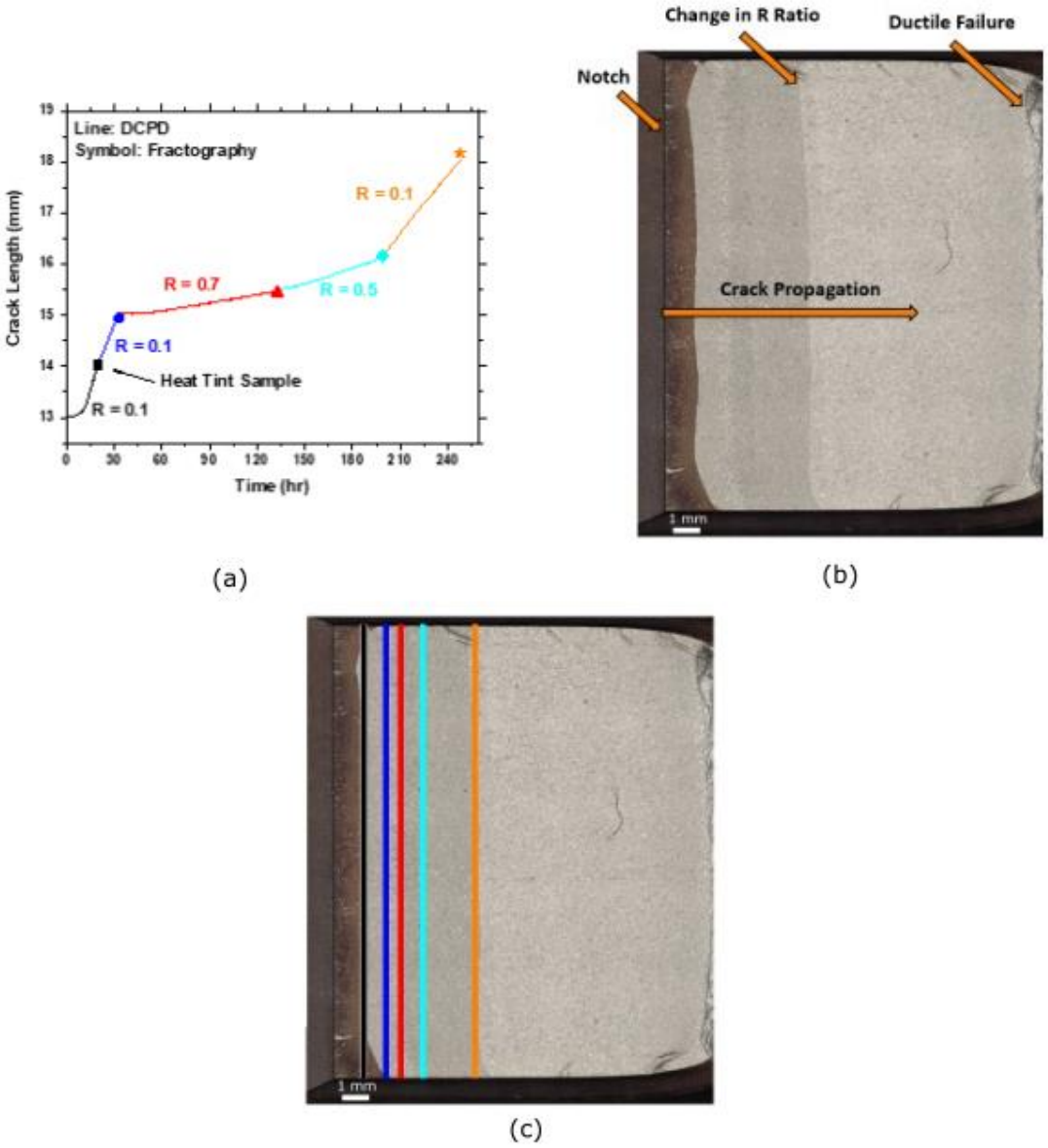

Figure 76: (a) Crack Growth vs. time for Lot 1 under air fatigue for different r ratios. (b) Corresponding fractography for air fatigue test with different test steps labeled and (c) average measurement lines corresponding to the symbols in (a).

4.3 Crack Growth Rate Measurements and Fractography

A summary of observed constant K crack growth rates and tests ran to date is presented in Table 21. Within this section an overview of important tests, new fractography results including novel analysis of the crack tip, and an investigation of solution effects is presented. Again, the overall goal of this work is to begin to establish an understanding of potential governing material and environmental influences relevant to SNF canister environments on CGR. Testing conditions applied to date are summarized in Table 20 and will be described in further detail within.

Table 20. Summary of CGR testing including sample and environment conditions.

Sample ID	Lot	Sample	Solution	Temperature (°C)	Conditions (Comments)
SN0007	1	¾ CT	Saturated $MgCl_2$	55	Cut at 1/3 & 2/3; Ran at DNV-GL
SN0009	1	SENT	Saturated $MgCl_2$	55	Cut at 1/3 & 2/3; Ran at DNV-GL
SN0012	1		Air		Air fatigue - Bench Marking DCPD Systems
SN0017	1		Air		Air fatigue - Bench Marking DCPD Systems
SN0022	1	¾ CT	Saturated $MgCl_2$	22	Rising K
SN0025	1	¾ CT	Saturated $MgCl_2$	55	Rising K
SN0028	1	¾ CT	Saturated NaCl	22	
SN0030	1		Air		Air fatigue - Bench Marking DCPD Systems
SN0033	1	¾ CT	Saturated $MgCl_2$	22	
SN0037	1	¾ CT	Saturated NaCl	55	Rising K
SN0093	3	¾ CT	Artificial seawater 40 % RH brine	55	Artificial seawater 40 % RH brine, 55 ˚C (3/4 CT; Lot 3)
SN0093	3	¾ CT	3 m $MgCl_2$	55 and 75	
SN0095	3	¾ CT	Saturated NaCl	55	
SN0096	3	¾ CT	Saturated $MgCl_2$	55	
SN0097	3	¾ CT	Saturated NaCl	60	
SN0098	3	¾ CT	Saturated $MgCl_2$	55	
SN0107	3	½ CT	Saturated $MgCl_2$	55	L-S*
SNL0001	3	½ CT	3 M NaCl	22	L-S*
SNL0002	3	½ CT	3 M NaCl	22	L-S*

4.3.1 $MgCl_2$

The crack extension vs. time for Sample SN0007 (Lot 1) is presented in Figure 77-a. This test was performed in saturated $MgCl_2$ at 55 ˚C. It is noted that in Figure 77-a, upon transitioning to constant K, the sample did not exhibit measurable crack growth. After roughly 700 hours, cracking ensued, and had a

measured crack growth rate of $6.13 \cdot 10^{-7}$ mm/sec. The sample was cross-sectioned (Figure 75) and then heat tinted such that any dark surface occurred during transitioning to SCC and during the constant K observation. Examining Figure 77-b, the crack front displays a non-linear crack front, with two regions that appear to be dominating crack growth during the constant K portion. Figure 77-c overlays the measured DCPD and highlights important features of interest, such as the end of the pre-crack (i.e., start of solution fatigue), before transitioning to constant K (i.e., end of the 900/100+9000 second holds), and the end of indicated DCPD testing. The overlay of DCPD and fractography seems to indicate that the crack may have stopped at the transition to constant K (i.e., end of the 900/100+9000 second holds) and some portions of the crack front did not nucleate later in the constant K region. A more complete story can be obtained by investigating the cross-section (Figure 77-d). Significant branching of the crack is observed in the cross-section with branches extending both above and below the pre-crack. In a similar manner, the DCPD progression of the test was overlaid with the cross-section. It appears that branching occurs near the transition to constant K however it is difficult to line up DCPD with a single cross-section image due to the fact that DCPD is a measure of the average crack front. Therefore, serial section of sample SN0007 has commenced, and initial results are presented.

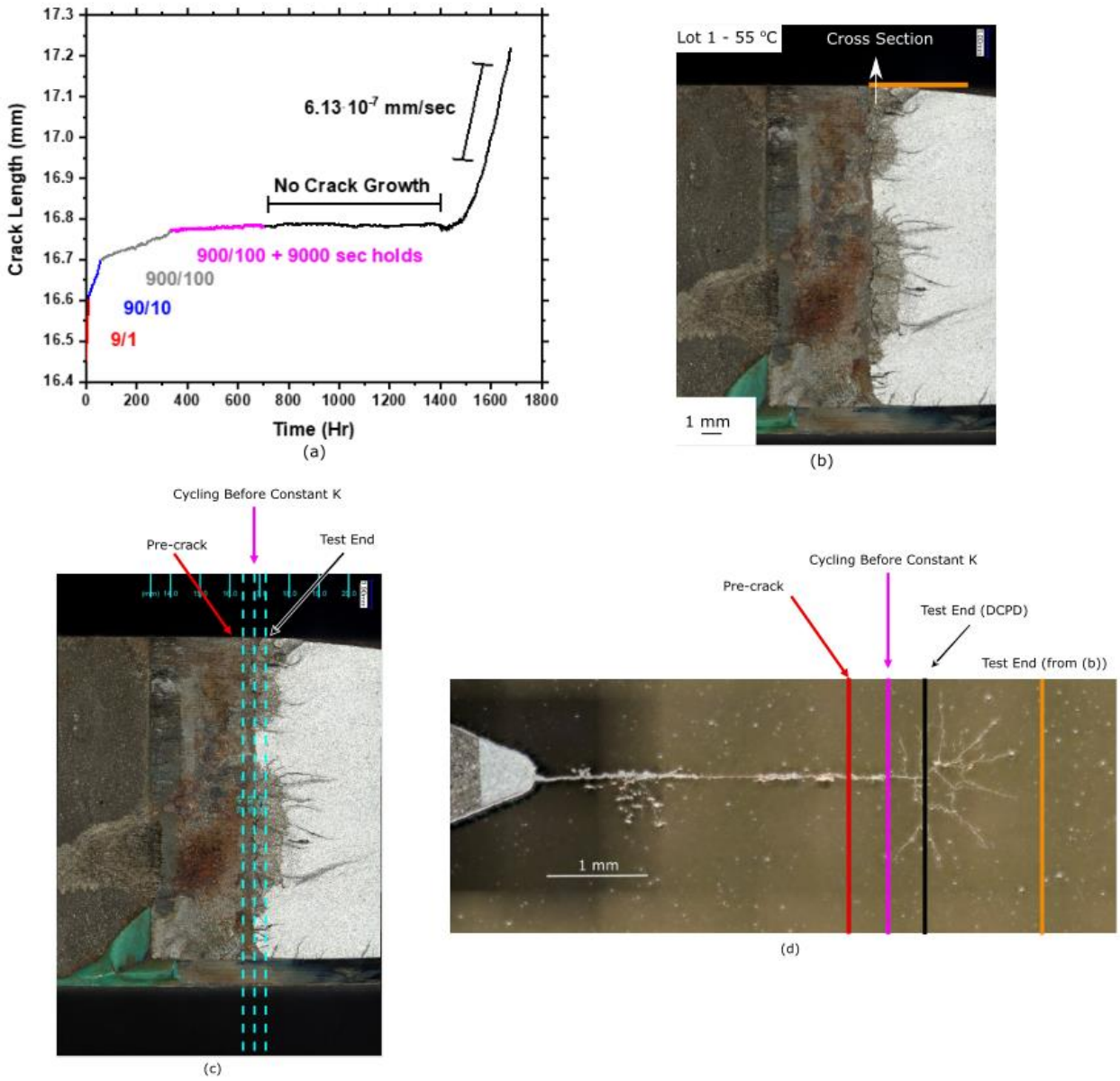

Figure 77: (a) Crack length vs. time for SN0007 (Lot 1) in saturated $MgCl_2$ at 55 ˚C. (b) A portion of the fracture surface and (c) optical cross section of the crack tip.

The cross-section of SN0007 has undergone roughly 2 mm of serial sectioning and three images from this serial sectioning are presented in Figure 78-a, b, and c. The serial sectioning was made in the direction from the cross-section edge outwards towards the original outer edge of the CT sample. These represent the first serial section, a serial section from the middle (roughly 1 mm depth from the section), and the last image taken after roughly 2 mm. Slightly over 500 slices with 5X brightfield reflected light imaging for an in-plane resolution of 1.08 micron/pixel were obtained. This resulted in 80 tiles per slice for a total of 1.4 TB of raw data. The polishing conditions consisted of: (i) 6 micron diamond for 20 seconds (composite polishing disk), (ii) 3 micron diamond for 180 seconds (woven acetate cloth), and (iii) 1 micron diamond for 120 seconds (woven silk cloth). In preliminary analysis there are artifacts from the stitching processes. Additionally, throughout the serial sectioning, a reduced removal rate due to pad wear was present as collection went on. There were also water spots later in the serial sectioning (Figure

78(c)) as result of pad wear, but should not interfere with further planned analysis. Work in FY23 will seek to remove imaging artifacts prior to 3d processing of the images.

The serial sections presented in Figure 78 show that the branching behavior changes throughout the through thickness of the sample. At the end of the serial section (Figure 78-c) it is noted that the branching can no longer be seen in the image. Additionally, an overlay of the measured DCPD with the fracture surface in Figure 78-c indicates that the branching could have started during or after the transition to constant K. Further, it is possible that blunting of the crack tip could have occurred, and a closer look at the crack tip is presented in Figure 79-c showing a fairly rounded crack front. SEM analysis of the final sample is needed to determine the nature of the crack front.

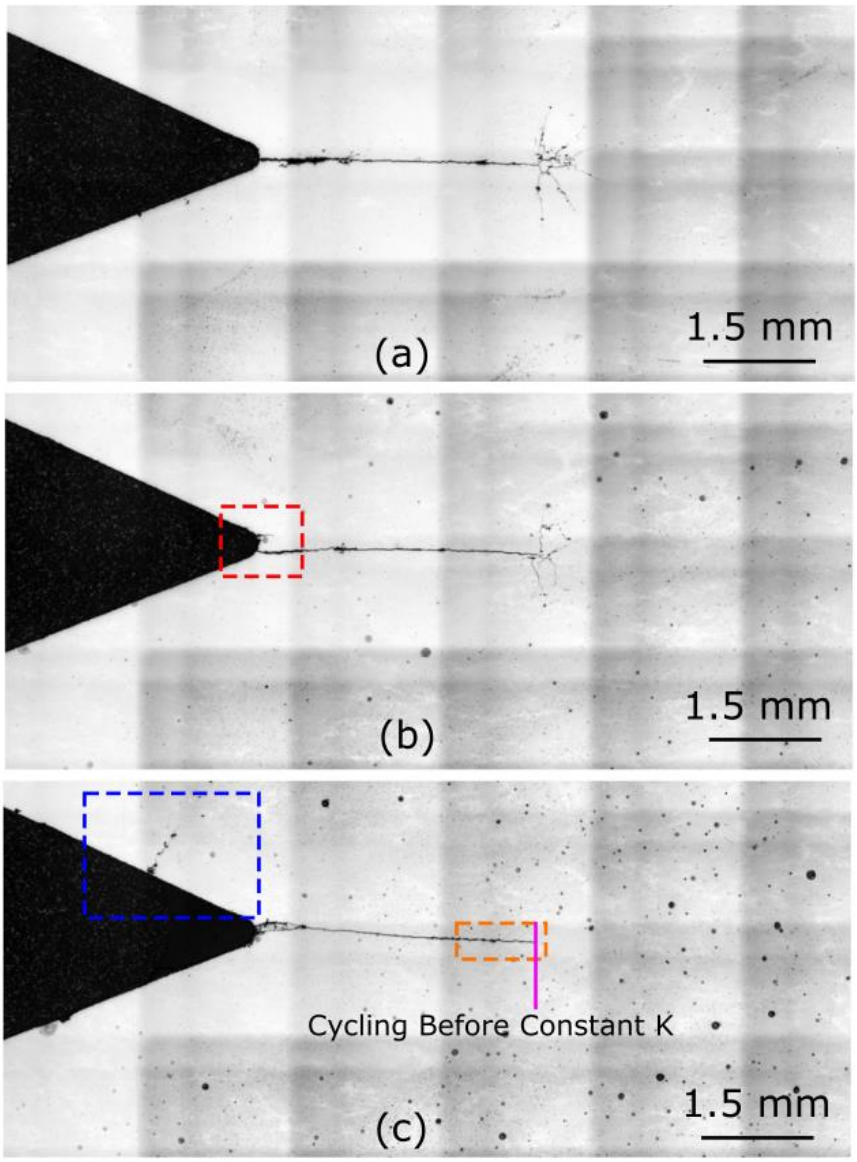

Figure 78: Detailed serial sectioning of SN0007 from Figure 77.

Secondary cracking is observed throughout the serial sectioning. In Figure 79-a it appears that a secondary crack has been nucleated near the notch, however, the propagation of the crack during the exposure time-period was less than 0.5 mm in the specific cross-section. In Figure 79-b, it is possible that a crack was nucleated from a corrosion feature in the notch as indicated by the pit like feature near the surface of the alloy. Very minimal load should be present in the notch, therefore, the potential for corrosion nucleated crack growth under these conditions indicates a strong corrosion response in $MgCl_2$ solutions. While only three images from the serial sections are shown, the other images will be processed in FY23 yielding a complete 3D reconstruction of this portion of sample SN0007.

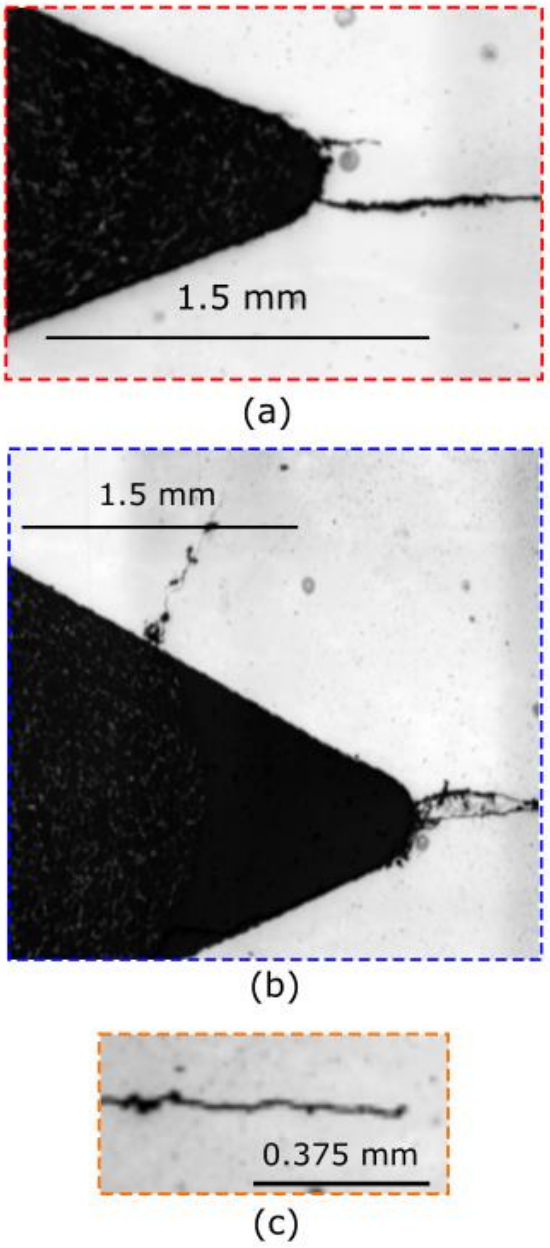

Figure 79: Detailed look at the serial cross section from Figure 78.

The crack length vs. time for sample SN0033 exposed to saturated $MgCl_2$ at 22 ˚C is presented for the entire test duration and the constant K portion in Figure 80-a and b respectively. While it may look like no crack extension is present for the $MgCl_2$ under constant K conditions in Figure 80-a, zooming into the

constant K portion in Figure 80-b, it can be seen that that a CGR of $1.12 \cdot 10^{-8}$ mm/sec ($1.12 \cdot 10^{-11}$ m/sec) is observed during this period and is greater than the noise/drift of the system indicating stable, measurable crack growth. The sample was subsequently heat tinted and fractured open with fatigue. The fracture surface is presented in Figure 80-c and similar to SN0007 (Figure 77) protrusions ahead of the crack front are observed. Two CGR values from this sample are reported: (i) average crack extension as indicated by DCPD and (ii) fractography measured CGR. For the CGR indicated from fractography, it was assumed that crack extension from the white line in Figure 80-c occurred during the constant K growth. Thus, the deepest point of protrusion from the white line was used to calculate a CGR over the time-period of constant K. The CGR from fractography is roughly an order of magnitude higher than the average crack growth from DCPD and is shown in Figure 81. In other material systems, it has been observed that a crack does not nucleate intergranular features along the crack front during the transitioning protocol [58]. However, from the observations here,there is strong evidence that this is not the case in concentrated chloride environments, as two samples have indicated potential nucleation after the transition period. Overall, examination of crack growth predictions with deepest extension vs. average DCPD signal warrants further study as irregular crack morphologies seem highly likely in canister relevant brines, as apparent from the fracture surfaces in high chloride solutions (SN0007 and SN0033). Further, the scatter of literature crack growth rates presented in Figure 81 were obtained with *in-situ* methods combined with fracture surface determined crack growth rates and such an exercise presented within can help explain for significant scatter in the data.

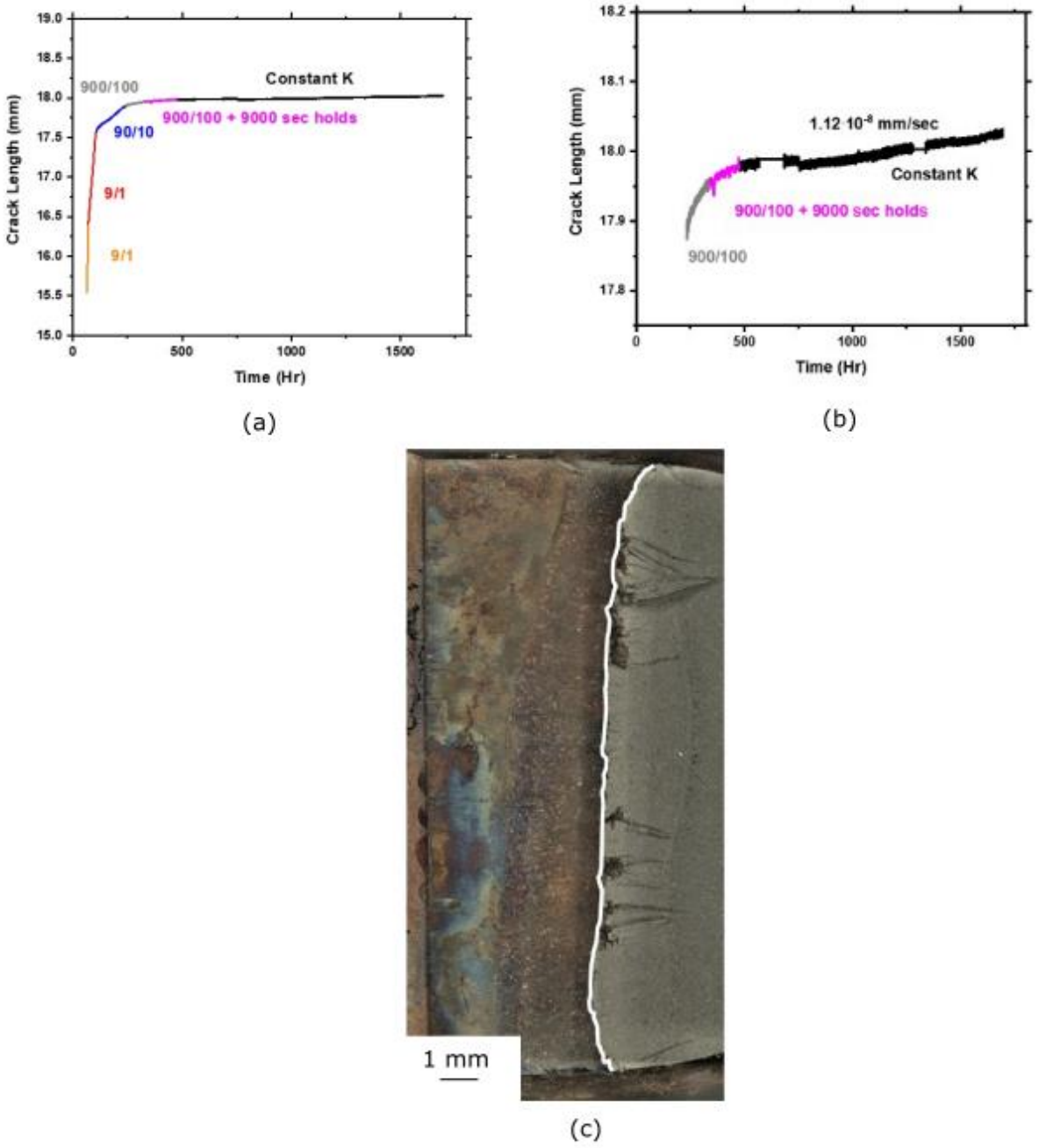

Figure 80: (a) Crack Growth vs. time for SN0033 from Lot 1 exposed to saturated $MgCl_2$ at 22 ˚C for the entire test duration and (b) zoomed in showing the constant K behavior. (c) Optical fractography for sample SN0033 with overlay of CGR measurement line.

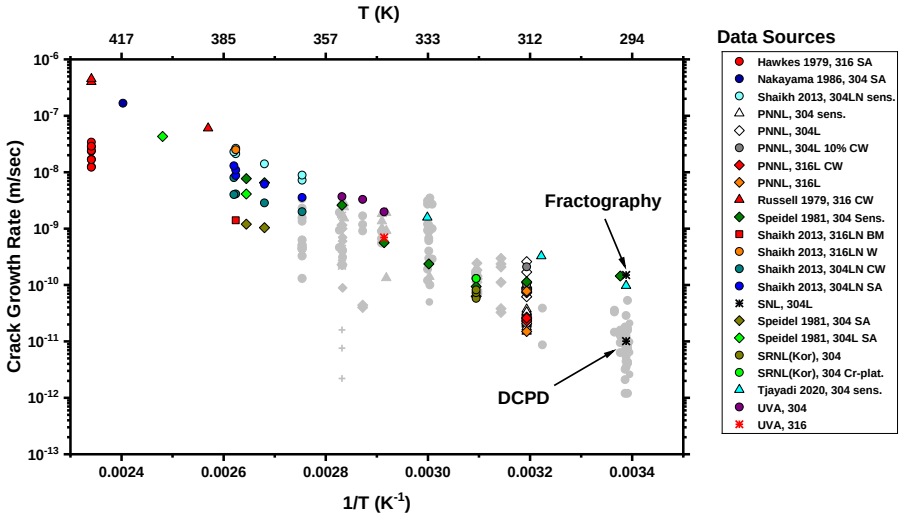

Figure 81: Comparison of CGR measured by DCPD and fractography for SN0033 with literature values for CGR [ref-CRB report].

Optical and SEM images of protrusions present on SN0033 are presented in Figure 82-a and b respectively. It is noted that determining the exact mode of fracture from these images is difficult due to the presence of corrosion products on the surface of these alloys despite cleaning procedures. Further investigations of cleaning methods will be carried out in FY23. Despite the presence of corrosion products, it is evident that SN0033 exhibited crack branching similar to SN0007. This can be seen on both optical and SEM images. In the SEM image in Figure 82-b, striations formed during the post-test fatigue are indicative of out of plan cracking (i.e., crack branching).

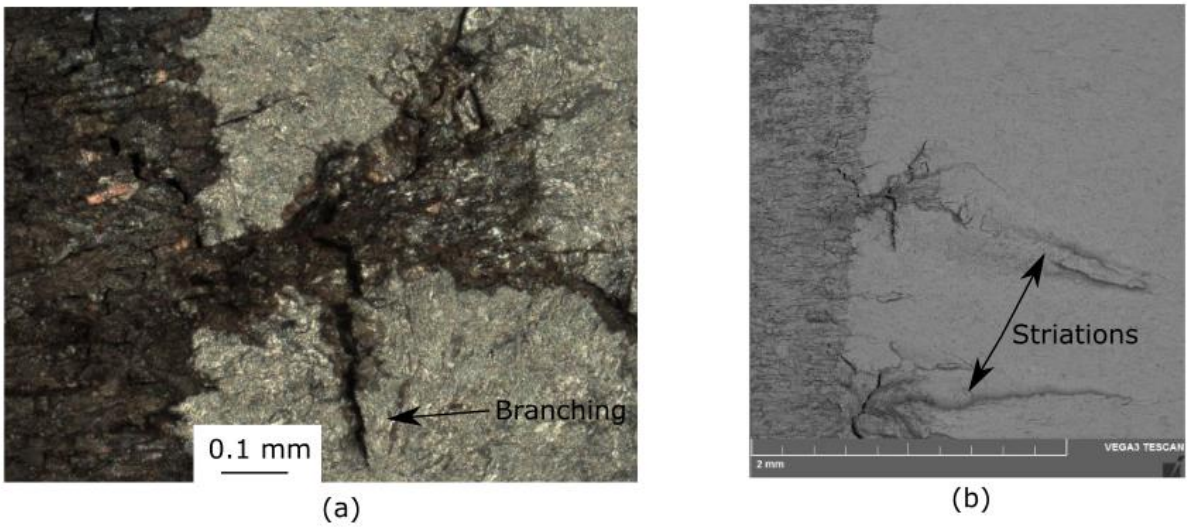

Figure 82: (a) Optical and (b) SEM image of protrusions on the fracture surface of SN0033.

A summary of fractography obtained from various tests in saturated $MgCl_2$ brines is presented in Figure 83. Significant influences of temperature are shown on the fracture morphology for Lot 1 in Figure 83-a

and b. It appears as though there are more localized, discrete attacks across the sample that underwent constant K at 22 ˚C in comparison to that performed at 55 ˚C. Additionally, comparing lots at 55 ˚C, significant differences in fracture morphologies are observed, with Lot 3 exhibiting more frequent and longer protrusions in front of a nominally linear crack front in comparison to Lot 1. Finally, in a comparison of cracking orientation, Lot 3 exhibited a much more linear crack front in the T-S direction in comparison to the L-T direction as displayed in Figure 83-d and c, respectively. Although the crack front appears linear in nature with less protrusions, there are still differences between the crack front produced in $MgCl_2$ and what is observed for NaCl solutions (Figure 86). Overall, the crack front has shown a dependence on the temperature, lot, as well as cracking direction.

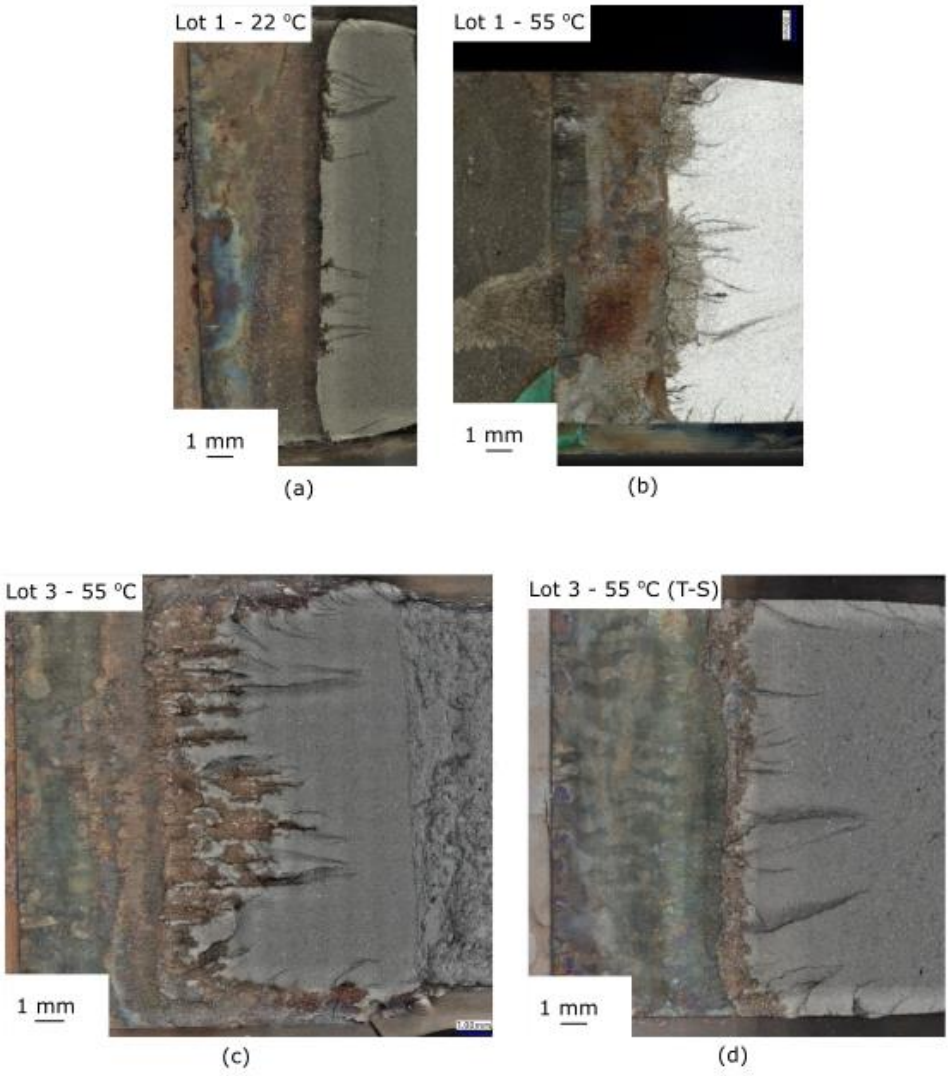

Figure 83: Fractography for samples ran in saturated $MgCl_2$ on various lots, temperatures, and directions. The figures correspond to (a) Lot 1 - 22 ˚C (SN0033), (b) Lot 1 - 55 ˚C (SN0007), (c) Lot 3 - 55 ˚C (SN0100), (d) Lot 3 - 55 ˚C (SN0107), T-S. It is noted that if the directions are not noted they are performed in the L-T direction.

A further look at SN0107 (testing in saturated $MgCl_2$ at 55 ˚C) is presented in Figure 84 and highlights the cracking observed on the two sides of the specimen prior to the sample being broken open with fatigue. The sample exhibits significant crack branching with cracks grown in multiple directions ranging from parallel to perpendicular to the target crack path. Various perpendicular cracks are highlighted in Figure 84-c and d with some cracks extending roughly 4-5 mm perpendicular from the main crack path. As presented in the FY21 report [47], significant variations in the underlying microstructure exist due to the rolling process and it is possible that such variances (likely body-centered cubic (BCC) ferrite stringers) influence the cracking paths.

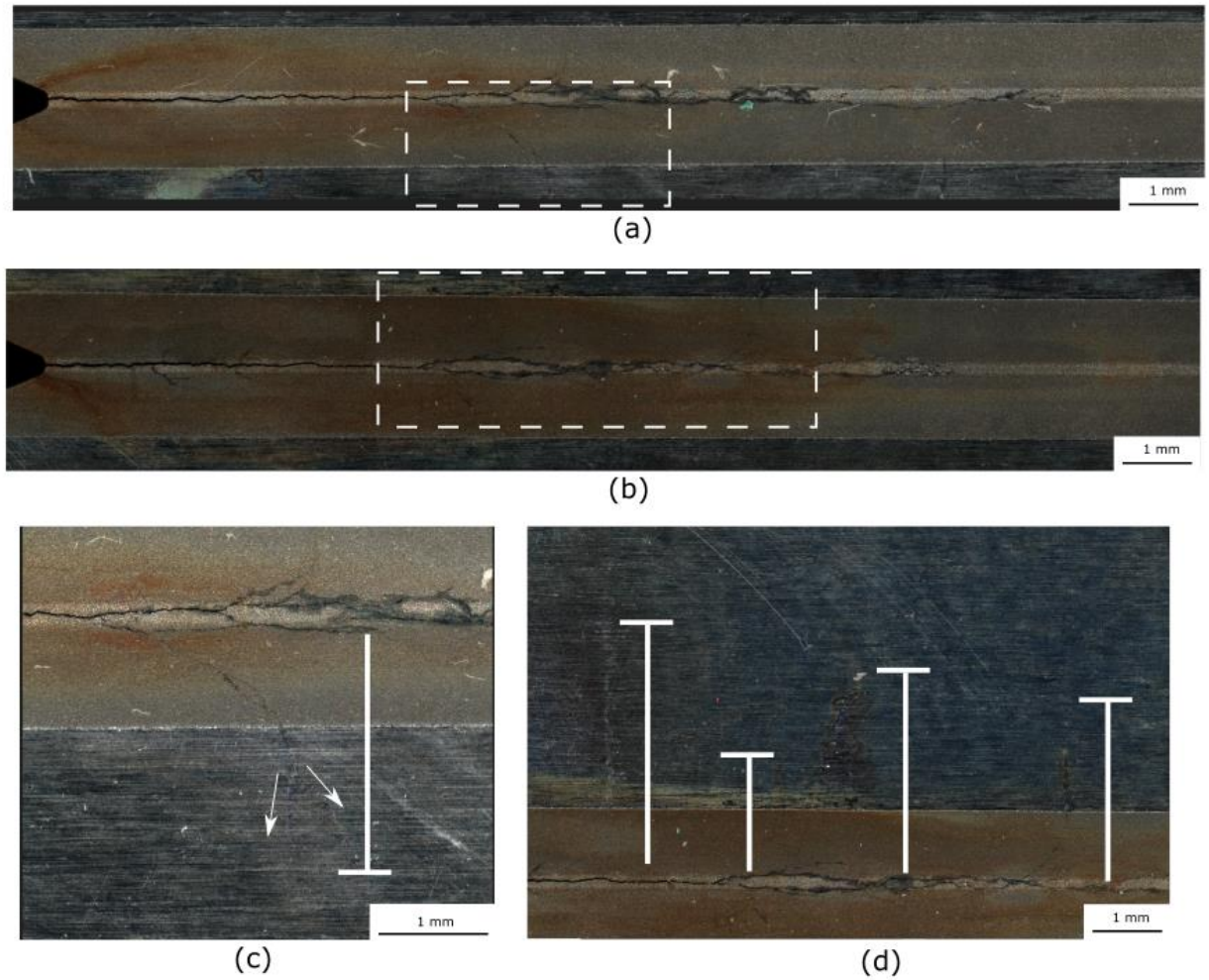

Figure 84: Fractography of the crack path for Sample SN0107 ran in saturated $MgCl_2$ at 55 ˚C.

The strong influence of electrochemical potential was investigated for a SENT sample in saturated $MgCl_2$ at 55 ˚C and is shown in Figure 85 for sample SN0009. Prior to polarization, the open circuit potential was roughly -475 mV_{SCE} and the CGR was not growing (crack growth of $4.4 \cdot 10^{-12}\ m/sec$ is below the system resolution limit). Upon applying a potential greater than -375 mV_{SCE} crack growth rate increased roughly two orders of magnitude above the resolution limit. At an applied potential of roughly -270 mV_{SCE} the CGR was $1.81 \cdot 10^{-9}\ m/sec$. After applying electrochemical potentials, the stable open circuit potential was higher (-410 mV_{SCE}) than previously (-475 mV_{SCE}) and exhibited a faster cracking rate of $8.1 \cdot 10^{-12}\ m/sec$ than prior to polarization.

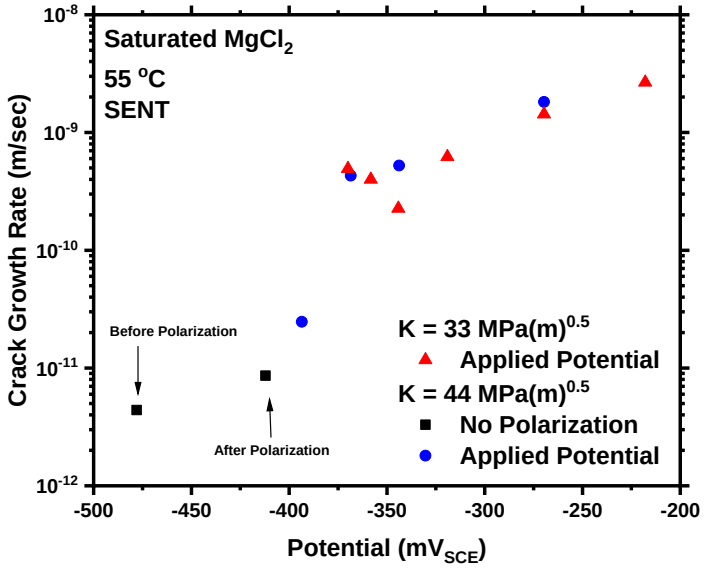

Figure 85: Influence of electrochemical polarization level on crack growth rate responses at various *K* levels in saturated $MgCl_2$ at 55 ˚C for sample SN0009.

4.3.2 NaCl

Similar to $MgCl_2$ solutions, CGR measurements in concentrated NaCl brines were explored both to develop a better understanding of SNF relevant environmental variables and to establish comparable tests to both collaborators (PNNL and UVA) as well as historical literature. A summary of all CGR tests to date was presented in Table 20, with detailed analysis of select samples presented below.

The fracture morphologies of SN0028 and SN0095 are shown in Figure 86-a and b respectively. In comparison to crack fronts observed for $MgCl_2$ exposures (Figure 83), the crack fronts for NaCl solutions (Figure 86) are linear in nature and do not contain protrusions ahead of the primary crack front. Additionally, there is not significant evidence of the cracks branching as indicative striations did not appear during the final fatiguing process as were present in the samples cracked in $MgCl_2$ (Figure 82). Despite the linear crack fronts, significant corrosion is present in the crack wakes of these samples and is shown in the SEM micrographs in Figure 87 for SN0095. It is possible that due to the selective trench-like behavior of these features that the microstructure is playing a significant role in the corrosion and SCC behavior of these materials.

Figure 86: Fractography for samples ran in saturated $MgCl_2$ on various lots, temperatures, and directions. The figures correspond to (a) SN0028 (Lot 1 - 22 ˚C) and (b) SN0095 (Lot 3 - 60 ˚C). It is noted that if the directions are not noted they are performed in the L-T direction.

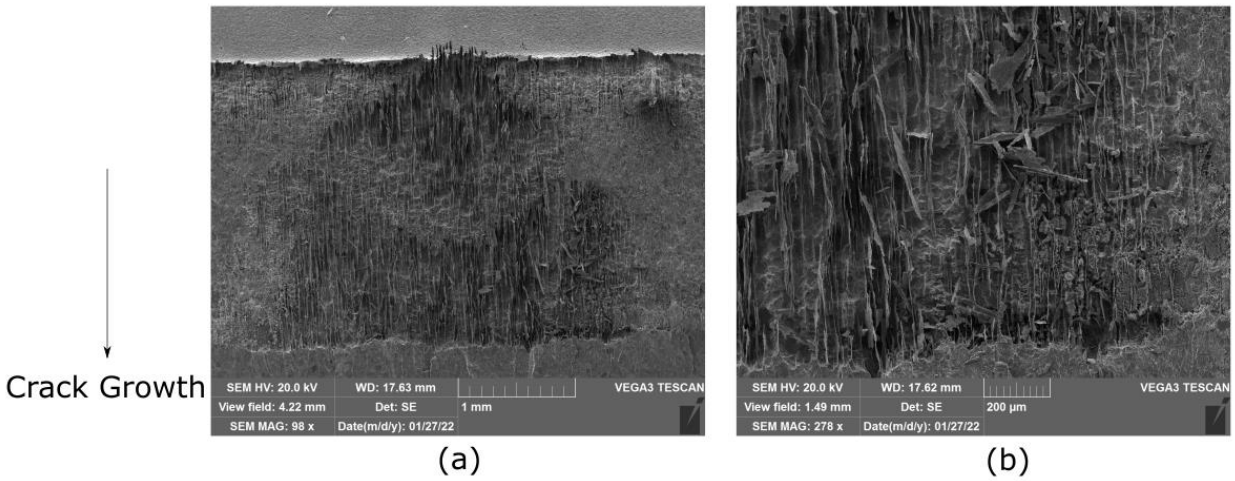

Figure 87: SEM images showing crack wake corrosion in SN0095.

The influence of sample polarization was also explored in NaCl solutions [59]. In a 3M NaCl environment at 22 ˚C, a strong influence on resultant CGR was observed. Similar to $MgCl_2$ (Figure 85), polarizing the sample to a more anodic potential (0 $V_{Ag/AgCl}$ = -0.045 V_{SCE}) immediately induced cracking with a rate of $3 \cdot 10^{-9}\ m/sec$. Further, decreasing the sample potential to -1.2 $V_{Ag/AgCl}$ (-1.245 V_{SCE}) immediately stopped crack growth. Over the time periods tested, it is noted that increased crack growth rates are observed for anodic polarizations. In other alloy systems, such as Monel K-500[60] and

AA7075-T651[61], cathodic polarization to -1.2 V causes for an increased SCC susceptibility and crack growth rate due to hydrogen embrittlement susceptibility. While increased crack growth rates were observed for those alloy systems, crack growth was not observed for SS304L during the time frame of polarization to -1.2 V. The CGR behavior observed under these different polarized conditions may indicate that anodic dissolution is the active mechanism for SCC, however, further exploration is needed.

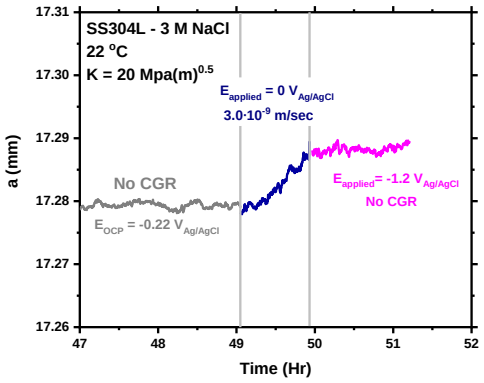

Figure 88: Influence of anodic and cathodic polarizations on sample SNL0001.

The influence of polarization on subsequent SCC behavior may have implications not only for CGR measurements relevant to SNF canisters, but also to potential mitigation and repair strategies. The polarization (or surface potential) of a material can also be influenced by contact with another material. Introduction of coatings, such as cold spray, in which dissimilar metals are in physical contact with one another could induce such a polarization. If a cold spray material is used that is more noble than SS304L, enhanced anodic dissolution or corrosion of the SS304L could be present potentially leading to conditions under which enhanced cracking of the substrate could occur. Further, strong influences of polarization levels are shown in $MgCl_2$ and NaCl environments, indicating that anodic polarization influences on CGR are present across many environments relevant to SNF storage.

Finally, the influence of loading protocol was explored for SN0095 as presented in Figure 89(a) and (b) for a rising K transition and a decreasing frequency transition. For the rising K test, the K was increased from 15 to 30 $MPa\sqrt{m}$ at a rate of 0.33 $MPa\sqrt{m}/hr$. Upon reaching 30 $MPa\sqrt{m}$ the stress intensity weas then maintained for crack growth observation. As shown in Figure 89(a) utilizing the rising K transition yielded a higher crack growth rate during the constant K portion in comparison to that of the decreasing frequency method described in Section 4.1.

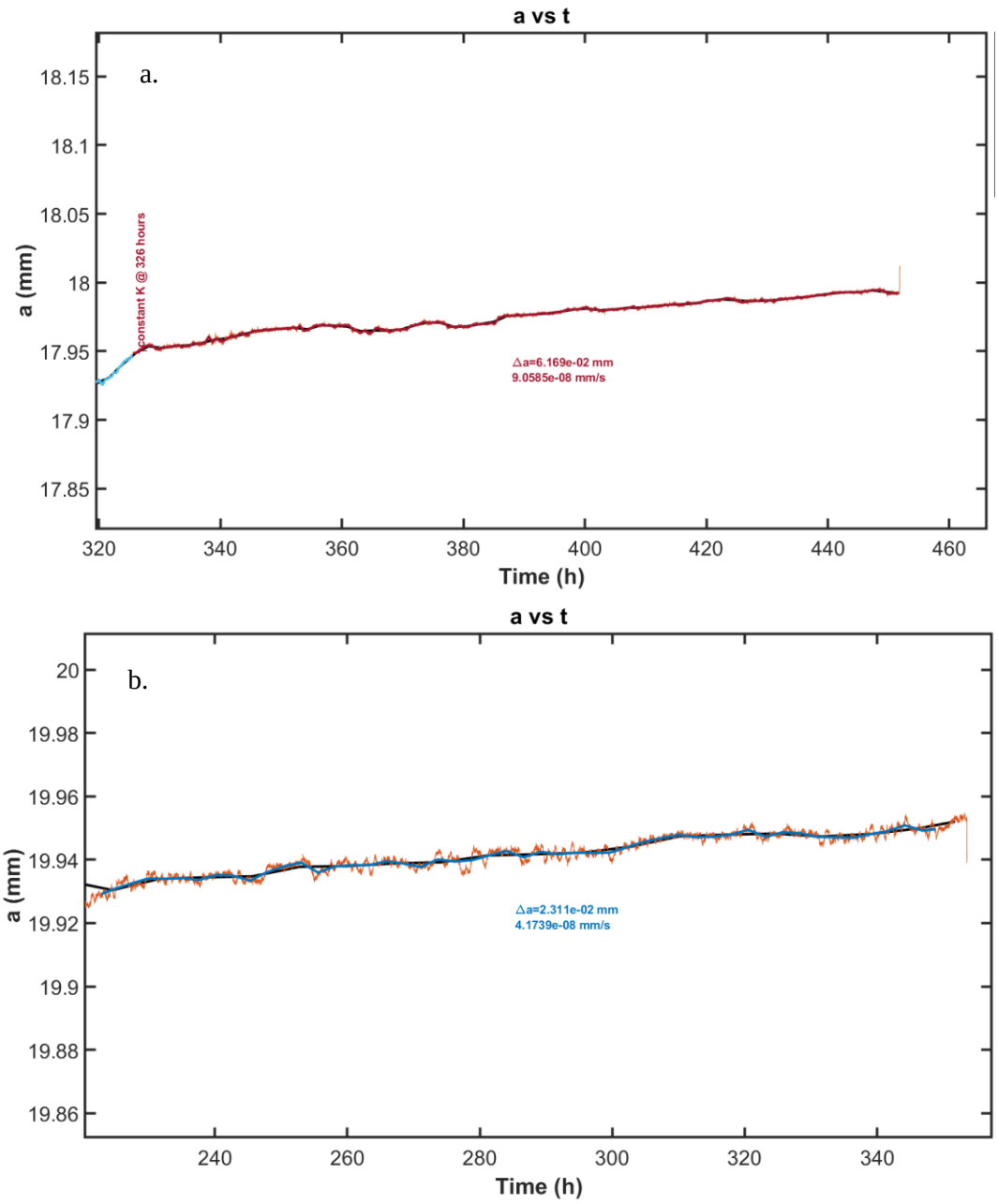

Figure 89: Influence of (a) rising K transition to constant K and (b) decreasing frequency to constant K for SN0095.

4.4 Summary of FY22 CGR Testing

A summary of samples tested to date with corresponding conditions and observed constant K CGR values is presented in Table 21. Additionally, CGR values for $MgCl_2$ and NaCl are compared to literature obtained CGR in Figure 90 and Figure 91 respectively. There are a few interesting things to note from the data in Table 21. First, the transition to constant K influences the resultant CGR during the constant K portion. For samples exposed to both NaCl and $MgCl_2$ solutions (SN0095 and SN0096, respectively) a greater constant K CGR was observed when the sample was transitioned via a rising K method in

comparison to the decreasing frequency tests. It is possible that the due to the fact that constant K is achieved in a shorter time period in comparison to the decreasing frequency tests, fewer corrosion processes take place, therefore potentially reducing the chance of crack tip blunting due to corrosion.

Another significant influence is the effect of solution compositions. At most temperatures and K levels evaluated, saturated $MgCl_2$ solutions resulted in a higher CGR than NaCl solutions. Additionally, as previously highlighted, $MgCl_2$ solutions produced highly non-linear crack fronts with significant amounts of crack branching. The non-linear behavior in $MgCl_2$ is also dependent upon the lot of material, temperature, as well as loading-cracking orientation. Overall, examination of crack growth predictions with deepest extension vs. average DCPD signal warrants further study as irregular crack morphologies seem highly likely in canister relevant brines, as apparent from the fracture surfaces in high chloride solutions.

Table 21. Summary of SCC testing to date.

Sample ID	Conditions (Comments)	Constant K Crack Growth Rate (Conditions of interest)
SN0007	Saturated $MgCl_2$, 55 ˚C (3/4 CT; Lot 1; Cut at 1/3; Ran at DNV)	$6.13 \cdot 10^{-10}$ m/sec ($20\ MPa\sqrt{m}$)***
SN0009	Saturated $MgCl_2$, 55 ˚C (SENT; Lot 1; Cut at 1/3; Ran at DNV)	No CGR ($44\ MPa\sqrt{m}$; $-412\ mV_{sce}$) $1.81 \cdot 10^{-9}$ $m/$sec ($44\ MPa\sqrt{m}$; $-270\ mV_{sce}$)******
SN0012	Air fatigue (Lot 1; Bench Marking DCPD Systems)	N/A
SN0017	Air fatigue (Lot 1; Bench Marking DCPD Systems)	N/A
SN0022	Saturated $MgCl_2$, 22 ˚C (3/4 CT; Lot 1; Rising K)	In analysis*****
SN0025	Saturated $MgCl_2$, 55 ˚C (3/4 CT; Lot 1; Rising K)	In analysis*****
SN0028	Saturated NaCl, 22 ˚C (3/4 CT; Lot 1)	No CGR ($20\ MPa\sqrt{m}$)
SN0030	Air Fatigue (Lot 1; Bench Marking DCPD Systems)	N/A
SN0033	Saturated $MgCl_2$, 22 ˚C (3/4 CT; Lot 1)	$1.12 \cdot 10^{-11}$ m/sec ($20\ MPa\sqrt{m}$) $1.08 \cdot 10^{-10}$ m/sec ($20\ MPa\sqrt{m}$)****
SN0037	Saturated NaCl, 55 ˚C (3/4 CT; Lot 1; Rising K)	In analysis*****
SN0093	Artificial seawater 40 % RH brine, 55 ˚C (3/4 CT; Lot 3)	Currently testing (55 ˚C, 30 $MPa\sqrt{m}$)
SN0093	3 m $MgCl_2$, 55 ˚C, 75 ˚C (3/4 CT; Lot 3)	No CGR (55 ˚C, 30 $MPa\sqrt{m}$) Currently testing (75 ˚C, 30 $MPa\sqrt{m}$)
SN0095	Saturated NaCl, 55 ˚C (3/4 CT; Lot 3)	$4.17 \cdot 10^{-11}$ m/sec ($30\ MPa\sqrt{m}$) No CGR ($20\ MPa\sqrt{m}$) $9.06 \cdot 10^{-11}$ m/sec ($20\ MPa\sqrt{m}$)*****
SN0096	Saturated $MgCl_2$, 55 ˚C (3/4 CT; Lot 3)	$5.65 \cdot 10^{-11}$ m/sec ($30\ MPa\sqrt{m}$) $9.81 \cdot 10^{-11}$ m/sec ($30\ MPa\sqrt{m}$)*****
SN0097	Saturated NaCl, 60 ˚C (3/4 CT; Lot 3)	$2.1 \cdot 10^{-11}$ m/sec ($20\ MPa\sqrt{m}$)
SN0098	Saturated $MgCl_2$, 55 ˚C (3/4 CT; Lot 3)	$2.49 \cdot 10^{-10}$ m/sec ($20\ MPa\sqrt{m}$)**
SN0107	Saturated $MgCl_2$, 55 ˚C (1/2 CT; Lot 3; L-S)*	$1.88 \cdot 10^{-10}$ m/sec ($20\ MPa\sqrt{m}$)**
SNL0001	3 M NaCl, 22 ˚C (1/2 CT; Lot 3; LS)	No CGR ($20\ MPa\sqrt{m}$)* $3.0 \cdot 10^{-9}$ $m/$sec ($20\ MPa\sqrt{m}$; $-45\ mV_{sce}$)******
SNL0002	3 M NaCl, 22 ˚C (1/2 CT; Lot 3; LS)*	$4.39 \cdot 10^{-10}$ m/sec ($30\ MPa\sqrt{m}$)*

*Indicates testing presented in SAND report from LDRD as referenced in Section 3.3
**No pre-crack data
***After incubation period
****Measured from fractography
*****Transitioned from rising K
******Applied potential

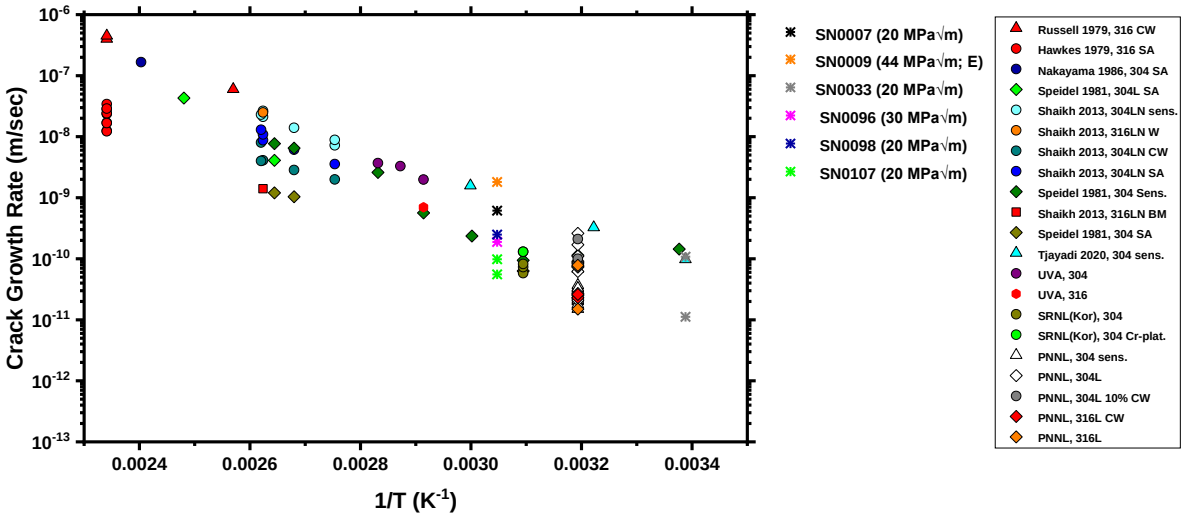

Figure 90: Comparison of CGR in saturated $MgCl_2$ with literature obtained CGR values.

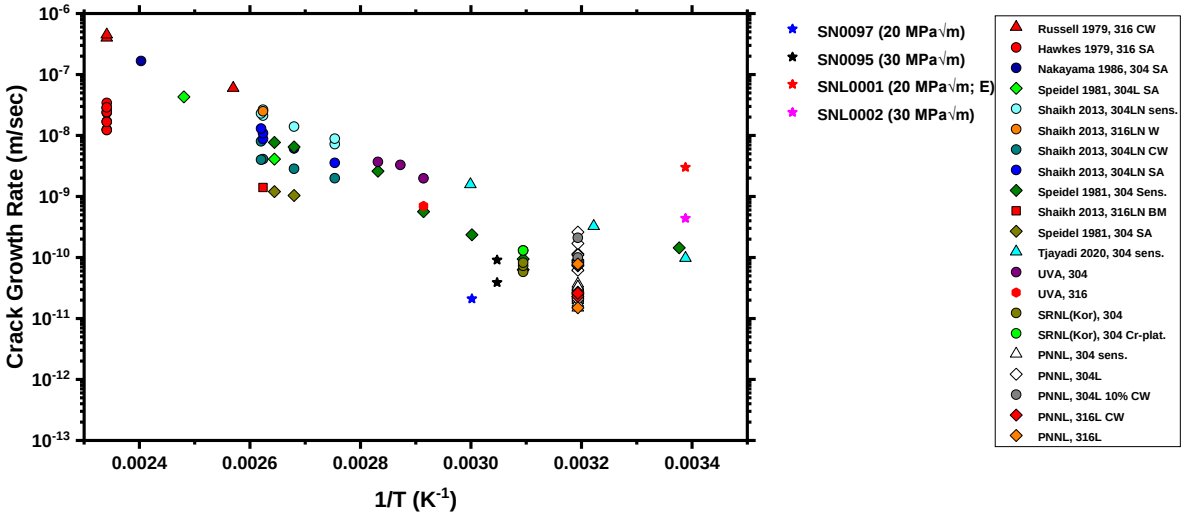

Figure 91: Comparison of CGR in Saturated and 3 M NaCl with literature obtained CGR.

4.5 FY23 Expansion of SCC Testing Environments

4.5.1 Full Immersion

Further testing of CGR protocol, i.e. rising K vs. decreasing frequency tests, is necessary in order to investigate the potential for influence of crack tip blunting due to corrosion and/or the crack growth rate

responses. Explorations in FY22 established a difference between rising K and decreasing K frequency tests in the CGR response. This will be carried out in FY23 with significant characterization comparison to post-test imaging. Without a full understanding of a correct loading protocol to reduce crack tip blunting, transition to realistic, atmospheric conditions is difficult as significant time could be wasted in collection of CGR data under environments and loading protocols that are not representative or cannot be extrapolated to that of the final application.

A significant influence of brine chemistry during constant K is observed both in the measured CGR as well as the propensity of crack branching, crack wake corrosion, and the presence of protrusions in the crack front. It is possible that crack tip chemistry is playing an important role in determining these behaviors. Therefore, in-situ crack tip chemistry measurements will be made in relevant environments for SNF canisters during crack growth rate testing. Further, the SCC behavior of SS304L in ASW at various representative brine compositions [20] will be evaluated and has already started in FY22. Overall, brine chemistry has been shown to play a significant role in corrosion damage morphology and extent, to potentially play a role in the pit to crack transition and may be a governing factor for the crack growth rate in austenitic stainless steels.

FY22 research has shown the significant influence of applied polarization on subsequent crack growth rate (and local crack tip electrochemical environment) and helps us to understand the potential cracking mechanisms present in SS304L. Further exploration of the mechanism of SCC in highly concentrated chloride environments will be undertaken in FY23 as this further helps to develop accurate and representative testing methods. Additionally, by understanding the mechanism of SCC the development of more effective mitigation strategies is possible.

It is evident that the underlying microstructure influences crack path and crack branching. Therefore, the influence of loading and cracking direction is necessary to explore due to the nature of horizontal and vertical welds on the canister. Two sample orientations will be evaluated in FY23 (T-S and L-S).

As highlighted as an extremely valuable validation method in FY22, future work will continue to include validation of crack growth with DCPD and fractography for SNL-tested specimens. Further characterization of the crack tip portion will also examine potential microstructural influences, such as strain-induced martensite and compositional differences, on the CGR and crack morphology.

4.5.2 Atmospheric SCC

To develop CGR measurements in more canister relevant environments, it is desired to move to atmospheric CGR testing. While a loading protocol has not been fully established for an atmospheric environment, development of an RH and temperature-controlled chamber representative of atmospheric SCC conditions on a load frame was performed. A temperature-controlled humidity generator was used to provide humid air for the chamber. Additionally, the chamber was wrapped with heater tape to maintain the temperature of interest. The RH stability of the humidity chamber is presented in Figure 92 and good stability was achieved for the 85 % RH and 55 ^{o}C set points that were utilized.

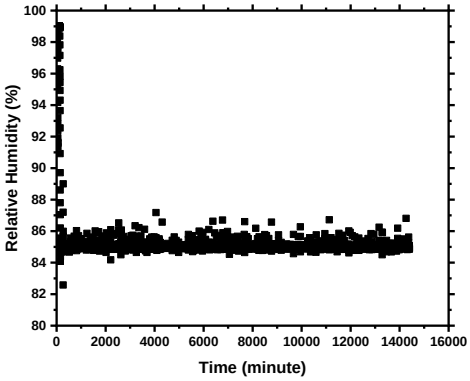

Figure 92: Relative humidity vs. time for the developed SCC chamber at 55 ˚C. The set RH value was 85 %.

Efforts in FY23 will focus on continued testing in more relevant conditions including CGR measurements in the described atmospheric chamber with enhanced loading protocol development.

This page is intentionally left blank.

5. Mitigation and Repair

As previously discussed, the potential conditions necessary for canister SCC exist at many ISFSI locations. The likelihood of a stable, corrosive Cl-rich surficial brine increases as storage times in these environments continue to increase (as the canister cools) thus it is becoming increasingly important to consider methods to prevent, mitigate, and/or repair potential SCC. As discussed in the SNL FY22 reports on corrosion resistant coatings and cold spray for mitigation and repair [18, 19], there are three main reasons why the application of a mitigation or repair strategy is unique for SNF canister conditions (as compared to other corrosion resistant coatings): 1) the specific dynamic and varied environment, 2) the space limitations/constraints for application, and 3) the necessity to comply with regulations and licenses set forth by the Nuclear Regulatory Commission (NRC). Additional challenges arise dependent on the intention or method of application of the mitigation and repair strategy. Three scenarios have been previously identified in the SNL FY20 Report on Corrosion-Resistant Coatings [62], and are discussed as ex-situ prevention, ex-situ repair, and in-situ repair, all of which have their own demands, some of which are described in Figure 93. Further complicating mitigation and repair efforts is the concept of "first do no harm" which requires demonstration that surface preparation processes, application processes, and the coating itself will not introduce additional risks or hazards to the storage system.

While acceptance criteria for any potential mitigation or repair strategy have yet to be defined, SNL seeks to better understand potential mitigation and repair strategies, the conditions and/or constraints that they will face during application, and their long-term materials degradation behavior. It must be ensured that any applied repair or mitigation strategy "does no harm" to the integrity or materials lifetime of the canister itself. SNL's ongoing work with respect to corrosion-resistant coatings and cold spray was detailed in two M3 reports in 2022 [18, 19] and summaries of the significant details of each are provided in the following sections.

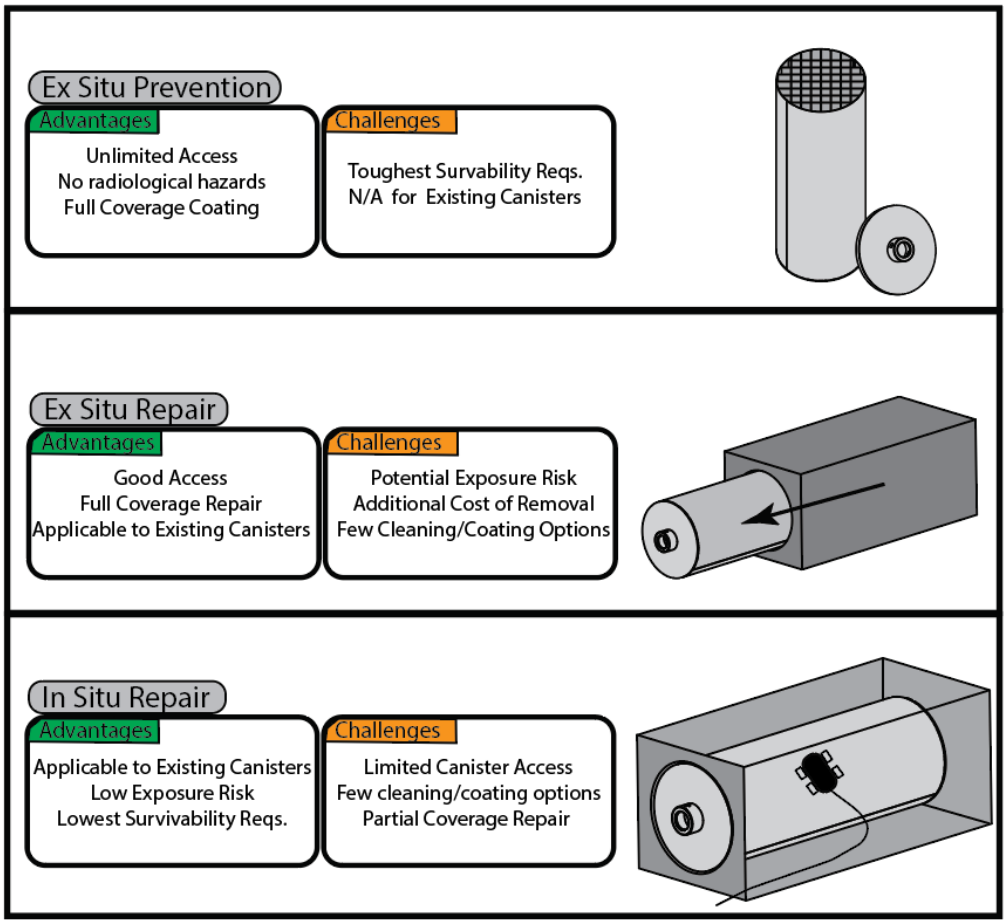

Figure 93. SNF Canister SCC prevention and repair coating scenarios [63].

5.1 Corrosion-Resistant Coatings

As corrosion resistant coatings are common across many areas of industry, SNL set up a memorandum of understanding (MOU) with four commercial coatings manufacturers in FY21 to make use of valuable expertise in the corrosion resistant coating area [63]. While specific coatings for SNF canister environments have not been developed or tested, the establishment of this MOU enabled SNL to utilize the wealth of information that coatings companies have developed over the years for corrosion resistant applications to help propose potential candidates for use with SNF canisters. The MOU allows SNL to evaluate a large matrix of possible coatings options to develop a collaborative exchange of information with the coatings vendors regarding both the production of the candidate coatings and the results of the performance testing. The four vendors were: LUNA Labs USA (LUNA), Flora Coatings Inc. (FC), Oxford Performance Materials (OPM) and White Horse R&D (WHRD). Performance testing began in FY22 on a total of 11 candidate coatings provided by the four vendors provided to SNL free of charge (Table 22) [63]. The coatings generally fell into two classes, polymeric coatings, and hybrid ceramic coatings. One subset of the ceramic coatings was investigated with and without a Zn-rich primer, which was added for galvanic protection. All coatings were applied on 3 x 6” rectangular SS304L coupons, in total SNL received 176 coated coupons for testing.

Table 22 Details of the provided candidate coatings

Coating Type	Coating Manufacturer	Variant	Trade Name	Details
Polymeric	OPM-21	01	OX-PEKK RESIN©	Polyetherketoneketone (PEKK) resin powder coat
		02	OX-PEKK SC©	Sulfonated PEKK solution cast
	WHRD-21	01	CRACKSTOP©	Polyurea-polyimide-phenolic composite
		02	GAMMABLOCK©	Polyurea-polyimide-phenolic composite
		03	GAMMABLOCK *PLUS*©	Polyurea-polyimide-phenolic composite
Organic/ Inorganic Hybrid Ceramic	FC-21	01	CLADCO©	1-part modified polyurethane macromolecule with quasi-ceramic structure
	LUNA-21	01	GENTOO© V1	2-part silica-ceramic with polyurethane linker
		02	GENTOO© V1	2-part silica-ceramic with polyurethane linker on Zn-rich primer
		03	GENTOO© V2	2-part silica-ceramic with polyurethane linker
		04	GENTOO© V2	2-part silica-ceramic with polyurethane linker on Zn-rich primer
		05	N/A	Commercial Zn-rich primer

Candidate coatings were evaluated to characterize their physical properties (such as thickness, surface finish, water contact angle, etc.) and their materials degradation performance in canister relevant corrosion environments. The basic physical and electrochemical performance of the coatings was evaluated using a suite of measurements as shown in Table 23. The volume of work performed in FY22 was focused on building an understanding of the properties of the candidate coatings and their baseline corrosion resistance. Each coating was treated identically, to represent a survey of the properties and performance of each coating system objectively. In some cases, treating the coatings identically was appropriate, but in other cases the chemical and mechanical differences between the coatings limited direct comparison of certain properties such as corrosion resistance and adhesion pull-off strength.

Table 23 Measurements performed on candidate coatings and methods used.

Measurement	Evaluation Method
Roughness	Optical Interferometry
Thickness	Ultrasonic, Eddy-Current, Optical Microscopy
Adhesion	ASTM D4541-17 Pull-Off Testing
Toughness	ASTM D7027-13 Scratch Testing
Hydrophobicity	Water Contact Angle Testing and Surface Tensiometry
Permeability	Electrochemical Impedance Spectroscopy

Upon receipt, all 176 coupons were photographed as a reference of the pristine coating surface. An example of each coating type is shown in Figure 94. The polymeric coatings were PEKK and polyurea/polyimide/phenolic composite resins and the hybrid ceramic coatings consisted of a silica-based ceramic with a polyurethane linker. Each coating type had multiple variants, some provided from different vendors (such as in the case of the hybrid ceramics; three variants were provided by two vendors). OPM provided two variants of their PEKK coating; a thick powder coated resin and a thin solution cast variant. WHRD provided three variants of their polyurea/polyimide/phenolic composite resin with varying amounts of proprietary fillers. LUNA provided five variants which included two hybrid ceramics, the same hybrid ceramic variants coated on top of a commercial Zn-rich primer and the same commercial Zn-rich primer without a top layer. FC provided a single hybrid ceramic variant.

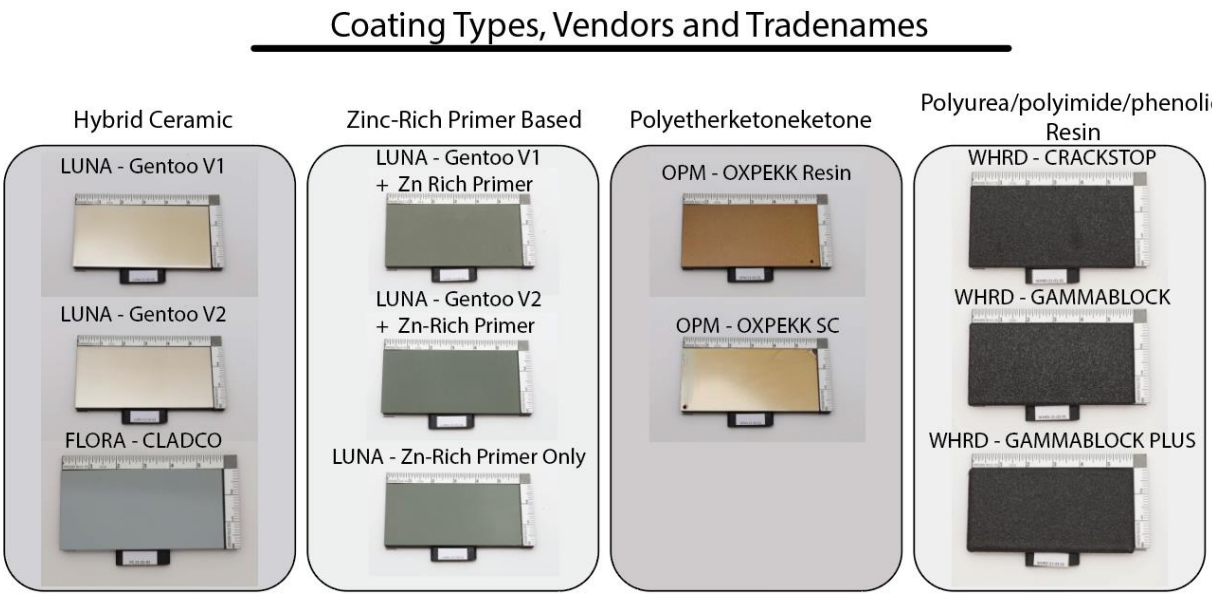

Figure 94. An example photo of each coating provided to SNL by each of the 4 vendors.

Mechanical characteristics such as surface roughness, adhesive strength, scratch toughness, and hydrophobicity were measured on the coatings. The Root Mean Square (RMS) area calculated surface roughness of the coatings ranged from 5.6-301.7 µm. The thickness of the coatings ranged from <0.0002 to 2.5mm. The pull-off force ranged from 675 to 2033 psi, however complete adhesive failure of all coatings was not achieved (likely meaning some measurements were minimum values). The scratch toughness of the coatings was highly dependent on the type of coating and ranged from 1-50 N. The hybrid ceramic coatings exhibited the lowest scratch toughness while the thick polymeric coatings (such as OPM OXPEKK Resin and all WHRD coatings) exhibited the highest. Hydrophobicity was expressed using two metrics: water contact angle and a maximum surface tension (mN/mm^2). These measurements were performed using pure DI water and two brines. The water contact angle for the coatings varied between 77.4 and 142.8 degrees with deionized water though there was a strong dependence on the surface finish of the coating (observed Cassie-Baxter state). Surface tensiometry is less dependent on surface finish than water contact angle and thus was used to determine the peak surface tension of water and brines on the surface of the coatings. The maximum surface tension ranged from 0.07 to 0.12 mN/mm^2 for deionized water. The water contact angle and the maximum surface tension also varied depending on the type of brine used to perform the measurement, indicating that surficial chemical interactions play an important role in how the brine wets the surface of the coatings. These interactions will be explored further in FY23.

The motivation to apply coatings on canisters is to prevent or eliminate corrosion of the underlying metal. Thus, the corrosion resistance of the coating was measured using electrochemical impedance spectroscopy (EIS). EIS is a powerful technique that measures the impedance of a material as a function of frequency. The permeability of water and ions through the coatings was expressed using three metrics obtained from an equivalent circuit fit of the raw impedance data as a function of cumulative immersion time: the absorbed volume fraction of water, the charge transfer resistance, and pore resistance. The absorbed volume fraction of water for most coatings was less than 0.12. The charge transfer and pore resistances varied over several orders of magnitude for the coatings from 10^5 to 10^{12} Ohms-cm^2. The high initial reactivity of the zinc-rich primers meant that the equivalent circuit used to fit the raw impedance was not ideal and misrepresented the performance of that type of coating. Efforts to improve the equivalent circuit used to interpret the zinc-rich primer data are underway.

30-day and 90-day atmospheric exposures were also performed to determine the susceptibility of the candidate coatings to atmospheric degradation. Following the atmospheric exposures, potential degradation was evaluated via colorimetric analysis and adhesion testing as well as EIS. The most dramatic colorimetric changes were observed after the 30-day exposure and were most pronounced on the thinnest coatings. The atmospheric exposures caused decreased adhesive pull-off forces in most of the coatings, though paradoxically also caused increased pull-off forces in some coatings likely caused by an increased adhesion of the pull-off dolly to the coating surface. The EIS behavior of the coatings after 30-days was nearly unchanged as compared to baseline EIS results for most of the coatings with exception of two WHRD variants which showed significantly decreased pore resistance and charge transfer resistance. At the time of writing, the 90-day EIS results had not yet been completed.

Collectively these results can provide indications for specific application scenarios for a given coating or identify specific attributes to be improved upon.

5.1.1 Experimental Plans for FY23

As described previously, the work performed in FY22 focused on baseline performance of the coatings under ambient temperature and radiolytic conditions [63]. In FY23, work will focus on evaluating the physical and electrochemical properties of the coatings after exposure to relevant thermal and radiolytic environments. Radiolytic exposures will be performed at the Gamma Irradiation Facility (GIF) at SNL. Thermal exposures will mimic realistic temperatures of the canister in a few application scenarios. Work will also focus on assessing the outgassing behavior of the coating at elevated temperatures (after curing) to understand what chemical species are liberated from the coating during its lifetime.

Results from these analyses will be combined with previous results to enable a data-driven down selection of the candidate coatings. Down selection of the coatings is an important step in the research process as it will allow the concentration of research resources on fewer candidates which should yield more detailed data on the selected coatings.

5.2 Cold Spray

Cold spray is a low heat input, additive metals technology, that has shown initial promise to both meet application needs for in-situ scenarios and have the initial desirable qualities to help prevent or repair canister SCC. SNL has worked on a collaborative effort with PNNL to evaluate various cold spray coatings with respect to canister application. This work has applied both accelerated ASTM standard tests for optimization and relevant atmospheric exposures for comparison. Additionally, as CS coatings may not be applied to the entire canister surface (for example in the case of in-situ repair as detailed in Figure 93), edge effects may play a role in material lifetime performance. Therefore, a large part of SNL and PNNL's work in FY22 has focused on evaluating potential edge effects and understanding factors that may enhance optimization. The following is a summary of the SNL FY2022 M3 on "Cold Spray for Canister SCC Mitigation and Repair".[19]

5.2.1 FY22 Cold Spray Experimental Evaluation

Much of the corrosion testing conducted in FY22 utilized similar accelerated corrosion testing as outlined in [40] for cold spray optimization. These included both potentiodynamic polarizations and Ferric Chloride pitting tests (ASTM G48 method A). Additionally, in FY22, a subset of samples were evaluated using boiling $MgCl_2$ accelerated conditions for SCC susceptibility (ASTM G36-94). Finally, more relevant atmospheric corrosion exposures for SNF canisters were explored including two static tests with deposited artificial seawater (40 and 75% RH at 35 ºC) and a cyclic test following procedures outlined in [40]. The samples evaluated in FY22 (with detailed descriptions of cold spray, experimental procedures, and results provided in the SNL FY22 M3 on Cold Spray [19]) are presented in Table 24.

Table 24. Cold Spray FY22 Exposures (x: exposed, -: insufficient samples to expose).

Cold Spray Sample	Potentiodynamic Polarization		Accelerated Pitting Exposure	Atmospheric Exposure			Boiling $MgCl_2$ Exposure
	NaCl	$FeCl_3$		40 % RH, 35 ºC	75 % RH, 35 ºC	Cyclic	
Inc He Tapered	x	x	x	x	-	x	x
Inc N Tapered	x	x	x	-	-	x	x
Inc N Masked	-	-	x	x	x	x	x
Ni N Tapered	x	x	x	x	-	x	x
Ni N Masked	-	-	x	x	x	x	x
Ni He Tapered	-	-	x	-	-	-	-
Ni He Masked	-	-	x	-	-	-	-
SC N Tapered	x	x	x	x	x	x	-
SC He Tapered	-	-	x	-	-	-	-
SC He Masked	-	-	x	-	-	-	-
SS316 + 25% CrC 410 N Tapered	-	-	x	-	-	-	-
SS316 + 25% CrC 410 N Tapered	-	-	x	-	-	-	-
SS316 + 25% CrC 410 N Tapered	-	-	x	-	-	-	-

Further materials characterization was carried out in FY22. This included powder analysis to accurately determine particle size and distribution post-sieving. Coatings were also analyzed for porosity and roughness. Hardness measurements were performed of the coatings, near-interface regions, and

underlying substrates. Finally, all samples that were received were characterized with optical microscopy prior to any further corrosion testing. A summary of these analyses can be found in the FY22 M3 report.[19]

5.2.2 Summary of FY22 Cold Spray Results

Potentiodynamic polarization scans were conducted in 0.6 M NaCl solutions and plotted along with the data obtained previously in FY21. All samples displayed higher open circuit potential values compared to the SS304 substrate material. Potentiodynamic polarizations for the as-sprayed and polished conditions are presented in Figure 95. In all cases, polishing reduced the instances of metastable pitting (seen as sharp increases in current on the polarization curves in a, but are absent in b). The breakdown potential of the nickel sample remains low in both as-sprayed and polished conditions for the helium processed condition. The samples processed with helium, which have lower porosities, exhibit in general lower passive current densities for the polished surfaces. Further summaries of the open circuit potentials in NaCl and $FeCl_3$ are presented in the FY22 M3.[19]

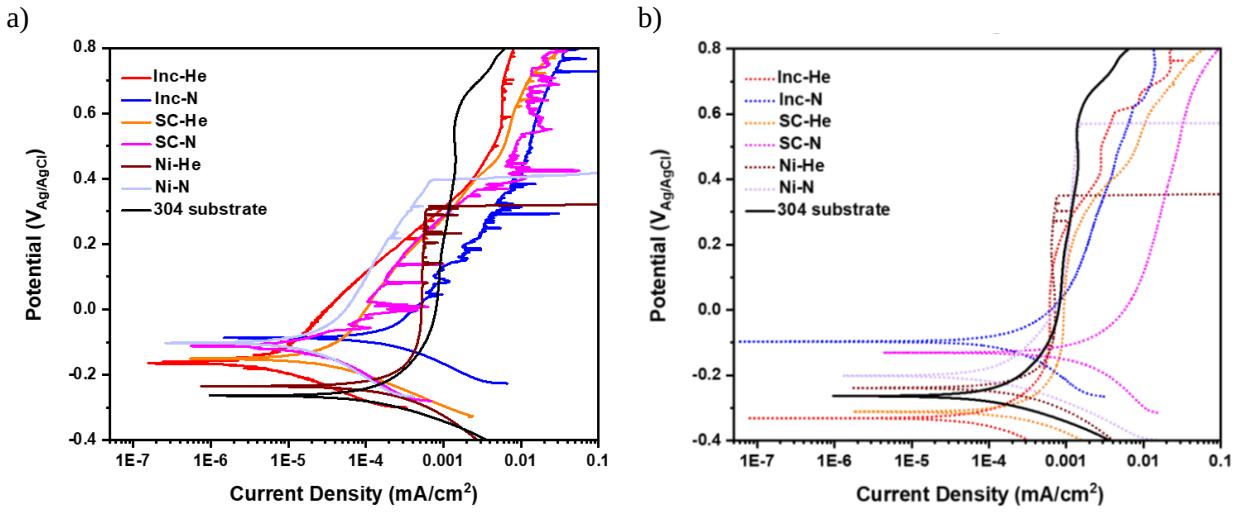

Figure 95. Potentiodynamic scans of cold spray materials for (a) as-sprayed and (b) samples polished to 1200 grit. All scans were conducted in 0.6 M NaCl solution and are compared to the base material (black).

All samples exposed under the accelerated pitting conditions displayed enhanced attack that occurred at the interface between the SS304L base material and the cold spray. Example top-down SEM images are provided for two masked samples in Figure 96. Noticeably, for the masked edge samples, pits occur at a distance from the cold spray edge combined with additional attack at the cold spray edge itself. A similar attack morphology was observed through atmospheric testing, as evidenced by the Inconel and Nickel samples in Figure 96. The FY22 M3 report delves further into the details of the corrosion morphology. Overall, the M3 [19] displays that the accelerated ferric chloride pitting test (ASTM G48 method A) provides a good option for accelerated testing for cold spray optimization for corrosion resistance as it replicates similar corrosion attack observed on the sample surfaces. However, further analysis of the potential attack beneath the cold spray itself will be carried out in FY23. Underlying attack was observed for the ferric chloride pitting tests, an example is displayed in Figure 97-d for the Inconel nitrogen masked sample. However, it is unknown whether similar attack morphology beneath the cold spray formed in the atmospheric exposures.

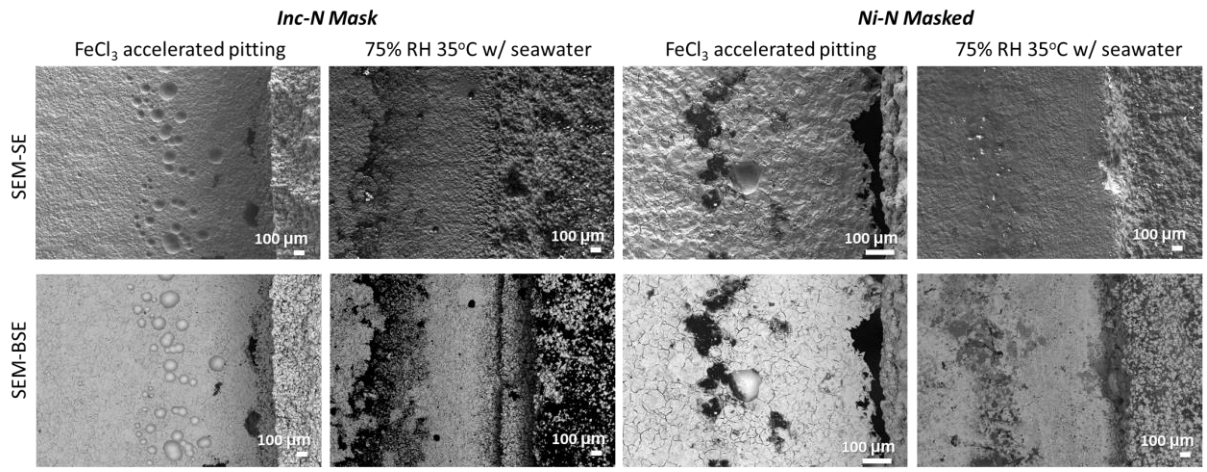

Figure 96. Scanning electron microscopy images at the interface regions after ferric chloride exposure compared to post-atmospheric exposure at 75% RH and 35 ºC with printed seawater for Inconel-nitrogen masked and Nickel-nitrogen masked. The top row of images are secondary electron (SE) images and the bottom are back-scattered electron (BSE) images. For all images, the base material is oriented to the left and the cold spray to the right.

Work in FY22 also sought to determine the potential underlying mechanisms that led to enhanced corrosion attack at the cold spray base material interfaces. While the attack can be attributed in part to materials selection and the extent of the potential galvanic couple formed at the interface, the morphology of the underlying attack was additionally found to be influenced by two other factors; the porosity of the cold spray coating and the deformation of the underlying substrate. As described further in the year-end report [19], the extent to which the underlying corrosion also attacked into the cold spray layer itself correlated directly with the porosity. Additionally, it appears that the underlying attack may have initiated due to deformation in the substrate at the near interface layer from the cold spray process. Figure 97 displays the cross-sectional analysis with phase identification and EBSD inverse pole figures (which display crystal orientation). The phase maps in Figure 97-b and f display that there is no enhanced concentration of BCC phases (potentially martensitic phases) near the interface. However, it is important to note that the very near interface region does not provide a clear signal (appears black) due to high deformation. The EBSD far from the patch edge, Figure 97-c, does reveal a layer of deformation appearing as a watercolor-like pattern in the phase image, extending approximately 20 µm into the substrate. This layer is much thinner than that of the corrosion damage. At the corrosion front, however, the corroded area is much narrower, similar in magnitude to the deformation layer. The deformed layer in the SS304L substrate material is likely the region in which the underlying attack initiates, but it may not be the sole contributor to the corrosion front. Further details, including analysis of multiple samples, are provided in the FY22 M3.[19]

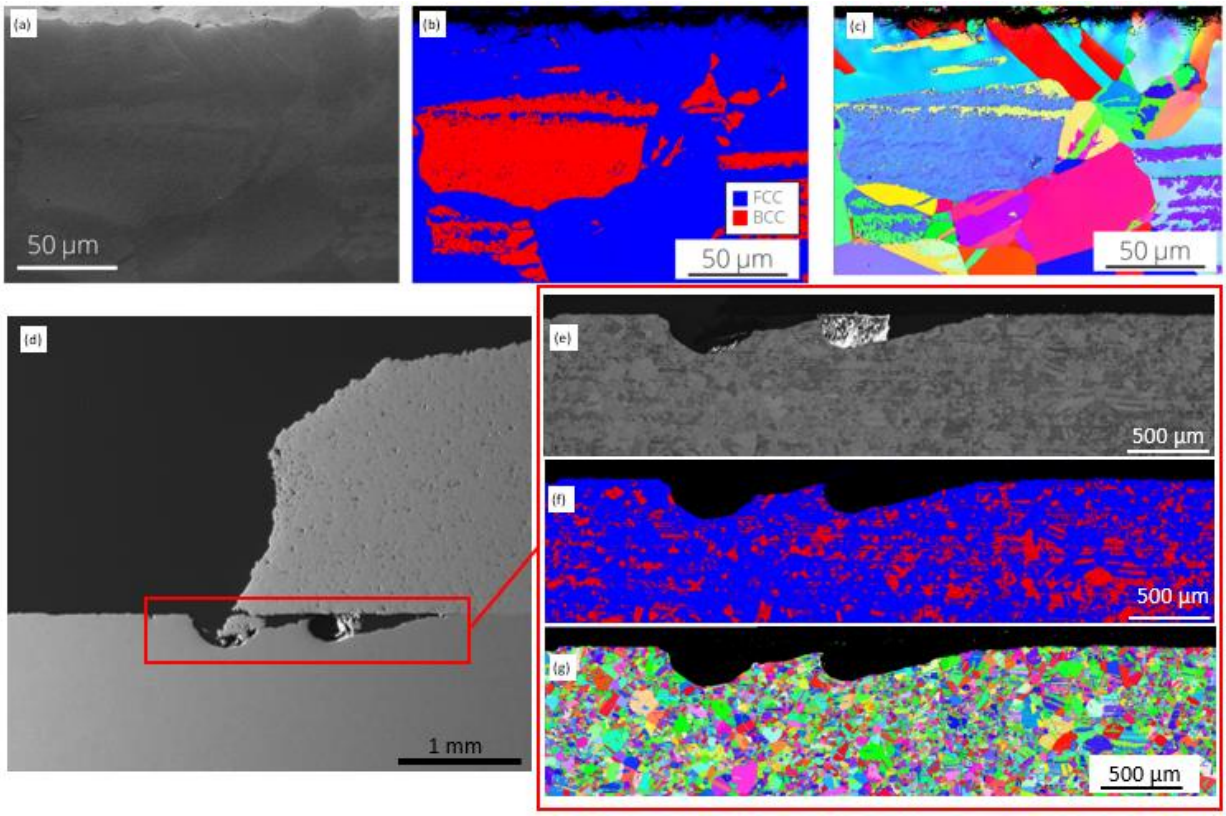

Figure 97. (a) Forward scatter detector micrograph, (b) phase map, and (c) EBSD inverse pole figure (displaying crystal orientation in the x direction) for the Inconel-nitrogen masked sample, far from the patch edge. Also shown is (d) scanning electron microscopy at the patch edge and the corresponding (e) band contrast, (f) phase map, and (g) electron backscatter diffraction.

In FY22, a subset of the cold spray coupons was also exposed in boiling $MgCl_2$ solution for one week. While coupons were exposed without applying an external stress, the objective was to determine if the cold spray deposition process itself induced significant strain at the patch edges (to counterbalance the compressive stress beneath the patches) that might potentially reduce the resistance to SCC. Optical images were taken of the interface regions post exposure and are provided in Figure 98. While significant corrosion damage is observed, no visual signs of cracking at the interface were observed. However, further investigation with SEM and cross-sectional analysis are planned to be carried out in FY23 to fully determine the extent of the damage. Additional plans may include larger sample sets (when coupons are available) and sets of cold spray on stressed samples to better mimic weld regions and weld residual stresses.

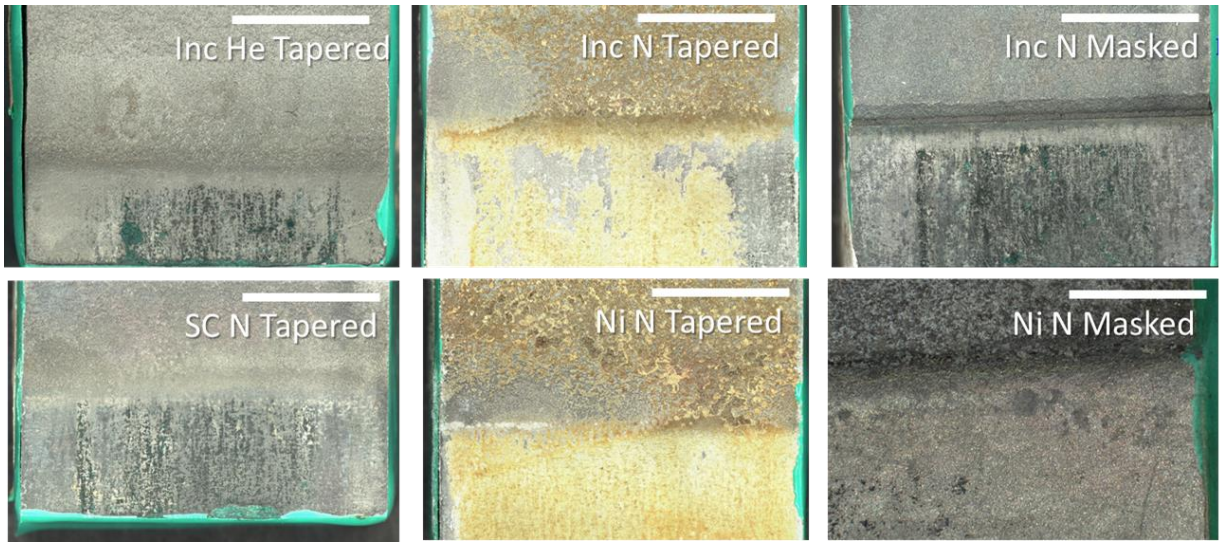

Figure 98. Optical images of interface regions post-boiling $MgCl_2$ exposures for one week. Samples display corrosion attack, but no SCC indication visibly (note samples were not stressed during exposure, only residual stresses due to CS are present). Scale bars are 10 mm for all.

5.2.3 Cold Spray Conclusions and Future Work

High pressure cold spray is considered a leading technology as a barrier coating for mitigation and repair of SNF dry storage canisters. Cold spray has been shown to be a promising technique as a corrosion barrier in various applications yet needs further evaluation in canister relevant conditions. The work presented herein was a preliminary analysis to help understand the corrosion behavior of cold spray to aid in its optimization as a coating barrier for relevant environments.

Consistent with learnings in FY21, full immersion accelerated electrochemical testing continued to indicate that the surface roughness of the cold spray material plays a role in its susceptibility to metastable pitting; grinding the surface improved the resistance to metastable pitting. Additionally, the role of the dissimilar metals at the interface was further explored in FY22. This was observed in $FeCl_3$ accelerated pitting testing where all interfaces of the samples examined presented the most deleterious regions for corrosion. Cross-sectioning of the exposed samples displayed that the attack at the interface extended beneath the cold spray patches in all cases for the accelerated $FeCl_3$ immersion exposure. In samples with greater porosity in the cold spray coating, the attack was observed to extend into the cold spray itself. Additional metallography was carried out on these cross-sections and a region of deformation of the substrate was observed near the interfaces. It is believed that the underlying attack initiates in this highly deformed layer and then continues further with expanded growth near the mouth due to the crevice formed and the galvanic conditions present. However, this still warrants further analysis under relevant atmospheric conditions to establish if underlying attack will also occur in these. Also, in FY22, relevant atmospheric exposures were carried out for times of up to 10 weeks exposure. Both optical and SEM imaging indicated enhanced attack at the cold spray/base material interface under all atmospheric exposure conditions. Additionally, the morphology of attack for both the masked and tapered samples from the top-down images displayed the same form as the morphology of attack in the full immersion accelerated tests. While further cross-sectional analysis is necessary to determine the full extent of attack at the interface and the potential subsurface attack, these studies indicate that the selected accelerated corrosion tests are applicable tools for optimization of cold spray coating for use under marine atmospheric exposure conditions. Finally, in FY22, initial exposures were carried out in boiling $MgCl_2$

solutions to evaluate the potential effects of the cold spray process itself on SCC resistance. Initial optical images indicated that corrosion attack occurred, but did not indicate enhanced SCC susceptibility.

Thus far, from both accelerated and relevant atmospheric examinations of cold spray samples, three main factors have been determined to influence corrosion and could benefit most from process optimization; cold spray porosity, cold spray material selection, and interface geometry. With regards to porosity, lowered porosity of the cold spray led to reduced attack of the cold spray layer itself. Thus, optimization of spray processes to reduce porosity may enhance cold spray as a protective coating. Material selection, specifically materials that were closer in composition and corrosion potential to the base material, showed less influence of galvanic attack. Ni, which is farther from SS304L stainless steel than the other tested cold spray materials showed the highest signs of attack. Optimizing material selection to reduce galvanic potentials may enhance overall protection capabilities. Finally, the interface morphology itself led to different modes of attack, with tapered interfaces spreading the damage and masked interfaces concentrating it further near the interface. It has not been determined which is better yet for overall protection, but further optimization of the morphology may help reduce the long-term attack. Optimization of coatings with respect to all three of these properties and analysis of the subsequent corrosion performance of the coatings will be the focus of work to be carried out in future FYs.

This page is intentionally left blank.

6. Summary and Future work

This report summarizes work carried out by Sandia National Laboratories (SNL) in the fiscal year 2022 (FY22) to evaluate the potential occurrence of stress corrosion cracking (SCC) on spent nuclear fuel (SNF) dry storage canisters. Gap analyses by the US Department of Energy (DOE), the Nuclear Regulatory Commission (NRC), the Nuclear Waste Technical Review Board (NWTRB), and the Electric Power Research Institute (EPRI) have all determined that an improved understanding of the occurrence and risk of canister SCC is critical to demonstrating the safety of long-term dry storage. Should canister penetration by SCC occur, the containment boundary represented by the canister would be breached, leading to loss of the inert environment (helium) within the canister and intrusion of air and moisture, which could react with and damage the fuel within the canister. For this reason, the DOE is funding an effort to evaluate the occurrence and potential consequences of storage canister SCC and to develop prevention, mitigation, and repair technologies for this degradation mechanism, if it should occur.

The SCC program has three primary thrusts: (1) Define the canister surface environment, as this affects corrosion initiation and growth, (2) evaluate corrosion as a function of material and environment: pitting, SCC initiation, and growth, and (3) evaluate mitigation and repair technologies for SCC, should it occur on in-service canisters.

The context for the first two thrusts is provided by a probabilistic model, developed by SNL, to estimate timing of canister SCC. As large uncertainties currently exist for certain model parameters, this model is not used to predict canister penetration times by SCC, but rather to perform parameter sensitivity studies to focus experimental work. Several parts of the probabilistic model were updated in FY22, including the weather, dust deposition, and maximum pit size modules, and the model was then exercised to evaluate model behavior. These updates were documented in a L3 milestone in July 2022 and were only mentioned briefly in this report.

Canister surface environment:

At near-marine sites, corrosive brines form by deliquescence of sea-salt aerosols on the canister surfaces. Using thermodynamic modeling and laboratory testing, brine compositions and properties for a range of canister conditions were characterized. These will be utilized to inform corrosion modeling and testing. The data directly feed the maximum pit size model in the SNF probabilistic canister SCC model. A manuscript was published in FY22 (*Science of the Total Environment*) on the evolution of sea-salt deliquescent brines as a function of temperature (T) and relative humidity (RH).

Also, in FY22 dusts were collected and analyzed from in-service dry storage canisters from two ISFSI sites, an east-coast estuarine site, and an inland site. These analyses are critical to understanding canister surface environments and defining the range of conditions necessary for modeling and corrosion testing. Dust from the estuarine site consisted largely of organic particles—pollen and plant fibers (stellate trichomes); soluble salts were dominated by sulfate and nitrate, but significant chloride was present. Data from the inland site were restricted to samples from the overpack outlet vents and were almost entirely calcium carbonate and calcium sulfate. These data are provided to site operators to aid in development of aging management plans.

On the surface of SNF dry storage canisters, elevated temperatures will restrict sea-salt deliquescent brines to $MgCl_2$-rich compositions for hundreds of years; understanding the T and RH conditions at which those brines will persist stably is critical to evaluating the timing of corrosion and canister SCC. Analysis of $MgCl_2$ brine stability at elevated temperatures was continued in FY22. Two experiments were carried out, and the results indicated that chloride loss, coupled with carbonate absorption and hydroxide formation, had occurred. However, apparent chloride loss was less than expected at the higher-temperature experiment, and additional testing is necessary. In addition to the testing, a thermodynamic database for modeling $MgCl_2$ brine stability was completed. New thermodynamic data was developed for several Mg-hydroxychlorides, allowing for evaluation of Mg-brine stabilities as a function of T and RH.

In addition to being necessary to determine the potential timing and surface conditions for corrosion and SCC, this database is also critical for interpreting the results of elevated temperature accelerated laboratory tests, which in some case, have resulted in brine dry-out, as Mg-hydroxychloride phases precipitate.

Finally, several support studies for the CDFD project were carried out. SNL has developed techniques to measure canister surface roughness via the combination of molds and laser surface profilometry , to quantitatively hand-sample canister surface deposits using templates and moist sponges, and to monitor ambient aerosol particles using several different aerosol characterization instruments. Finally, corrosion testing was also performed on canister marking and thermocouple attachment techniques, to determine which are least detrimental to the canister surface in anticipated exposure conditions. This work was documented in a L3 milestone submitted in April 2022; a summary is provided here, along with updates on work performed since then.

Corrosion testing:

In FY-22, several ongoing tests evaluating environmental effects on pitting were continued, and additional testing was initiated. First, brine composition effects, including the influence of carbonates in $MgCl_2$ dominated brines, were evaluated. Pit morphology displays a dependence not only on NaCl vs $MgCl_2$ dominated brines, but also an association of microcrack formation with the presence of carbonate in the $MgCl_2$ brines was observed. This is significant, as in near-marine environments, where salt aerosols are sea-salt particles, $MgCl_2$-rich brines will form first as the canister cools (and will be present for up to hundreds of years for typical canister heat loads). As these brines may also contain carbonates, the correlation to microcracking formation may have a significant implication for pit to crack transition and SCC.

Also, in FY22, as a part of the overall probabilistic SCC model, the environmental dependencies of the maximum pit size model were evaluated. This model, developed at SNL, is a critical factor in determining the timing of pit-to-crack transition. Sea-salt deliquescent brine physical, chemical, and electrochemical properties were determined via thermodynamic modeling and laboratory measurements to parameterize this model. Developing and parameterizing the maximum pit size predictions over such a large variable space in FY22 enabled a better understanding of the key influencing variables and prediction of environments and conditions that will likely lead to higher corrosion susceptibility, and thus SCC susceptibility.

SNL also has several ongoing long-term atmospheric environmental exposures. SNL has defined relevant exposure testing conditions (based on canister dust sampling and geochemical modeling) to evaluate three significant parameters for corrosion and potentially pit to crack transition:

- *Diurnal cycles in temperature and RH*. A two-year exposure at the canister-relevant cycle was completed in FY22 and post-exposure processing of samples is in progress. The development of qualitative SEM analysis combined with electrochemistry and cross-sectional images with HREBSD for dislocation density maps, has helped to elucidate additional influential variables for corrosion damage and morphology. Initial observations have shown that a combined influence of brine composition, material surface finish, and material composition govern the pit morphology, with rougher surfaces, $MgCl_2$ dominated brines, and less corrosion resistant SS resulting in more irregular shaped pits with microcracking. In environments with brines that are dominated by NaCl, reduced surface roughness (and residual stresses), and more passive SS, the pit morphologies become more hemispherical with crystallographic attack. These initial findings help establish variables that may increase the susceptibility for a pit to crack transition and potential for SCC, however ongoing research will further elucidate these.
- *Presence of inert dust particles*. Inert particles can potentially affect corrosion by spreading brine layers via capillary processes or by acting as crevice formers. A 2-year exposure test is in progress; initial observations are summarized in this report. It appears that the larger dust

particles (75 µm) do not play a role in spreading electrolyte on the surface for the lower RH or cyclic exposures. However, at higher RH, larger droplet or electrolyte spreading can be observed, but needs further analysis. Very preliminary corrosion observations have maintained that characteristic pit morphologies form under the higher RH exposures, even in the presence of dust, but appear to be much larger in size than those previously observed, but further analysis is necessary to make any definitive comparisons.

- *Effect of brine chemistry (nitrate)*. Nitrate is a major component in canister surface salts. A series of potentiodynamic polarization studies were completed displaying a dependence of passivity on nitrate: chloride ratio (increasing with increased nitrates), temperature (inversely proportional), and scan rate (passivity decreased at slower scan rates). Preliminary atmospheric exposure tests were carried out to evaluate the impact of nitrate under more canister relevant conditions. However, even under very high nitrate:chloride ratios of 4:1, corrosion was still observed under atmospheric exposure. As the developed cycle tested alters both the brine volume and brine composition with the changing RH, and additionally, as precipitates may form, this does not necessarily contradict the full immersion experiments, but highlights the need to better understand the dynamic nature of the electrolyte and the resultant corrosion response under atmospheric conditions.

Additional studies were carried out to begin evaluating the process of SCC crack initiation. As SCC cracks initiate from pits, this is commonly referred to as the pit to crack transition. An exposure matrix was developed to evaluate the effects of RH/brine composition as well as material surface finish. Exposures were completed in FY22 and initial analysis is underway, indicating there may be an influence of surface finish on the resultant corrosion damage. A manuscript reviewing literature data on pit-to-crack transition processes was submitted as an "invited critical review" (*CORROSION Journal*).

Stress corrosion cracking work at SNL included both modeling and experimental work. SNL, in collaboration with UVA, developed a reactive transport finite element model to determine the influence of environmental parameters on crack tip electrochemistry and SCC. This model illustrated the importance of crack and sample geometry in crack tip electrochemistry and crack growth rates. A manuscript detailing initial 2D variations of this model was accepted in September 2022 (*Corrosion Science*). SCC crack growth rate testing in different relevant brines (NaCl and $MgCl_2$) is also in progress. The direct current potential drop (DCPD) system was benchmarked for crack growth measurements using fractography. Also, measured crack growth rates in corrosive environments were correlated to fractography to enhance the understanding of environmental influences on CGR and on crack morphologies observed under SNF-relevant conditions (saturated NaCl, $MgCl_2$, and sea-salt deliquescent brines). Finally, an in-situ crack tip electrochemistry measurement technique was developed and implemented to better understand the influence of environmental parameters on CGR. Initial findings highlighted both the significance of sample geometry and external polarization on CGR measurements.

Mitigation and Repair:

The potential use of corrosion-resistant coatings is being evaluated at SNL. Although a different work package, there is considerable technical overlap, and the coatings work, described in detail in an L3 Milestone report submitted in August 2022, is summarized here. A suite of coating samples obtained from industry have undergone adhesion, scratch, and wettability testing, and pre- and post-exposure electrochemical testing. These Phase I analyses will be used to screen the coatings for Phase 2 Analysis in FY23, which will include evaluations of thermal and radiation-induced degradation.

SNL also has an effort to evaluate the potential use of cold spray as a mitigation and repair technique. SNL used samples provided by PNNL, performing corrosion evaluation, both under accelerated testing conditions to aid optimization and in more relevant atmospheric exposures to understand aging and lifetime properties. This is high priority work, as industry is working to develop a procedure for CS

application to dry storage canisters. In FY22, Sandia evaluated several CS compositions and began exposure testing in relevant T/RH environments. SNL submitted a Level 3 Milestone on the CS work in September 2022 and identified three areas of optimization to reduce corrosion effects and aid in development of CS for canister-relevant applications: 1) reduction of CS layer porosity, 2) proper selection of compatible CS materials to reduce electrochemical effects (e.g., galvanic coupling), and 3) geometric optimization of the CS/base material edge interface. A short summary is provided in this report.

Planned work in FY23

In FY 23, work will continue on all three fronts. Characterization of canister surface environments will continue including further anticipated sampling from in-service canisters which will be analyzed to add to the growing database of dust soluble salt compositions. The newly developed thermodynamic database for Mg-hydroxychlorides will be utilized to model $MgCl_2$ brine stabilities over a range of canister-relevant conditions and also, at conditions used for accelerated corrosion testing. Thermodynamic modeling and experimental studies will be used to measure deliquescence RH values for complex brine mixtures—specifically, those containing nitrate salts (current databases offer conflicting predictions). These data provide information on the potential timing of corrosion as SNF dry storage canisters cool. They will also be used to define the relevant T/RH ranges for corrosion testing. For the CDFD project, the aerosol sampling equipment will be exercised to verify proper operation and to train personnel. Aerosol sampling will be performed at the proposed field site to determine site-specific sampling parameters necessary to set up the equipment for the CDFD test itself. Finally, hand-sampling techniques will continue to be improved and will be tested on a real canister to evaluate the effects of geometry and access limitations.

Corrosion work will include continuing environmental exposures to evaluate pertinent variables (diurnal cycling, inert dust, and nitrates) and post-test analysis to inform governing factors for corrosion. The pit-to-crack transition work will be expanded based upon the knowledge gained from both large-scale corrosion exposures and initial U-bend matrices. The data produced will be applied to understand governing variables for both development of critical pits (pits that transition to cracks) and conditions under which these are expected to form. Of interest in FY23, research will be carried out to evaluate the effects of iron contamination and rust on pitting and SCC initiation in stainless steel. Finally, we will move into a new phase of CGR studies, with the goals of establishing proper SCC testing protocol, developing valuable measurements under canister-relevant conditions, and expanding testing conditions to atmospheric scenarios more representative of actual canister exposures.

FY23 will also continue further investigation and evaluation of potential mitigation and repair strategies. Although funding limitations will limit sample availability, continued testing of existing CS materials and post-test analysis of exposed CS samples to further evaluate effects of significant variables, both in terms of material and environment, that are valuable to understand for future optimization. With respect to corrosion-resistant coatings, Phase 2 of evaluating industry-provided corrosion-resistant coatings will be initiated, with a focus on evaluating thermal and radiation degradation of those coatings that survived the initial screening tests.

Overall, SNL has continued to advance the understanding of the potential for canister CISCC through establishing a better knowledge of the probable canister surface environment and how in turn, this effects the subsequent corrosion and SCC susceptibility. Work in FY22 elucidated strong links between the developed environment and the corrosion damage, pit to crack transition, and crack growth rates. In FY23, SNL will continue to pursue research that furthers understanding of these dependencies of CISCC through the mentioned three-pronged approach and develop mitigation and repair strategies based upon knowledge from these learnings.

7. References

1. Hanson, B., H. Alsaed, C. Stockman, D. Enos, R. Meyer, and K. Sorenson, *Gap Analysis to Support Extended Storage of Used Nuclear Fuel*. 2012, Pacific Northwest National Laboratory: Hanford, WA. p. 218.
2. NWTRB, *Evaluation of the Technical Basis for Extended Dry Storage and Transportation of Used Nuclear Fuel*. 2010, Nuclear Waste Technical Review Board. p. 145.
3. NRC, *Identification and Prioritization of the Technical Information Needs Affecting Potential Regulation of Extended Storage and Transportation of Spent Nuclear Fuel.* 2014, U.S. Nuclear Regulatory Commission: Washington, D.C. p. 138.
4. EPRI, *Extended Storage Collaboration Program (ESCP) Progress Report and Review of Gap Analyses*. 2011, Electric Power Research Institute: Palo Alto, CA. p. 234.
5. Teague, M., S. Saltzstein, B. Hanson, K. Sorenson, and G. Freeze, *Gap Analysis to Guide DOE R&D in Supporting Extended Storage and Transportation of Spent Nuclear Fuel: An FY2019 Assessment*. 2019, Sandia National Laboratories: Albuquerque, NM. p. 42.
6. Bryan, C.R. and A.W. Knight, *Analysis of Dust Samples Collected from an Inland ISFSI Site ("Site A")*. 2020, Sandia National Laboratories: Albuquerque, NM. p. 44.
7. Knight, A.W. and C.R. Bryan, *Analysis of Dust Samples Collected from an Inland ISFSI Site ("Site B")*. 2020, Sandia National Laboratories: Albuquerque, NM. p. 61.
8. Bryan, C.R., A.W. Knight, and M.K. Maguire, *Analysis of Dust Samples Collected from a Near-Marine East Coast ISFSI Site ("Site C")*. 2022, Sandia National Laboratories. p. 42.
9. Lindgren, E.R., S.G. Durbin, S.R. Suffield, and J.A. Fort, *Status Update for the Canister Deposition Field Demonstration*. 2021, Sandia National Laboratories: Albuquerque, NM. p. 42.
10. Bryan, C., A. Knight, R. Schaller, S. Durbin, B. Nation, and P. Jensen, *Surface Sampling Techniques for the Canister Deposition Field Demonstration*. 2021, Sandia National Laboratories: Albuquerque, NM. p. 34.
11. Knight, A., R. Schaller, B. Nation, S. Durbin, and C. Bryan, *FY22 Update: Development of Surface Sampling Techniques for the Canister Deposition Field Demonstration* 2022, Sandia National Laboatories: Albuquerque, NM. p. 54.
12. Srinivasan, J., A.M. Parey, A.W. Knight, R.F. Schaller, J.S. Locke, and E.J. Schindelholz, Correlation of Stainless Steel Pit Morphology to Humidity-Specific Sea Salt Brine Constituents. *Corrosion Journal*, 2022. **4143**.
13. Gilkey, L., D. Brooks, R. Katona, C. Bryan, and R.F. Schaller, *FY22 Status Update: A Probabilistic Model for Stress Corrosion Cracking of SNF Dry Storage Canisters*. 2022, Sandia National Laboratories.
14. Katona, R.M., E.K. Karasz, and R.F. Schaller, *A Review of the Governing Factors in Pit to Crack Transitions in Metallic Structures*, in *Corrosion Journal*. 2022: Under Review.
15. Katona, R.M., Burns, J.T., Schaller, R.F., Kelly, R.G., *Insights from Electrochemical Crack Tip Modeling of Atmospheric Stress Corrosion Cracking*. 2022: Submitted to Corrosion Science.
16. Newman, J. and I. Raju, An Empirical Stress-Intensity Factor Equation for the Surface Crack. *Engineering Fracture Mechanics*, 1981. **15**(1): p. 185-192.
17. Newman, J.C. and I.S. Raju, *Analysis of Surface Cracks in Finite Plates Under Tension or Bending Loads*. 1979, NASA: Hampton, VA.
18. Knight, A.W., Nation, B.L., Maguire, M., Schaller, R.F., Bryan, C., *FY22 Status: Corrosion Resistant Coatings on Spent Nuclear Fuel Canisters to Mitigate and Repair Potential Stress Corrosion Cracking*, U.S.D.o. Energy, Editor. 2022.
19. Schaller, R.F., E. Karasz, T. Montoya, J. Taylor, and K. Ross, *FY22 Status Report: Cold Spray for Canister SCC Mitigation and Repair*. 2022, Sandia National Laboratories: Albuquerque, NM. p. 52.

20. Bryan, C.R., A.W. Knight, R.M. Katona, A. Sanchez, E.J. Schindelholz, and R.F. Schaller, Physical and Chemical Properties of Sea Salt Deliquescent Brines as a Function of Temperature and Relative Humidity. *Science of the Total Environment*, 2022. **824**: p. 154462.
21. Kahnt, A., Y. Iinuma, F. Blockhuys, A. Mutzel, R. Vermeylen, T.E. Kleindienst, M. Jaoui, J.H. Offenberg, M. Lewandowski, O. Böge, H. Herrmann, W. Maenhaut, and M. Claeys, 2-Hydroxyterpenylic Acid: An Oxygenated Marker Compound for α-Pinene Secondary Organic Aerosol in Ambient Fine Aerosol. *Environmental Science & Technology*, 2014. **48**(9): p. 4901-4908.
22. Bryan, C. and D. Enos, *Analysis of Dust Samples Collected from Spent Nuclear Fuel Interim Storage Containers at Hope Creek, Delaware, and Diablo Canyon, California*. 2014, Sandia National Laboratories: Albuquerque, NM. p. 281.
23. NADP. *National Atmospheric Deposition Program (NRSP-3)*. 2022 9/19/2022]; Available from: https://nadp.slh.wisc.edu/.
24. Bryan, C. and D. Enos, *Analysis of Dust Samples Collected from an In-Service Interim Storage System at the Maine Yankee Nuclear Site*. 2016, Sandia National Laboratories: Albuquerque, NM. p. 51.
25. Bryan, C. and E. Schindelholz, *FY18 Status Report: SNL Research into Stress Corrosion Cracking of SNF Interim Storage Canisters*. 2018, Sandia National Laboratories: Albuquerque, NM. p. 77.
26. Schaller, R., A. Knight, C. Bryan, and E. Schindelholz, *FY19 Status Report: SNL Research into Stress Corrosion Cracking of SNF Dry Storage Canisters*. 2019, Sandia National Laboratories: Albuquerque,NM. p. 98.
27. Schaller, R.F., A.W. Knight, C.R. Bryan, B.L. Nation, T.J. Montoya, and R.M. Katona, *FY20 Status Report: SNF Interim Storage Canister Corrosion and Surface Environment Investigations*. 2020, Sandia National Laboratories: Albuquerque, NM. p. 209.
28. Schindelholz, E., C. Bryan, and C. Alexander, *FY17 Status Report: Research on Stress Corrosion Cracking of SNF Interim Storage Canisters*. 2017, Sandia National Laboratories: Albuquerque, NM. p. 59.
29. Weirich, T.D., J. Srinivasan, J.M. Taylor, M.A. Melia, P.J. Noell, C.R. Bryan, G.S. Frankel, J.S. Locke, and E.J. Schindelholz, Humidity Effects on Pitting of Ground Stainless Steel Exposed to Sea Salt Particles. *Journal of The Electrochemical Society*, 2019. **166**(11): p. C3477-C3487.
30. Katona, R.M., J.C. Carpenter, A.W. Knight, C.R. Bryan, R.F. Schaller, R.G. Kelly, and E.J. Schindelholz, Importance of the Hydrogen Evolution Reaction in Magnesium Chloride Solutions on Stainless Steel. *Corrosion Science*, 2020. **177**: p. 108935.
31. Katona, R.M., R.G. Kelly, C.R. Bryan, R. Schaller, and A.W. Knight, Use of In Situ Raman Spectroelectrochemical Technique to Explore Atmospheric Corrosion in Marine-Relevant Environments. *Electrochemistry Communications*, 2020. **118**: p. 106768.
32. SNL, *In-Drift Precipitates/Salts Model*. 2007, Sandia National Laboratories: Las Vegas, NV. p. 358.
33. Dinnebier, R.E., M. Pannach, and D. Freyer, $3Mg(OH)_2 \cdot MgSO_4 \cdot 8H_2O$: A Metastable Phase in the System $Mg(OH)_2$-$MgSO_4$-H_2O. *Zeitschrift für anorganische und allgemeine Chemie*, 2013. **639**(10): p. 1827-1833.
34. Pannach, M., S. Bette, and D. Freyer, Solubility Equilibria in the System $Mg(OH)_2$-$MgCl_2$-H_2O from 298 to 393 K. *Journal of Chemical and Engineering Data*, 2017. **62**(4): p. 1384-1396.
35. Dinnebier, R.E., M. Oestreich, S. Bette, and D. Freyer, $2Mg(OH)_2$:$MgCl_2$: $2H_2O$ and $2Mg(OH)_2$: $MgCl_2$:$4H_2O$, Two High Temperature Phases of the Magnesia Cement System. *Zeitschrift Fur Anorganische Und Allgemeine Chemie*, 2012. **638**(3-4): p. 628-633.
36. Christov, C., Chemical Equilibrium Model of Solution Behavior and Bishofite ($MgCl_2$: $6H_2O_{(cr)}$) and Hydrogen-Carnallite (HCl: $MgCl_2$:$7H_2O_{(cr)}$) Solubility in the $MgCl_2$ + H_2O and HCl-$MgCl_2$ + H_2O Systems to High Acid Concentration at (0 to 100) degrees C. *Journal of Chemical and Engineering Data*, 2009. **54**(9): p. 2599-2608.

37. Miron, G.D., T. Wagner, D.A. Kulik, and B. Lothenbach, An Internally Consistent Thermodynamic Dataset for Aqueous Species in the System Ca-Mg-Na-K-Al-Si-O-H-C-Cl to 800 C and 5 KBar. *American Journal of Science*, 2017. **317**: p. 755-806.
38. Li, D.D., D.D. Gao, Y.P. Dong, and W. Li, Modeling of Phase Relations and Thermodynamics in the $Mg(OH)_2 + MgSO_4 + H_2O$ System with Implications on Magnesium Hydroxide Sulfate Cement. *Calphad-Computer Coupling of Phase Diagrams and Thermochemistry*, 2019. **67**.
39. Schindelholz, E. and R.G. Kelly, Application of Inkjet Printing for Depositing Salt Prior to Atmospheric Corrosion Testing. *Electrochemical and Solid State Letters*, 2010. **13**(10): p. C29-C31.
40. Bryan, C.R., A.W. Knight, B.L. Nation, T. Montoya, E. Karasz, R. Katona, and R.F. Schaller, *FY21 Status Report: SNF Interim Storage Canister Corrosion and Surface Environment Investigations*. 2021, Sandia National Laboratories: Sandia National Laboratories.
41. Bryan, C. and A.W. Knight, *Analysis of Dust Samples Collected from an Inland ISFSI Site ("Site A")*. 2020, Sandia National Laboratories: Albuquerque, NM.
42. Knight, A.W. and C.R. Bryan, *Analysis of Dust Samples Collected from an Inland ISFSI Site ("Site B")*. 2020, Sandia National Laboratories: Albuquerque, NM
43. Novak, A.H. and B. Runje, *Influence of Object Surface Roughness in CT Dimensional Measurements*, in *7th Conference on Industrial Computed Tomography*. 2017: Leuven, Belguim.
44. Dashti, M. and A. Abdulaziz, A Review on Surface Roughness (Ra) Ranges for Some Finishing Processes. *International Journal of Scientific and Engineering Research*, 2020. **11**(4).
45. Whitehorse, D.J., *Surfaces and Their Measurement* 1st ed. 2002, Boston, MA: CRC Press.
46. Tanbakuchi, A., *Photometrics Report: Cylinder Image Mapping*. 2021, Sandia National Laboratories: Albuquerque, New Mexico.
47. Bryan, C., A. Knight, B. Nation, T. Montoya, E. Karasz, R. Katona, and R. Schaller, *FY21 Status Report: SNF Interim Storage Canister Corrosion and Surface Environment Investigations*. 2021, Sandia National Laboratories: Albuquerque, NM. p. 199.
48. Knight, A., R. Schaller, B. Nation, S. Durbin, and C. Bryan, *FY22 Update: Development of Surface Sampling Techniques for the Canister Deposition Field Demonstration* 2022, Sandia National Laboratories: Albuquerque, New Mexico.
49. Enos, D.G. and C.R. Bryan, *Final Report: Characterization of Canister Mockup Weld Residual Stresses*. 2016, Sandia National Laboratories: Albuquerque, NM. p. 62.
50. *Dekati Accessory: Dekati Dryer DD-600*, D. Ltd, Editor. 2015: Kangasala, Finland.
51. Porter, N.W., D. Brooks, C. Bryan, R. Katona, and R.F. Schaller, *FY21 Status Report: Probabilistic SCC Model for SNF Dry Storage Canisters*. 2021, Sandia National Laboratories: Albuquerque, NM.
52. Chen, Z.Y. and R.G. Kelly, Computational Modeling of Bounding Conditions for Pit Size on Stainless Steel in Atmospheric Environments. *Journal of the Electrochemical Society*, 2010. **157**(2): p. C69-C78.
53. Srinivasan, J., T.D. Weirich, G.A. Marino, A.R. Annerino, J.M. Taylor, P.J. Noell, J.J.M. Griego, R.F. Schaller, C.R. Bryan, J.S. Locke, and E.J. Schindelholz, Long-Term Effects of Humidity on Stainless Steel Pitting in Sea Salt Exposures. *Journal of the Electrochemical Society*, 2021. **168**(2).
54. Weirich, T.D., J. Srinivasan, J.M. Taylor, M.A. Melia, P.J. Noell, C.R. Bryan, G.S. Frankel, J.S. Locke, and E.J. Schindelholz, Humidity Effects on Pitting of Ground Stainless Steel Exposed to Sea Salt Particles. *Journal of The Electrochemical Society*, 2019. **166**: p. C3477-C3487.
55. ASTM International, *ASTM E1457 Standard Test Method for Measurement of Creep Crack Growth Times in Metals*. 2020.
56. ASTM International, *E1681–03 Standard Test Method for Determining Threshold Stress Intensity Factor for Environment-Assisted Cracking of Metallic Materials*. 2008.
57. ASTM International, *E647-15 Standard Test Method for Measurement of Fatigue Crack Growth Rates*. 2015.

58. Ford, F.P., D.F. Taylor, P.L. Andresen, and R.G. Ballinger, *Corrosion-Assisted Cracking of Stainless and Low-Alloy Steels in LWR Environments*. 1987, Electric Power Research Institute Palo Alto, CA. p. 1-128.
59. Katona, R.M., Schaller, R.F., *Stress Corrosion Cracking: Discovery of Governing Mechanisms*, D.o. Energy, Editor. 2022.
60. Harris, Z.D., E.M. Dubas, A.S. Popernack, B.P. Somerday, and J.T. Burns, Elucidating the Loading Rate Dependence of Hydrogen Environment-Assisted Cracking in a Ni-Cu Superalloy. *Theoretical and Applied Fracture Mechanics*, 2020. **111**: p. 102846.
61. Harris, Z.D. and J.T. Burns, The Effect of Loading Rate on the Environment-Assisted Cracking Behavior of AA7075-T651 in Aqueous NaCl Solution. *Corrosion and Materials Degradation*, 2021: p. in review.
62. Knight, A.W., R.F. Schaller, C.R. Bryan, T.J. Montoya, A.M. Parey, J. Carpenter, M. Maguire, and K. Ross, *Corrosion-Resistant Coatings for Mitigation and Repair of Spent Nuclear Fuel Dry Storage Canisters*. 2020, Sandia National Laboratories: Albuquerque, NM.
63. Knight, A.W., B. Nation, M. Maguire, R. Schaller, and C. Bryan, *FY22 Status: Corrosion-Resistant Coatings on Spent Nuclear Fuel*

Canisters to Mitigate and Repair Potential Stress Corrosion Cracking. 2022, Sandia National Laboratories Albuquerque, New Mexico

Appendix A

Bryan, C.R., Knight A.W., Katona R.M., Sanchez A., Schindelholz E.J., and Schaller R.F. (2022). Physical and Chemical Properties of Sea Salt Deliquescent Brines as a Function of Temperature and Relative Humidity. *Science of the Total Environment*, *824*, 154462.

Science of the Total Environment 824 (2022) 154462

Contents lists available at ScienceDirect

Science of the Total Environment

journal homepage: www.elsevier.com/locate/scitotenv

Physical and chemical properties of sea salt deliquescent brines as a function of temperature and relative humidity

C.R. Bryan [a], A.W. Knight [a], R.M. Katona [a,*], A.C. Sanchez [a], E.J. Schindelholz [b], R.F. Schaller [a]

[a] Sandia National Laboratories, Albuquerque, NM 87123, United States of America
[b] Department of Materials Science and Engineering, The Ohio State University, Columbus, OH 43210, United States of America

HIGHLIGHTS

- Validated thermodynamic modeling of deliquesced sea salts
- Deliquesced sea salt changes composition and concentration as a function of relative humidity
- NaCl rich electrolyte above relative humidity of 75 % and $MgCl_2$ rich below
- Investigation of oxygen concertation, density, conductivity, volume, and viscosity across relative humidity and temperature
- Solution deliquescence influences localized corrosion and storage of spent nuclear fuel

GRAPHICAL ABSTRACT

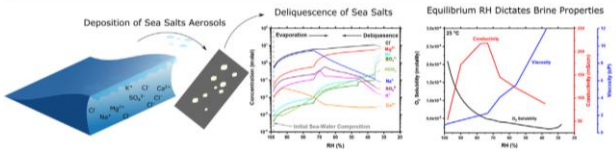

ARTICLE INFO

Article history:
Received 10 January 2022
Received in revised form 25 February 2022
Accepted 6 March 2022
Available online 10 March 2022

Editor: Daniel Alessi

Keywords:
Seawater
Aerosol
Deliquescence
Brine
Localized corrosion
Sea-salt

ABSTRACT

Thermodynamic modeling has been used to predict chemical compositions of brines formed by the deliquescence of sea salt aerosols. Representative brines have been mixed, and physical and chemical properties have been measured over a range of temperatures. Brine properties are discussed in terms of atmospheric corrosion of austenitic stainless steel, using spent nuclear fuel dry storage canisters as an example. After initial loading with spent fuel, during dry storage, the canisters cool over time, leading to increased surface relative humidities and evolving brine chemistries and properties. These parameters affect corrosion kinetics and damage distributions, and may offer important constraints on the expected timing, rate, and long-term impacts of canister corrosion.

1. Introduction

Metallic structures in both near-marine and marine environments typically have a reduced service lifetime in comparison to non-marine environments due to the presence of a corrosive environment. In near-marine and marine settings, the corrosive environment is established when sea salt aerosols are deposited on the metal surfaces and deliquesce to produce chloride-rich brines. The rate and extent of corrosion damage is a function of the chemical and physical properties of the deliquescent brines, and these properties are strongly governed by environmental parameters including relative humidity (RH), temperature, salt loading density (LD), and distribution of salts on the metal surface.

* Corresponding author.
E-mail address: rmkaton@sandia.gov (R.M. Katona).

http://dx.doi.org/10.1016/j.scitotenv.2022.154462

Appendix B

Srinivasan, J., Parey, A., Knight, A., Schaller, R., Locke, J., & Schindelholz, E. (2022). Correlation of Stainless Steel Pit Morphology to Humidity-Specific Sea Salt Brine Constituents. *CORROSION*, 4143.

Correlation of Stainless Steel Pit Morphology to Humidity-Specific Sea Salt Brine Constituents

J. Srinivasan,[‡]* A. M. Parey,*,** A. W. Knight,** R. F. Schaller,** J. S. Locke,* and E. J. Schindelholz[‡,]*

[‡]Corresponding authors. Email: (JS) – srinivasan.82@osu.edu, (EJS) – schindelholz.2@osu.edu

*Fontana Corrosion Center, Department of Materials Science and Engineering, The Ohio State University, Columbus, OH, USA 43210

**Materials Science and Engineering, Sandia National Laboratories, Albuquerque, NM, USA 87185

ABSTRACT

Immersion exposures of 304 stainless steel ground to a #4 finish were conducted in brines representative of the chemistry of sea salt aerosols at low (40%) and high (76%) relative humidity (RH). Low-RH-equivalent brines resulted in cross-hatched pits, whereas high-RH-equivalent brines produced ellipsoidal, faceted pits. Distinct surface micro-cracking was observed to be associated only with cross-hatched pits and appeared to correlate with a high concentration of dissolved carbonate species in low-RH-equivalent solutions, while being absent in the high-RH-equivalent brines. Correlating these results to brine composition suggested that the concentrations of $MgCl_2$ and dissolved carbonate species in the brines could, in the presence of machining-induced surface microstructure and residual stress, determine pit morphology in marine atmospheres, potentially impact stress corrosion cracking susceptibility and lifetime prediction.

KEY WORDS: Austenitic stainless steel, Marine atmospheric corrosion, Relative humidity, Stress corrosion cracking

Appendix C

Katona R.M, Karasz, E.K., & Schaller, R.F. (2022). *An Invited Critical Review:* A Review of the Governing Factors in Pit to Crack Transition of Metallic Structures, *under review in Corrosion Journal.*

A Review of the Governing Factors in Pit to Crack Transitions of Metallic Structures

R. M. Katona[1,=,*], E. K. Karasz[1,=], R. F. Schaller[1]

[1] Sandia National Laboratories, Albuquerque, NM 87123 USA

*Corresponding Author E-mail Address [rmkaton@sandia.gov]

=denotes equal contribution

Key Words

stress corrosion cracking; corrosion fatigue; crack initiation; localized corrosion; pit-to-crack

Abstract

Through a combination of mechanical stresses and corrosive environments, a material's performance may be hindered by the complex evolution of damage due to stress corrosion cracking. Understanding the contribution of the localized corrosion features, loading state, crack-formation features, local microstructure, and environment remains a critical issue when predicting crack initiation and propagation leading to potential metal failure. As such, lifetimes of many exposed alloys are greatly reduced by the presence of corrosion damage and the prediction of this deleterious influence via standard fracture mechanics methods is non-trivial. Current knowledge

Appendix D

Katona, R.M., Burns, J.T., Schaller, R.F., & Kelly, R.G. (2022). Insights from electrochemical crack tip modeling of atmospheric stress corrosion cracking, *accepted in Corrosion Science.*

Insights from electrochemical crack tip modeling of atmospheric stress corrosion cracking

R. M. Katona[1,2,*], J. T. Burns[2], R. F. Schaller[1], and R. G. Kelly[2]

[1] Sandia National Laboratories, Albuquerque, NM 87123 USA
[2] Materials Science and Engineering, University of Virginia, Charlottesville, VA 22904 USA

[*] Corresponding Author E-mail Address [rmkaton@sandia.gov]

Abstract

Crack tip electrochemical conditions are explored utilizing a reactive transport Finite Element Method model for stainless steel 304 exposed to 3 M NaCl. Under simulated full immersion conditions, a steady state pH of 3 and metal chloride concentration of 1.4 M were calculated. It was determined that an increase in cathode length and a decrease in water layer thickness increases total cathodic current per unit thickness, metal chloride concentrations, and decreases crack tip pH. The presented results and discussion call into question whether electrochemical similitude is achieved between different specimens, crack lengths, and between laboratory specimen and field relevant samples.

Key words:
Stainless steel, environmentally assisted cracking, crack tip electrochemistry, finite element model, similitude, modeling, atmospheric corrosion

Graphical abstract

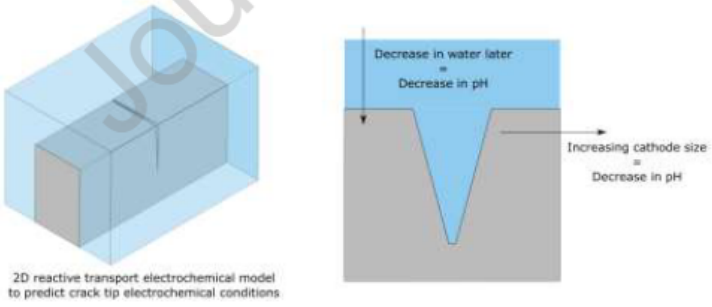

Introduction

Stress corrosion cracking (SCC) and corrosion fatigue (CF) are intrinsically complex processes that are governed by the interaction of the environment, mechanical properties, and material